Spacer Cation Engineering in 2D Hybrid Perovskite

Ph.D. Thesis

by

ETI MAHAL

DEPARTMENT OF CHEMISTRY
INDIAN INSTITUTE OF TECHNOLOGY INDORE

JULY 2024

Spacer Cation Engineering in 2D Hybrid Perovskite

A THESIS

Submitted in partial fulfilment of the

requirements for the award of the degree

of

DOCTOR OF PHILOSOPHY

by

ETI MAHAL

DEPARTMENT OF CHEMISTRY
INDIAN INSTITUTE OF TECHNOLOGY INDORE
JULY 2024

INDIAN INSTITUTE OF TECHNOLOGY INDORE

CANDIDATE'S DECLARATION

I hereby certify that the work which is being presented in the thesis entitled **Spacer Cation Engineering in 2D Hybrid Perovskite** in the partial fulfilment of the requirements for the award of the degree of **DOCTOR OF PHILOSOPHY** and submitted in the **DEPARTMENT OF CHEMISTRY, Indian Institute of Technology Indore**, is an authentic record of my own work carried out during the time period from January 2020 to June 2024 under the supervision of **Prof. BISWARUP PATHAK**, Professor, Department of Chemistry, IIT Indore.

The matter presented in this thesis has not been submitted by me for the award of any other degree of this or any other institute.

Eti Mahal
01/07/2024
Signature of the student with date
(ETI MAHAL)

This is to certify that the above statement made by the candidate is correct to the best of my/our knowledge.

01/07/2024
Signature of Thesis Supervisor with date
(Prof. BISWARUP PATHAK)

ETI MAHAL has successfully given her Ph.D. Oral Examination held on 20/09/2024………………

20/09/2024
Signature of Thesis Supervisor with date
(Prof. BISWARUP PATHAK)

ACKNOWLEDGEMENTS

I would like to express my sincere gratitude to my supervisor Professor Biswarup Pathak, for his constant guidance and encouragement throughout my work. I express profound gratitude to him for fostering the growth of my research ideas and their practical implementation. His encouragement has played a crucial role in my development as an independent researcher. The opportunities he provided to define my research objectives and contribute to lab projects have significantly contributed to my growth over the past five years.

I also thank my PSPC members, Dr. Parimal Kar, and Dr. Selvakumar Sermadurai, for their effective comments and critical analysis of my work during the yearly evaluation. I extend my thanks to all the faculty, staff members, and technicians at the Department of Chemistry, IIT Indore, for their guidance and support during my coursework, department-related activities, and documentations.

I would like to thank my experimental collaborators Professor Sukhendu Mandal, IISER Thiruvananthapuram and Dr. Abhijit Shrotri, Hokkaido University for providing me opportunities to explore diverse theoretical tools and working in tandem with their students (Ms. Saniya Gratious, and Dr. Yayati Naresh Palai) in collaborative projects.

I would like to thank IIT Indore for providing laboratory, computational facilities, and financial support during my work.

I also thank MoE, India, for the research fellowship and travel grant to present my thesis work.

I want to express my sincere gratitude to Dr. Arup Mahata for his guidance, which indeed helped me to start my thesis work, and for always being available to solve my problems. I want to give special thanks to Dr. Gargee Bhattacharya for motivating me to work in a new research area. I would like to thank Dr. Shyama Charan Mandal for his support in the initial days of my doctoral study. Also, I want to thank Dr. Akhil S. Nair, Dr. Sandeep

Das, Dr. Surya Sekhar Manna, and Mr. Diptendu Roy for their help in continuing my research. Special thanks to Mr. Amitabha Das, Mrs. Nishchal Bharadwaj, Mr. Souvik Manna, Ms. Poulami Paul and Ms. Priyanka Ghosh for always being there like brothers and sisters.

I extend my deep appreciation to all my past and present group members Dr. Preeti Bhaurial, Dr. Sourabh Kumar, Dr. Chiranjit Mondal, Dr. Rameshwar Lal Kumawat, Dr. Arunendu Das, Mr. Milan Kumar Jena, Ms. Sneha Mittal, Mr. Rahul Kumar Sharma, Ms. Harpriya Minhas, Mr. Mohd Rashid and Ms. Dipti Maurya for their generous help and co-operation to make my work successful.

I am personally very much grateful to my friends, Mrs. Vinita Singh Patel, Ms. Rajni, and Mrs. Meenu Sharma, for their constant support during my doctoral study. Here, it is specially to be mentioned that it has been a wonderful experience to work with many friends and seniors/juniors at IIT Indore during my work who really helped me in many aspects.

My special thanks to Dr. Avishek Das for everything.

Finally, I would like to thank my parents, Mr. Chittaranjan Mahal, and Mrs. Sefali Mahal for all the love and trust they gave for being able to reach here. I want to offer special thanks to my uncle, Mr. Nitai Chandra Mahal, for giving me my childhood education and love. I want to thank my sisters Samapti Mahal and Santwana Mahal, my brother-in-law Bablu Das, and my son, Ahan Das for all their love and support. I extend my sincere gratitude to everyone who has played a direct or indirect role in this venture.

ETI MAHAL

Dedicated to

My Teachers

SYNOPSIS

1. Introduction

The current energy landscape demands the development of cost-effective renewable energy technologies. In this regard hybrid perovskites have gained numerous attentions since last decade for their application in photovoltaic devices as an intrinsic absorber.[1-3] They can be easily synthesized using solution based low cost methods which is a major advantage for using hybrid perovskites. Additionally, they have excellent properties useful for photovoltaics like high optical absorption coefficient (~105 cm−1), well balanced charge transfer as well as defect tolerance. Unfortunately, this unique material possess very low formation energy and is very much prone to degrade in presence of light and moisture.[4-5] In this context 2D hybrid perovskites containing large organic cation emerged as a potential alternative. Owing to the presence of strong van der Waals forces in the large organic molecules, this group of materials possesses very high formation energy and thus are much more stable compared to their 3D counterpart.[6-8] Due to replacement of small cations by large cations, these organic cations cannot fit inside the octahedral cavity and thus form layered structures separating the inorganic metal halide layers (Figure 1).

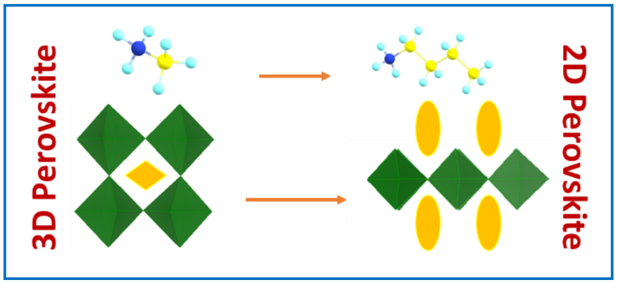

Figure 1: Representation of the separation of inorganic layers by organic cations in 2D hybrid perovskites.

Due to this layer separation and dielectric mismatch between organic and inorganic layers, this class of materials are considered as naturally occurring multiple quantum wells (MQW).[9-10] As a result of this MQW structure, these materials possess large band gap, strongly bound excitons and large charge carrier masses. In general, the valence band edge of hybrid perovskites is dominated by halogen p-orbitals with a small contribution from metal s orbitals. On the other hand, the conduction band edge is mainly composed of metal p orbitals.[11] In case of 2D hybrid perovskites, the widespread presence of organic spacers enabled the presence of organic atomic orbitals at the band edges. Based on the arrangement of organic and inorganic molecular orbitals at the band edges, the 2D perovskites found their application in various devices. This arrangement is known as intramolecular band alignment and can be of four types. When both valence and conduction bands dominate either by inorganic elements or by organic elements they are termed as type I material (either both from inorganic (I_a) or organic (I_b) elements). On the other hand, in type II material, different elements contribute to the band edges (inorganic-organic (II_a) and organic-inorganic (II_b)). Type I materials are useful for the application in LEDs as well as laser due to selective light emission from inorganic-inorganic (I_a) or organic-organic (I_b) transitions.[12-13] Variation of spacer cations can enable us to find all these four types of materials.

Therefore, in this thesis we have taken the help of DFT, ab initio molecular dynamics (AIMD) simulations and machine learning (ML) based tools to understand the stability and optoelectronic properties of various types of 2D hybrid perovskites.

2. Objectives

The main objective of this thesis is to find out the controlling ability of organic spacer cations in the structure and optoelectronic properties of 2D hybrid perovskites. The chapter wise objectives of this thesis are as follows:

i. To understand the stability of 2D hybrid perovskites at the water interfaces as well as to study the different kind of interactions that could take place at three possible surfaces terminations (metal- iodide termination, iodine termination and cation termination).

ii. To understand the influence of spacer cations on the structure of the 2D perovskite which indeed controls the electronic structure of the material.
iii. To achieve the organic cation dominated conduction band edge of 2D hybrid perovskites by introducing oxygen (pyrylium) and sulphur (thiopyrylium) containing heterocyclic ring-based spacer cations.
iv. To reveal the controlling factor among conjugation and functional group substitution in the alignment of energy levels between inorganic and organic layers of 2D hybrid perovskites.
v. To develop a machine learning model that can identify the intramolecular band alignment type of a 2D hybrid perovskites using simple elemental and molecular based features.

3. Summary of the research work

Chapter wise contents of the thesis are discussed in the following sections:

1.1. Introduction (Chapter 1)

In this chapter, we have briefly discussed about the necessities of renewable energy at the current energy landscape. The history of the discovery of the hybrid perovskite solar cell were given. The structure and unique properties of 3D hybrid perovskites which make them the most suitable material for solar cell were discussed. Also, the drawbacks of these champion materials which forces to think about possible alternatives were included. Then we have introduced the 2D perovskites and their advantages over 3D perovskites. Also, we have mentioned the strategies that could be used to tune the properties of 2D hybrid perovskites.

The works which we have included in this thesis involves density functional theory (DFT), ab initio molecular dynamics (AIMD) and machine learning (ML) to explore the role of spacer cations on the optoelectronic properties of 2D hybrid perovskites. Thus, we have discussed the theories involved in these computational as well as machine learning techniques.

1.2. Stability of 2D hybrid perovskites at water interfaces (Chapter 2)

In this chapter, the stability and interaction nature of 2D hybrid perovskites at water interfaces were studied using ab initio molecular dynamics simulations. All possible surface terminations (PbI2, I-, organic cation-) of Ruddlesden-Popper (RP) and Dion-Jacobson (DJ) phases of 2D perovskites was considered. Two perovskites RP phase (BA)2PbI4 and DJ phase (3AMP)PbI4 with different terminations interfacing water molecules were modelled for the study. The time averaged structures were analyzed with the help of radial pair distribution functions to decipher the degradation mechanisms of the 2D hybrid perovskites in moist environment. A comparison between three different surface terminations were done to find the most robust surface in presence of water. Different surface terminations were found to undergo distinct interactions with water molecules. Pb-O interactions are found to be the most prominent for the PbI2 terminated surfaces where RP phase interacts more strongly compared to DJ. In case of I terminated surfaces, the more pronounced interaction is the I2 formation which results due to the nucleophilic substitution of water molecules at Pb metal centres. This could be the possible degradation route for this surface. The cation terminated surfaces are observed as the most robust in contact with water molecules resisting them to infiltrate through the hydrophobic organic layer (Figure 2). In this interface, very poor interaction between lead iodide layer and water molecules was observed keeping the H-bonding interaction between organic ammonium hydrogen and axial iodide intact.

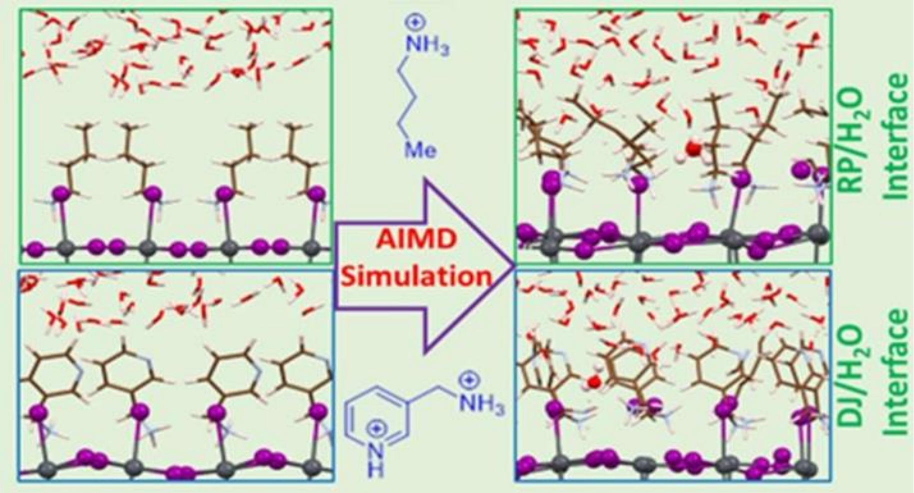

Figure 2: Considered RP and DJ phase cation terminated perovskite/water interface models before and after simulation.

1.3. Understanding the Role of Spacer Cation on the Electronic Structure of 2D Hybrid Perovskites (Chapter 3)

In this chapter, the role of spacer cation on the structure and optoelectronic properties of 2D hybrid perovskites were studied considering seven perovskite systems. Among considered systems three contains monovalent spacer cations (n-butylammonium ((BA)2PbI4), 3-aminopropionitrile ((3-APN)2PbI4), phenyl ethyl ammonium ((PEA)2PbI4)) whereas four contains divalent spacer cations (geometrical isomers of pyridinium ethyl ammonium ((PyrEA)PbI4, (2-PyrEA)PbI4, (3-PyrEA)PbI4 and (4-PyrEA)PbI4). Size and geometry of the spacer cation was found to have a major role in controlling the structural patterns of the metal halide layers. (BA)2PbI4 and (PEA)2PbI4 perovskites faces strong octahedral distortion with large deviation in Pb-I-Pb bond angle from ideal. Also, ((PEA)2PbI4 possess dissimilar Pb-I bond distances with one much elongated axial Pb-I bond. Another monopositive spacer cation 3-APN found to provide exceptional reduction in the octahedral distortion with Pb-I-Pb bond angle close to 180° providing substantial overlap between Pb and I atomic orbitals. Also, this 3-APN cation provides small inorganic layer separation due to strong intermolecular H-bonding present between two cation that makes the organic layer rigid. Good overlap between metal and halide orbitals as well as smaller inorganic layer separation decreases the band gap and carrier masses of this material (Figure 3). Dications found to provide smaller inorganic layer separation deceasing the band gap and carrier masses of perovskites containing dicationic spacers. This work reveals the influence of spacer cation on the octahedral distortion of the metal-halide layer as well as inorganic layer separation which indeed controls the electronic properties of the 2D hybrid perovskite systems.

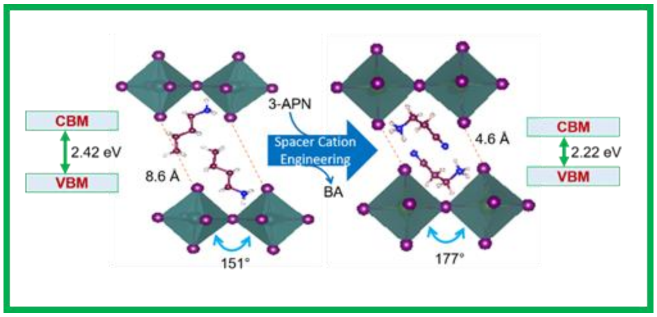

Figure 3: Decrease in inorganic layer separation by changing spacer cation from BA to 3-APN with ultimate reduction in material band gap.

1.4. Tuning Band Edge Composition of 2D Hybrid Perovskites with Spacer Cations (Chapter 4)

In this chapter, considering Dion–Jacobson phases of 2D perovskites the band edge compositions were tuned using heterocyclic ring based spacer. The commonly found hybrid perovskite materials possess band edge electronic structure composed of metal and halide atomic orbitals. Organic cations usually do not contribute to the band edges. In this chapter four new 2D hybrid perovskite materials were designed with oxygen (pyrylium) and sulphur (thiopyrylium) containing heterocyclic ring based spacer cation. Thermodynamic, structural as well as electronic properties of these designed materials were compared with the previously reported pyridinium based Dion-Jacobson phase perovskite. In all these four materials conduction band edges were dominated by the cation composition (Figure 4). This result is due to the stabilized lowest unoccupied orbitals of the considered spacer cation. Also due to this downshifting of the conduction band edge the band gaps of these materials were significantly smaller compared to similar pyridinium ring based perovskites. Band gap value as low as 1.90 eV was achieved in one of the designed materials. Along with this band structure as well as carrier masses were also calculated.

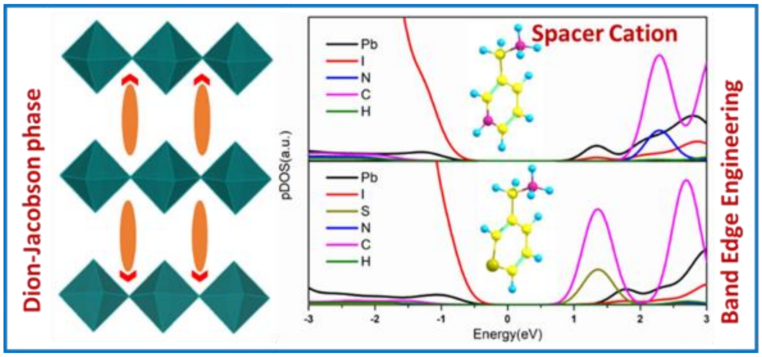

Figure 4: Obtaining organic cation contribution to the conduction band edge by replacing pyridinium with thiopyrylium.

1.5. Optimizing Alignment of Energy Levels between Organic and Inorganic Layers of 2D Hybrid Perovskites (Chapter 5)

In this chapter, a detailed analysis about the predictability of the energy level alignment between inorganic and organic layers of the 2D hybrid perovskites were done. The electronic structure of perovskites containing 3-phenyl-2-propenammonium cation as a spacer was explored which displayed the active participation of conjugated ammonium spacers in the electronic structure of the perovskite. Following this, variety of amines were considered to find out the controlling factor among substituents and conjugation on the energy level alignment. The excitation levels of the organic spacer molecules were calculated and possible alignments with the perovskite excitonic levels were predicted. Importance of extended conjugation over functional group substitution to modulate the organic inorganic energy level alignments was revealed. By performing molecular dynamics simulations we have also verified the feasibility of our results at finite temperature conditions. Preferred combination of inorganic and organic layer to induce the excitonic energy transfer from inorganic to organic were obtained. After the transfer of inorganic excitonic energy to organic triplet excited state, the radiative emission could happen in the 2D hybrid perovskites with the proposed combination (Figure 5). Different possible colors that can be emitted from these proposed combinations were also analyzed which have potential applications in different light emitting devices.

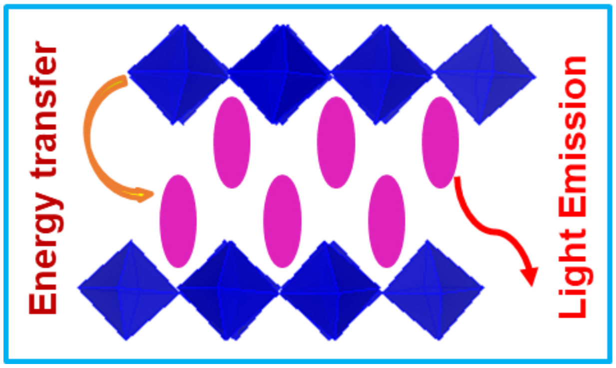

Figure 5: 2D hybrid perovskites featuring excitonic energy transfer from inorganic to organic layer and radiative emission from organic spacer.

1.6. Machine Learning Driven Prediction of Intramolecular Band Alignment Types in 2D Hybrid Perovskites (Chapter 6)

In this chapter, using machine learning algorithms 2D hybrid perovskites were classified based on the intramolecular band alignment types. There are four type of intramolecular band alignment possible for 2D hybrid perovskites which are applicable for specific devices (Figure 6). Collecting material from available 2D perovskite database their electronic structure calculations were performed to obtain the intramolecular band alignment type. Physical as well as chemical properties that influence the band alignment type were considered as features to develop the machine learning model. Hyperparameter tuning with various available machine learning algorithm like logistic regression, ridge classifier, random forest classifier, bagging classifier were performed to find out the best fitted model. Logistic regression was found to give good test as well as cross validation accuracy. Feature contribution coefficients were calculated using logistic regression and finally selected nine features. Also, the given model equation can predict the band alignment type of any 2D hybrid perovskites with the help of molecular and elemental features.

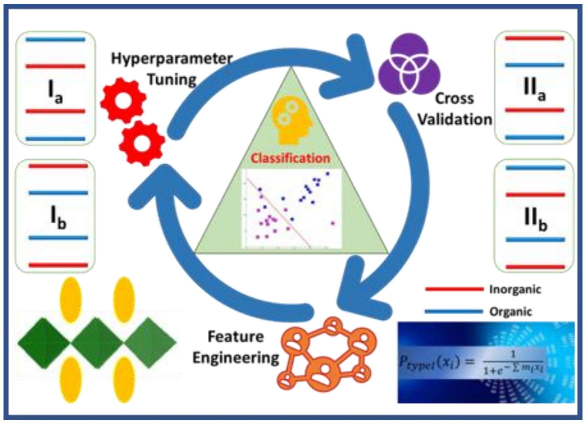

Figure 6: Intramolecular band alignment types, machine learning workflow.

4. Conclusions

The conclusion of these chapters are as follows:

1. The cation terminated surfaces are most robust compared to PbI2 and iodine terminations in presence of moisture due to the strong van der Waals interactions present in the organic cations. Iodine terminated surface is most reactive at the water interface. Also, in PbI2 and iodine terminated surfaces hydrophobic organic cations keep inner layers protected from the water molecules.
2. Size and shape of the organic cations have significant role in the structure and electronic properties of the 2D hybrid perovskites. Our considered 3-aminopropionitrile cation possess strong intermolecular hydrogen bonding between them making the organic layer rigid which indeed results small inorganic layer separation and nearly ideal Pb-I-Pb bond angle leading to substantial overlap between Pb and I atomic orbitals and small band gap.
3. Band edge compositions of the 2D hybrid perovskites are tunable with by varying the organic cations. Replacing the heteroatom(N) of pyridine

ring in 3-aminomethylpyridinium by oxygen and sulphur the organic dominant conduction band edge was obtained along with reduced band gap.

4. Effect of conjugation in obtaining organic cation contribution in band edges as well as organic inorganic energy level alignments were revealed. Aligning singlet as well as triplet excitation levels of a set of organic spacers with the excitonic energies of the perovskite preferable energy level alignments were obtained. A set of organic-inorganic combinations with potential in various light emission was proposed.
5. 2D hybrid perovskites were classified based on their intramolecular band alignments. Simple logistic regression model was able to classify them with good accuracy score (0.86). Given model equation is able to predict the band alignment type of any 2D hybrid perovskite using some easily affordable elemental and molecular features.

5. References

1. Kojima A., Teshima K., Shirai Y., Miyasaka T. (2009), Organometal Halide Perovskites as Visible-Light Sensitizers for Photovoltaic Cells, J. Am. Chem. Soc., 131, 6050−6051. (DOI: 10.1021/ja809598r)
2. Lee M. M., Teuscher J., Miyasaka T., Murakami T. N., Snaith H. J. (2012), Efficient hybrid solar cells based on meso-superstructured organometal halide perovskites, Science, 338, 643−647. (DOI: 10.1126/science.1228604)
3. Jena A. K., Kulkarni A., Miyasaka T. (2019), Halide Perovskite Photovoltaics: Background, Status, and Future Prospects, Chem. Rev., 119, 3036−3103. (DOI: 10.1021/acs.chemrev.8b00539)
4. Frost J. M., Butler K. T., Brivio F., Hendon C. H., van Schilfgaarde M., Walsh A. (2014) Atomistic Origins of High-Performance in Hybrid Halide Perovskite Solar Cells, Nano Lett., 14, 2584− 2590. (DOI: 10.1021/nl500390f)

5. Zhao Y., Zhu K. (2014), Optical Bleaching of Perovskite (CH3NH3)PbI3 Through Room-Temperature Phase Transformation Induced by Ammonia, Chem. Commun., 50, 1605−1607. (DOI: 10.1039/C3CC48522F)
6. Smith I. C., Hoke E. T., Solis-Ibarra D., McGehee M. D., Karunadasa H. I. (2014), A Layered Hybrid Perovskite Solar-Cell Absorber with Enhanced Moisture Stability, Angew. Chem., Int. Ed., 53, 11232−11235. (DOI: 10.1002/anie.201406466)
7. Stoumpos C. C., Cao D. H., Clark D. J., Young J., Rondinelli J. M., Jang J. I., Hupp J. T., Kanatzidis M. G. (2016), Ruddlesden−Popper Hybrid Lead Iodide Perovskite 2D Homologous Semiconductors, Chem. Mater., 28, 2852−2867. (DOI: 10.1021/acs.chemmater.6b00847)
8. Quan L. N., Yuan M., Comin R., Voznyy O., Beauregard E. M., Hoogland S., Buin A., Kirmani A. R., Zhao K., Amassian A., et al. (2016), Ligand-Stabilized Reduced-Dimensionality Perovskites, J. Am. Chem. Soc., 138, 2649−2655. (DOI: 10.1021/jacs.5b11740)
9. Katan C., Mercier N., Even J. (2019), Quantum and Dielectric Confinement Effects in Lower-Dimensional Hybrid Perovskite Semiconductors, Chem. Rev., 119, 3140−3192. (DOI: 10.1021/acs.chemrev.8b00417)
10. Sapori D., Kepenekian M., Pedesseau L., Katan C., Even J. (2016), Quantum confinement and dielectric profiles of colloidal nanoplatelets of halide inorganic and hybrid organic-inorganic perovskites, Nanoscale, 8, 6369−6378. (DOI: 10.1039/C5NR07175E)
11. Umebayashi T., Asai K., Kondo T., Nakao A. (2003), Electronic Structures of Lead Iodide Based Low-Dimensional Crystals, Phys. Rev. B, 67, 155405. (DOI: 10.1103/PhysRevB.67.155405)
12. Liu C., Huhn W., Du K.-Z., Vazquez-Mayagoitia A., Dirkes D., You W., Kanai Y., Mitzi D. B., Blum V. (2018), Tunable Semiconductors: Control Over Carrier States and Excitations in Layered Hybrid Organic-

Inorganic Perovskites, Phys. Rev. Lett., 121, 146401. (DOI: 10.1103/PhysRevLett.121.146401)

13. Zhang L., Zhang X., Lu G. (2020), Intramolecular Band Alignment and Spin-Orbit Coupling in Two-Dimensional Halide Perovskites, J. Phys. Chem. Lett., 11, 6982−6989. (DOI: 10.1021/acs.jpclett.0c02135)

List of Publications

Publications included in Thesis:

1. Mahal E., Mandal S. C., Pathak B. (2022), Understanding the role of spacer cation in 2D layered halide perovskites to achieve stable perovskite solar cells, Mater. Adv., 3, 2464−2474. (DOI: 10.1039/D1MA01135A) (Impact Factor: 5.0)
2. Mahal E., Mandal S. C., Pathak B. (2022), Band Edge Engineering of 2D Perovskite Structures through Spacer Cation Engineering for Solar Cell Applications, J. Phys. Chem. C, 126, 9937–9947. (DOI: 10.1021/acs.jpcc.2c01840) (Impact Factor: 3.7)
3. Mahal E., Mandal S. C., Roy D., Pathak B. (2023), Energy level alignments between organic and inorganic layers in 2D layered perovskites: conjugation vs. substituent, Nanoscale, 15, 7962-7970. (DOI: 10.1039/D3NR01105D) (Impact Factor: 6.7)
4. Mahal E., Roy D., Manna S. S., Pathak B. (2023), Machine Learning Driven Prediction of Band Alignment Types in 2D Hybrid Perovskites, J. Mater. Chem. A, 11, 23547-23555. (DOI: 10.1039/D3TA05186B) (Impact Factor: 11.9)
5. Mahal E., Manna S. S., Das S., Pathak B. Understanding Moisture Stability and Degradation Mechanisms in 2D Hybrid Perovskites: Insights from Ab Initio Molecular Dynamics Simulations, (Manuscript communicated))

Publications apart from Thesis

1. Gratious S., Afreen,‡ Mahal E.,‡ Thomas J., Saha S., Nair A. S., Adarsh K. V., Pathak B., Mandal S. "Visualizing" the partially reversible conversion of gold nanoclusters via Au23(S-c-C6H11)17 intermediate, Chemical Science, (Just accepted) (‡ These authors contributed equally to this work.) (Impact Factor: 8.4)

Table of Contents

Chapter 2: Stability of 2D hybrid perovskites at water interfaces

Chapter 3: Understanding the Role of Spacer Cation on the Electronic Structure of 2D Hybrid Perovskites

Chapter 4: Tuning Band Edge Composition of 2D Hybrid Perovskites with Spacer Cations

Chapter 5: Optimizing Alignment of Energy Levels between Organic and Inorganic Layers of 2D Hybrid Perovskites

Chapter 6: Machine Learning Driven Prediction of Intramolecular Band Alignment Types in 2D Hybrid Perovskites

Chapter 7: Scope for Future Works

List of Figures and Schemes

Chapter 1

Chapter 2

Chapter 3

Chapter 4

Chapter 5

Chapter 6

List of Tables

Chapter 1

Chapter 2

Chapter 3

Chapter 4

Chapter 5

Chapter 6

Acronyms

3D	Three Dimensional
2D	Two Dimensional
RP	Ruddlesden-Popper
DJ	Dion-Jacobson
MA	Methyl Ammonium
BA	Butyl Ammonium
MQW	Multiple Quantum Well
LED	Light Emitting Diodes
HOMO	Highest Occupied Molecular Orbital
LUMO	Lowest Unoccupied Molecular Orbital
DFT	Density functional theory
LDA	Local density approximation
GGA	Generalized Gradient Approximation
PBE	Perdew-Burke-Ernzerhof
HSE	Heyd-Scuseria-Ernzerhof
PAW	Projector augmented wave
QE	Quantum Espresso
VASP	Vienna Ab initio Simulation Package
PBC	Periodic Boundary Conditions
RDF	Radial Distribution Function
PDOS	Projected Density of States
ML	Machine Learning
PCC	Pearson correlation coefficients

Chapter 1

Introduction

1.1. Energy Landscape

Energy is the outmost necessity towards development of the society. With increasing population, the global energy demand is increasing day by day in terms of transport as well as electricity. Till now the energy demand is majorly fulfilled by the fossil fuels, which is limited. In a few years, there may be a severe energy crisis due to the exhaustion of fossil fuels. Also, using fossil fuel as a source of energy generates greenhouse gases such as CO_2, which are causing global warming and climate change, which is the current threat to humanity.*[1]* The current energy landscape requires advancement in renewable energy technology such as solar, wind power and hydraulic. Considering the availability and power generation ability solar power can be considered as best alternative.*[2-4]* Among developed solar cell technologies silicon solar cells are considered as the first generation solar cells which uses crystalline silicon as the absorber. The processing technique of pure crystalline silicon is extremely costly that limits its use as the alternative to fossil fuels. In cost effective technologies the dye-sensitized solar cells (DSSCs) have emerged but their low efficiency limits their commercialization. In this context, hybrid perovskite photovoltaics have received numerous attentions since last decade due to high performance along with low cost.*[5]*

1.2. History of Perovskite Solar Cell

The field of photovoltaics have witnessed the most distinguished development through the perovskite solar cells using organic-inorganic hybrid lead halide perovskite as the intrinsic absorber. Since their discovery in 2009 the power conversion efficiency (PCE) efficiency has reached a record high value of 26.1% (Figure 1.1) according to the last report giving tough competition to the single junction and multi junction solar cells based on traditional semiconductors like Si, GaAs among others.*[6,7]* Along with the high performance, the low cost solution processed synthesis methodologies are the main reason of interest. Most notably, owing to their unique properties' perovskites have applications in many other devices beyond solar cells like in light emitting diodes, memory devices, photodetectors, X-ray detectors, and so on.*[5]*

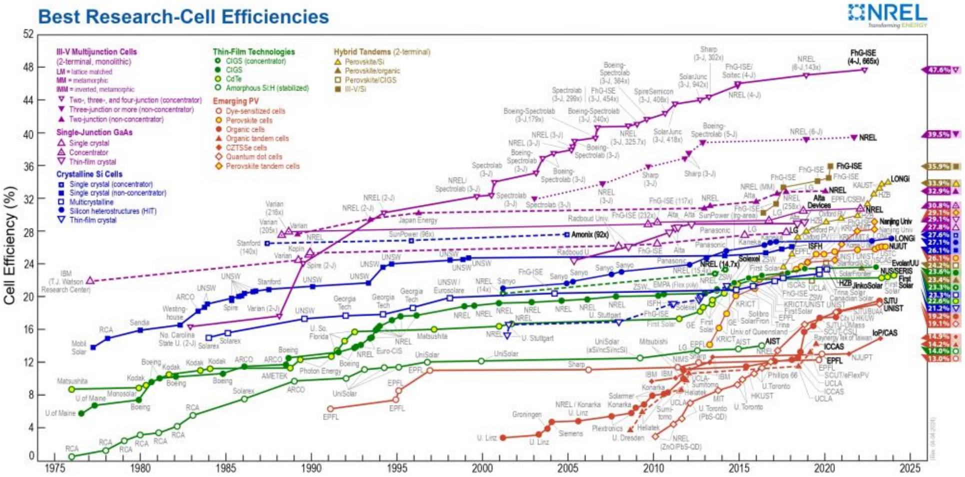

Figure 1.1: Year wise power conversion efficiencies of emerging photovoltaic technologies published by NREL. (Reprinted with permission from Ref. 7)

Initially, the term "perovskite" were referred as metal oxides with perovskite type structures, which are generally either ferroelectric or piezoelectric in nature.*[8-10]* In 1978, Weber has first analysed the crystallographic structure of organic inorganic hybrid lead halide perovskite ($CH_3NH_3PbX_3$).*[11-12]* Later in 1990's, David Mitzi's group have used small and large organic cations and synthesized 3D and 2D hybrid perovskites respectively.*[13-15]* They have mainly focused on the physical properties of 2D perovskites. In 2009, Miyasaka and co-workers have first reported the perovskite solar cells with a power conversion efficiency around 3.81% using $CH_3NH_3PbI_3$.*[6]* Later, in 2012 in collaboration with Snaith's group they have achieved a PCE of 10.9% with mixed halide perovskites ($CH_3NH_3PbI_{3-x}Cl_x$).*[16]* Till then with a constant effort made by the perovskite community the PCE of perovskite solar cells has achieved a remarkably high efficiency of 26.1% (Figure 1.1).

1.3. Hybrid Perovskites

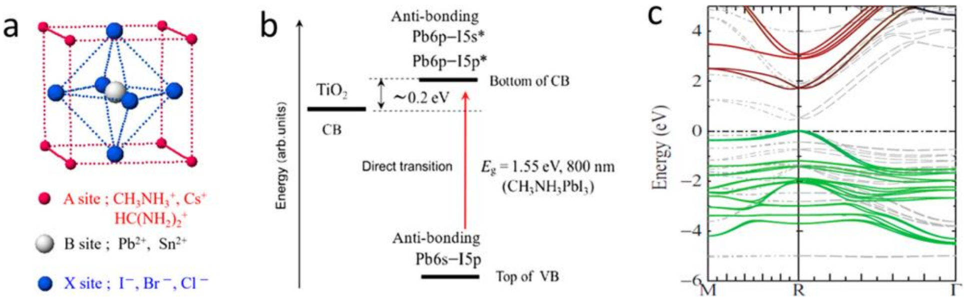

Figure 1.2: (a) Hybrid perovskite crystal structure. (b) Band gap and band edge compositions of $CH_3NH_3PbI_3$. (c) Band structure of $CH_3NH_3PbI_3$ using QSGW method, valence band maximum has been set to zero. Bands of Pb 6s, Pb 6p, and I 5p are depicted by blue, red, and Green solid lines, respectively. Corresponding bands using Local Density Approximation are shown by Light-gray dashed lines. (Reprinted with permission from Ref. 5; Copyright 2019, American chemical society)

Hybrid perovskites are a class of material that posses the general formula ABX_3 where A is a small organic cation such as methylammonium (MA), formamidinium (FA); B is divalent metal atom preferably Pb^{2+} and Sn^{2+} and X is a halide (Cl, Br, I). Metal and halides form a corner sharing octahedral arrangement where the organic cation sits inside the octahedral cavity (Figure 1.2a).*[5]* Since the organic cation needs to fit inside the cavity, there is a rule known as Goldschmidt's Tolerance Factor (Eqn. 1) which decides the structural stability of the hybrid perovskites.*[17]* These materials can be synthesized using solution processed methodologies which demands low cost.

$$t = \frac{r_A + r_B}{\sqrt{2}(r_B + r_X)} \qquad (1.1)$$

Where, r_A, r_B, and r_X represents the ionic radii for the organic cation, metal ion, and halide, respectively.

Unlike the typical semiconductor materials such as Si, CdTe, GaAs which are essentially covalent in nature, hybrid perovskites are ionic crystals that behave as semiconductor. Band gap as well as the absorption wavelength of the hybrid perovskite materials can be easily tuned by varying the halides. This excellent optical absorption property is highly useful in visible light optoelectronics. The most common material $MAPbI_3$ posses some unique semiconductor property for which it is a standard intrinsic absorber for the photovoltaic cell.*[18]* Density functional theory based studies revealed that the valence band (VB) of $MAPbI_3$ is dominated by I atomic orbitals with 70% of I 5p contribution and 25% of Pb $6s^2$ contribution whereas, the conduction band (CB) majorly controlled by the Pb 6p orbitals.*[19-21]* Also, the band structure calculations revealed the direct band gap nature of this material.*[22]* Because of the direct band gap and p-p electronic transition $MAPbI_3$ possess exceptionally high optical absorption coefficients (10^5 cm^{-1}).*[23]* Owing to this rare band composition $MAPbI_3$ keep unique defect properties where the defect generated trap states either lie between the bands or remained as shallow traps near the band edges. In addition due to small effective masses the photogenerated carriers are highly mobile and owing to the rashba spin splitting they preserve longer lifetime.*[24-28]*

1.3.1. Environmental Stability Issue

Even after this exceptionally high efficiencies, hybrid perovskite solar cells are still not commercialised due to their stability issues. For the application of hybrid perovskites in solar cell they need to be exposed in open space but these materials are not stable in such operational condition. There are reports of their reactivity with Lewis bases.*[29-30]* In presence of NH_3 the brown colour of the $MAPbI_3$ film changes to colourless and the reaction is reversible in nature.*[29]* Whereas, in presence of water perovskite film permanently becomes yellow. There are many possible mechanisms of the decomposition reaction (Figure 1.3). According to one report, a single water molecule has the ability to efficiently decompose the perovskite material forming byproducts like HI and CH_3NH_2 whereas in presence of sufficient water $MAPbI_3$ completely decomposed to PbI_2.*[30]*

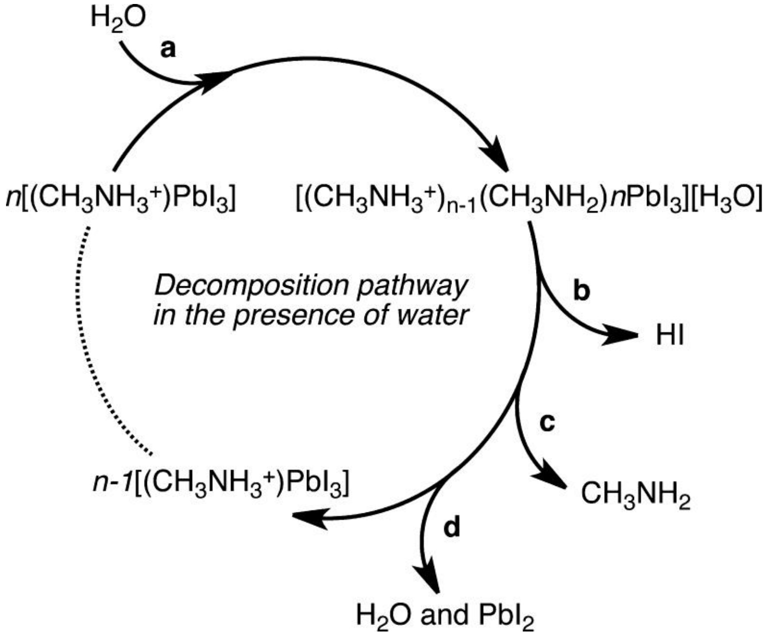

Figure 1.3: Possible pathway for water induced decomposition of hybrid halide perovskites. Initially, single water molecule, can start the process followed by the phase changes of both hydrogen iodide, (b, soluble in water) and the methylamine (c, volatile and soluble in water) which fuels the decomposition. Water induced decomposition results formation of a yellow solid corresponding to the experimentally observed PbI_2, d. (Reprinted with permission from Ref. 30; Copyright 2014, American chemical society)

1.3.2. 2D Hybrid perovskites

To address the stability issue, large organic cations are introduced to replace the small organic cation which is the main reason of the degradation.*[31-32]* The large organic ammoniums possess strong van der Waals forces that enriches these materials with high formation energy (Figure 1.4).*[33]* Because of very high formation energies the perovskites containing large organic ammoniums are highly stable compared to $MAPbI_3$.

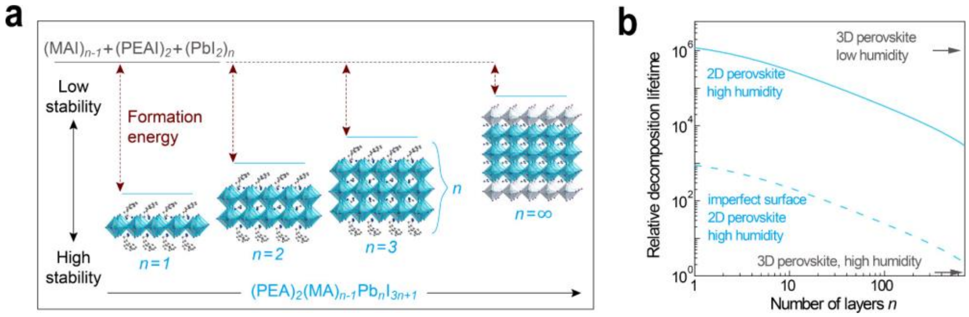

Figure 1.4: Comparison between formation energy and stability of perovskites. (a) Unit cell crystal structure of perovskites with formula $(C_8H_9NH_3)_2(CH_3NH_3)_{n-1}Pb_nI_{3n+1}$ where increase in the layer thickness indicates the change of dimensionality from 2D (n = 1) to 3D (n = ∞). (b) DFT simulated formation energy of perovskite through a range of n values in different atmospheres. (Reprinted with permission from Ref. 33; Copyright 2016, American Chemical Society)

However, the large cations cannot fit inside the octahedral cavity thereby resulting layered type structure. In addition, the large organic molecules are very much low dielectric in nature compared to the metal halide layer. Due to this large dielectric mismatch between organic and inorganic layers electronic movement is confined along the stacking direction and this type of layered perovskites are termed as 2D hybrid perovskites where the organic ammoniums are called spacer cations. This class of perovskites can be characterized by the general formula A_mBX_4 where m=1,2 depending on the charge of the spacer cation. 2D hybrid perovskites are example of naturally occurring multiple quantum wells (MQW, Figure 1.5b) where the organic cationic layers act as barriers and metal halide layers act as wells.*[34-35]* Owing to the relaxation of the Goldschmidt's Tolerance Factor, the class of 2D hybrid perovskites possess high chemical flexibility allowing the utilisation of enormous available organic ammoniums as spacer cation. However, all these advantages come in expense of the excellent optoelectronic properties. Due to the MQW nature 2D perovskites possess larger bandgap compared to their 3D counterpart along with poor carrier properties.

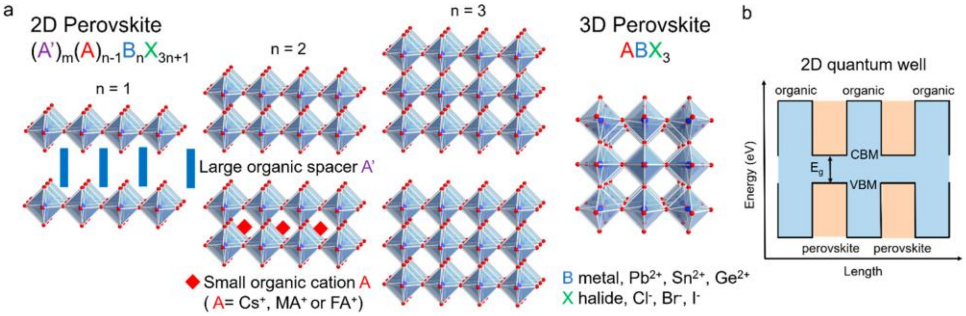

Figure 1.5: (a) Schematic illustration of the connection between 2D, quasi 2D, and 3D perovskite. (b)Illustration of 2D quantum well structure. (Reprinted with permission from Ref. 36; Copyright 2019, American Chemical Society)

1.3.3. Quasi 2D Hybrid Perovskites

Quasi 2D perovskites are in recent focus due to their better stability compared to the 3D perovskite materials.*[31]* This class of materials are bridge between 3D and 2D perovskites. Here, by separating corner sharing metal halide octahedra of 3D perovskite along a particular direction, large organic spacer cations are inserted to make 2D perovskites where one octahedral layer is separated from others by spacer cation layer.*[36]* The general formula of quasi 2D perovskites is $A'_mA_{n-1}B_nX_{3n+1}$ where A′ and A are large spacer cation and small cage cation respectively, m=1,2, n=1-∞, n value defines the thickness of the 3D layer. In the formula when n value is 1 the perovskite becomes a pure 2D perovskite, whereas n=∞ directs to the pure 3D perovskite (Figure 1.5a). This class of materials possess properties of both 3D and 2D perovskites. They are more stable compared to the 3D analogues due to the 2D insertion whereas their optoelectronic properties are much better compared to the pure 2D systems.

1.3.4. Phases of 2D Hybrid Perovskites

There are different phases of 2D hybrid perovskites.*[37]* The reported phases are Ruddlesden−Popper (RP), Dion−Jacobson (DJ) (Figure 1.6), perovskites based on alkyl diammonium cations (DC) and alternating cations in the interlayer space (ACI). Among these the RP and DJ phases are most found. RP phases contain mono ammoniums as spacer whereas DJ phases are comprised of dicationic spacers. The general formula of RP phases perovskites is $A'_2A_{n-1}B_nX_{3n+1}$ whereas the DJ phases are defined by the general stoichiometry $A'A_{n-1}B_nX_{3n+1}$. Where A′ is the large organic spacer cation monovalent and divalent for RP and DJ phases respectively.

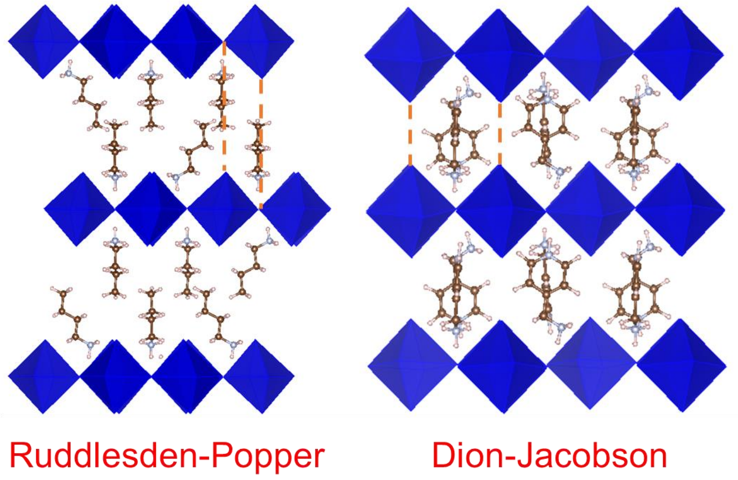

Figure 1.6: Two most common phases of 2D hybrid perovskites.

In RP phases the inorganic layers acquire staggered arrangement where the consecutive metal halide octahedrons are half unit cell shifted from each other. Whereas the DJ phase perovskites possess eclipsed arrangement with consecutive MX_6 units aligning exactly on top of each other. In RP phases two layers of organic cations present between inorganic layers developing van der Waals gap between spacer cations. On the other hand, DJ phase possess one cationic layer due to their dipositive charge and perovskites of this phase are much more rigid in nature.

1.3.5. Moisture Stability of 2D Hybrid Perovskites

For application of these materials in optoelectronic devices their open exposure to the nature is necessary. In this regard stability of 2D hybrid perovskites in operational conditions is an outmost interest. There are experimental reports of degradation of 2D hybrid perovskites in presence of water.

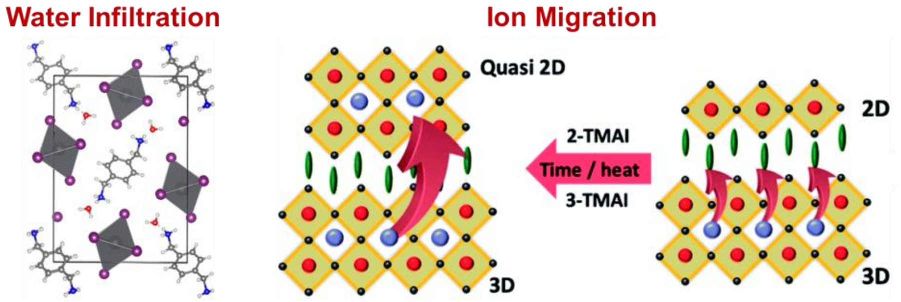

Figure 1.7: Experimental reports of water infiltration and dynamical nature of 2D perovskites. (Reprinted with permission from Ref. 41 and Ref 39; Copyright 2021, American Chemical Society; Copyright 2020, Royal Society of Chemistry)

Rapid disproportionation of phenylethylamine based n=5 quasi 2D perovskite to perovskite with smaller n value in presence of humidity was reported.*[38]* Similar dynamical nature of 2D/3D interfaces also reported by Sutanto et al (Figure 1.7). They have mentioned molecular design of spacer cation as the potential way to improve the stability of such interfaces.*[39]* Other reports are there demonstrating degradation behavior of 2D perovskites under thermal stress. Also, they have reported formation of hydrant form of 2D perovskites under humidity.*[40]* Grätzel’s group has experimentally studied the effect of humidity on DJ phase 2D hybrid perovskites and observed disruption of the perovskite structure within minutes forming 1D like structures (Figure 1.7).*[41]* Very recently researchers have showcased the cation dependent moisture stability of 2D perovskites achieving improved moisture resistance by introducing cyclohexane-based spacer cations. In this study they have mentioned the importance of hydrophobic group in resisting the penetration of water molecules through perovskite crystal.*[42]* Moreover, decomposition tendency of 2D hybrid perovskites in humid environment is evidenced from these studies. Hence, the stability of 2D hybrid perovskites in presence of moisture and most importantly their degradation mechanism needs to be studied thoroughly. In this context, theoretical analysis using molecular dynamics simulations can give insightful findings in this issue. Herein, we have performed a systematic study using molecular dynamics to understand the stability and degradation nature of 2D hybrid perovskites at the water interfaces. We have considered both the RP and DJ phases along with different possible surface (PbI_2, Iodine, Cation) terminations.

1.3.6. Structure Property Relationship

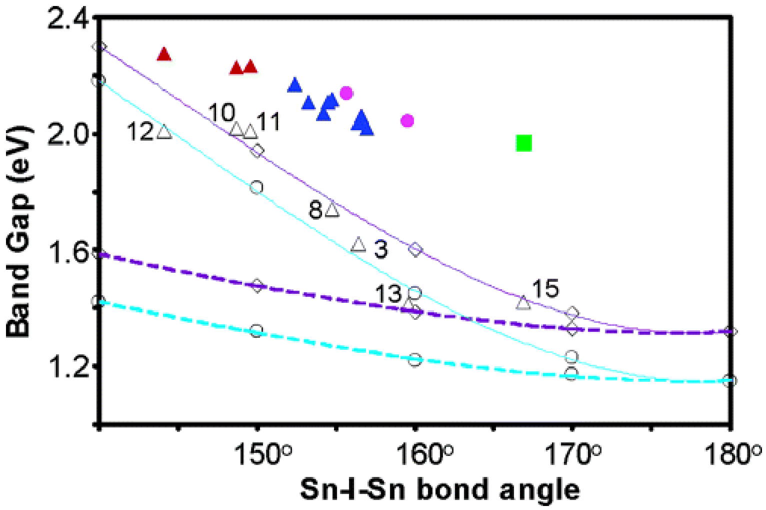

Figure 1.8: Correlation between M-X-M bond angle and band gap of different 2D hybrid perovskites. (Reprinted with permission from Ref. 45; Copyright 2005, American Chemical Society)

Spacer cations have strong influence on the structure of the 2D perovskite. Interactions between ammonium hydrogens of spacer cation and halides of the metal halide layer stabilizes the system. An experimental study reported the importance of primary ammonium group in the formability of 2D perovskite.*[43]* Also, the interaction strength between metal and halide in the inorganic layer is also defined by the spacer cations. Depending on the size and shape of the spacer cation the metal-halide (M-X) bond distance, metal-halide-metal (M-X-M) bond angle and distance between two inorganic layer varies significantly. In some cases, spacer cation can induce stronger octahedral distortion in the metal halide octahedral layer resulting unequal M-X bond length in a MX_6 octahedra and M-X-M bond angle highly deviated from ideal.*[44]* Moreover, all these structural distortions have strong correlation with the optical as well as electronic properties of the perovskite system.*[45-46]* It was reported experimentally that subtle difference in organic spacer can cause significant influence in the optical properties by affecting the M-X-M bond angle (Figure 1.8). In this regard, using density functional theory based methodologies we have tried to realize the control of spacer cations on the electronic structure of 2D hybrid perovskites. Considering a set of 2D perovskites we have thoroughly analyzed their electronic structure, carrier properties as well as optical properties. Also, we have tried to find out the way to improve band gap, carrier mobility and optical properties of these materials.

1.3.7. Electronic Structure

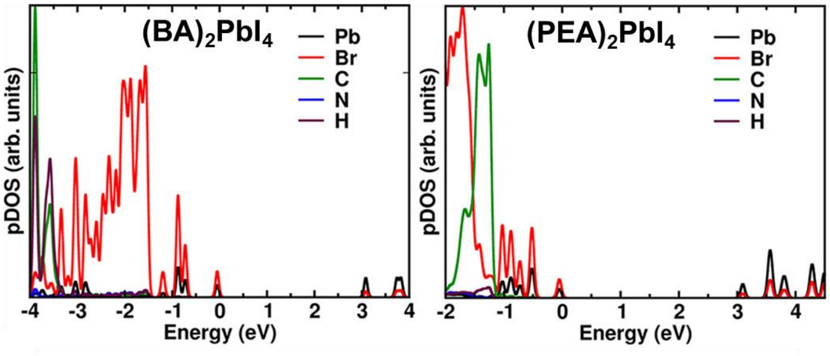

Figure 1.9: Electronic structure of 2D hybrid perovskites. (Reprinted with permission from Ref. 44; Copyright 2020, American Chemical Society)

Spacer cations have strong impact on the electronic structure of 2D perovskites. However, in common 2D hybrid perovskites spacer molecules do not have direct contribution to the band edges. Both the valence band maxima and conduction band minima are composed of metal and halide atomic orbitals (Figure 1.9). Like the 3D perovskites valence band is dominated by halogen p orbital and conduction band have major contribution from metal p orbital.*[44]* However, it was observed that spacer cations having aromatic ring comes close to the valence band edge and pyridinium ring containing spacer cations contribute close to the conduction band edge.*[47]* It was reported that high energy HOMO of organic ammonium resulting from extended conjugation can make the perovskite valence band edge dominated by organic contributions.*[48]* In a similar way organic spacer having a low energy LUMO can contribute to the material conduction band edge. One experimental combined with DFT study highlighted the thiophene heterocyclic ring based spacer cation with the organic components close to the conduction band edge.*[49]* Obtaining perovskite band structure composed of organic molecular orbitals can open up another direction to regulate their optoelectronic properties with cation engineering. In this context we have designed 2D hybrid perovskites containing spacer cations with pyrylium and thiopyrylium rings and analyzed their electronic structure and carrier properties.

1.3.8. Energy Level Alignments

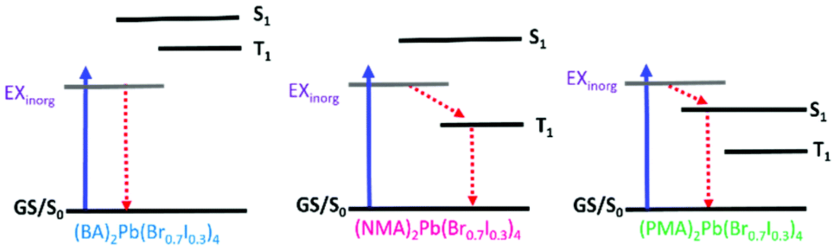

Figure. 1.10: A schematic diagram of the energy transfer dynamics in 2D hybrid perovskites. (Reprinted with permission from Ref. 52; Copyright 2021, Royal Society of Chemistry)

Owing to the broad absorption, 2D hybrid perovskites are potential candidates for light emitting devices.*[50]* Spacer cation modulation is an ingenuous way to obtain perovskite having emission in the required range. Transferring excitonic energy of the inorganic layer to the organic cation can give rise to radiative emission from the cation. This excitonic energy transfer can be induced by the spacer cation having excited energy level slightly below the excitonic energy level (Figure 1.10).*[51-52]* Spacer cations with extended conjugation was found to contribute in the material electronic structure.*[48]* Herein we took help of extended conjugation as well as functional group substitution to align cationic energy level with excitonic level of the inorganic layer.

1.3.9. Intramolecular Band Alignments

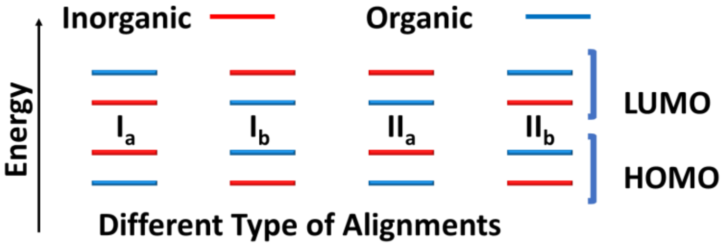

Figure 1.11: Different Band alignments.

Depending on the composition of the band edges 2D perovskites can have four possible intramolecular band alignments (Figure 1.11).*[53]* When both the valence band and conduction band are composed of inorganic or organic layers then they are called type I band alignment (I_a for organic and I_b for inorganic). Whereas, when different units contribute to the band edges then they are called type II band alignment. Whereas, a material with valence band from inorganic and conduction band from organic is called type II_a and vice-versa is true for type II_b. Now, this intramolecular band alignment decides the application of a materials to the specific optoelectronic device. For example, type I materials will be good for excitonic emission as well as phosphorescence and fluorescence emission hereby good choices for the light emitting applications like Lasers, LEDs. Whereas, the type II materials have good potential for the photovoltaic applications.*[54-58]* In this regard, we have developed machine learning based model to classify the perovskites to the intramolecular band alignments using some molecular as well as elemental features.

1.4. Theoretical Methods

1.4.1. Density Functional Theory

1.4.1.1. Schrödinger Equation

The Schrödinger equation for a many particle system containing n electrons with coordinates r_1, r_2, ..., r_n and N nuclei at coordinates R_1, R_2, ..., R_N in atomic units can be described as;

$$\left[-\frac{1}{2}\sum_{n}\nabla_n^2-\frac{1}{2}\sum_{N}\nabla_N^2-\sum_{N,n}\frac{1}{|R_{N-}r_n|}\right]\psi + \left[\frac{1}{2}\sum_{N\neq M}\frac{1}{|R_{N-}R_M|}+\frac{1}{2}\sum_{n\neq m}\frac{1}{|r_{n-}r_m|}\right]\psi = E\psi \qquad (1.2)$$

The first and second terms in the Hamiltonian represent the kinetic energy for the electron-electron and nuclei-nuclei interaction and the last three terms correspond to the potential energy coming from electron-nuclei, nuclei-nuclei, and electron-electron coulomb interactions, respectively. Considering the Born-Oppenheimer approximation that assumes the motion of nuclei neglected compared to the electronic motion owing to the high relative mass ratio of nuclei and electrons, eqn. 1 can be written as*[59]*,

$$\left[-\frac{1}{2}\sum_n\nabla_n^2-\sum_{N,n}\frac{1}{|R_{N-}r_n|}+\frac{1}{2}\sum_{n\neq m}\frac{1}{|r_{n-}r_m|}\right]\psi = E\psi \qquad (1.3)$$

However, the Eqn. 1.3 becomes more and more complicated with increase in system size and finding an exact solution is very difficult. So, to solve the many-body Schrödinger equation we need some approximations.

1.4.1.2 Mean-Field Approximation

Mean field approximation considers, average coulomb interaction experienced by each electron from the rest. According to this approximation, each electron is moving under a potential known as Hartree potential which can be described as,

$$V_H(r) = \int \frac{n(r')}{|r-r'|} dr' \tag{1.4}$$

Hence, the N particle problem can be represented by N one particle problem,

$$\left[-\frac{\nabla^2}{2} - \sum_{N,n} \frac{1}{|R_{N-}r_n|} + \int \frac{n(r')}{|r-r'|} dr'\right] \phi_i(r) = \epsilon_i \phi_i(r) \tag{1.5}$$

where $\phi_i(r)$ correspond to the single electron wavefunction with eigenvalue ϵ_i. However, this approximation does not account the quantum nature of electron correlation precisely.

1.4.1.3 Hartree-Fock Method

Hartree and Fock formulated a method to determine the wavefunctions mentioned in Eqn. 1.5. According to this method energy minimization with respect to these wavefunctions give rise to a set of single-particle equations written below recognised as Hartree-Fock equations *[60]*,

$$\left[-\frac{\nabla^2}{2} - \sum_{N,n} \frac{1}{|R_{N-}r_n|} + \int \frac{n(r')}{|r-r'|} dr'\right] \phi_i(r) + \int V_x(r,r')\phi(r')dr = \epsilon_i \phi_i(r) \tag{1.6}$$

where the extra potential which accounts all occupied single particle states is described as,

$$V_x(r,r') = -\sum_i \frac{\phi_i(r)\phi_i(r')}{|r-r'|} \tag{1.7}$$

Compared to the classical mean-field approximation, this is a more accurate approximation. The energy and properties of the system can be obtained by solving these single particle equations.

1.4.1.4 Hohenberg-Kohn Theorems

Theorem 1

The first theorem proposed by Hohenberg and Kohn states that the external potential $V_{ext}(r)$ of any system of interacting electrons is uniquely determined by the ground state electron density $\rho_0(r)$. According to this theorem, ground state properties of a system can be expressed in terms of ground state electron density.

$$\langle\psi|\Omega|\psi\rangle = \Omega[\rho_0(r)] \tag{1.8}$$

Theorem 2

In their second theorem Hohenberg and Kohn stated that, for any considered system the minimum value of the functional of energy is the exact ground state energy E_0 and the corresponding density is the exact ground state density. Hence, the energy corresponding to any trial density $\rho(r)$ should be greater than the true ground state energy.

$$E_0 \leq E[\rho(r)] = T[\rho(r)] + E_{Nn}[\rho(r)] + E_{nn}[\rho(r)] \tag{1.9}$$

Here, $T[\rho(r)]$ account the kinetic energy of electrons, $E_{Nn}[\rho(r)]$ defines the potential energy due to nuclei-electron interaction and $E_{nn}[\rho(r)]$ correspond to the electron-electron interaction.*[61-62]*

1.4.1.5 Kohn-Sham Equations

considering a many-body system to a fictious noninteracting system with the same density, Kohn and Sham formulated an equation (Eqn. 1.10) to construct the energy functional of electron density by [63].

$$E[\rho(r)] = T[\rho(r)] + V_{ext}[\rho(r)] + V_H[\rho(r)] + E_{xc}[\rho(r)] \qquad (1.10)$$

In Eqn. 1.10, the first three terms represent kinetic energy functional, potential energy functional of nuclear-electron interaction, and functional for electron-electron coulomb interaction (Hartree energy), respectively. These can be expressed as

$$T[\rho(r)] = \sum_i \int \phi_i^* \frac{\nabla^2}{2} \phi_i(r) dr \qquad (1.11)$$

$$V_{ext}[\rho(r)] = \int V_{ext}(r) d^3r \qquad (1.12)$$

$$V_H[\rho(r)] = \int \int \frac{\rho(r)\rho(r')}{|r-r'|} dr^3 dr'^3 \qquad (1.13)$$

The last term $E_{xc}[\rho(r)]$ is the exchange-correlation energy that incorporates the non-classical contributions in the functional. The first three terms are equivalent to Eqn. 1.5 and can be determined from the electron density obtained by the variational approach. This results a set of equations analogous to Hartree-Fock equations which are known as Kohn-Sham equations described as,

$$\left[-\frac{\nabla^2}{2} - \sum_{N,n} \frac{1}{|R_{N-}r_n|} + \int \frac{n(r')}{|r-r'|} dr' + V_{xc}(r)\right] \phi_i(r) = \epsilon_i \phi_i(r) \qquad (1.14)$$

where $\phi_i(r)$ denotes for the Kohn-Sham orbitals and the external potential, $V_{xc}(r)$ corresponds to the exchange-correlation energy as follows,

$$V_{xc}(r) = \frac{\delta E_{xc}[\rho(r)]}{\delta \rho(r)} \qquad (1.15)$$

Once the exchange-correlation energy is known, the ground state density can be obtained by solving the Kohn-Sham equations using self-consistent field method.*[63]* Hence the most crucial part of any DFT calculations is the choice of exchange-correlation functional that can give reasonable results. In this regard, several approximations have been formulated, few of which are discussed below.

1.4.1.6 Exchange-Correlation Functional

Local Density Approximation (LDA)

According to the local density approximation, the system's energy density at every point is the equivalent to the electron density of a homogeneous electron gas [64-65]. The exchange correlation functional formulated as

$$E_{xc}^{LDA} = \int \varepsilon_{xc}(\rho_0) d^3r|_{\rho_0 \to \rho_r} \quad (1.16)$$

Here, $\varepsilon_{xc}(\rho_0)$ denotes the exchange correlation energy of a homogeneous system considering its electron density ρ_0 is equal to that (system ρ_r) of a real inhomogeneous. Although, LDA can predict properties of certain systems, majorly it fails to account the geometry and energy accurately.

Generalized Gradient Approximation (GGA)

Generalized gradient approximation is a modified version of LDA, where along with the electron density, its gradient is also considered to account the inhomogeneity in the electron density. This changes the local nature of LDA density functional to nonlocal. The GGA exchange-correlation functional can be formulated as,

$$E_{xc}^{GGA} = E_{xc}[\rho_r, \nabla_{\rho_r}] \quad (1.17)$$

The most popular among GGA functionals is Perdew-Burke-Ernzerhof (PBE) [66-68]. GGA based functionals have been established to calculate the structural as well as energetic properties of both solid-state and molecular systems with good agreement with experimental results.

Hybrid Functionals

As a correction to the coulomb exchange, hybrid functionals include a Hartree-Fock level exchange correlation obtained by solving noninteracting Kohn-Sham orbitals. [69] Several different hybrid functionals has developed with variation in the percentage of Hartree-Fock exchange. One of the most widely used hybrid functionals for solid state systems is Heyd-Scuseria-Ernzerhof Screened-Exchange Hybrid functional (HSE) which considers short range Hartree-Fock exchange along with the GGA-PBE approximation [70-71]. The HSE functional is formulated as,

$$E_{xc}^{HSE} = aE_{xc}^{SR,HF}(\omega) + (1-a)E_{x}^{SR,PBE} + E_{x}^{LR,PBE}(\omega) + E_{c}^{PBE} \qquad (1.18)$$

Where SR and LR signifies short range and long-range exchanges, a is the mixing coefficient and ω is the Hartree-Fock screening parameter. The HSE functional considers 25% short-range HF exchange without any long-range HF exchange along with a PBE correlation. The modified version of HSE (HSE06) includes an ω value of 0.11 Bohr^{-1}.

1.4.1.7 Bloch Method and Plane-Wave Basis Set

The wavefunctions of electrons within a solid system can be obtained by using the method proposed by Bloch by making them quasi-periodic with incorporating a function that defines the periodicity of the potential [120] in the following form,

$$\psi_k(r) = u_k(r)e^{ikr} \qquad (1.19)$$

where k is the wave vector. By using this approach, real space quantities, such as energy, charge density can be determined, in the periodic form. The periodic function $u_k(r)$ can be expanded in three dimensions as

$$u_k(r) = \sum_G c_n(G)e^{iGr} \qquad (1.20)$$

Now, Eqn. 1.19 can be written as

$$\psi_k(r) = \sum_G c_n(G)e^{i(k+G)r} \qquad (1.21)$$

Now, the Kohn-Sham equations for the periodic wave function can be described by using a plane wave basis set containing basis functions of the form $\phi_i(r) = Ae^{ikr}$.

$$\left[-\frac{1}{2}\nabla^2 + U_{eff}\right]\sum_G c_n(G)e^{i(k+G)r} = \varepsilon_{nk}\sum_G c_n(G)e^{i(k+G)r} \qquad (1.22)$$

where U_{eff} represents the effective potential acting on the electrons. the wave functions $\phi_i(r)$ and corresponding eigenvalues ε_{nk} can be calculated by diagonalizing a matrix obtained from these equations followed by self-consistent approach [121, 122]. Electronic as well as optical properties of the system can be calculated from the band structure obtained by the plot of these eigenvalues versus the wave vector k.

1.4.1.8. Dispersion Corrected Density Functional Theory

The methods discussed yet are insufficient to account long distance dispersion interactions. Precisely, both Coulomb and exchange interactions are dependent on the electron transition density of interacting units. To account the long range interactions, methods like van der Waals (vdW) functionals, dispersion-corrected density functional theory (DFT-D) are developed. These methodologies offer a complete understanding of dispersion interactions in molecular as well as solid-state systems.

$$\mathrm{E}_{\mathrm{Disp}}^{(2)} = \sum_{\mathrm{ia}}\sum_{\mathrm{jb}}\frac{(\mathrm{ia|jb})[(\mathrm{ia|jb})-(\mathrm{ja|ib})]}{\varepsilon_{\mathrm{a}}+\varepsilon_{\mathrm{b}}-\varepsilon_{\mathrm{i}}-\varepsilon_{\mathrm{j}}} \qquad (1.23)$$

Here, where E represents the energy of the corresponding orbital, the addition of all particle-hole excitations between orbitals i → a and j → b localized on fragments A and B is considered which were not considered in standard DFT.*[72]* In addition, empirical dispersion corrections are also developed where the most relevant method is DFT-$\mathrm{D_n}$ method formulated by Grimme is as follows:

$$\mathrm{E}_{\mathrm{Disp}}^{\mathrm{DFT-D}} = \sum_{\mathrm{AB}}\sum_{\mathrm{n=6,8,10,....}}\mathrm{S_n}\frac{\mathrm{C_n^{AB}}}{\mathrm{R_{AB}^n}}\mathrm{f_{damp(R_{AB})}} \qquad (1.24)$$

Here, $\mathrm{R_{AB}^{n}}$is the distance between A and B, $\mathrm{C_{n}^{AB}}$ is the dispersion coefficient, $\mathrm{S_n}$ correspond to the adjusted correction for the repulsion and $\mathrm{f_{damp(R_{AB})}}$ is the double counting effect of correlation used at intermediate distances.

In this thesis, we have used Grimme's DFT-D3 approach, which account three-body effects by including triplets of atoms.*[72-74]*

1.4.2. Molecular Dynamics Simulations

By solving Newton's equations of motion for a particular system we can obtain the time evolution of that system. We will get a trajectory containing Cartesian coordinates of each atom for each timescale from the solution of the equation of motion.

1.4.2.1. Evaluating the Equation of Motion

In this section, we will give a brief overview of Newton's equations of motion and discuss their application in molecular mechanics.*[75,76]*

Considering a system with N number of particle, the force (F_i) working on the $\mathrm{i^{th}}$ particle can be described as,

$$F_i = m_i a_i \tag{1.25}$$

Here, m_i and a_i are the mass and acceleration of the $\mathrm{i^{th}}$ particle, respectively. Now, the force can also be obtained from the potential gradient using the following equation,

$$F_i = -\frac{\delta U(r^N)}{\delta r_i} \tag{1.26}$$

In general, the total energy of a system is related to the position (r_i) and momenta (p_i) of its particles by the Hamiltonian operator $\mathscr{H}$. Where, the instantaneous momentum and position of the $\mathrm{i^{th}}$ particle can be given as,

$$p_i = -\frac{\delta \mathcal{H}}{\delta r_i} \tag{1.27}$$

$$r_i = -\frac{\delta \mathcal{H}}{\delta p_i} \tag{1.28}$$

$$\mathcal{H}(p_i, r_i) = \sum_{i=1}^{N} \frac{P_i^2}{2m_i} + U(r_i) \tag{1.29}$$

First and second terms in the right hand side of equation 1.29 corresponds to the kinetic and potential energy, respectively.

$$r = r_1, r_2, r_3, \ldots\ldots, r_N \tag{1.30}$$

$$p = p_1, p_2, p_3, \ldots\ldots, p_N \tag{1.31}$$

$$\mathcal{H}(r,p) = E_k(p) + U(r) \tag{1.32}$$

The kinetic energy can be given as,

$$E_k = \sum_{i=1}^{N} \frac{1}{2m_i}\left(p_{ix}^2 + p_{iy}^2 + p_{iz}^2\right) \tag{1.33}$$

Here m_i, P_{ix}, P_{iy}, and P_{iz} corresponds to the mass and momenta of the ith particle along x, y, and z directions, respectively. One can obtain the entire trajectory over time by knowing the potential function. Utilizing various available approximate methods based on finite-difference integration finding the solution for a many particle system is possible. All these uses Taylor series expressed as,

$$r(t+\Delta t) = r(t) + \Delta t V(t) + \frac{1}{2}\Delta t^2 a(t) + \frac{1}{6}\Delta t^3 b(t) + \cdots \tag{1.34}$$

$$v(t+\Delta t) = v(t) + \Delta t a(t) + \frac{1}{2}\Delta t^2 b(t) \tag{1.35}$$

$$a(t+\Delta t) = a(t) + \Delta t b(t) \tag{1.36}$$

Where, r, v, a, b denotes position, velocity, acceleration, and the third derivative, respectively. There are various available algorithms for these calculations. Among those, the Verlet algorithm found out to be a well-trusted method for integrations.*[77]* It combines Taylor expansions for positions at both time t and $t - \Delta t$.

$$r(t+\Delta t) = r(t) + \Delta t V(t) + \frac{1}{2}\Delta t^2 a(t) + \cdots \tag{1.37}$$

$$r(t-\Delta t) = r(t) - \Delta t V(t) + \frac{1}{2}\Delta t^2 a(t) - \cdots \tag{1.38}$$

Adding equations 1.36 and 1.37,

$$r(t+\Delta t) = 2r(t) - r(t-\Delta t) + \Delta t^2 a(t) \tag{1.39}$$

Therefore, the Verlet algorithm can predict the new positions of the system by estimating the positions and accelerations at current and position at previous timesteps. The velocity of the system can be calculated using the following equation,

$$v(t) = \frac{r(t+\Delta t) - r(t-\Delta t)}{2\Delta t} \tag{1.40}$$

Principally, the Verlet algorithm computes the position at two distinct times and operates in two steps. As a result, this method requires additional computer memory to store the positions from three consecutive timesteps. Hereafter, a modified version of this algorithm has been developed which is termed as velocity Verlet algorithm. In the velocity Verlet algorithm, velocity is first calculated at step n + 1, followed by the calculation of coordinates at step n + 1. In this approach the positions and velocities are calculated using the following equations,

$$r(t+\Delta t)=r(t)+\Delta tV(t)+\frac{1}{2}\Delta t^2a(t) \tag{1.41}$$

$$v(t+\Delta t)=v(t)+\frac{1}{2}\Delta t[a(t)+a(t+\Delta t)] \tag{1.42}$$

After obtaining the positions and velocities, the position of the subsequent timestep is predicted using equation 1.40, which is then utilized to calculate the acceleration.

There is another revised version of Verlet algorithm, where the velocities computed at $t+\frac{1}{2}\Delta t$ time is utilized to predict the positions at time $t+\Delta t$. Since the velocities "leap over" the positions, and vice versa this approach is known as leapfrog algorithm. This method explicitly calculates velocity independent of the positions.

$$r(t+\Delta t)=r(t)+v\left(t+\frac{1}{2}\Delta t\right)\Delta t \tag{1.43}$$

$$v\left(t+\frac{1}{2}\Delta t\right)=v\left(t-\frac{1}{2}\Delta t\right)+a(t)\Delta t \tag{1.44}$$

The advantage of leapfrog algorithm over the Verlet algorithm is that it only stores one set of positions and velocities, whereas the later requires storage for three consecutive positions for a single set of velocities.

1.4.2.2. Statistical Ensembles

Statistical mechanics is the connection between the macroscopic observables and its microscopic particles of a system. Carrying out MD simulations with a macroscopic number of particles is still not feasible. Hence, the utilization of statistical mechanical approach is necessary to extract important information. A macroscopic observable is a combination of several distinct microscopic states, where an ensemble includes all possible microstates under specific constant parameters.

An isolated system can be described using a microcanonical ensemble (NVE), where the total number of particles (N), volume (V), and total energy (E) are kept constant. Therefore, in case of microcanonical ensemble we consider potential energy surface due to higher free energy barriers relative to the total energy of the system.

Other possibilities are the canonical ensemble (NVT) where volume and temperature kept constant and the isobaric-isothermal ensemble (NPT) where pressure and temperature are kept constant. In general, a closed system which can transfer heat from an external source resembles to the NVT ensemble. Whereas, more realistic scenarios are best described by the NPT ensemble. However, in these ensembles, the system's energy is not fixed, allowing systems to spontaneously surmount large potential energy barriers through fluctuations in total energy.*[77-79]*

1.4.2.3. Temperature and Pressure Coupling

Usually, chemical reactions are performed with constant temperature environments. So, NVT ensemble is common methodology of MD simulation for realization of experimental circumstances. Whereas, reactions performed at constant pressure conditions can executed theoretically with the isobaric-isothermal (NPT) ensemble. To perform MD simulations projecting these ensembles several methods are developed where the Langevin and Andersen thermostats are common which operate by restricting a system variable to a predetermined distribution function.*[80-81]* The Andersen thermostat, one of the earliest developed thermostat, predicts a new velocity to a random particle from a Boltzmann distribution during a collision event, thereby maintaining the preselected temperature. Another popular method is the Berendsen thermostat, which considers weak coupling methods to approach the desired value of the target variable (temperature or pressure).*[82]*

The simulation temperature is related to the time average of the kinetic energy by the following equation,

$$\langle E_k \rangle = \frac{1}{2}\sum_{i=1}^{N} m_i v_i^2 = \frac{3}{2} N k_B T \tag{1.45}$$

Control over velocity can be achieved by varying the temperature since they are directly proportional to each other. In this method weak coupling is being employed by an external heat bath with temperature T_{bath}, introducing a softening effect maintained by the time constant r. Velocities at each timestep are adjusted by a factor λ. Therefore, the change in temperature when the temperature is $T(t)$ at a a specific time t can be given as,

$$\Delta T = \frac{1}{2}\sum_{i=1}^{N} \frac{2}{3}\frac{2m_i(\lambda v_i)^2}{N k_B} - \frac{1}{2}\sum_{i=1}^{N} \frac{2}{3}\frac{2m_i v_i^2}{N k_B} \tag{1.46}$$

$$\Delta T = (\lambda^2 - 1)T(t) \tag{1.47}$$

By velocity rescaling, the rate of temperature change can become directly proportional to the difference in temperature between the heat bath and the system,

$$\frac{dT(t)}{dt} = \frac{1}{\tau}\left(T_{bath} - T(t)\right) \tag{1.48}$$

Now, the temperature change between timestep is,

$$\Delta T = \frac{\delta\tau}{\tau}\left(T_{bath} - T(t)\right) \tag{1.49}$$

where τ controls the coupling strength between the system and the heat bath. The scaling factor can be given as,

$$\lambda^2 = 1 + \frac{\delta t}{\tau}\left(\frac{T_{bath}}{T(t)} - 1\right) \tag{1.50}$$

Coupling strength becomes weak for high τ values. Another popular method is the Nosé-Hoover thermostat where a new variable denoted by ζ is introduced.*[83]* Here ζ works as friction, either accelerates or decelerates the particles till the desired temperature is achieved.

$$m_i \frac{d^2 r_i}{dt^2} = F_i - \zeta m_i v_i \tag{1.51}$$

$$\frac{d\zeta(t)}{dt} = \frac{1}{Q}\left[\sum_i^N m_i \frac{v_i^2}{2} - \frac{3N+1}{2} k_B T\right] \tag{1.52}$$

Here, Q is the coupling strength of the friction $\zeta(t)$. In this thermostat the temperature is not exactly fixed, instead approaches to the target value.

1.4.3. Computational Tools

1.4.3.1. Bader Charge Analysis

We can calculate the charges associated with each atom within a molecule using Bader charge analysis by partitioning the molecule into individual atoms. This method is based on the Bader partitioning scheme and for analysis it takes help of electronic charge density. The partitioning of the charge density is obtained from the 2-D surfaces where perpendicular to the surface the charge density is minimum, known as zero-flux surfaces.

In this thesis, we have used the algorithm developed by Henkelman and coworkers to calculate Bader charges.*[84-85]* This algorithm is believed to perform reliably based on the charge density grid and is exactly designed to calculate the electronic charge density of the molecule into its atomic contributions.

1.4.4. Machine Learning

Machine Learning has rapidly emerged as a transformative technology across various domains. Supervised Machine Learning (ML) models, depending on the nature of the target variable, can be categorized into two main types: regression and classification.1 When the target variable is consisting of continuous values, the problem belongs to regression whereas if the target variable indicates certain class, then it belongs to classification problem.2 The classification can be binary or multi-class classification depending on the number of classes present the working dataset. Herein, we have focused on the classification ML models as the ML work included in the thesis is based on the classification problem.

1.4.4.1. Binary Classification

Binary classification is a fundamental task in machine learning where the goal is to categorize data points into one of two distinct classes, often referred to as "class 0" and "class 1" or "negative" and "positive." This type of supervised learning involves using input features (X) to predict a binary output label (Y). Examples include spam detection, medical diagnosis, and credit scoring. The workflow typically involves data collection, preprocessing (such as cleaning, normalization, and encoding), feature selection, model selection, training, and evaluation using metrics like accuracy, precision, recall, and the F1 score. Common algorithms for binary classification include logistic regression, support vector machines (SVM), decision trees, random forests, and neural networks. Evaluating model performance often involves constructing a confusion matrix and analysing the ROC curve and AUC. Challenges include handling imbalanced data, avoiding overfitting, and effective feature engineering.

1.4.4.2. Multiclass Classification

Multiclass classification is an essential task in machine learning, where the objective is to categorize instances into one of three or more classes.[88] Unlike binary classification, which deals with only two possible outcomes, multiclass classification involves a broader set of categories, making it more complex. A common and effective strategy for handling multiclass problems is the One-vs-Rest (OvR) method, also known as One-vs-All (OvA). This method decomposes the multiclass problem into multiple binary classification problems, facilitating the application of binary classification algorithms to multiclass scenarios.

The One-vs-Rest approach functions by training a separate binary classifier for each class. Specifically, for a problem with K classes, K individual binary classifiers are constructed. Each classifier is trained to distinguish between one particular class (the positive class) and all other classes combined (the negative class). For instance, in a three-class problem with classes labelled Red, Green, and Blue, the OvR method would create three binary classifiers: one to distinguish Red from Green and Blue, another to distinguish Green from Red and Blue, and a third to distinguish Blue from Red and Green. During the training phase, each binary classifier learns to predict whether an instance belongs to its assigned class versus all other classes. This results in K binary classifiers, each specialized in recognizing one specific class against the backdrop of the remaining classes. The prediction phase involves applying each of these classifiers to a new instance. Each classifier outputs a confidence score, indicating the likelihood that the instance belongs to its particular class. The final classification decision is made by selecting the class with the highest confidence score among all K classifiers.

The OvR method offers several advantages. Its simplicity and ease of implementation make it a popular choice, especially when existing binary classification algorithms can be directly applied without modification. Furthermore, its flexibility allows it to be used with a wide range of binary classifiers, enhancing its versatility across different types of data and applications. However, the method also has certain limitations. Each binary classifier in the OvR framework deals with an imbalanced dataset, as it contrasts one class against all others, which can sometimes skew the training process. Additionally, the assumption that each binary classifier operates independently may not hold in practice, potentially affecting overall performance. The requirement to train K separate classifiers can also be computationally intensive, particularly for problems with a large number of classes.

1.4.4.3. Feature Selection

Feature selection is a crucial step in the machine learning pipeline that involves identifying and selecting the most relevant features from a dataset to improve the model’s performance.[89-90] This process aims to enhance the efficiency and effectiveness of a model by reducing the dimensionality of the data, thereby simplifying the model and reducing the risk of overfitting. Feature selection can be broadly categorized into three types: filter methods, wrapper methods, and embedded methods. Filter methods assess the relevance of features based on statistical measures, independent of the learning algorithm, and often include techniques like correlation coefficients, chi-square tests, and mutual information. Wrapper methods, on the other hand, evaluate feature subsets by training and testing a specific machine learning algorithm, using methods such as recursive feature elimination and cross-validation to find the best subset. Embedded methods incorporate feature selection as part of the model training process itself, with techniques like LASSO (Least Absolute Shrinkage and Selection Operator) and tree-based methods that inherently select important features during the learning process. Effective feature selection not only improves model performance by eliminating irrelevant or redundant data but also reduces computational costs and improves interpretability, making it a vital step in the development of robust and efficient machine learning models.

1.4.4.4. Correlation Matrix

A correlation matrix is a table that displays the correlation coefficients between pairs of variables in a dataset, providing a quantitative measure of the linear relationship between them. Each cell in the matrix contains a correlation coefficient, ranging from -1 to 1, indicating the strength and direction of the relationship. A coefficient close to 1 signifies a strong positive correlation, meaning that as one variable increases, the other also tends to increase. Conversely, a coefficient close to -1 indicates a strong negative correlation, where one variable tends to decrease as the other increases. A coefficient around 0 suggests no linear relationship between the variables. The correlation matrix is symmetric, with the diagonal elements always equal to 1, representing the perfect correlation of each variable with itself. This matrix is particularly useful in feature selection and exploratory data analysis, as it helps identify pairs of highly correlated variables, which might indicate redundancy. By analysing the correlation matrix, researchers and data scientists can make informed decisions about which features to retain, transform, or eliminate, thereby improving the efficiency and performance of machine learning models.

1.4.4.5. Hyperparameter Tuning: Grid Search CV

Hyperparameter tuning is a critical step in optimizing machine learning models, and Grid Search Cross-Validation (Grid Search CV) is a widely used method for this purpose.[91] Grid Search CV systematically explores a predefined set of hyperparameter values by performing an exhaustive search over the specified parameter grid.[92] For each combination of hyperparameters, the method trains and evaluates the model using cross-validation, typically k-fold cross-validation, which involves dividing the dataset into k subsets and training the model k times, each time using a different subset as the validation set and the remaining subsets as the training set. The performance of each hyperparameter combination is averaged across the k validation sets to ensure robustness and reduce overfitting. By comparing the cross-validation scores, Grid Search CV identifies the combination of hyperparameters that yields the best performance. This method is computationally intensive but thorough, ensuring that the selected hyperparameters are optimal for the model. As a result, Grid Search CV enhances the model's accuracy and generalization capabilities, making it a valuable tool in the machine learning workflow.

1.4.4.6. Cross Validation: Repeated Stratified K-Fold

Repeated Stratified K-Fold Cross-Validation is a robust technique for evaluating the performance of machine learning models, particularly when dealing with imbalanced datasets.[93] This method combines two concepts: stratification and repetition, enhancing the reliability and stability of model assessment. Stratified K-Fold Cross-Validation ensures that each fold, or subset, of the data maintains the same class distribution as the original dataset. This stratification is crucial when dealing with classification problems where some classes may be underrepresented. By preserving the class balance in each fold, stratified k-fold cross-validation provides a more accurate estimate of the model's performance across different classes.

In standard K-Fold Cross-Validation, the dataset is divided into K equal-sized folds. The model is then trained K times, each time using K-1 folds for training and the remaining fold for validation. This process is repeated K times, ensuring that each fold is used as the validation set exactly once. The performance metrics from each of the K iterations are averaged to obtain a more reliable estimate of the model's performance.

Repeated Stratified K-Fold Cross-Validation takes this a step further by repeating the entire stratified k-fold cross-validation process multiple times (e.g., 5 or 10 repetitions). Each repetition involves randomly reshuffling the data and then applying stratified k-fold cross-validation. By averaging the performance metrics across all repetitions and folds, this method reduces the variance and provides a more stable and generalized estimate of model performance. This approach is particularly beneficial in scenarios where the dataset is small or the class distribution is highly imbalanced, as it ensures that every data point is used for both training and validation multiple times. Repeated Stratified K-Fold Cross-Validation thus combines the benefits of stratification and repeated trials, making it a powerful tool for model validation and hyperparameter tuning in machine learning.

1.4.4.7. Machine Learning Algorithms

1.4.4.7.1. Logistic Regression

Logistic regression is a widely used statistical method in machine learning for binary classification problems, where the goal is to predict the probability that a given input belongs to one of two classes.[94] Unlike linear regression, which predicts continuous outcomes, logistic regression models the probability of a binary outcome using a logistic function, also known as the sigmoid function.

The logistic regression model is based on the following logistic function:

$$P(x_i) = \frac{1}{1+e^{-z}} \tag{1.53}$$

Where $z = \beta_0 + \beta_1 x_1 + \beta_2 x_2 + \cdots + \beta_n x_n$ is a linear combination of the input features. The parameters $\beta_0, \beta_1, \ldots, \beta_n$ are the coefficients of the model, which are estimated from the training data. Each coefficient represents the change in the log-odds of the probability of the event occurring for a one-unit change in the corresponding feature, holding all other features constant. The log-odds are the logarithm of the odds, where the odds are the ratio of the probability of the event occurring to the probability of it not occurring.

Training a logistic regression model involves estimating the coefficients β that maximize the likelihood of the observed data. This is typically done using a method called Maximum Likelihood Estimation (MLE). The likelihood function for logistic regression is derived from the Bernoulli distribution, given the binary nature of the outcome. The objective is to find the values of β that maximize the likelihood function, which measures how well the model explains the observed data.

1.4.4.7.2. Ridge Classifier

The Ridge Classifier converts binary targets to {-1, 1} and treats the problem as a regression task. Ridge regression addresses some of the issues associated with ordinary least squares by imposing a penalty on the size of the coefficients. The ridge coefficients minimize a penalized residual sum of squares, which helps to reduce overfitting and improve model stability.

$$\min_{w} \|X_w - y\|_2^2 + \alpha \|w\|_2^2$$

The complexity parameter α≥0 controls the amount of shrinkage: the larger the value of α, the greater the amount of shrinkage and thus the coefficients become more robust to collinearity.

1.4.4.7.3. Support Vector Machine (SVM)

Support Vector Machine (SVM) is a robust supervised learning algorithm employed for both classification and regression tasks. When used for classification, it is specifically referred to as a Support Vector Classifier (SVC). SVM is particularly renowned for its efficiency in high-dimensional spaces and its ability to mitigate overfitting, especially when there is a clear margin of separation between classes.*[95]*

Linear Separability and Hyperplanes

SVM's primary objective is to identify a hyperplane that maximally separates data points of different classes. In an n-dimensional space, a hyperplane is an (n-1)-dimensional affine subspace. For instance, in a two-dimensional space, the hyperplane is a line, whereas, in a three-dimensional space, it is a plane.

Support Vectors

Support vectors are the data points nearest to the hyperplane, making them the most challenging to classify. These points are crucial as they determine the hyperplane's position and orientation. The margin is defined as the distance between the support vectors and the hyperplane, and SVM aims to maximize this margin.

Hyperplane Determination and Kernels

SVM encompasses various supervised learning methods, including regression, classification, and outlier detection. The algorithm's goal is to discover a hyperplane in an N-dimensional space that distinctly classifies data points. To achieve the optimal hyperplane, different kernel functions can be utilized, which enhance accuracy. Additionally, tuning other hyperparameters, such as gamma and degree, is essential for optimizing performance. Consequently, fine-tuning all these hyperparameters is critical. This approach is also well-suited for high-dimensional datasets.

1.4.4.7.4. K-Nearest Neighbour (KNN)

K-Nearest Neighbour (KNN) is a machine learning algorithm utilized for both classification and regression tasks.*[96]* For classification, the algorithm identifies the K nearest data points to a given test data point and classifies it based on the majority class among these nearest neighbours. The value of K is a user-defined hyperparameter that can be selected based on the specific problem and dataset.

The KNN algorithm works by calculating the distance between the test data point and all training data points using a chosen distance metric, such as Euclidean distance, Manhattan distance, or another suitable metric. The overall steps are as follows:

1. Select Neighbors: Identify the K nearest data points to the test data point based on the calculated distances.

2. Assign Class: Assign the majority class label to the test data point based on the class labels of the K nearest neighbors. If there is a tie, the algorithm can either randomly choose a class or use another method to break the tie.

1.4.4.7.5. Bagging Classifier

When random subsets of the dataset are drawn as random subsets of the samples, then this algorithm is known as Pasting. If samples are drawn with replacement, then the method is known as Bagging.*[97]* A Bagging classifier is an ensemble meta-estimator that trains base classifiers on random subsets of the original dataset and then aggregates their individual predictions (either by voting or averaging) to form a final prediction. This meta-estimator can typically be used to reduce the variance of a black-box estimator (e.g., a decision tree) by introducing randomization into its construction procedure and then creating an ensemble from it. In this context, we use Random Forest as the base classifier.

1.4.4.7.6. Random Forest Classifier

Random Forest Classifier is an extension of the Decision Tree algorithm that operates by constructing a multitude of decision trees at training time and outputting the class that is the mode of the classes (classification).*[98]* During training, trees are grown using bootstrapped samples of the data and a random subset of the features, which results in low correlation between the trees and reduces overfitting. For prediction, the algorithm averages the predictions from all the trees, providing greater stability and robustness to outliers. The Random Forest Classifier is adept at handling high-dimensional and non-linear data and is considered a robust algorithm for classification tasks. However, it is computationally expensive and may require longer training times compared to other algorithms.

1.4.4.8. Recursive Feature Elimination

Recursive Feature Elimination (RFE) is a widely-used feature selection technique in machine learning that aims to enhance model performance by systematically selecting the most relevant features. The method works by recursively fitting a model and removing the least important feature(s) at each iteration, based on the model’s performance metrics.

RFE starts with all available features and iteratively removes the least important ones, reducing the feature set until the desired number of features is reached. The importance of a feature is typically determined by the magnitude of the model coefficients (for linear models) or feature importance scores (for tree-based models).

First, we need to train the chosen machine learning model on the entire set of features followed by ranking the features based on their importance scores, which are derived from the trained model. For instance, in linear regression, this could be the absolute values of the coefficients, and in decision trees, it could be the feature importance scores. They we identify and remove the least important feature(s). The number of features to remove at each step can be set by the user, but often one feature is removed per iteration. Repeat the process of training, ranking, and eliminating until the specified number of features is reached or until no further improvement in model performance is observed.

Thus, by removing less important features, RFE can significantly reduce the dimensionality of the dataset, leading to faster model training and prediction times. Reducing irrelevant or redundant features often enhances the model’s performance by reducing overfitting and improving generalization to unseen data. Also, a smaller set of features simplifies the model, making it easier to interpret and understand.

1.4.4.9. Classification Metrics

Classification metrics are essential tools for evaluating the performance of classification models in machine learning. Among these metrics, the confusion matrix is a fundamental and comprehensive method for visualizing the performance of a classification algorithm. It provides a detailed breakdown of the model's predictions compared to the actual outcomes, offering insights into various types of prediction errors.

Confusion Matrix

A confusion matrix is a table that summarizes the performance of a classification model by comparing the predicted labels with the true labels. It is particularly useful for binary classification problems but can be extended to multiclass classification as well. For a binary classification problem, the confusion matrix is a 2x2 table consisting of four entries:

True Positives (TP): The number of instances where the model correctly predicted the positive class.

True Negatives (TN): The number of instances where the model correctly predicted the negative class.

False Positives (FP): The number of instances where the model incorrectly predicted the positive class (Type I error).

False Negatives (FN): The number of instances where the model incorrectly predicted the negative class (Type II error).

Several important classification metrics can be derived from the confusion matrix:

Accuracy

Accuracy measures the proportion of correctly classified instances out of the total instances. However, it can be misleading in cases of imbalanced datasets.

Precision

Precision, also known as Positive Predictive Value, measures the proportion of true positive predictions out of all positive predictions. It indicates the accuracy of the positive predictions made by the model.

Recall

Recall measures the proportion of true positive instances that were correctly identified by the model. It indicates the model’s ability to capture all positive instances.

F1 Score

The F1 Score is the harmonic mean of precision and recall. It provides a balanced measure of the two metrics, especially useful when the dataset is imbalanced.

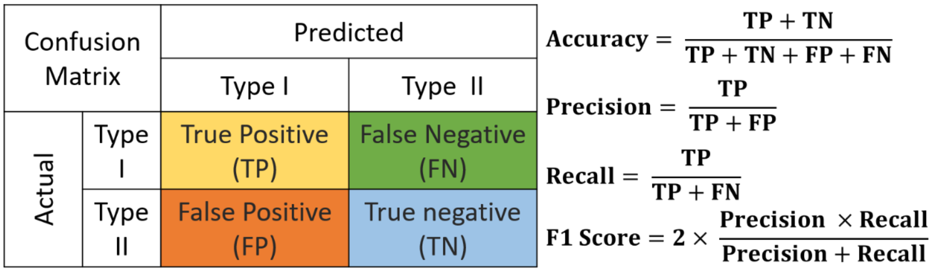

Confusion Matrix		Predicted	
		Type I	Type II
Actual	Type I	True Positive (TP)	False Negative (FN)
	Type II	False Positive (FP)	True negative (TN)

$$\textbf{Accuracy} = \frac{\textbf{TP} + \textbf{TN}}{\textbf{TP} + \textbf{TN} + \textbf{FP} + \textbf{FN}}$$

$$\textbf{Precision} = \frac{\textbf{TP}}{\textbf{TP} + \textbf{FP}}$$

$$\textbf{Recall} = \frac{\textbf{TP}}{\textbf{TP} + \textbf{FN}}$$

$$\textbf{F1 Score} = 2 \times \frac{\textbf{Precision} \times \textbf{Recall}}{\textbf{Precision} + \textbf{Recall}}$$

Figure 1.12: Confusion matrix and derived classification metrics.

For multiclass classification problems, the confusion matrix is extended to an $N \times N$ matrix, where N is the number of classes. Each cell (i, j) in the matrix represents the number of instances of class i that were predicted as class j. The metrics are then averaged or otherwise aggregated to provide overall performance measures.

1.4.4.10. Confidence Interval

A confidence interval is a range of values that is likely to contain a population parameter with a certain level of confidence. When the underlying distribution of the data is unknown, or when the sample size is small, bootstrapping is a powerful statistical method to estimate confidence intervals. Bootstrapping involves repeatedly resampling with replacement from the observed data and calculating the statistic of interest for each resample. This method leverages the empirical distribution of the resampled data to make inferences about the population.

Bootstrapping and Confidence Intervals

The steps are as follows,

Original Sample:

Start with your original sample of data, consisting of n observations. Let's denote this sample as $X = \{x_1, x_2, \dots, x_n\}$

Resampling:

Generate a large number of resampled datasets, each of size n, by sampling with replacement from X. Each resampled dataset is called a bootstrap sample. For example, if we use 1000 bootstrap iterations, meaning we need to create 1000 bootstrap samples.

Statistic Calculation:

For each bootstrap sample, calculate the statistic of interest (e.g., the mean, median, standard deviation). This will give us a distribution of the statistic across the 1000 bootstrap samples.

Confidence Interval Construction:

Use the distribution of the bootstrap statistics to construct the confidence interval. For a 95% confidence interval, we typically take the 2.5th percentile and the 97.5th percentile of the bootstrap distribution as the lower and upper bounds of the interval respectively.

Hence, the confidence interval obtained from the bootstrap distribution provides an estimate of the range within which the true population parameter lies, with a certain level of confidence (e.g., 95%). The bootstrap method is particularly advantageous because it does not assume any specific distribution for the data, making it a versatile tool for estimating confidence intervals in various contexts. This method is robust and widely applicable, providing valuable insights into the variability and reliability of the estimated parameter.

1.5. References

1. Kannan N., Vakeesan D. (2016), Solar energy for future world: - A review, Renewable and Sustainable Energy Reviews, 62, 1092–1105 (DOI: 10.1016/j.rser.2016.05.022)
2. Panwar N. L., Kaushik S. C., Kothari S. (2011), Role of renewable energy sources in environmental protection: A review, Renewable and Sustainable Energy Reviews, 15, 1513–1524 (DOI: 10.1016/j.rser.2010.11.037)
3. Lewis N. S. (2007), Toward Cost-Effective Solar Energy Use, Science, 315, 798–801 (DOI: 10.1126/science.113701)
4. Nozik A. J. Photoelectrochemistry: Applications to Solar Energy Conversion.http://dx.doi.org/10.1146/annurev.pc.29.100178.001201 29, 189–222 (2003).
5. Jena A. K., Kulkarni A., Miyasaka T. (2019), Halide Perovskite Photovoltaics: Background, Status, and Future Prospects, Chem. Rev., 119, 3036– 3103 (DOI: 10.1021/acs.chemrev.8b00539)
6. Kojima A., Teshima K., Shirai Y., Miyasaka T. (2009), Organometal Halide Perovskites as Visible-Light Sensitizers for Photovoltaic Cells, J. Am. Chem. Soc., 131, 6050−6051 (DOI: 10.1021/ja809598r)
7. NREL. Best Research-Cell Efficiency Chart. https://www.nrel.gov/pv/cell-efficiency.html.
8. Chakhmouradian A. R., Woodward P. M. (2014), Celebrating 175 Years of Perovskite Research: A Tribute to Roger H. Mitchell, Phys. Chem. Miner., 41, 387−391 (DOI: 10.1007/s00269-014-0678-9)
9. Brenner T. M., Egger D. A., Kronik L., Hodes G., Cahen D. (2016), Hybrid organic−inorganic Perovskites: Low-cost Semiconductors with Intriguing Charge-transport Properties, Nat. Rev. Mater., 1, 15007 (DOI: 10.1038/natrevmats.2015.7)

10. Yuan Y., Xiao Z., Yang B., Huang J. (2014), Arising Applications of Ferroelectric Materials in Photovoltaic Devices, J. Mater. Chem. A, 2, 6027−6041 (DOI: 10.1039/C3TA14188H)
11. Weber D. (1978), CH3NH3PbX3, ein Pb(II)-System mit kubischer Perowskitstruktur/CH3NH3PbX3, a Pb(II)-System with Cubic Perovskite Structure, Zeitschrift für Naturforschung B, 33, 1443−1445 (DOI: 10.1515/znb-1978-1214)
12. Weber D. (1978), CH3NH3SnBrxI3-x (x = 0−3), ein Sn(II)-System mit kubischer Perowskitstruktur/CH3NH3SnBrxI3-x(x = 0−3), a Sn(II)-System with Cubic Perovskite Structure, Zeitschrift für Naturforschung B, 33, 862−865 (10.1515/znb-1978-0809)
13. Mitzi, D. B. (1999), Synthesis, Structure, and Properties of Organic-Inorganic Perovskites and Related Materials, Progress in Inorganic Chemistry, John Wiley and Sons, Vol. 48, pp 1−122.
14. Mitzi D. B. (2000), Organic−Inorganic Perovskites Containing Trivalent Metal Halide Layers: The Templating Influence of the Organic Cation Layer, Inorg. Chem., 39, 6107−6113 (DOI: 10.1021/ic000794i)
15. Mitzi D. B., Wang S., Feild C. A., Chess C. A., Guloy A. M. (1995), Conducting Layered Organic-inorganic Halides Containing < 110>-Oriented Perovskite Sheets, Science, 267, 1473 (DOI: 10.1126/science.267.5203.147)
16. Lee M. M., Teuscher J., Miyasaka T., Murakami T. N., Snaith H. J. (2012), Efficient Hybrid Solar Cells Based on Meso-Superstructured Organometal Halide Perovskites, Science, 338, 643– 647 (DOI: 10.1126/science.1228604)
17. Goldschmidt V. M. (1926), Naturwissenschaften, 14, 477 (DOI: 10.1007/BF01507527)
18. Miyano K., Tripathi N., Yanagida M., Shirai Y. (2016), Lead Halide Perovskite Photovoltaic as a Model p−i−n Diode, Acc. Chem. Res., 49, 303−310 (DOI: 10.1021/acs.accounts.5b00436)

19. Kondo T., Iwamoto S., Hayase S., Tanaka K., Ishi J., Mizuno M., Ema K., Ito R. (1998), Resonant Third-order Optical Nonlinearity in The Layered Perovskite-type Material (C6H13NH3)2PbI4, Solid State Commun., 105, 503−506 (DOI: 10.1016/S0038-1098(97)10166-1)
20. Tanaka K., Takahashi T., Ban T., Kondo T., Uchida K., Miura N. (2003), Comparative Study on The Excitons in Lead-halide-based Perovskite-type Crystals CH3NH3PbBr3 CH3NH3PbI3, Solid State Commun., 127, 619−623 (DOI: 10.1016/S0038-1098(03)00566-0)
21. Brivio F., Butler K. T., Walsh A., van Schilfgaarde M. (2014), Relativistic Quasiparticle Self-Consistent Electronic Structure of Hybrid Halide Perovskite Photovoltaic Absorbers, Phys. Rev. B: Condens. Matter Mater. Phys., 89, 155204 (DOI: 10.1103/PhysRevB.89.155204)
22. Yin W.-J., Shi T., Yan Y. (2015), Superior Photovoltaic Properties of Lead Halide Perovskites: Insights from First-Principles Theory, J. Phys. Chem. C, 119, 5253−5264 (DOI: 10.1021/jp512077m)
23. Green M. A., Ho-Baillie A., Snaith H. J. (2014), The Emergence of Perovskite Solar Cells. Nat. Photonics, 8, 506−514 (DOI: 10.1038/nphoton.2014.134)
24. Giorgi G., Fujisawa J.-I., Segawa H., Yamashita K. (2013), Small Photocarrier Effective Masses Featuring Ambipolar Transport in Methylammonium Lead Iodide Perovskite: A Density Functional Analysis, J. Phys. Chem. Lett., 4, 4213−4216 (DOI: 10.1021/jz4023865)
25. de Quilettes D. W., Vorpahl S. M., Stranks S. D., Nagaoka H., Eperon G. E., Ziffer M. E., Snaith H. J., Ginger D. S. (2015), Impact of Microstructure on Local Carrier Lifetime in Perovskite Solar Cells, Science, 348, 683−686 (DOI: 10.1126/science.aaa5333)

26. Stranks S. D., Snaith H. J. (2015), Metal-halide Perovskites for Photovoltaic and Light-emitting Devices, Nat. Nanotechnol., 10, 391−402 (DOI: 10.1038/nnano.2015.90)
27. Stranks S. D., Eperon G. E., Grancini G., Menelaou C., Alcocer M. J. P., Leijtens T., Herz L. M., Petrozza A. Snaith H. J. (2013), Electron-Hole Diffusion Lengths Exceeding 1 Micrometer in an Organometal Trihalide Perovskite Absorber, Science, 342, 341−342 (DOI: 10.1126/science.1243982)
28. Dong Q., Fang Y., Shao Y., Mulligan P., Qiu J., Cao L., Huang J. (2015) Electron-hole Diffusion Lengths > 175 μm in Solutiongrown CH3NH3PbI3 Single Crystals, Science, 347, 967−969 (DOI: 10.1126/science.aaa576)
29. Zhao Y., Zhu K. (2014), Optical Bleaching of Perovskite (CH3NH3)PbI3 Through Room-Temperature Phase Transformation Induced by Ammonia, Chem. Commun., 50, 1605−1607 (DOI: 10.1039/C3CC48522F)
30. Frost J. M., Butler K. T., Brivio F., Hendon C. H., Van Schilfgaarde M., Walsh A. (2014), Atomistic Origins of High-Performance in Hybrid Halide Perovskite Solar Cells, Nano Lett., 14, 2584– 2590 (DOI: 10.1021/nl500390f)
31. Smith I. C., Hoke E. T., Solis-Ibarra D., McGehee M. D., Karunadasa H. I. (2014), A Layered Hybrid Perovskite Solar-Cell Absorber with Enhanced Moisture Stability, Angew. Chem., Int. Ed. 53, 11232– 11235 (DOI: 10.1002/anie.201406466)
32. Stoumpos C. C., Cao D. H., Clark D. J., Young J., Rondinelli J. M., Jang J. I., Hupp J. T., Kanatzidis M. G. (2016), Ruddlesden–Popper Hybrid Lead Iodide Perovskite 2D Homologous Semiconductors, Chem. Mater., 28, 2852– 2867 (DOI: 10.1021/acs.chemmater.6b00847)
33. Quan L. N., Yuan M., Comin R., Voznyy O., Beauregard E. M., Hoogland S., Buin A., Kirmani A. R., Zhao K., Amassian A., Kim

D. H., Sargent E. H. (2016), Ligand-Stabilized Reduced-Dimensionality Perovskites, J. Am. Chem. Soc., 138, 2649–2655 (DOI: 10.1021/jacs.5b11740)

34. Katan C., Mercier N., Even J. (2019), Quantum and Dielectric Confinement Effects in Lower-Dimensional Hybrid Perovskite Semiconductors, Chem. Rev., 119, 3140-3192 (DOI: 10.1021/acs.chemrev.8b00417)
35. Sapori D., Kepenekian M., Pedesseau L., Katan C., Even J. (2016), Quantum Confinement and Dielectric Profiles of Colloidal Nanoplatelets of Halide Inorganic and Hybrid Organic–Inorganic Perovskites, Nanoscale, 8, 6369– 6378 (DOI: 10.1039/C5NR07175E)
36. Mao L. L., Stoumpos C. C., Kanatzidis M. G. (2019), Two-Dimensional Hybrid Halide Perovskites: Principles and Promises, J. Am. Chem. Soc., 141, 1171−1190 (DOI: 10.1021/jacs.8b10851)
37. Li X., Ke W., Traoré B., Guo P., Hadar I., Kepenekian M., Even J., Katan C., Stoumpos C. C., Schaller R. D., Kanatzidis M. G. (2019), Two-Dimensional Dion-Jacobson Hybrid Lead Iodide Perovskites with Aromatic Diammonium Cations, J. Am. Chem. Soc., 141, 12880-12890 (DOI: 10.1021/jacs.9b06398).
38. Schlipf J., Hu Y., Pratap S., Bießmann L., Hohn N., Porcar L., Bein T., Docampo P., Müller-Buschbaum P. (2019), Shedding Light on the Moisture Stability of 3D/2D Hybrid Perovskite Heterojunction Thin Films, ACS Appl. Energy Mater., 2, 1011–1018 (DOI: 10.1021/acsaem.9b00005)
39. Sutanto A. A., Drigo N., Queloz V. I. Perdew E., Garcia-Benito I., Kirmani A. R., Richter L., Schouwink P., Cho K. T., Paek s., Nazeeruddin M. K. (2020), Dynamical Evolution of the 2D/3D Interface: A Hidden Driver behind Perovskite Solar Cell Instability, J. Mater. Chem. A, 8, 2343– 2348 (DOI: 10.1039/C9TA12489F)

40. Meng K., Wang X., Li Z., Liu Z., Qiao Z., Wang C., Hu Y., Li S., Cheng L., Zhai Y., Chen G. (2021), Self-passivation of low-dimensional hybrid halide perovskites guided by structural characteristics and degradation kinetics, Energy Environ. Sci., 14, 2357–2368. (DOI: 10.1039/d0ee03836a)
41. Ducinskas A., Kim G. Y., Moia D., Senocrate A., Wang Y. R., Hope M. A., Mishra A., Kubicki D. J., Siczek M., Bury W., Schneeberger T., Emsley L., Milic J. V., Maier J., Gratzel M. (2021), Unravelling the Behavior of Dion–Jacobson Layered Hybrid Perovskites in Humid Environments, ACS Energy Lett., 6, 337−344 (DOI: 10.1021/acsenergylett.0c02344)
42. Yang K., Zhao J., Zhang K., Shao B., Cui F., Yang X. (2023), Humidity Stability of 2D Dion–Jacobson-Phase Perovskites with Hydrophobic Groups in Diammonium Spacers, Ind. Eng. Chem. Res., 62, 16154–16162 (DOI: 10.1021/acs.iecr.3c01656)
43. Febriansyah B., Lekina Y., Ghosh B., Harikesh P. C., Koh T. M., Li Y., Shen Z., Mathews N., England J. (2020), Molecular Engineering of Pure 2D Lead-Iodide Perovskite Solar Absorbers Displaying Reduced Band Gaps and Dielectric Confinement, ChemSusChem, 13, 2693-2701 (DOI: 10.1002/cssc.20200002)
44. Ghosh D., Neukirch A. J., Tretiak S. (2020), Optoelectronic Properties of Two-Dimensional Bromide Perovskites: Influences of Spacer Cations, J. Phys. Chem. Lett., 11, 2955– 2964 (DOI: 10.1021/acs.jpclett.0c00594)
45. Knutson J. L., Martin J. D., Mitzi D. B. (2005), Tuning the Band Gap in Hybrid Tin Iodide Perovskite Semiconductors Using Structural Templating, Inorg. Chem., 44, 4699– 4705 (DOI: 10.1021/ic050244q)
46. Mitzi D. B. (1996), Synthesis, Crystal Structure, and Optical and Thermal Properties of (C4H9NH3)2MI4 (M = Ge, Sn, Pb), Chem. Mater., 8, 791– 800 (DOI: 10.1021/cm9505097)

47. Mahal E., Mandal S. C., Pathak B. (2022), Understanding the role of spacer cation in 2D layered halide perovskites to achieve stable perovskite solar cells, Mater. Adv., 3, 2464−2474 (DOI: 10.1039/D1MA01135A)
48. Han D., Chen S., Du M.-H. (2021), Role of Polycyclic Aromatic Alkylammonium Cations in Tuning the Electronic Properties and Band Alignment of Two-Dimensional Hybrid Perovskite Semiconductors, J. Phys. Chem. Lett., 12, 9754−9760 (DOI: 10.1021/acs.jpclett.1c02603)
49. Ni C., Huang Y., Zeng T., Chen D., Chen H., Wei M., Johnston A., Proppe A. H., Ning Z., Sargent E. H. (2020), Thiophene Cation Intercalation to Improve Band-Edge Integrity in Reduced Dimensional Perovskites, Angew. Chem., 132, 14081−14087 (DOI: 10.1002/ange.202006112)
50. Smith M. D., Connor B. A., Karunadasa H. I. (2019), Tuning the Luminescence of Layered Halide Perovskites, Chem. Rev., 119, 3104−3139 (DOI: 10.1021/acs.chemrev.8b00477)
51. Ema K., Inomata M., Kato Y., Kunugita H., Era M. (2008), Nearly Perfect Triplet-Triplet Energy Transfer from Wannier Excitons to Naphthalene in Organic-Inorganic Hybrid Quantum-Well Materials, Phys. Rev. Lett., 100, 257401 (DOI: 10.1103/PhysRevLett.100.257401)
52. Elshanawany M. M., Ricciardulli A. G., Saliba M., Wachtveitl J., Braun M. (2021), Mechanism of ultrafast energy transfer between the organic–inorganic layers in multiple-ring aromatic spacers for 2D perovskites, Nanoscale, 13, 15668−15676 (DOI: 10.1039/D1NR04290D)
53. Zhang L., Zhang X., Lu G. (2020), Intramolecular Band Alignment and Spin-Orbit Coupling in Two-Dimensional Halide Perovskites, J. Phys. Chem. Lett., 11, 6982−6989 (DOI: 10.1021/acs.jpclett.0c02135)

54. Wei K., Jiang T., Xu Z., Zhou J., You J., Tang Y., Li H., Chen R., Zheng X., Wang S., Yin K., Wang Z., Wang J., Cheng X. (2018), Ultrafast Carrier Transfer Promoted by Interlayer Coulomb Coupling in 2D/3D Perovskite Heterostructures Laser Photonics Rev., 12, 1800128. (DOI: 10.1002/lpor.201800128)
55. Chondroudis K., Mitzi D. B. (1999), Electroluminescence from an Organic−Inorganic Perovskite Incorporating a Quaterthiophene Dye within Lead Halide Perovskite Layers, Chem. Mater., 11, 3028−3030 (DOI: 10.1021/cm990561t)
56. Liang D., Peng Y., Fu Y., Shearer M. J., Zhang J., Zhai J., Zhang Y., Hamers R. J., Andrew T. L., Jin S. (2016), Color-Pure Violet-Light-Emitting Diodes Based on Layered Lead Halide Perovskite Nanoplates, ACS Nano, 10, 6897−6904 (DOI: 10.1021/acsnano.6b02683)
57. Yin J., Li H., Cortecchia D., Soci C., Bredas J.-L. (2017), Excitonic and Polaronic Properties of 2D Hybrid Organic–Inorganic Perovskites, ACS Energy Lett., 2, 417−423 (DOI: 10.1021/acsenergylett.6b00659)
58. Blancon J. C., Stier A. V., Tsai H., Nie W., Stoumpos C. C., Traore B., Pedesseau L., Kepenekian M., Katsutani F., Noe G. T., Kono J., Tretiak S., Crooker S. A., Katan C., Kanatzidis M. G., Crochet J. J., Even J., Mohite A. D. (2018), Scaling law for excitons in 2D perovskite quantum wells, Nat. Commun., 9, 2254 (DOI: 10.1038/s41467-018-04659-x)
59. Born M., Oppenheimer J. (1927), Zur quantentheorie der molekeln, J. Ann. Physik, 84, 457 (DOI: 10.1002/andp.19273892002)
60. Hartree DR. (1928), The Wave Mechanics of an Atom with a Non-Coulomb Central Field. Part I. Theory and Methods, Mathematical Proceedings of the Cambridge Philosophical Society, 24(1), 89-110 (DOI: 10.1017/S0305004100011919)

61. Hohenberg P., Kohn W. (1964), Inhomogeneous electron gas, Phys. Rev. B, 136, B864-B871 (DOI: 10.1103/PhysRev.136.B864)
62. Kohn W., Sham L. J. (1965), Self-consistent equations including exchange and correlation effects, Phys. Rev. 140, A1133-A1138 (DOI: 10.1103/PhysRev.140.A1133)
63. Hohenberg P. C., Kohn W., Sham L. J. (1990), The Beginnings and Some Thoughts on the Future, Advances in Quantum Chemistry, 21, 7-26 (DOI: 10.1016/S0065-3276(08)60589-4)
64. Martin, R. M. (2004), Electronic structure: basic theory and practical methods, Cambridge University press.
65. Ceperley D. M., Alder B. (1980), Ground State of the Electron Gas by a Stochastic Method, J. Phys. Rev. Lett. 45, 566 (DOI: 10.1103/PhysRevLett.45.566)
66. Perdew J. P., Burke K., Ernzerhof M. (1996), Generalized gradient approximation made simple, Phys. Rev. Lett., 77, 3865-3868 (DOI: 10.1103/PhysRevLett.77.3865)
67. Perdew J. P., Wang Y. (1992), Accurate and simple analytic representation of the electron-gas correlation energy, Phys. Rev. B, 45, 13244-13249 (DOI: 10.1103/PhysRevB.45.13244)
68. Perdew J. P., Ruzsinszky A., Csonka G. I., Vydrov O. A., Scuseria G. E., Constantin L. A., Zhou X., Burke K. (2008), Restoring the density-gradient expansion for exchange in solids and surfaces, Phys. Rev. Lett., 100, 136406 (DOI: 10.1103/PhysRevLett.100.136406)
69. Janesko B. G., Henderson T. M., Scuseria G. E. (2009), Phys. Chem. Chem. Phys., 11, 443-454 (DOI: 10.1039/B812838C)
70. Heyd J., Scuseria G. E., Ernzerhof M. (2003), Hybrid functionals based on a screened Coulomb potential, The Journal of chemical physics, 118, 8207-8215 (DOI: 10.1063/1.1564060)
71. Heyd J., Scuseria G. E. (2004), Efficient hybrid density functional calculations in solids: Assessment of the Heyd–Scuseria–Ernzerhof

screened Coulomb hybrid functional, The Journal of chemical physics, 121, 1187-1192 (DOI: 10.1063/1.1760074)

72. Grimme S., Antony J., Ehrlich S., Krieg H. (2010), A consistent and accurate ab initio parametrization of density functional dispersion correction (DFT-D) for the 94 elements H-Pu, J. Chem. Phys. 132, 154104 (DOI: https://doi.org/10.1063/1.3382344)
73. Grimme S. (2011), Density functional theory with Londondispersion corrections, WIREs Comput. Mol. Sci., 1, 211-228 (DOI: 10.1002/wcms.30)
74. Grimme S. (2004), Accurate description of van der Waals complexes by density functional theory including empirical corrections, J. Comput. Chem., 25, 1463-1473 (DOI:10.1002/jcc.20078)
75. Frenkel D., Smit B. (2002), Understanding Molecular Simulation: From Algorithms to Applications, Academic Press, London.
76. Allen M. P., Tildesley D. J. (1987), Computer Simulation of Ionic Liquids, Clarendon Press, Oxford.
77. Grubmüller, H.; Heller, H.; Windemuth, A.; Schulten, K. (1991), Generalized Verlet Algorithm for Efficient Molecular Dynamics Simulations with Long-Range Interactions. Molecular Simulation, 6 (1–3), 121– 142 (DOI: 10.1080/08927029108022142)
78. Hansen J.-P., McDonald I. (2013), Theory of Simple Liquids, Academic Press.
79. McQuarrie D. (2000), Statistical Mechanics; University Science Books, California.
80. Pastor, R. W.; Brooks, B. R.; Szabo, A. (1998), An Analysis of the Accuracy of Langevin and Molecular Dynamics Algorithms. Mol. Phys., 65, 1409–1419 (DOI: 10.1080/00268978800101881)
81. Andersen, H. C. (1980), Molecular Dynamics Simulations at Constant Pressure and/or Temperature. The J. Chem. Phys., 72, 2384–2393 (DOI: 10.1063/1.439486)

82. Berendsen, H. J. C.; Postma, J. P. M.; van Gunsteren, W. F.; DiNola, A.; Haak, J. R. (1984), Molecular Dynamics with Coupling to an External Bath, J. Chem. Phys., 81 (8), 3684–3690 (DOI: 10.1063/1.448118)
83. Nosé, S. (1984), A Unified Formulation of the Constant Temperature Molecular Dynamics Methods, J. Chem. Phys., 81 (1), 511–519 (DOI: 10.1063/1.447334)
84. Bader, R. F. W. (1994), Atoms in Molecules: A Quantum Theory, Oxford University Press: USA.
85. Henkelman G., Arnaldsson A., Jonsson H. (2006), A fast and robust algorithm for Bader decomposition of charge density, Comput. Mater. Sci., 36, 354-360 (DOI: 10.1016/j.commatsci.2005.04.010)
86. Montesinos López O. A., Montesinos López A., Crossa J. (2022), Elements for Building Supervised Statistical Machine Learning Models, Multivariate Statistical Machine Learning Methods for Genomic Prediction, 71–108 (DOI: 10.1007/978-3-030-89010-0_3)
87. Montgomery, D. C.; Peck, E. A.; Vining, G. G. Introduction to Linear Regression Analysis. 673.
88. Carr D. A., Lach-hab M., Yang S., Vaisman I. I., Blaisten-Barojas E. (2009), Machine Learning Approach for Structure-Based Zeolite Classification, Microporous and Mesoporous Materials, 117, 339–349 (DOI: 10.1016/J.MICROMESO.2008.07.027)
89. Liu Y., Zou X., Ma S., Avdeev M., Shi S. (2022), Feature Selection Method Reducing Correlations among Features by Embedding Domain Knowledge, Acta Mater, 238, 118195 (DOI: 10.1016/j.actamat.2022.118195)
90. Deng Q., Lin B. (2021), Exploring Structure-Composition Relationships of Cubic Perovskite Oxides via Extreme Feature Engineering and Automated Machine Learning, Mater Today Commun, 28, 102590. (DOI: 10.1016/J.MTCOMM.2021.102590)

91. Schratz P., Muenchow J., Iturritxa E., Richter J., Brenning A. (2019), Hyperparameter Tuning and Performance Assessment of Statistical and Machine-Learning Algorithms Using Spatial Data, Ecol Modell, 406, 109–120 (DOI: 10.1016/J.ECOLMODEL.2019.06.002)
92. Ahmad G. N., Fatima H., Shafiullah, Salah Saidi A., Imdadullah. (2022), Efficient Medical Diagnosis of Human Heart Diseases Using Machine Learning Techniques with and Without GridSearchCV, IEEE Access, 10, 80151-80173 (DOI: 10.1109/ACCESS.2022.3165792)
93. Shao Z., Er M. J., Wang N. (2015), An Effective Semi-Cross-Validation Model Selection Method for Extreme Learning Machine with Ridge Regression, Neurocomputing, 151 (P2), 933–942 (DOI: 10.1016/J.NEUCOM.2014.10.002)
94. Shrivastava Scribe By, A.; Sanclemente, K.; Kafer, J.; Houlette, T.; McDonnell, S. COMP 642-Machine Learning Lecture 5: Deep Learning: Logistic Regression 1 Multi-Class Classification: One-vs-All. 2022.
95. Schölkopf B., Smola A. J. (2018), Learning with Kernels: Support Vector Machines, Regularization, Optimization, and Beyond.
96. Huang G., Guo Y., Chen Y., Nie Z. (2023), Application of Machine Learning in Material Synthesis and Property Prediction, Materials, 16, 5977 (10.3390/ma16175977)
97. Ge J., Zhao L., Yu Z., Liu H., Zhang L., Gong X., Sun H. (2022), Prediction of Greenhouse Tomato Crop Evapotranspiration Using XGBoost Machine Learning Model, Plants, 11, 1923 (DOI: 10.3390/PLANTS11151923)
98. R 42. Pedregosa F., Varoquaux Gramfort G., A., Michel V., Thirion B., Grisel O., Blondel M., Prettenhofer P., Weiss R., Dubourg V., Vanderplas J., Passos A., Cournapeau D. (2011),

Scikit-learn: Machine learning in Python, J. Mach. Learn. Res., 12, 2825–2830.

Chapter 2

Stability of 2D Hybrid Perovskites at Water Interfaces

2.1. Introduction

Hybrid halide perovskites with general formula AMX_3, where A is a monovalent cation (formamidinium (FA) or methylammonium (MA)), M a divalent metal (Pb, Sn), and X a halide (I, Br, Cl) have emerged as potential choice of material for the optoelectronic devices. *[1-7]* However, these exceptionally efficient materials commonly known as 3D perovskites suffer from instability issue in the operational circumstances (toward light, oxygen, and moisture). *[8-9]* The methylammonium cations can be replaced with bulkier cations such as butylammonium, phenylethyl ammonium to tune the perovskite systems. *[10-12]* Although, according to the Goldschmidt tolerance factor, these large cations cannot fit into the metal-halide octahedral cavity but separate two consecutive inorganic layers and act as spacer cation connecting the inorganic metal-halide layers. *[13]* Low dielectric nature of the large cations makes the perovskite to be multiple quantum-well type in nature and the materials are referred as 2D hybrid perovskites. *[14-15]* There are two major classes of 2D perovskites, namely, Ruddlesden-Popper (RP) phases and Dion-Jacobson (DJ) phases. *[16]* Ruddlesden−Popper (RP) phase contains bilayers of monovalent organic spacer (A′) with chemical formula $A'_2A_{n-1}M_nX_{3n+1}$. Whereas perovskites featuring monolayers of bivalent organic spacer (A″) with the formula of $A''A_{n-1}M_nX_{3n+1}$ are referred as Dion−Jacobson (DJ) phase. Here n represents the thickness of metal-halide layers between organic spacer layers.

However, the degradation mechanism of perovskites necessitates special attention to address the stability issue. There are experimental reports of degradation of RP phase quasi 2D perovskites to n-1 2D and 3D perovskites when exposed to water vapour. *[17]* Also, poor stability of RP perovskites based on 1-propylamine compared to 1,3-diaminopropane based DJ perovskites was reported. *[18]* This observation was justified owing to the absence of the van der Waals gap between organic spacer layers in DJ phase

2D hybrid perovskites. Again, hydration tendency of some bifunctional spacer based perovskites are reported. *[19]* These reports indicate the role played by perovskite structure towards their moisture stability and distinct behaviour of two phases towards humidity. As of now, the detailed studies on the degradation behaviour of the 3D methylammonium lead iodide ($MAPbI_3$) perovskite in presence of heat and moisture have shed light on their future design strategy. *[20-21]* In these studies, degradation mechanism of different surface terminations in presence of water interfaces were demonstrated using ab initio molecular dynamics (AIMD) simulations. Comparative analysis of MAI terminated surfaces with PbI_2 terminated surfaces showed robustness of the latter over former. *[20]* Such insights help to understand the design principle and scope of the material. However, there are no such theoretical insights provided yet on the interaction nature of 2D perovskites at the water interfaces. Compared to methyl ammonium cations present in 3D counterparts, large organic spacers present in 2D perovskite are expected to be more reluctant towards water. Moreover, an atomic level study on the behaviour of two phases of 2D perovskites towards moisture is of utmost importance. A proper insight on the degradation mechanism of these 2D hybrid perovskites could enlighten understanding of their stability criterion and further application.

In this work we have carried out the ab initio molecular dynamics (AIMD) simulations to understand the nature of interactions of 2D hybrid perovskites at water interfaces. Here, we have focused on the different behaviour of two perovskite phases DJ and RP towards water. Two perovskite systems we have considered in this study are RP phase $(BA)_2PbI_4/H_2O$ interface and DJ phase $(3AMP)PbI_4/H_2O$ interface (Where, BA and 3AMP are n-butylammonium and 3-aminomethylpyridinium, respectively). For both the systems we have considered possible surface terminations as follows, (i) PbI_2 termination where PbI_2 layer is present in the direct contact with water molecules, (ii) iodine termination where axial iodides are interfaced with the water environment, (iii) organic spacer cation termination where organic spacer molecules are interfaced with water molecules (Figure 2.1).

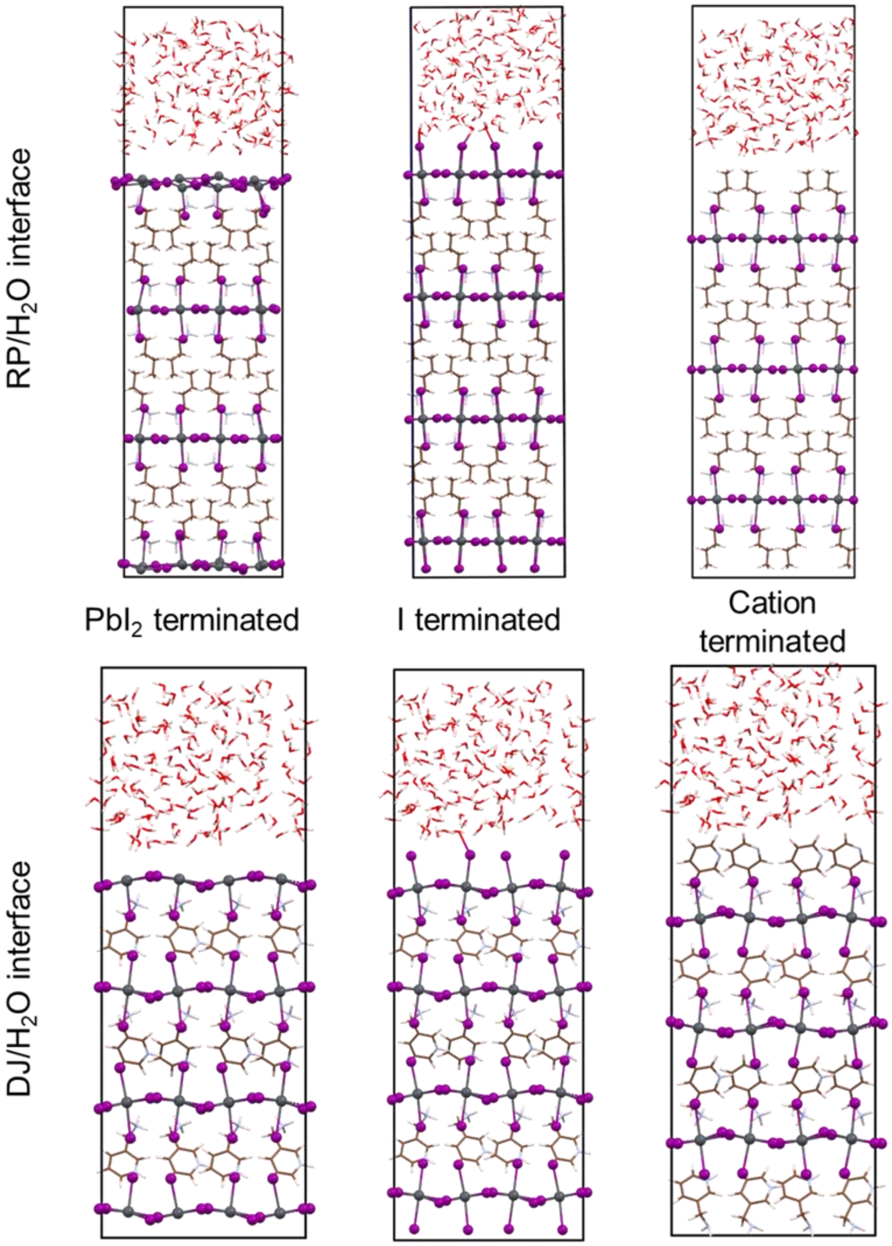

Figure 2.1: Hydrated interface models of RP ($(BA)_2PbI_4$) and DJ ($(3AMP)PbI_4$) phase perovskites with different terminations. Color codes: hydrogen (pink), carbon (brown), nitrogen (blue), oxygen (red), iodine (purple) and lead (grey).

2.2. Methodology

For the considered RP and DJ phase perovskites we have modelled 2×2 supercells of the respective (001) surfaces of PbI_2-, I- and organic layer-terminated systems. The considered crystal structure for modelling of these systems agree with reported lattice parameters from experiment agreeing with the experimental lattice parameters. *[16,22]* Further a vacuum region of 15 Å on top of the perovskite slabs is considered to be filled up with water molecules. Owing to the experimental density of liquid water (1.003 g/cm3), we have filled the vacuum region with 150 water molecules with the help of PACKMOL software thereby creating surface-water interface models of the 2D halide perovskites as shown in Figure 2.1. *[23]* The lattice parameters of all the considered systems are mentioned in Table 2.1.

Table 2.1: Lattice parameters of all considered models.

Phase	**Cell Parameters**	**PbI_2 termination (Å)**	**I termination (Å)**	**Cation termination (Å)**
RP/H_2O	*a*	17.65	17.65	17.65
	b	17.14	17.14	17.14
	c	62.50	63.82	59.94
DJ/H_2O	*a*	18.32	18.32	18.32
	b	17.01	17.01	17.01
	c	51.00	53.74	48.62

The AIMD simulations of the considered models have been carried out in the CP2K package implementing the Quickstep module which has emerged as a robust tool for carrying out large scale simulations in rapid time. *[24-26]* A double-ζ basis set (DZVPMOLOPT) along with norm-conserving Goedecker−Teter−Hutter (GTH) pseudopotentials was used. *[27-28]* A wave function CUTOFF = 500 Ry, and for the expansion of the electron density a REL_CUTOFF = 50 Ry was used. The exchange correlation potentials were implemented using PBE functional with the DFT-D3 van der Waals corrections as described by Grimme. *[29-30]* A canonical ensemble method was appointed to fix the volume and the temperature was controlled using a Nosé−Hoover thermostat with a target temperature of 350 K. *[31-32]* For all the considered models, AIMD simulations were performed till 10 ps with a time step of 1 fs to understand the evolution of the perovskite surfaces in presence of water. Similar timescales have been reported to be enough for 3D perovskite systems. *[20,21]* Also, we have performed Bader charge analysis with the help of Henkelman program to quantify the results and understand the impact of charges on elements as well as layers. *[33-36]* To analyze the interactions between various kinds of atoms throughout the simulations we have calculated the radial distribution functions (RDF), g(r) as,

$$g_{ij}(r) = \frac{<n_{ij}(r)>}{4\pi r^2 \rho_j dr} \tag{2.1}$$

where $< n_{ij}(r) >$ is the ensemble average number of jth type particles present at distance r from the ith type particles within a volume of $4\pi r^2 dr$. ρ_j is the bulk density of jth type particles. The RDFs are integrated to obtain the number of jth type species at a distance r around the ith type species,

$$int\left[g_{ij}(r)\right] = 4\pi\rho_j \int_0^r g_{ij}(r) r^2 dr \tag{2.2}$$

2.3. Results

Now, we have considered the simulations of all the three terminated surfaces of both RP and DJ phases of 2D halide perovskites which have been discussed separately henceforth.

2.3.1. PbI_2 Termination

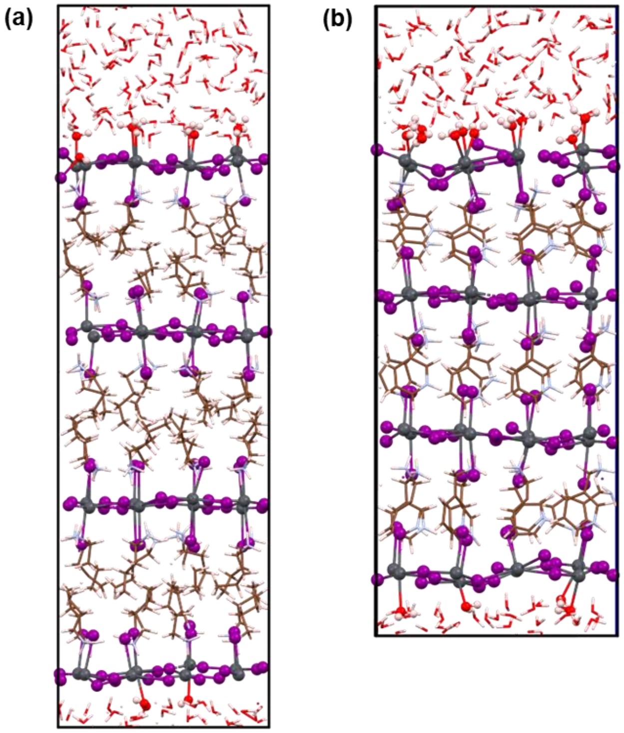

Figure 2.2: Post simulation geometries of PbI_2 terminated (a) RP/H_2O interface and (b) DJ/H_2O interface. Color codes: hydrogen (pink), carbon (brown), nitrogen (blue), oxygen (red), iodine (purple) and lead (grey).

First, we analyze the PbI_2-terminated surface-water interfaces of RP and DJ phases (Figure 2.1). The post simulation structures are provided in Figure 2.2, and a zoomed view is presented in Figure 2.3. From both Figure 2.2 and Figure 2.3, structural distortions of Pb-I surface are visible in the surface-water interfaces for both the phases. Thus, we have analyzed the various interactions using RDF plots.

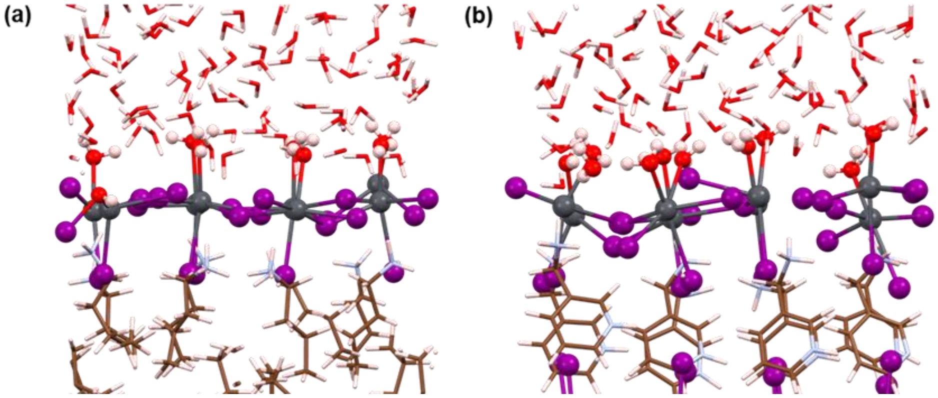

Figure 2.3: PbI_2 terminated (a) RP/H_2O interface, and (b) DJ/H_2O interface after 10ps simulation. Color codes: hydrogen (pink), carbon (brown), nitrogen (blue), oxygen (red), iodine (purple) and lead (grey).

To understand the effect of water, we have separately plotted the Pb-I RDFs for the surface and inner bulk layers as shown in Figure 2.4a-b. Two Pb-I layers which are in contact with water are referred as surface layers whereas, two inner Pb-I layers are referred as bulk layers. From Figure 2.4a, the peaks for surface Pb-I bonds are found to be broader than those of bulk layers for both the phases. This shows that the Pb-I bonding interactions at the surface layer are being influenced by the presence of water environment. In other words, the interaction with nearby water molecules leads variation in the existing Pb-I interactions as reflected by the broad peaks. From the integrated RDFs shown in Figure 2.4b, the coordination environment of the Pb atoms can be grasped. The number of Pb-I interactions for each Pb atoms is nearly 4 (Figure 2.4b) for the surface layers compared to 5 for bulk layers at 3 Å in both the phases. Upon comparing the surface layers for both phases, we can say that the coordination number for Pb-I bonds is less in RP phase compared to DJ phase (Figure 2.4b). This suggest that stronger interaction with water is experienced by the RP phase compared to the DJ/H_2O interface. From Bader analysis, we have observed that surface layer Pb atoms are more electropositive in nature (~ 0.99 |e|) compared to the bulk layer Pb atoms (~ 0.90 |e|) which results from the interaction with water environment at the surface.

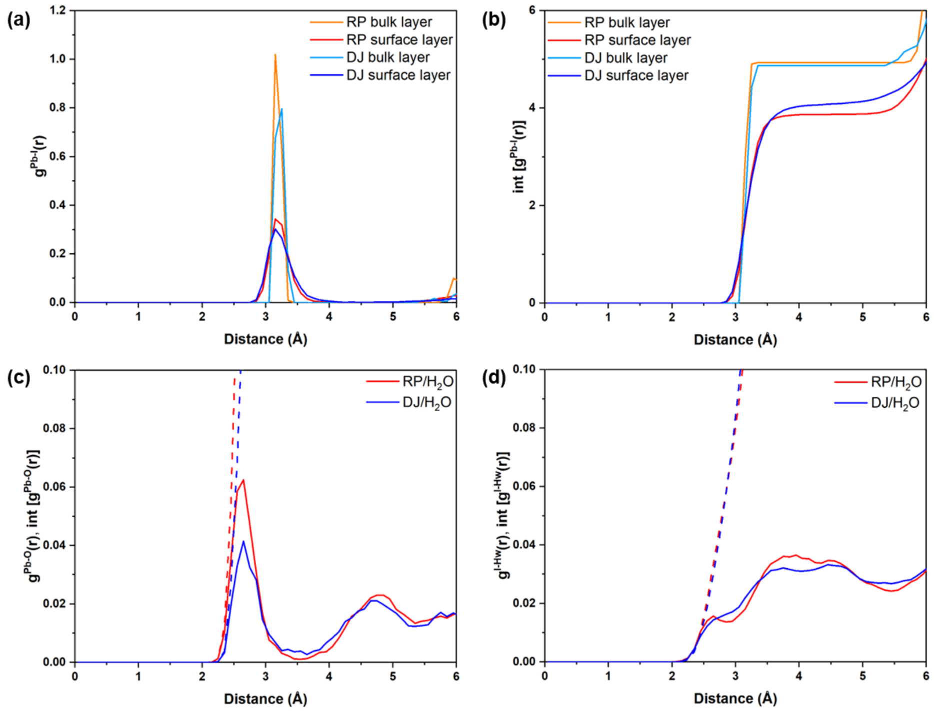

Figure 2.4: (a) Radial pair distribution plots and (b) Integrated distribution plots of Pb-I for RP and DJ interfaces for the PbI_2 terminated surface-water interfaces. Radial pair distribution and integrated distribution plots of (c) Pb−O, and (d) I−H_w for the PbI_2 terminated surface-water interfaces. Regular lines represent g(r), and dashed lines represent int[g(r)].

Also, we have studied the interactions happening at the interface between the surface atoms and water molecules. The possible interactions could be between Pb and water O atoms (Pb-O) and between I and water H atoms (I-H_w) (Figure 2.3). Thus, we have plotted the RDFs for Pb-O and I-H_w interactions as presented in Figure 2.4c-d. From Figure 2.4c, the average Pb-O distance is found to be ~ 2.6 Å which suggests interaction between surface Pb and lone pair of water O atoms. The Pb-O interaction is found to be stronger in RP phase compared to DJ phase (Figure 2.4c). This can also be confirmed from the integrated distribution plot in Figure 2.5a, where larger number of Pb-O coordination is seen at shorter bond distances (till 3 Å) for RP/H_2O interface compared to DJ/H_2O interface. Such observation is supported by Pearson's hard-soft acid-base principle. Similar interactions are also found for 3D perovskites as reported by De Angelis and coworkers.*[21]*

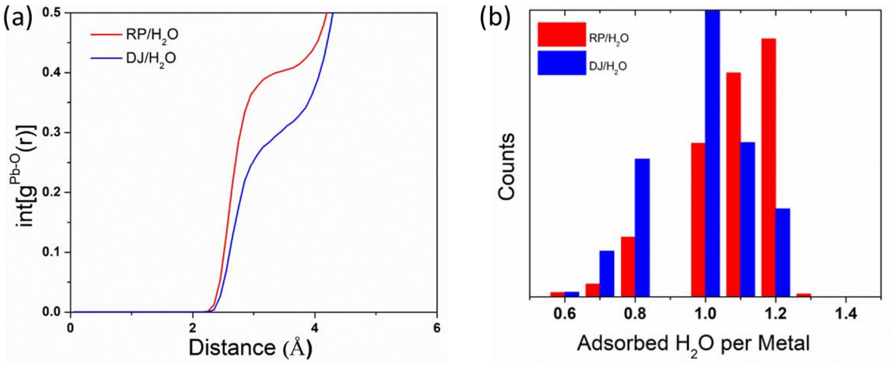

Figure 2.5: (a)Integrated distribution plots of Pb–O radial pair distribution of PbI_2 terminated RP/H_2O interface and DJ/H_2O interface. (b) Histograms of the number of adsorbed waters per metal for the PbI_2 terminated water interfaces throughout the MD trajectories.

However, I-H_w interactions show wide distribution in the RDF plot without any distinct peak for both phases (Figure 2.4d). The distributions start at ~2.2 Å in both the interfaces thereby indicating the presence of hydrogen bonding interactions between I and water. From these findings, we can say that RP/H_2O interface experiences stronger Pb-O interaction whereas both interfaces experience similar I-H_w interaction. Also, comparing peak intensity of Pb-O and I-H_w RDFs (at 3 Å) we can see stronger interaction through Pb-O bond formation. So, we can mention that PbI_2 terminated RP phase interacts with the water at a larger extent compared to DJ phase. Also, to understand the water adsorption nature of the perovskite surface, we have calculated adsorbed water molecules per metal for both the phases. In Figure 2.5b, we have presented the histograms for the number of water molecules adsorbed per metal over the simulation trajectories. From the plot we can notice high frequencies of the numbers 1.1 and 1.2 in case of RP/H_2O interface compared to DJ/H_2O interface, inferring adsorption of water molecules on the surface at a larger extent. Hence, we can conclude that decomposition via water adsorption would happen faster in RP than DJ phase.

2.3.2. Iodine Termination

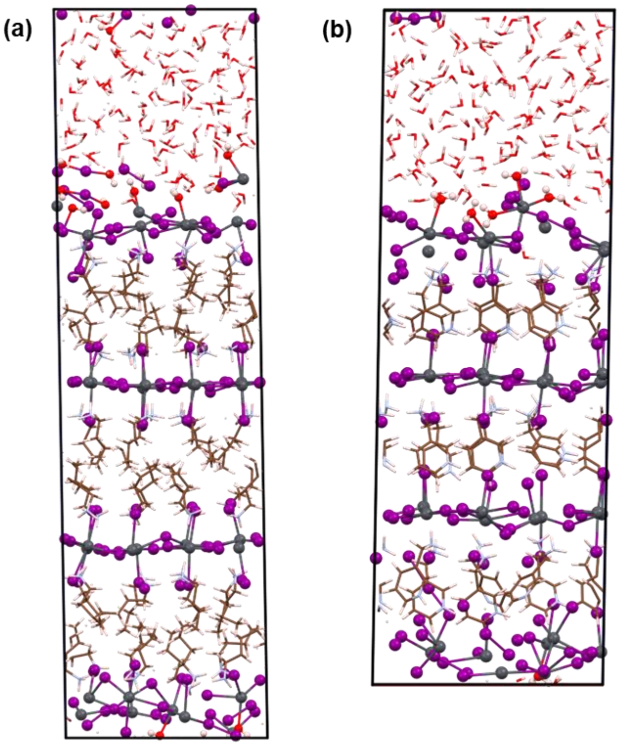

Figure 2.6: Post simulation geometries of I terminated (a) RP/H_2O interface and (b) DJ/H_2O interface. Color codes: hydrogen (pink), carbon (brown), nitrogen (blue), oxygen (red), iodine (purple) and lead (grey).

Here we have analyzed the I-terminated surface-water interfaces of RP and DJ phases (Figure 2.1). The simulated structures of the same are presented in Figure 2.6 with a zoomed view of the interface given in Figure 2.7. From the simulated figures (Figure 2.6 and Figure 2.7), the distortion in the interfaces is very evident, especially the formation of I_2 molecules. Figure 2.6 shows that the inner layers are largely unaffected whereas the surface layers react with the water environment.

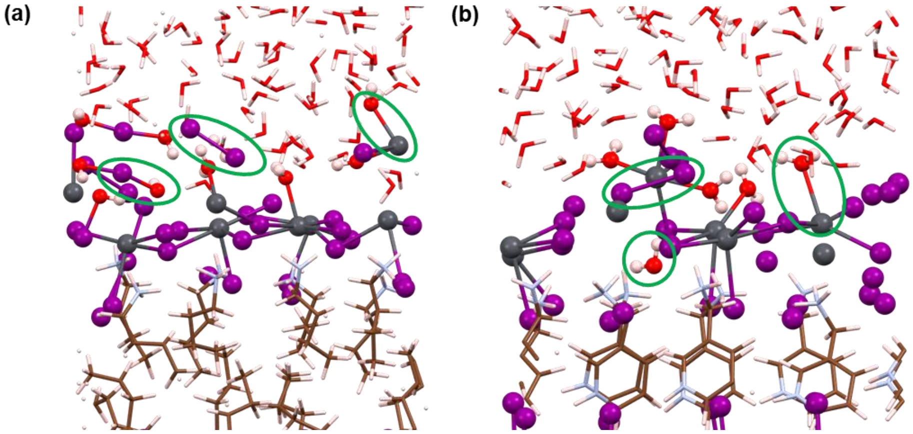

Figure 2.7: I terminated (a) RP/H_2O interface, and (b) DJ/H_2O interface after 10ps simulation. Color codes: hydrogen (pink), carbon (brown), nitrogen (blue), oxygen (red), iodine (purple) and lead (grey).

To quantify these changes, we have plotted the RDFs averaged throughout the simulation trajectories. Again, we have categorized the inorganic layers as surface and bulk layers and the RDF plots for Pb-I are represented in Figure 2.8a. From Figure 2.8a, sharp peaks are observed for bulk Pb-I layers compared to the broad peaks for surface Pb-I layers which interact with water molecules. For RP/H_2O interface, Pb-I RDF gives a sharp peak at 3.26 Å for the bulk layers whereas the broad peak at 3.16 Å is observed for surface layers (Figure 2.8a). Similarly, for the DJ/H_2O interface the bulk and surface Pb-I RDF peaks are found at 3.16 Å and 3.14 Å with sharp and broad distribution, respectively (Figure 2.8a). From the integrated RDF plots, the number of bulk Pb-I interactions reaches 5 at 3.27 Å, whereas for surface Pb atoms it ranges from 2 to 4 within 4 Å in the RP phase (Figure 2.8b). Also, in case of DJ phase the number of bulk Pb-I interactions reaches 5 within 3.60 Å, whereas for surface it ranges from 2 to 4 within 4 Å (Figure 2.8b). These observations suggest the complete breakdown of octahedral framework at the surface of I terminated perovskites for both the water interface models.

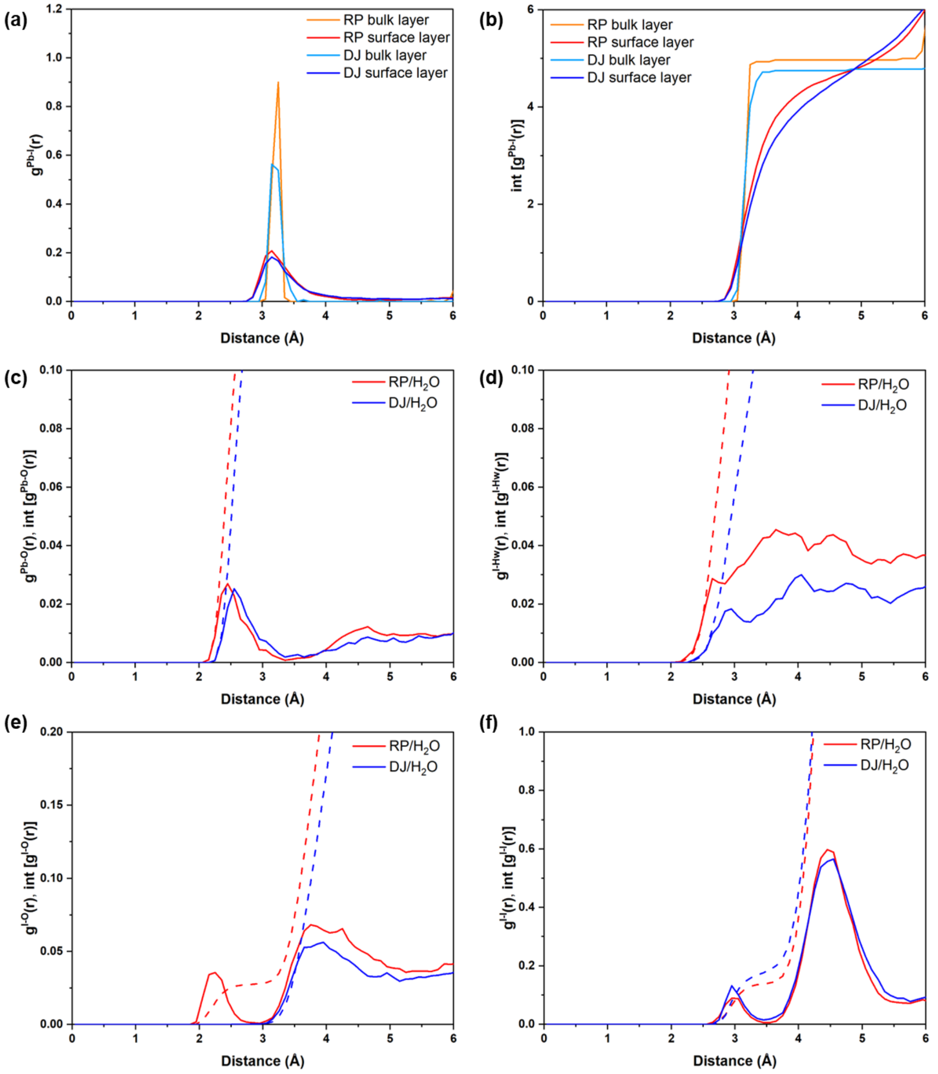

Figure 2.8: (a) Radial pair distribution plots and (b) integrated distribution plots of Pb-I for RP and DJ interfaces for the I terminated surface-water interfaces. Radial pair distribution and integrated distribution plots of (c) Pb–O, (d) I–H_w, (e) I–O and (f) I–I for the I terminated surface-water interfaces. Regular lines represent g(r), and dashed lines represent int[g(r)].

During the simulation different type of interactions occur between the surface and the water environment. In Figure 2.7a we have highlighted the bonding interactions experienced by RP/H_2O interface. Also, the decomposition of Pb-I bonds due to interaction with water is visible leading to the formation of I_2. Interestingly for DJ/H_2O interface we noticed one of the water molecules diffusing towards the spacer cation layer through inorganic slabs (Figure 2.7b). Infiltration of water molecules through the DJ phase perovskite in presence of moisture was also observed experimentally by Grätzel and coworkers.*[19]* Infiltration of water can lead to nucleophilic substitution at the Pb metal centres which triggers the release of I leading to I_2 formation (Figure 2.7).*[21]* Thus, to quantify the interactions between surface Pb atoms and water O atoms, we have plotted the RDFs for Pb-O averaged over the simulation as shown in Figure 2.8c. The peaks for Pb-O interaction are seen at 2.45 and 2.56 Å for RP/H_2O and DJ/H_2O perovskite water interface models, respectively. Thus, the interaction between Pb from the surface layer and O from water is evident. The stronger interaction in case of RP phase is also supported by the more positive charge on surface Pb atoms in this case (0.99 |e| for RP vs 0.89 |e| for DJ). Next, we investigate the RDFs for interaction between surface I atoms and water H atoms (H_w) as shown in Figure 2.8d. I-H_w interaction is detected supported by the peak starting at 2.65 Å for the RP/H_2O interface whereas for the DJ/H_2O interface the peak is broader, and a little right shifted at 2.86 Å referring weaker interaction strength compared to RP phase (Figure 2.8d). Noticeably for both cases the RDF broadens substantially after the peak due to long range interactions. From these findings we can highlight an unusual observation that RP/H_2O interface is much more sensitive to both the Pb-O and I-H_w interactions than DJ phase. Despite the water infiltration that happens, DJ/H_2O interface is robust towards moisture compared to RP phase. Similar observations are reported for the 3D analogue where the PbI_2 terminated $MAPbI_3$ perovskite structure remains undistorted even after water infiltration.*[21]*

Notably, from the AIMD simulation we noticed significant interaction between surface I atoms and water oxygen atoms (Figure 2.7a). To support this observation, we have calculated the RDFs for I-O as presented in Figure 2.8e. For the RP/H_2O interface, peak at 2.24 Å indicates the formation of I-O bond whereas no such interaction is present in DJ/H_2O interface (Figure

2.8e). This observation is also supported by the fact that few of the surface I atoms are positively charged in RP/H_2O interface having charges around 0.43 |e|. These positively charged I atoms are responsible for the formation of I-O bonds. For both the phases broad peak is observed close to 4 Å due to the water molecules present at larger distances. To investigate the I_2 molecule formation detected in Figure 2.7a-b as some surface I atoms diffuse into the water environment we have plotted the RDFs for I-I interaction as presented in Figure 2.8f. The peak observed at 3 Å indicates the formation of I_2 molecule (Figure 2.8f). The later peak arising around 4.5 Å region is due to other I atoms present in the inorganic layer. From charge analysis, the positively charged I (~ 0.21 |e|) atoms combine with negatively charged I (~ -0.50 |e|) atoms to form the I_2 molecule for both the phases of water interfaces. This occurrence can be correlated with the decrease in Pb-I coordination number discussed earlier. Since the surface I atoms originally bonded with Pb diffuses and forms I_2, Pb-I coordination number decreases eventually. From these observations, we can say that the I terminated water interfaces of both the RP and DJ perovskite phases face similar interactions with water differing only in the I-O interactions. For both phases, I termination cannot be considered as a preferable termination from water stability perspective due to the formation of I_2 because of nucleophilic substitution of H_2O at the Pb centres.

2.3.3. Cation Termination

Now, we move on to study the simulation results of the cation terminated surface-water interfaces for both phase perovskites (Figure 2.1). In Figure 2.9 we have presented the simulated geometries of two considered perovskites and a zoomed view of the interfaces are shown in Figure 2.10. Extensive water infiltration through the organic cation layer at surface can be observed in the simulated structures (Figure 2.9 and Figure 2.10). In this case as the PbI layers are not at the surface, they are mostly found to be intact.

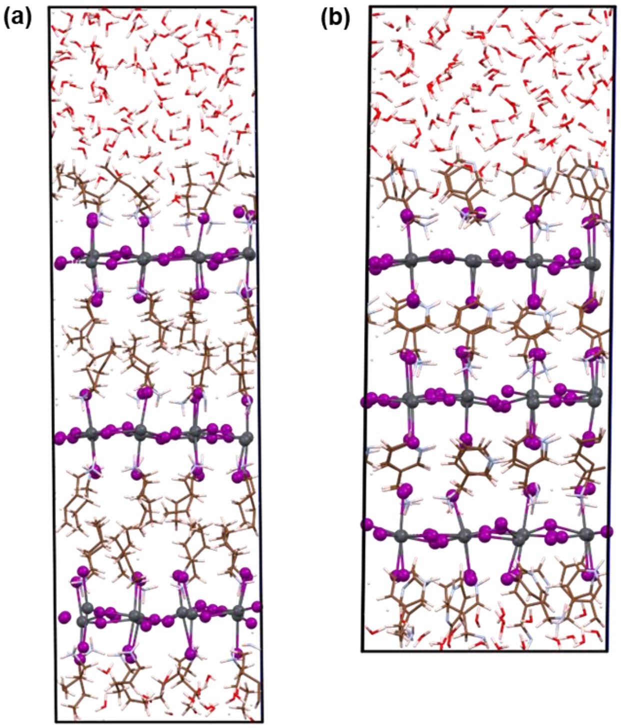

Figure 2.9: Post simulation geometries of cation terminated (a) RP/H_2O interface and (b) DJ/H_2O interface. Color codes: hydrogen (pink), carbon (brown), nitrogen (blue), oxygen (red), iodine (purple) and lead (grey).

Although within the simulation time, water molecules did not cross the organic layer completely and react with the inorganic layer, we have analyzed the robustness of the two cation terminated interfaces towards surface water molecules. Thus, we have further calculated the RDFs for interaction between Pb atoms and water O atoms for the cation terminated water interface models (Figure 2.11a). From Figure 2.11a, Pb-O RDF in RP/H_2O interface (BA cation) show a broad distribution starting at 4.2 Å and a peak located at 4.55 Å. However, the Pb-O RDF in DJ/H_2O interface (3AMP cation) shows a weak distribution starting as far as 5.2 Å (Figure 2.11a). Thus, the 3AMP cation in the DJ/H2O interface is found to be more resistive towards the water environment. This is also supported by the presence of more charge present on the oxygen atoms of the water layer in RP/H_2O interface (-1.33 |e| per O) compared to DJ/H_2O interface (-1.29 |e|

per O). This further supports the robustness of the 3AMP cation in comparison to the BA. Further, we have analyzed the RDF for the interaction between I and water H atoms as presented in Figure 2.11b. The I-H_w RDFs show a peak at ~2.55 Å (Figure 2.11b). High intensity of peak for the DJ/H_2O interface indicates its preferability to interact through I-H_w hydrogen bonding. The less pronounced nature of Pb-O interaction than I-H_w can be seen upon comparing the intensity of Pb-O and I-H_w RDFs.

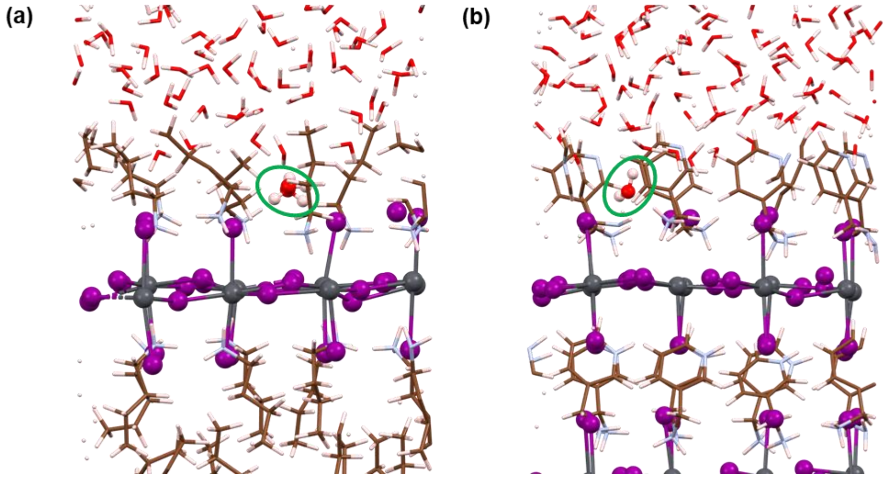

Figure 2.10: Cation terminated (a) RP/H_2O interface, and (b) DJ/H_2O interface after 10ps simulation. Colour codes: hydrogen (pink), carbon (brown), nitrogen (blue), oxygen (red), iodine (purple) and lead (grey).

Since the polar water molecules are not able to diffuse into the perovskite through the hydrophobic organic chain, they could only reach up to an interacting distance of axial iodides of the inorganic layer (Figure 2.10). This observation can be attributed to the robustness of organic cations that keep the PbI layer protected from the water infiltration. To support the robustness of organic cations, we have verified the H-bonding interaction nature of the axial I and ammonium H of the surface organic layer. For both the perovskite phases, consistent interaction between axial I of inorganic layer and ammonium H of surface organic cations interfacing with water environment is observed throughout the simulations (Figure 2.11c-d).

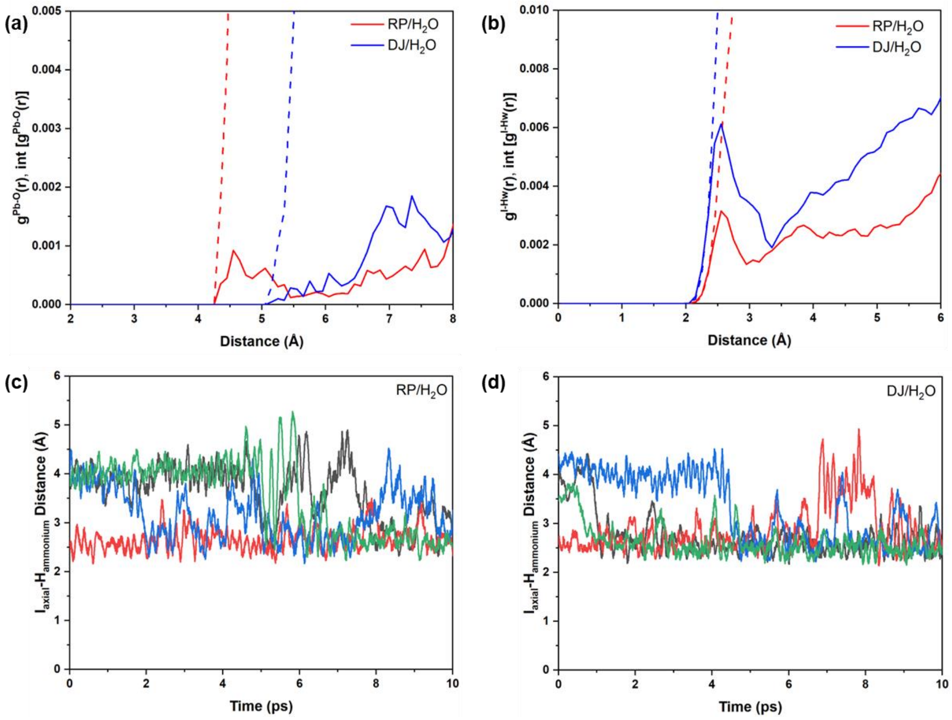

Figure 2.11: Radial pair distribution plots and integrated distribution plots of (a) Pb-O, and (b) I−H_w for the cation terminated surface-water interfaces. Regular lines represent g(r), and dashed lines represent int[g(r)]. H-bonding interaction between axial iodine and ammonium hydrogens of surface organic layer of (c) RP/H_2O interface and (d) DJ/H_2O interface.

2.4. Discussions

Finally, one of the main goals of this study is to find the possible ways of degradation of the perovskite structure in presence of water/moisture. In other words which terminations are more prone to structural distortion in presence of water. In this context, we have compared the RDFs of Pb-I interactions for all the considered systems as the Pb-I bond decomposition has been found to be the possible way for the initiation of instability in presence of water. From Figure 2.12a-b one can notice that cation and PbI_2 terminated water interfaces possess more intense peak compared to the I terminated for both the RP and DJ phases. In addition, Figure 2.12c-d shows highest number of Pb-I interactions for the cation terminated water interfaces. For RP/H_2O interface, the Pb-I coordination number reaches 4.95 at 3.8 Å for cation terminated models whereas it remains at ~ 4.5 for other two surfaces (Figure 2.12c). Similarly for DJ/H_2O interface, till 3.8 Å bond length, Pb-I coordination number for the PbI_2, I and cation termination are 4.45, 4.05 and 4.8, respectively (Figure 2.12d). Hence, we claim that there is much stronger bonding interaction between Pb and I in case of cation terminated perovskite water interfaces compared to the PbI_2 and I terminated models. The retention of bonding interactions in the cation terminated structure is due to the hydrophobicity of bulky surface cations which keep the inorganic layer safe from degradation. The same is also visible from the post simulation geometries of cation terminated models in Figure 2.9.

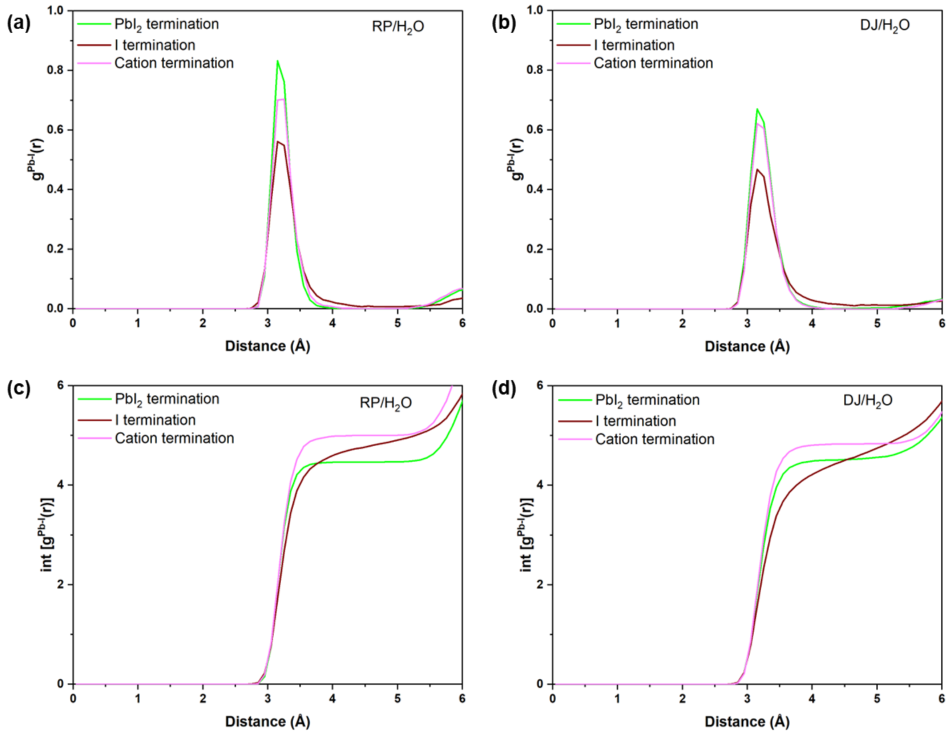

Figure 2.12: Radial pair distribution plots of Pb-I for (a) RP/H_2O, and (b) DJ/H_2O interfaces. Integrated distribution plots of Pb-I for (c) RP/H_2O, and (d) DJ/H_2O interfaces.

From our findings we can mention some major events which could possibly happen with 2D perovskites in presence of moisture. At the foremost, 2D hybrid perovskites surfaces terminated with large organic spacer molecules emerge as the most stable terminated structures against moisture. Among inorganic layer terminated surfaces, PbI_2 termination is found to be more stable compared to I termination. This happens due to the stability of PbI_2 surface fulfilling the charge and coordination number of Pb and I. On the other hand, in I terminated interface presence of unsaturated iodides lead to locally charged surfaces making them more reactive towards water environment. Another point worth mentioning is that even for the I terminated water interface models, the inside Pb-I layers away from the surface do not undergo much change during the simulations (Figure 2.6). This can be attributed to the robustness of the large organic ammonium layers which prevent water infiltration owing to their hydrophobic nature. Similarly, the cation terminated water interfaces are also quite robust. The possible degradation pathway of the I terminated surface could be through I_2 formation.

De Angelis and coworkers have carried out some very fundamental research work on the stability of 3D halide perovskites in presence of water.*[20-21]* For the most studied system $MAPbI_3$, they reported that PbI_2 termination is much more stable at water interfaces due to strong Pb-I bonds compared to MAI terminated surface, in which case both MA and I are prone to dissolution as water molecules interact with the Pb nodes.*[20]* In another work they have considered only the metal-I_2 terminations to compare $MAPbI_3$, $MASnI_3$ and $DMASnBr_3$.*[21]* Here they found that Sn-I bonds of the SnI_2 layer also break in presence of water. On the other hand, $SnBr_3$ is found to form amorphous surface layer preventing water infiltration, but such layers can be detrimental for photovoltaic applications. In our work, we have found that in case of the considered 2D halide perovskites, the PbI_2 termination is quite stable due to strong Pb-I bonds. The most noteworthy feature is the unique arrangement of organic cation layer which prevents the water infiltration by virtue of hydrophobicity which also protects the inner inorganic Pb-I layers. The bulky organic cation layer also remains intact unlike MA or similar small cations in 3D perovskites.*[20-21]*The cation termination can be helpful to maintain stability in presence of moisture without the requirement of an amorphous surface layer thereby preserving the optoelectronic properties of 2D halide perovskites.

2.5: Conclusion

Understanding the stability of perovskite systems in environmental conditions especially in presence of water is crucial towards the application of these materials towards photovoltaics or other applications. In this regard, we have carried out a systematic ab initio molecular dynamics-based study to investigate the stability of 2D halide perovskites at the water interface. Analysing the time averaged structures, we have been able to figure out possible degradation pathways of the 2D perovskites in presence of liquid water environment. We have considered all possible terminations (PbI_2, I-, organic cation-) of both the Ruddlesden−Popper (RP) and Dion−Jacobson (DJ) phases. PbI_2 terminated surfaces are found to experience interaction through Pb-O bond formation and in this case the DJ/H_2O interface is more robust compared to RP/H_2O interface. In case of the I terminated interfaces, I_2 formation is most prominent resulting from nucleophilic substitution of water molecules at Pb metal centres. This phenomenon is expected to be the possible degradation route for this type of 2D halide perovskite systems in contact with water molecules. Despite of water infiltration through surface PbI_6 octahedral layer, DJ phase perovskites possess less pronounced interaction compared to the RP phase. Cation terminated interfaces are found out to be more robust towards water environment. The presence of bulky organic cations (like 3AMP and BA) in 2D perovskites play an important role in both PbI_2 terminated and organic cation terminated structures by preventing water infiltration to the inside inorganic layers. Also, we observed BA and 3AMP cations to interact differently with water molecules. Thus, tuning the organic cation layer can be an ingenious way to maintain moisture stability of the optoelectronic devices based on 2D perovskites. Overall, our work represents the fundamental understanding regarding the stability and degradation of 2D DJ and RP phase perovskites in presence of moisture and direct the perovskite community towards further design and development in perovskite research and application.

2.6. References

1. Kojima A., Teshima K., Shirai Y., Miyasaka T. (2009), Organometal Halide Perovskites as Visible-Light Sensitizers for Photovoltaic Cells, J. Am. Chem. Soc., 131, 6050−6051 (DOI: 10.1021/ja809598r)
2. Lee M. M., Teuscher J., Miyasaka T., Murakami T. N., Snaith H. J. (2012), Efficient Hybrid Solar Cells Based on Meso-Superstructured Organometal Halide Perovskites, Science, 338, 643– 647 (DOI: 10.1126/science.1228604)
3. Burschka J., Pellet N., Moon S. J., Humphry-Baker R., Gao P., Nazeeruddin M. K., Grätzel M. (2013), Sequential Deposition as a Route to High-Performance Perovskite-Sensitized Solar Cells, Nature, 499, 316 (DOI: 10.1038/nature12340)
4. Saliba M., Orlandi S., Matsui T., Aghazada S., Cavazzini M., Correa-Baena J. P., Gao P., Scopelliti R., Mosconi E., Dahmen K.-H., De Angelis F., Abate A., Hagfeldt A., Pozzi G., Graetzel M., Nazeeruddin M. K. (2016), A Molecularly Engineered Hole-transporting Material for Efficient Perovskite Solar Cells, Nat. Energy, 1, 15017 (DOI: 10.1038/nenergy.2015.17)
5. Yang W. S., Noh J. H., Jeon N. J., Kim Y. C., Ryu S., Seo J., Seok S. I. (2015), High-Performance Photovoltaic Perovskite Layers Fabricated through Intramolecular Exchange, Science, 348, 1234– 1237 (DOI: 10.1126/science.aaa9272)

6. Yoshikawa K., Kawasaki H., Yoshida W., Irie T., Konishi K., Nakano K., Uto T., Adachi D., Kanematsu M., Uzu H. (2017), Silicon Heterojunction Solar Cell with Interdigitated Back Contacts for A Photoconversion Efficiency over 26%, Nat. Energy, 2, 17032 (DOI: 10.1038/nenergy.2017.32)
7. Jena A. K., Kulkarni A., Miyasaka T. (2019), Halide Perovskite Photovoltaics: Background, Status, and Future Prospects, Chem. Rev., 119, 3036– 3103 (DOI: 10.1021/acs.chemrev.8b00539)
8. Frost J. M., Butler K. T., Brivio F., Hendon C. H., Van Schilfgaarde M., Walsh A. (2014), Atomistic Origins of High-Performance in Hybrid Halide Perovskite Solar Cells, Nano Lett., 14, 2584– 2590 (DOI: 10.1021/nl500390f)
9. Zhao Y., Zhu K. (2014), Optical Bleaching of Perovskite $(CH_3NH_3)PbI_3$ Through Room-Temperature Phase Transformation Induced by Ammonia, Chem. Commun., 50, 1605−1607 (DOI: 10.1039/C3CC48522F)
10. Smith I. C., Hoke E. T., Solis-Ibarra D., McGehee M. D., Karunadasa H. I. (2014), A Layered Hybrid Perovskite Solar-Cell Absorber with Enhanced Moisture Stability, Angew. Chem., Int. Ed. 53, 11232– 11235 (DOI: 10.1002/anie.201406466)
11. Stoumpos C. C., Cao D. H., Clark D. J., Young J., Rondinelli J. M., Jang J. I., Hupp J. T., Kanatzidis M. G. (2016), Ruddlesden–Popper Hybrid Lead Iodide Perovskite 2D Homologous Semiconductors, Chem. Mater., 28, 2852– 2867 (DOI: 10.1021/acs.chemmater.6b00847)
12. Quan L. N., Yuan M., Comin R., Voznyy O., Beauregard E. M., Hoogland S., Buin A., Kirmani A. R., Zhao K., Amassian A., Kim D. H., Sargent E. H. (2016), Ligand-Stabilized Reduced-Dimensionality Perovskites, J. Am. Chem. Soc., 138, 2649– 2655 (DOI: 10.1021/jacs.5b11740)

13. Kieslich G., Sun S., Cheetham A. K., Solid-State Principles Applied to Organic–Inorganic Perovskites: New Tricks for an Old Dog, Chem. Sci., 5, 4712– 4715 (DOI: 10.1039/C4SC02211D)
14. Katan C., Mercier N., Even J. (2019), Quantum and Dielectric Confinement Effects in Lower-Dimensional Hybrid Perovskite Semiconductors, Chem. Rev., 119, 3140-3192 (DOI: 10.1021/acs.chemrev.8b00417)
15. Sapori D., Kepenekian M., Pedesseau L., Katan C., Even J. (2016), Quantum Confinement and Dielectric Profiles of Colloidal Nanoplatelets of Halide Inorganic and Hybrid Organic–Inorganic Perovskites, Nanoscale, 8, 6369– 6378 (DOI: 10.1039/C5NR07175E)
16. Li X., Ke W., Traoré B., Guo P., Hadar I., Kepenekian M., Even J., Katan C., Stoumpos C. C., Schaller R. D., Kanatzidis M. G. (2019), Two-Dimensional Dion-Jacobson Hybrid Lead Iodide Perovskites with Aromatic Diammonium Cations, J. Am. Chem. Soc., 141, 12880-12890 (DOI: 10.1021/jacs.9b06398)
17. Sutanto A. A., Drigo N., Queloz V. I. Perdew E., Garcia-Benito I., Kirmani A. R., Richter L., Schouwink P., Cho K. T., Paek s., Nazeeruddin M. K. (2020), Dynamical Evolution of the 2D/3D Interface: A Hidden Driver behind Perovskite Solar Cell Instability, J. Mater. Chem. A, 8, 2343– 2348 (DOI: 10.1039/C9TA12489F)
18. Ahmad S., Fu P., Yu S., Yang Q., Liu X., Wang X., Wang X., Guo X., Li C. (2019), Dion-Jacobson Phase 2D Layered Perovskites for Solar Cells with Ultrahigh Stability, Joule, 3, 794– 806 (DOI: 10.1016/j.joule.2018.11.026)
19. Ducinskas A., Kim G. Y., Moia D., Senocrate A., Wang Y. R., Hope M. A., Mishra A., Kubicki D. J., Siczek M., Bury W., Schneeberger T., Emsley L., Milic J. V., Maier J., Gratzel M. (2021), Unravelling the Behavior of Dion–Jacobson Layered Hybrid Perovskites in Humid Environments, ACS Energy Lett., 6, 337−344 (DOI: 10.1021/acsenergylett.0c02344)

20. Mosconi E., Azpiroz J. M., De Angelis F. (2015), Ab Initio Molecular Dynamics Simulations of Methylammonium Lead Iodide Perovskite Degradation by Water, Chem. Mater., 27, 4885– 4892 (DOI: 10.1021/acs.chemmater.5b01991)
21. Kaiser W., Ricciarelli D., Mosconi E., Alothman A. A., Ambrosio F., De Angelis F. (2022), Stability of Tin- versus Lead-Halide Perovskites: Ab Initio Molecular Dynamics Simulations of Perovskite/Water Interfaces, J. Phys. Chem. Lett., 13, 2321– 2329 (DOI: 10.1021/acs.jpclett.2c00273)
22. Billing D. G., Lemmerer A. (2007), Synthesis, Characterization and Phase Transitions in the Inorganic-Organic Layered Perovskite-Type Hybrids $[(C_nH_{2n+1}NH_3)_2PbI_4]$, n = 4, 5 and 6, Acta Crystallogr., Sect. B: Struct. Sci., 63, 735– 747 (DOI: 10.1107/S0108768107031758)
23. Martinez L., Andrade R., Birgin E. G., Martinez J. M. (2009), Packmol: A Package for Building Initiial Configurations for Molecular Dynamics Simulations, J. Comput. Chem., 30, 2157–2164 (DOI: 10.1002/jcc.21224)
24. Hutter J., Iannuzzi M., Schiffmann F., VandeVondele J. (2014), CP2K: atomistic simulations of condensed matter systems, Wiley Interdiscip. Rev. Comput. Mol. Sci., 4, 15– 25 (DOI: 10.1002/wcms.1159)
25. Kühne T. D., Iannuzzi M., Del Ben M., Rybkin V. V., Seewald P., Stein F., Laino T., Khaliullin R. Z., Schütt O., Schiffmann F., Golze D., Wilhelm J., Chulkov S., Bani-Hashemian M. H., Weber V., Borštnik U., Taillefumier M., Jakobovits A. S., Lazzaro A., Pabst H., Müller T., Schade R., Guidon M., Andermatt S., Holmberg N., Schenter G. K., Hehn A., Bussy A., Belleflamme F., Tabacchi G., Glöß A., Lass M., Bethune I., Mundy C. J., Plessl C., Watkins M., VandeVondele J., Krack M., Hutter J. (2020), CP2K: An Electronic Structure and Molecular Dynamics Software Package Quickstep: Efficient and Accurate Electronic Structure Calculations, J. Chem. Phys.,152, 194103 (DOI: 10.1063/5.0007045)

26. VandeVondele J., Krack M., Mohamed F., Parrinello M., Chassaing T., Hutter J. (2005), QUICKSTEP: Fast and accurate density functional calculations using a mixed Gaussian and plane waves approach, Comput. Phys. Commun., 167, 103-128 (DOI: 10.1016/j.cpc.2004.12.014)
27. VandeVondele J., Hutter J. (2007), Gaussian basis sets for accurate calculations on molecular systems in gas and condensed phases, J. Chem. Phys., 127, 114105 (DOI: 10.1063/1.2770708)
28. Goedecker S., Teter M., Hutter J. (1996), Separable Dual-Space Gaussian Pseudopotentials, Phys. Rev. B: Condens. Matter Mater. Phys., 54, 1703 (DOI: 10.1103/PhysRevB.54.1703)
29. Perdew J. P., Burke K., Ernzerhof M. (1996), Generalized Gradient Approximation Made Simple, Phys. Rev. Lett., 77, 3865– 3868 (DOI: 10.1103/PhysRevLett.77.3865)
30. Grimme S., Antony J., Ehrlich S., Krieg H. (2010), A Consistent and Accurate Ab Initio Parametrization of Density Functional Dispersion Correction (DFT-D) For The 94 Elements H-Pu, J. Chem. Phys., 132, 154104 (DOI: 10.1063/1.3382344)
31. Nosé S. (1984), A Unified Formulation of the Constant Temperature Molecular Dynamics Methods, J. Chem. Phys., 81, 511– 519 (DOI: 10.1063/1.447334)
32. Bader R.F.W. (1991), A Quantum Theory of Molecular Structure and Its Applications, Chem. Rev., 91, 893-928 (DOI: 10.1021/cr00005a013)
33. Sanville E., Kenny S. D., Smith R., Henkelman G. (2007), Improved Grid-Based Algorithm for Bader Charge Allocation, J. Comput. Chem., 28, 899-908 (DOI: 10.1002/jcc.20575)
34. Tang W., Sanville E., Henkelman G. (2009), A grid-based Bader analysis algorithm without lattice bias, J. Phys.: Condens. Mat., 21, 084204 (DOI: 10.1088/0953-8984/21/8/084204)

35. Henkelman G., Arnaldsson A., Jónsson H. (2006), A fast and robust algorithm for Bader decomposition of charge density, Comput. Mater. Sci., 36, 354– 360 (DOI: 10.1016/j.commatsci.2005.04.010)

Chapter 3

Understanding the Role of Spacer Cation on the Electronic Structure of 2D Hybrid Perovskites

3.1. Introduction

Hybrid metal halide perovskites own amazing semiconducting properties which are in the focus of renewable energy research in recent times. Despite the remarkable advancement of three-dimensional (3D) organic-inorganic hybrid perovskites (formula AMX_3, A = $CH_3NH_3^+$ (methylammonium or MA), $NH_2CHNH_2^+$ (formamidinium or FA); M = Sn^{2+}, Pb^{2+}; X = Cl^-, Br^-, I^-) in next generation thin film photovoltaics, their large-scale commercialization is still suffering from environmental stability.*[1-7]* In this context, several studies have reported the instability of the 3D perovskite structure towards water, oxygen, and light. In particular, the metal halide unit interacts with water molecules through H-bonding leading to easy decomposition and the organic cation deprotonates in the presence of light and oxygen.*[8-9]* With the aim of reducing these obstacles, there have been attempts to find out new halide perovskites by compositional change, dimensional reduction, and encapsulation. In search of new materials, two-dimensional hybrid perovskites have emerged as the potential candidates for their application in photovoltaic devices due to their improved environmental stability.*[10-11]* In the case of 3D perovskite, such as $CH_3NH_3PbI_3$, the PbI_3 inorganic part forms corner-sharing PbI_6 octahedra and the methylammonium (MA) cation situates inside the cavity. Like 3D perovskites, the 2D perovskites are also made of a corner-sharing PbI_6 octahedra with intercalated large organic cation. The hydrophobic nature of large organic cations results superior moisture stability compared to the 3D systems. Sargent and co-workers have reported energetically stable 2D perovskites, owing to the appreciable van der Waals forces.*[12]* Moreover, incorporation of large organic cation between inorganic layer results in quantum confinement in the hybrid perovskite's structure. However, the 2D perovskites are examples of natural multiple quantum wells (MQW) that results from large difference of dielectric nature between organic and inorganic layers. Because of the smaller dielectric constant value, the organic spacer behaves as the "barrier", whereas due to the higher dielectric constant value, the inorganic framework behaves as the "well".*[13]* Even and co-workers have reported that variation of dielectric constant can yield dramatical effects on quantum well properties of 2D perovskites.*[14]* In addition to these, the large separation between two inorganic layers shows increment in the barrier height of the MQW.

The compositional designing approaches can be made by choice of metal cation, halide anion, organic spacer cation and thickness of inorganic layer to design an effective 2D perovskite material for photovoltaic applications. In this context, the intercalation of large hydrophobic organic cation between two inorganic layers makes this class of materials versatile towards dimensional and compositional engineering. Based on the charge of the large organic cation 2D perovskites can be of two types: A_2MX_4 and AMX_4 by mono- and di-cations, respectively which gives additional choice for material modelling. Several studies have reported that the choice of cation can significantly influence the electronic and optical properties of the 2D perovskites as the geometries of spacer cations have considerable effect on the structural distortion and octahedral tilting of the metal halide layer that determine the band gap and exciton binding energy. Additionally, restriction of carrier movement can be reduced by incorporating spacer cation that have better charge transport ability and able to reduce the inorganic layer separation. Moreover, introduction of organic spacer cation having conjugated functionalities and ability to form strong H-bond, increases the possibility of charge transfer between the inorganic and organic layers with improved band alignment. Also, spacer cation having compact structure can reduce the inorganic layer separation and distortion of the octahedral geometry. Hence, cation engineering can be a precise way to give right choice of 2D perovskites with improved performance of photovoltaic devices. However, an efficient theoretical study to understand the controlling factors behind this influence of spacer cation on the geometry of metal halide layer thereby optoelectronic properties of the perovskite system is necessary.

In this chapter, we have performed a detailed theoretical investigation of the atomic and electronic structure taking a set of 2D perovskite systems to shed light on their tunable optoelectronic properties. We have used density functional theory (DFT) calculations to give an insight about the clear influence of the organic spacers on the structural properties of the 2D perovskites that can indirectly control the photovoltaic properties of the materials. The inspiration behind the choice of considered systems are some experimental reports which indicate functional group modification in organic spacers can guide us to reach finer photovoltaic property. To execute versatility of 2D perovskites, our study ranges from aliphatic to aromatic mono- and aromatic di-ammonium based spacer cations. We have started with n-butylammonium (BA) and aromatic phenyl ethyl ammonium (PEA) which have been used earlier extensively to investigate the properties of 2D perovskites (Figure 3.1). To explore the scope of aliphatic spacer-based systems we have considered 3-aminopropionitrile (3-APN) containing cyanide group that can form strong H-bonding and acquire a rigid geometry. Reason behind choosing this spacer cation is a recent work of Wang and coworkers where they have employed the 3-APN spacer cation into the pure 2D perovskites and achieved best performance among the pure 2D perovskites based solar cells to the best of our knowledge.*[15]* Even after excellent experimental report, the underlying reason behind the impact of spacer cations in 2D perovskites is still unknown. Specifically, the sources of structural distortion and reason behind improved band edge properties are not fully understood. England and co-workers have illustrated in their recent work that the intercalation of di-cations between inorganic layers can be beneficial as it requires single organic layer stacking compared to double organic layer stacking in mono-cation based systems.*[16]* Motivated from their work, we have included pyridinium based di-cation, pyridinium ethyl ammonium and its positional isomers (Figure 3.1) in our study. The presence of dipositive charge develops more rigid geometry of the cations. Also, they have reported significant contributions of the dications in the band edge states but yet to be studied to understand their atomistic origin for the same. Here, we have also calculated the effective mass of electrons and holes to understand the optoelectronic device characteristic as it relates the key properties of semiconductor material like charge carrier mobility and diffusion length.

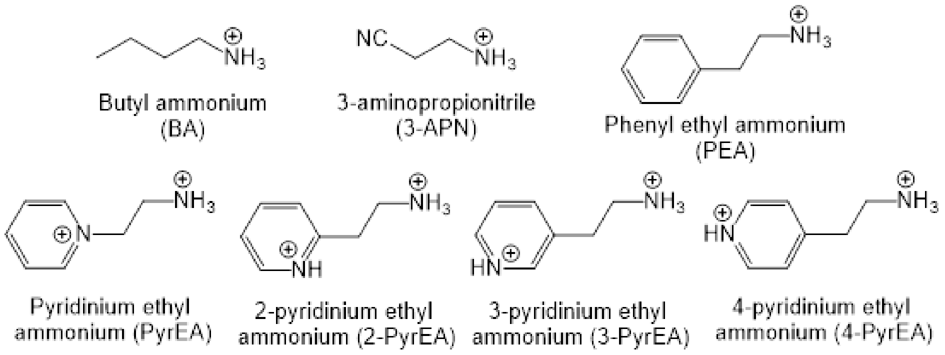

Figure 3.1: Structure of considered organic spacer cations in this work.

3.2. Methodology

First principles calculations have been performed using the plane wave code, Quantum Espresso (QE).*[17]* GGA-PBE functional*[18]* has been used with scalar relativistic ultrasoft pseudopotentials*[19]* that include 2s, 2p orbital for O, N, and C; 1s orbital for H; 5s, 5p orbital for I; and 6s, 6p, 5d orbital for Pb ions for geometry optimization. Plane wave basis set cutoffs were set to 25 and 200 Ry for the smooth part of the wave functions and the augmented density, respectively. Cell parameters of the considered systems for relaxation have been taken from available experimental reports. The optimized cell contains four formula units of the corresponding 2D perovskites such that there are 156 atoms for $(BA)_2PbI_4$, 188 atoms for $(PEA)_2PbI_4$, 116 atoms for $(3\text{-}APN)_2PbI_4$ and 104 atoms for all four $PyrPbI_4$ systems. We have used Monkhorst pack k-point sampling*[22]* of 4×4×1 and 6×4×1 for mono-cation ($(BA)_2PbI_4$; $(PEA)_2PbI_4$; $(3\text{-}APN)_2PbI_4$ and di-cation spacer-based systems ($(PyrEA)PbI_4$; $(2\text{-}PyrEA)PbI_4$; $(3\text{-}PyrEA)PbI_4$; $(4\text{-}PyrEA)PbI_4$), respectively. For better accuracy in electronic structure, we have carried out single point electronic structure calculations using HSE06 hybrid functional.*[20]* The Hartree-Fock exchange parameter has been set to 43%.*[21]* Keeping in mind the high sensitivity of lead towards relativistic effects, we have also included spin orbit coupling (SOC) in our HSE06 calculations. We have used norm-conserving pseudopotentials and electrons from I 5s, 5p; O, N, C 2s, 2p; H 1s; Pb 5s, 5p, 6s, 6p, 5d; and shells explicitly. The plane wave basis set cutoff for the smooth part of the wave functions and Fock energy cutoff have been set to 40 and 80 Ry, respectively, along with a Monkhorst pack k-point sampling of 2×2×1. Band structure calculations have been performed using GGA-PBE functional with SOC considering relativistic ultrasoft pseudopotentials.

For charge carrier effective mass calculations, we have taken the help of projector-augmented wave-based (PAW) pseudopotentials along with plane wave basis set as implemented in Vienna ab-initio Simulation Package (VASP).*[23-28]* Geometry optimizations were carried out using GGA-PBE functional*[18]* with a kinetic energy cutoff of 500 eV for the plane waves until the Hellmann–Feynman force on each atom was smaller than 0.01 eV/Å. The systems considered for relaxation here are same as earlier. Hence, similar Γ-centered k-point grid of 4×4×1 and 6×4×1 was used for mono- and di-cation based systems, respectively. For performing the single-point calculations to obtain the electronic structure, we have considered the effect of SOC with GGA-PBE functional. To obtain more accurate value of the charge carrier effective masses, non-self-consistent calculations were performed using a high k-grid of 30 points between two high-symmetry points. Electron and hole effective masses, m_e* and m_h* were calculated around Γ(0,0,0) towards X(0.5, 0, 0) and Γ(0,0,0) towards Y(0,0.5,0) high symmetry points in the Brillouin zone, because the fundamental band gap appears at the Γ-point. Subsequently, the effective masses were calculated using equation (3.1),*[29]*

$$\mathrm{m}^* = \hbar^2 \left(\frac{\partial^2 \mathrm{E}}{\partial \mathrm{k}^2}\right)^{-1} \tag{3.1}$$

where, $\hbar$ is the reduced Planck constant, E is the band edge eigen value and k is the wave vector.

Depending upon the calculated electronic structure, optical properties were calculated from the real and imaginary part of the dielectric function using equation (3.2),*[30]*

$$\alpha = \sqrt{2}\omega\left[\sqrt{\varepsilon_1(\omega)^2 + \varepsilon_2(\omega)^2} - \varepsilon_1(\omega)\right]^{1/2} \quad (3.2)$$

where, α is the absorption coefficient, ω is the frequency of light, ε_1 and ε_2 are the real and imaginary parts of the dielectric function.

3.3. Results & Discussion

3.3.1. Structural Properties

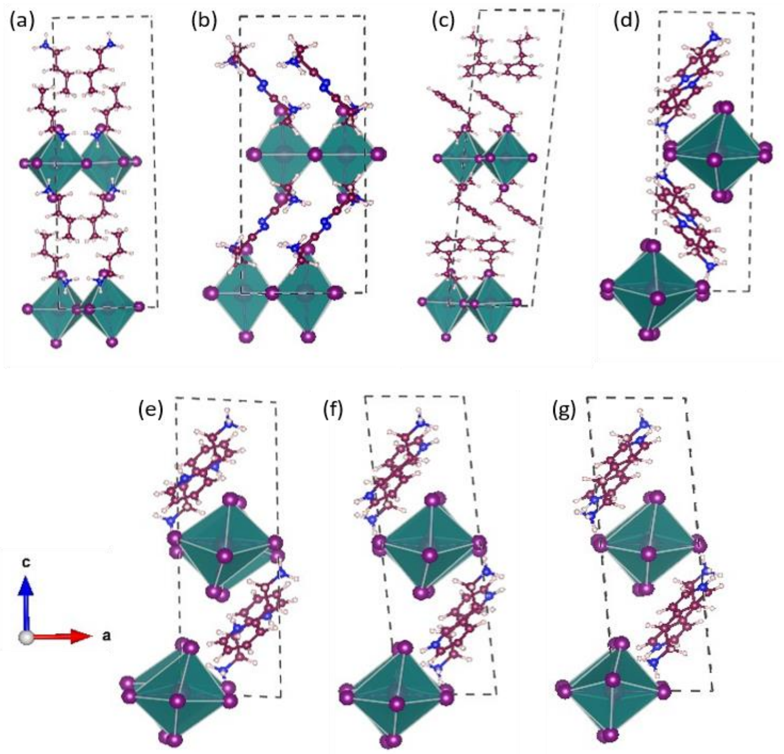

Figure 3.2: Optimized structures of unit cells of (a) $(BA)_2PbI_4$ (b) (3-APN)$_2$PbI$_4$, (c) $(PEA)_2PbI_4$ and (d) (pyridinium)PbI$_4$, (e) (2-PyrEA)PbI$_4$, (f) (3-PyrEA)PbI$_4$, (g) (4-PyrEA)PbI$_4$ Colors: hydrogen (white), carbon (magenta), nitrogen (blue), iodine (purple), lead (pink).

First, we have optimized the geometries by taking the experimentally reported crystal structures as the initial guess.*[31-33,16]* Optimized structures are shown in Figure 3.2.

Monovalent Spacer Cation: In this section, we have discussed about three 2D perovskites containing mono-cation spacer: $(BA)_2PbI_4$, $(3\text{-}APN)_2PbI_4$, and $(PEA)_2PbI_4$. In mono-cation containing systems, interaction of the intercalated large organic cations with the inorganic layer is mainly between hydrogen atoms on the ammonium groups and the I atoms of the inorganic layer. So, the noncovalent interaction can be due to the H-bond formation. Among three hydrogens of the ammonium group, two interacts with nearby axial I atoms and one interact with equatorial I atoms. In $(BA)_2PbI_4$ the distance between H and axial and equatorial I atom is ~2.5 Å and ~2.9 Å, respectively that indicates the presence of H-bonding interaction. Because of this H-bonding interaction between ammonium H and I of $[PbI_6]^{4-}$ inorganic layer, lead iodide octahedra gets distorted. The octahedral distortion results in reduction of Pb-I-Pb bond angles from ideal value (180°) to ~151° and the same has been observed for $(PEA)_2PbI_4$ (Table 3.1). Almost similar Pb-I-Pb bond angle and presence of H-bonding in $(BA)_2PbI_4$ was experimentally reported by Kanatzidis and co-workers.*[11]* In case of $(PEA)_2PbI_4$, the two axial Pb−I bond lengths are different, one elongates (3.87 Å) and other contracts (3.24 Å), whereas all equatorial Pb−I bond lengths (3.19 Å) are same. For $(BA)_2PbI_4$ the axial and equatorial Pb-I bonds have nearly same lengths (∼3.22 Å). Hence, PEA results higher octahedral distortion on PbI_6 unit compared to BA. Another candidate we have considered in this section is the $(3\text{-}APN)_2PbI_4$. In general, the two ends of the spacer cations used to be directed in opposite direction i.e., primary ammonium group is directed towards lead iodide layer and the other end towards another spacer cation. In the case of $(3\text{-}APN)_2PbI_4$ both the cyanide and primary ammonium groups of one 3-APN cation directs towards another 3-APN cation. Due to the presence of the distinct cyanide linkage in 3-APN the orientation of the cation changes i.e., the primary ammonium group one cation faces the cyanide group of another cation and vice versa. The distance between ammonium H and cyanide N is 1.84 Å that is the evidence for the formation of strong intermolecular H-bonding (Figure 3.3).

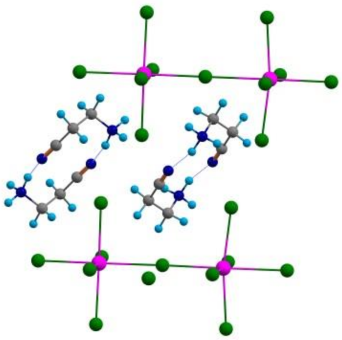

Figure 3.3: Intermolecular H-bonding interactions in $(3\text{-APN})_2PbI4$ (Colors: hydrogen (sky), carbon(grey), nitrogen(blue), iodine(green), lead(pink).

Due to this H-bonding interaction two 3-APN cation stacked between lead iodide layer forms a robust dimer pattern. Among three hydrogens of the primary ammonium functionality, one gets involved in this dimer formation and other two participate in H-bonding interaction with two nearest axial iodides. But with equatorial iodides no non-covalent interaction happens that is why the lead iodide layer remains undisturbed where Pb-I-Pb bond angles in $(3\text{-APN})_2PbI_4$ are ~ 172° and 177° (Table 3.1) that is close to ideal (180°) bond angle. As a result of almost ideal Pb-I-Pb angle, greater extent of overlap between Pb and I atomic orbitals pushes valence band maximum (VBM) and conduction band minimum (CBM) closure. Since, 3-APN cation is smaller in size and also forms dimer inside the inorganic layer via intermolecular H-bonding interactions, the inorganic layer separation (10.17 Å) as well as closest I···I contact (4.56 Å) are smaller than other considered mono-cation based systems (Table 3.1). Hence, several factors are making $(3\text{-APN})_2PbI_4$ distinguishable among other considered systems such as the smaller size of the cation and the presence of electronegative cyanide linkage that is responsible for dimer formation. These factors may result reduced band gap in (3-APN)$_2$PbI$_4$ compared to BA and PEA one and make it a best choice even though it is a mono-cation based system.

Table 3.1: Structural Properties of monovalent and divalent spacer cation based 2D perovskites.

Perovskite System	**Pb-I-Pb Angle-I (deg)**	**Pb-I-Pb Angle-II (deg)**	**Closest I⋯I contact (Å)**	**Inorganic layer separation (Å)**
(BA)$_2$PbI$_4$	151.54	151.45	8.57	13.80
(3-APN)$_2$PbI$_4$	171.85	177.42	4.56	10.17
(PEA)$_2$PbI$_4$	150.36	151.87	10.05	16.00
(PyrEA)PbI$_4$	157.47	169.63	4.23	9.90
(2-PyrEA)PbI$_4$	157.73	165.45	4.21	9.98
(3-PyrEA)PbI$_4$	156.47	168.41	4.36	10.19
(4-PyrEA)PbI$_4$	154.57	176.65	4.36	10.10

Divalent Spacer Cation: In this section we have discussed about the four di-cation based 2D perovskites: (PyrEA)PbI$_4$, (2-PyrEA)PbI$_4$, (3-PyrEA)PbI$_4$ and (4-PyrEA)PbI$_4$ (Figure 3.2). In this case, divalent nature of the pyridinium ring containing diammonium aromatic spacers results less distorted inorganic sheet and smaller inorganic layer separation. As these divalent spacer cations possess dipositive charge, only single organic layer is present between two lead iodide layers. Di-cations have one primary ammonium linkage and one positive charge centered in the pyridinium ring. Here, one organic spacer cation interacts with two different lead iodide layers, one layer interacts through the primary ammonium functionality and another lead iodide layer comes into contact with the pyridinium ring. Among three hydrogens of the primary ammonium group two interacts with two equatorial iodides and one interacts with one axial iodide. The distances between interacting hydrogen and iodide are around 2.5-2.9 Å that falls in H-bonding distance. But this type of H-bond formation happens only in alternative octahedral cavities due to presence of pyridinium ring in place of primary ammonium group in the neighboring cavity. Due to presence of insufficient H-bonding interaction, PbI_6 octahedral distortion is less with more ideal Pb-I-Pb bond angle compared to $(BA)_2PbI_4$ and $(PEA)_2PbI_4$. Extent of distortion depends on the strength of interaction i.e., on the H-bond length. The $(PyrEA)PbI_4$, $(2\text{-}PyrEA)PbI_4$, $(3\text{-}PyrEA)PbI_4$ and $(4\text{-}PyrEA)PbI_4$ perovskites have Pb-I-Pb bond angles of ~170°, 165°, 168° and 177°, respectively (Table 3.1). Therefore, the substantial overlap between Pb and I atomic orbitals can easily reduce the band gap of di-cation based systems. As the smaller primary ammonium tail and bulkier pyridinium ring places in alternative octahedral cavities, the Angle I of the lead iodide octahedra deviates markedly from ideal octahedral bond angle. In case of $(2\text{-}PyrEA)PbI_4$, $(3\text{-}PyrEA)PbI_4$ and $(4\text{-}PyrEA)PbI_4$ there is a secondary ammonium H present in the pyridinium ring which forms H-bonding with I. For this reason, the angle-I (table 3.1) of these three systems further distorts and may result enhanced band gap in comparison to $(PyrEA)PbI_4$. Single layer intercalation results inorganic layer separation in the range of 9.9 Å to 10.2 Å (Table 3.1). The closest I···I contact for these systems ranges from 4.21 Å to 4.36 Å (Table 3.1). This smaller layer separation reduces the barrier of the MQW. Moreover, studying the relaxed structures, we have figured out that the noncovalent interactions between lead iodide inorganic layer and the large organic spacer cations can strongly affect the geometry of the octahedral moiety. The di-cationic systems although have one Pb-I-Pb angle close to 180°, due the bulkiness of the pyridinium cations overall structural distortion increases but $(3\text{-}APN)_2PbI_4$ possess almost ideal octahedral geometry.

3.3.2. Electronic Structure

Next, we have explored the electronic structures of the 2D perovskites. In general, PBE functional underestimates the band gap and gives poor agreement with experimental reports. Several theoretical studies have reported hybrid functionals with SOC for the estimation of accurate band gap values.*[34-35]* Therefore, we have also used HSE06 hybrid functional with SOC for the band gap calculations. We have tabulated the band gap values obtained by using PBE and HSE06-SOC functionals (Table 3.2). Band gap values obtained using HSE-SOC are in good agreement with the experimental reports (Table 3.2). HSE06-SOC calculated band gap obtained for $(BA)_2PbI_4$ is 2.42 eV. Our calculated band gap value for $(BA)_2PbI_4$ is very much in agreement with the theoretical calculated value by the De Angelis and co-workers.*[36]* Replacing the BA cation with 3-APN, the band gap value changes from 2.42 to 2.22 eV. This observation is anticipated due to the reduction of the inorganic layer separation i.e., closest I···I contact distance and reduced octahedral distortion i.e., ideal Pb-I-Pb bond which results maximum orbital overlap. Whereas, in case of $(PEA)_2PbI_4$ no significant changes were found. Similar trend of band gap for BA and PEA based 2D perovskites have been observed by Tretiak and co-workers.*[37]* This can be due to the aromatic ring impact on the band edge states of $(PEA)_2PbI_4$. In spite of having an aliphatic spacer $(3\text{-}APN)_2PbI_4$ exhibits extraordinary feature due to presence of cyanide group that give rise to the formation of robust dimers through H-bonding.

In case of dipositive spacer cation-based 2D perovskites reduced band gap values were observed compared to $(BA)_2PbI_4$ and $(PEA)_2PbI_4$ because of their larger Pb-I-Pb bond angle and smaller inorganic layer separation which has been discussed previously. The trend of the calculated band gap of the four di-cationic systems are the clear consequence of their Pb-I-Pb bond angles discussed earlier. Our calculated band gap values show smallest band gap value for the $(3\text{-}APN)_2PbI_4$ (2.22 eV). Although $(3\text{-}APN)_2PbI_4$ has a comparable inorganic layer separation as $(PyrEA)PbI_4$ and also possess aliphatic spacer its impressive band gap is the example that aliphatic mono-cation spacer-based system is also capable to show better performance than aromatic spacer based as well as di-cation spacer-based systems.

Table 3.2: The calculated band gap values of considered perovskite systems using the PBE and HSE06+SOC functional and compared with the available experimental values.

Spacer Cation	**Perovskite System**	**Band gap in eV**		
		PBE	**HSE06+SOC**	**Expt.**
n-butylammonium	$(BA)_2PbI_4$	2.10	2.42	2.43[11]
3-aminopropionitrile	$(3\text{-}APN)_2PbI_4$	1.92	2.22	2.20[15]
Phenyl ethyl ammonium	$(PEA)_2PbI_4$	2.10	2.41	2.57[38]
Pyridinium ethyl ammonium	$(PyrEA)PbI_4$	1.65	2.24	2.35[16]
2-pyridinium ethyl ammonium	$(2\text{-}PyrEA)PbI_4$	1.89	2.38	2.46[16]
3-pyridinium ethyl ammonium	$(3\text{-}PyrEA)PbI_4$	1.85	2.36	2.34[16]
4-pyridinium ethyl ammonium	$(4\text{-}PyrEA)PbI_4$	1.83	2.32	2.38[16]

To confirm the position of atomic orbitals on the electronic structure of the system, we have calculated the projected density of states (pDOS) of all the considered materials. The pDOS components of the band edge states indicates that the VBM originates from the I atomic orbitals while the CBM mainly consists of Pb states (Figure 3.4). That clearly suggests, the VBM and CBM mostly spread over the lead iodide inorganic layer and lead and iodine atoms primarily controls the mobility of electron and holes in the 2D perovskites. But analyzing the pDOS plots we have observed that the C atomic orbitals of the aromatic spacers remain close to band edges. In case of $(PEA)_2PbI_4$, the prominent C-pDOS components appear near the valence band and conduction band edges that is because of the high energy of the sp2 carbons in PEA compared to sp3 carbons in BA. However, in case of $(3\text{-}APN)_2PbI_4$, the organic cationic states (C, H, N) appearing close to the conduction band edge in comparison to that in $(BA)_2PbI_4$. Due to the strong intermolecular H-bonding and dimer formation, the unoccupied orbitals of the organic part believed to be stabilized and shifted slightly towards the conduction band edge of the perovskite system. Hence, we show that introducing electronegative cyanide linkage, we can make the cationic states approaching to some extent towards the band edges even in absence of any aromatic core or sp2 carbons. In the pDOS plot of di-cation based four perovskites, cationic states appear close to the conduction band edges (Figure 3.4). In pyridinium ring cations, positive charges are extensively delocalized i.e., the LUMO gets stabilized. That brings the cationic states near the conduction band edge (~0.77 eV). However, no significant changes have been observed with the change in position of the ethyl ammonium functionality in the pyridine ring.

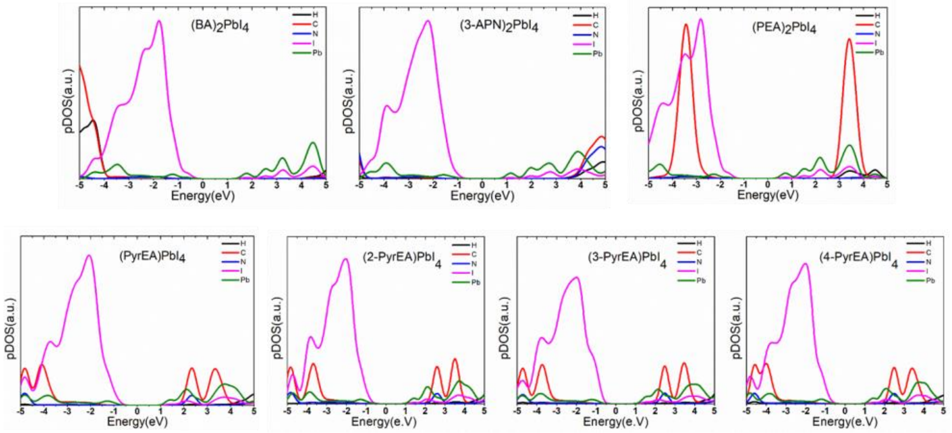

Figure 3.4: Projected density of states of the considered systems using HSE06+SOC level of calculations. Here the Fermi level is set to zero.

Moreover, we have calculated the band structure of all the considered 2D perovskites to check the dispersion of energy levels towards the high symmetry points of the Brillouin zone. The band structures have been calculated using the PBE + SOC method (Figure 3.5) to reduce the computational cost. All the considered systems are found to show direct band gap semiconductor property. The top of the valence band predominates antibonding linear combination of Pb 6s and I 5p orbitals and the bottom of the conduction band is mainly composed of Pb 6p orbitals with minor antibonding contributions of I 5s orbitals (Figure 3.4). Similar band edge states properties were distinctly characterized by Umebayashi and co-workers.*[39]* Reminiscing the substantial SOC constant of lead atoms, effects of SOC on the band structures are significant.

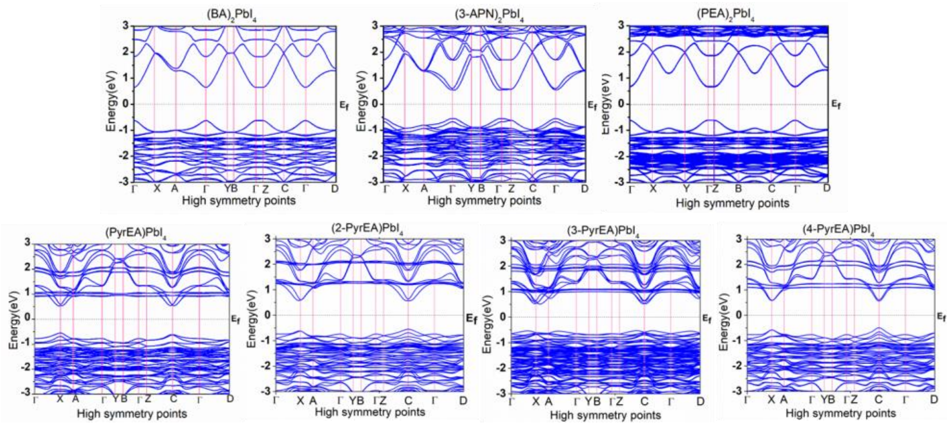

Figure 3.5: The calculated band structures of the 2D perovskites using the PBE+SOC level calculations. Here the Fermi level is set to zero and the high symmetry points are Γ = (0, 0, 0), X = (0.5, 0, 0), Y = (0, 0.5, 0), Z = (0, 0, 0.5), A= (0.5, 0.5, 0), B= (0, 0.5, 0.5), C= (0.5, 0, 0.5), and D = (0.5, 0.5, 0.5).

For the first three systems we have calculated the band structures using both with and without SOC correction (Figure 3.5 and Figure 3.6). The conduction band nature changes exceptionally by the introduction of the SOC. Specifically, the down shifting of the bottom of the conduction band happens. For all three systems it has been observed that incorporation of SOC reduces the band gap by around 0.8 eV. Here, the conduction band mainly originates from Pb 6p atomic orbitals which are highly sensitive towards relativistic effect and introduction of SOC splits the conduction band i.e., reduce the band gap. Even and co-workers have also investigated the dominating effect of SOC that mainly act on the conduction band in hybrid lead halide perovskites.*[40-41]*

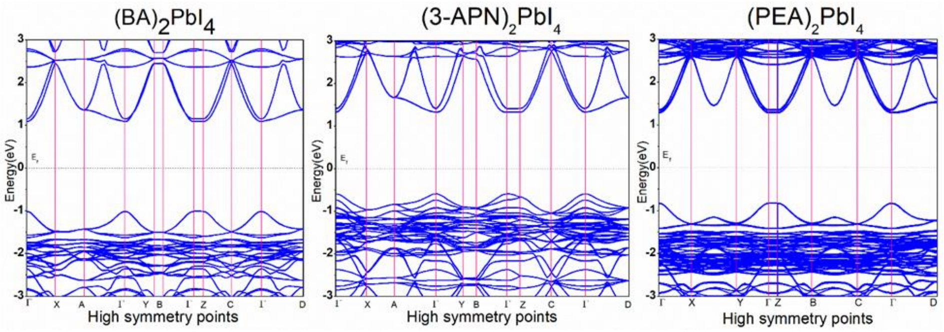

Figure 3.6: Calculated band structures of the 2D perovskites using PBE method. Here, high symmetry points are Γ = (0, 0, 0), X = (0.5, 0, 0), Y = (0, 0.5, 0), Z = (0, 0, 0.5), A= (0.5, 0.5, 0), B= (0, 0.5, 0.5), C= (0.5, 0, 0.5), and D = (0.5, 0.5, 0.5).

For monovalent spacer cation containing 2D perovskites we have observed the fundamental band gap at Γ high symmetry point whereas in case of the di-cationic based systems band gap appears at X high symmetry point. Moreover, the flat nature of the band has been observed in the Γ-Z direction which is expected due to the presence of organic spacers. Furthermore, the charge carrier effective masses of all the systems have been investigated to give insight on the carrier mobilities influenced by the choice of organic spacer cations. For the monovalent spacer-based systems, $(BA)_2PbI_4$ and $(PEA)_2PbI_4$, we have calculated electron and hole effective masses (m_e* and m_h*) in Γ-X and Γ-Y directions. Towards Z direction these systems have infinite value of carrier effective mass because of the low dielectric nature of the organic spacers. $(BA)_2PbI_4$ possess equal electron effective mass (m_e*= 0.19 m_0) towards X and Y directions of the Brillouin zone whereas hole effective mass (m_h*) in Γ-X direction is 0.29 m_0 and in Γ-Y direction is 0.28 m_0 which are almost identical (Table 3.3). Similar observation has been found for $(PEA)_2PbI_4$ where m_e* is 0.22 m_0 in Γ-X direction and 0.21 m_0 in Γ-Y direction whereas m_h* is 0.31 m_0 towards both X and Y directions from Γ point. Similar effective mass values of $(PEA)_2PbI_4$ have been reported by several earlier studies.*[42-43]*

Table 3.3: Effective masses of considered 2D perovskites.

System	Direction	$m_e^*(m_0)$	$m_h^*(m_0)$
$(BA)_2PbI_4$	Γ-X	0.19	0.29
	Γ-Y	0.19	0.28
$(3\text{-}APN)_2PbI_4$	Γ-X	0.18	0.38
	Γ-Y	0.16	0.49
	Γ-Z	-	1.9
$(PEA)_2PbI_4$	Γ-X	0.22	031
	Γ-Y	0.21	0.31
$(PyrEA)PbI_4$	X-Γ	0.15	0.40
	Γ-Z	-	1.9
$(2\text{-}PyrEA)PbI_4$	X-Γ	0.21	0.47
	Γ-Z	-	1.9
$(3\text{-}PyrEA)PbI_4$	X-Γ	0.26	0.49
	Γ-Z	-	0.63
$(4\text{-}PyrEA)PbI_4$	X-Γ	0.18	0.34
	Γ-Z	-	0.95

For $(3\text{-}APN)_2PbI_4$ we have calculated the electron and hole effective masses towards Γ-X and Γ-Y directions. In addition, seeing the nature of valence band near Γ-Z direction we have crosschecked the hole masses in this direction where we have observed heavy holes. However, in case of $(3\text{-}APN)_2PbI_4$ system, dissimilar effective masses were found towards X and Y high-symmetry points. Electron effective masses are nearly similar (0.18 m_0 in Γ-X and 0.16 m_0 in Γ-Y directions) while the holes have different effective masses along the Γ-X and Γ-Y directions (0.38 m_0 in Γ-X and 0.49 m_0 in Γ-Y directions). There is clear anisotropy of carrier masses in X and Y directions. This anisotropic carrier masses are result from unequal lattice parameter in X and Y directions. However, for pyridinium di-cation based perovskites we have calculated the carrier effective masses along X-Γ direction since the fundamental band gap appears at the X high symmetry point. All four pyridinium di-cation based systems have very small value of electron effective mass ranging from 0.15 m_0 to 0.26 m_0. Also, we have calculated the hole masses Γ-Z direction due to slight dispersive nature of valence band near this region. (3-PyrEA)PbI_4 possess comparatively small hole effective mass in the vertical direction. Hence, we can comment that with change in the position of secondary ammonium nitrogen in the pyridinium ring electron effective mass is regulating, although the spacer cations have no direct contribution to the upper band edge dispersion. Accounting the calculated results for the considered 2D perovskites, we observed lower effective masses for electrons than that of holes, that is the effect of dissimilar hybridization nature of the conduction and valence band edges. Larger values for holes are the result of Pb 6s orbital contribution in the valence band edges. As effective mass of electrons and holes are inversely proportional to the mobility for photoexcited electrons and holes so, for a particular system lower value of electron effective mass will result higher mobility for photoexcited electrons. The strong anti-bonding interaction results a relatively small effective electron mass compared to conventional semiconductors that results high mobility of the photo-excited electrons. Moreover, the calculated results of the carrier effective masses demonstrate the strong correlation with octahedral distortion in the metal halide layer. Octahedral distortion affects the overlapping of the Pb 6s and I 5p orbitals that enables tuning of effective masses with changing organic spacers. Despite being an aliphatic spacer cation-based system, (3-APN)$_2$$PbI_4$ possess comparable carrier masses compared to the aromatic core spacer-based systems and this is an interesting finding for the mono-cationic spacer based 2D perovskites. Hence, the directional anisotropic behavior expected in carrier mobility of (3-APN)$_2$$PbI_4$ can be beneficial for the fabrication of vertically oriented perovskite solar cells. Since we have observed carrier transport in the X direction will be better than along the Y direction. This observation can also be utilized during the film fabrication of mono-cationic 2D perovskites.

3.3.3. Optical Property

In addition, we have calculated the absorption co-efficient, another factor that dictates the scope of 2D perovskites for photovoltaic applications. Figure 3.7 show the optical absorption spectra of the seven studied system. Our calculated results show that all the seven systems have high extinction coefficients in the visible range. Since we have calculated the absorption coefficients using PBE+SOC method which in general, underestimates the band gap of the material, our calculated absorption peaks are somewhat downshifted towards IR region. For all the seven systems, the visible light absorption coefficients in the X and Y directions are significantly higher than those in Z direction. The absorption coefficients in the X and Y directions are similar for $(BA)_2PbI_4$ and $(PEA)_2PbI_4$. Similar kind of observations have been reported earlier.*[48-49]*

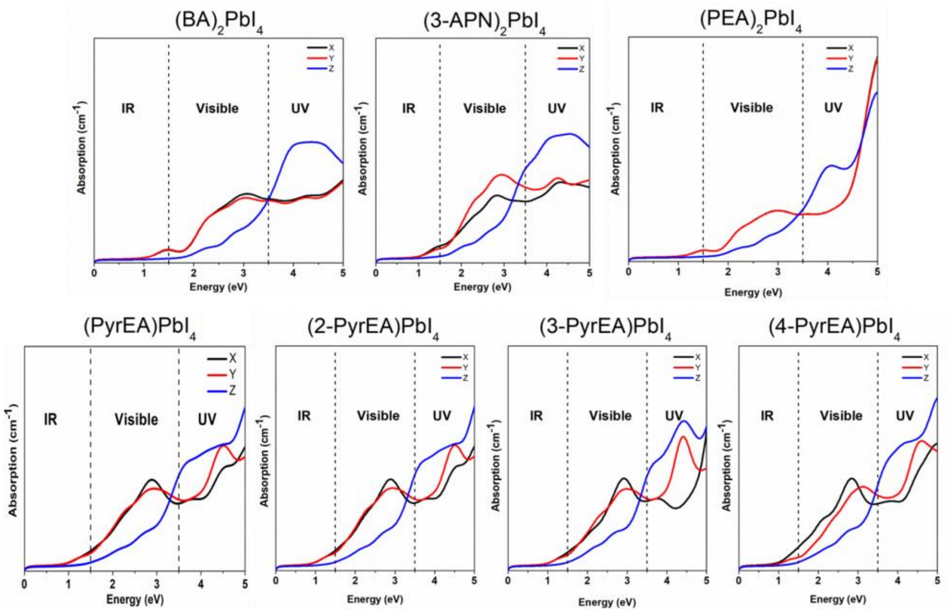

Figure 3.7: Calculated absorption spectra of considered 2D perovskites using PBE+SOC method.

In case of $(3\text{-}APN)_2PbI_4$, visible light absorption coefficient in the Y direction is a little higher than that in X direction that clearly signifies the optical anisotropy in X and Y direction. Since in Y direction absorption is higher for (3-APN)$_2$PbI$_4$, more efficient photon absorption is expected in Y direction compared to that in the X direction. Hence, observed optical anisotropy in X and Y directions can be important tool to develop efficient solar cell device using (3-APN)$_2$PbI$_4$ as perovskite absorber. In case of di-cationic systems almost identical visible light absorption coefficient have been observed in X and Y directions but there is a sharp peak in the X direction. Henceforth, the absorption coefficients in visible region are higher for (3-APN)$_2$PbI$_4$ than that of (PEA)$_2$PbI$_4$ and comparable with di-cationic based systems. The considered perovskite systems show high absorption results due to the direct band gap nature and p-p transition as the VBM of material mainly consists of I 5p states and the CBM mainly comprises of the Pb 6p states, the electronic transitions can be ascribed as p-p transition i.e., from the occupied I(5p) state to unoccupied Pb(6p) state. Improved visible light absorption properties of the di-cationic systems have also been reported experimentally. As we have already discussed, due to presence of organic spacer cations in the Z direction the VBM and CBM mainly located on the inorganic lead iodide layer i.e., in the X and Y directions. Therefore, charge density is expected to be distributed in the XY plane. These facts refer the visible light absorption is higher in the X and Y direction and significantly lower in the Z direction.

3.4. Conclusion

Here, we have performed a first principles study on the influence of spacer cations in the characteristic property of pure 2D perovskites. To show the versatility of 2D perovskites, we have studied three mono-cation based (BA)$_2$PbI$_4$ [(3-APN)$_2$PbI$_4$ and (PEA)$_2$PbI$_4$] and four di-cation based systems [(PyrEA)PbI$_4$, (2-PyrEA)PbI$_4$, (3-PyrEA)PbI$_4$ and (4-PyrEA)PbI$_4$]. Among all the studied systems the intermolecular H-bonding between spacer cations in (3-APN)$_2$PbI$_4$ results undistorted lead iodide layer and nearly ideal Pb-I-Pb bond angle. The calculated band gap for this system is 2.22 eV which is lowest among mono-cation based pure 2D perovskites. In

(PyrEA)PbI_4 due to the presence of a smaller number of primary ammonium functionality and structural rigidity of the spacer cation lead iodide layer remains less disturbed and improved band gap observed. These data displayed that variation of spacer cation mainly modulates the extent of octahedral distortion in the perovskite systems which is the controlling factor of the band edge states as well as effective mass and carrier mobility. Impressively lower effective masses found for the systems signifies good carrier mobility, the key property of a solar cell material. Implementation of 2D perovskites with least distorted lead iodide octahedra and reduced I···I contact can lead us the best choice of material. All the studied systems have considerable visible light absorption property in the XY plane. Analyzed properties of $(3\text{-APN})_2PbI_4$ clearly states, aliphatic spacer containing systems can also be a prominent choice of photovoltaic materials and electronegative group attached on the other end of mono-cation can lead us to a new way. Directional anisotropy characterized in $(3\text{-APN})_2PbI_4$ can be an important property to be considered during film fabrication. Hence, our study reveals that nitrile-based mono-cationic spacer-based system can as good as di-cationic organic spacer based systems for high performance photovoltaic based device applications.

3.5. References

1. Kojima A., Teshima K., Shirai Y., Miyasaka T. (2009), Organometal Halide Perovskites as Visible-Light Sensitizers for Photovoltaic Cells, J. Am. Chem. Soc., 131, 6050−6051 (DOI: 10.1021/ja809598r)
2. Lee M. M., Teuscher J., Miyasaka T., Murakami T. N., Snaith H. J. (2012), Efficient Hybrid Solar Cells Based on Meso-Superstructured Organometal Halide Perovskites, Science, 338, 643– 647 (DOI: 10.1126/science.1228604)
3. Burschka J., Pellet N., Moon S. J., Humphry-Baker R., Gao P., Nazeeruddin M. K., Grätzel M. (2013), Sequential Deposition as a

Route to High-Performance Perovskite-Sensitized Solar Cells, Nature, 499, 316 (DOI: 10.1038/nature12340)

4. Saliba M., Orlandi S., Matsui T., Aghazada S., Cavazzini M., Correa-Baena J. P., Gao P., Scopelliti R., Mosconi E., Dahmen K.-H. De Angelis F., Abate A., Hagfeldt A., Pozzi G., Graetzel M., Nazeeruddin M. K. (2016), A Molecularly Engineered Hole-transporting Material for Efficient Perovskite Solar Cells, Nat. Energy, 1, 15017 (DOI: 10.1038/nenergy.2015.17)
5. Yang W. S., Noh J. H., Jeon N. J., Kim Y. C., Ryu S., Seo J., Seok S. I. (2015), High-Performance Photovoltaic Perovskite Layers Fabricated through intramolecular exchange, Science, 348, 1234-1237 (DOI: 10.1126/science.aaa9272)
6. Yoshikawa K., Kawasaki H., Yoshida W., Irie T., Konishi K., Nakano K. , Uto T., Adachi D., Kanematsu M., Uzu H. (2017), Silicon Heterojunction Solar Cell with Interdigitated Back Contacts for A Photoconversion Efficiency over 26%, Nat. Energy, 2, 17032 (DOI: 10.1038/nenergy.2017.32)
7. Jena A. K., Kulkarni A., Miyasaka T. (2019), Halide Perovskite Photovoltaics: Background, Status, and Future Prospects, Chem. Rev., 119, 3036– 3103 (DOI: 10.1021/acs.chemrev.8b00539)
8. Frost J. M., Butler K. T., Brivio F., Hendon C. H., Van Schilfgaarde M., Walsh A. (2014), Atomistic Origins of High-Performance in Hybrid Halide Perovskite Solar Cells, Nano Lett., 14, 2584– 2590 (DOI: 10.1021/nl500390f)
9. Zhao Y., Zhu K. (2014), Optical Bleaching of Perovskite $(CH_3NH_3)PbI_3$ Through Room-Temperature Phase Transformation Induced by Ammonia, Chem. Commun., 50, 1605−1607 (DOI: 10.1039/C3CC48522F)
10. Smith I. C., Hoke E. T., Solis-Ibarra D., McGehee M. D., Karunadasa H. I. (2014), A Layered Hybrid Perovskite Solar-Cell Absorber with

Enhanced Moisture Stability, Angew. Chem., Int. Ed., 53, 11232– 11235 (DOI: 10.1002/anie.201406466)

11. Stoumpos C. C., Cao D. H., Clark D. J., Young J., Rondinelli J. M., Jang J. I., Hupp J. T., Kanatzidis M. G. (2016), Ruddlesden–Popper Hybrid Lead Iodide Perovskite 2D Homologous Semiconductors, Chem. Mater., 28, 2852-2867 (DOI: 10.1021/acs.chemmater.6b00847)
12. Quan L. N., Yuan M., Comin R., Voznyy O., Beauregard E. M., Hoogland S., Buin A., Kirmani A. R., Zhao K., Amassian A., Kim D. H., Sargent E. H. (2016), Ligand-Stabilized Reduced-Dimensionality Perovskites, J. Am. Chem. Soc., 138, 2649– 55 (DOI: 10.1021/jacs.5b11740)
13. Katan C., Mercier N., Even J. (2019), Quantum and Dielectric Confinement Effects in Lower-Dimensional Hybrid Perovskite Semiconductors, Chem. Rev., 119, 3140– 3192 (DOI: 10.1021/acs.chemrev.8b00417)
14. Sapori D., Kepenekian M., Pedesseau L., Katan C., Even J. (2016), Quantum Confinement and Dielectric Profiles of Colloidal Nanoplatelets of Halide Inorganic and Hybrid Organic–Inorganic Perovskites, Nanoscale, 8, 6369-6378 (DOI: 10.1039/C5NR07175E)
15. Li Y. R., Zhao Y., Cheng H. L., Zhao K., Wang Z. S. (2020), Highly Efficient and Stable Pure Two-Dimensional Perovskite-Based Solar Cells with the 3-Aminopropionitrile Organic Cation, ACS Appl. Mater. Interfaces, 12, 18590– 18595 (DOI: 10.1021/acsami.0c02295)
16. Febriansyah B., Lekina Y., Ghosh B., Harikesh P. C., Koh T. M., Li Y., Shen Z., Mathews N., England J. (2020), Molecular Engineering of Pure 2D Lead-Iodide Perovskite Solar Absorbers Displaying Reduced Band Gaps and Dielectric Confinement, ChemSusChem, 13, 2693-2701 (DOI: 10.1002/cssc.20200002)
17. Giannozzi P., Baroni S., Bonini N., Calandra M., Car R., Cavazzoni C., Ceresoli, D., Chiarotti G. L., Cococcioni M., Dabo I., Dal Corso A., de Gironcoli S., Fabris S., Fratesi G., Gebauer R., Gerstmann

U., Gougoussis C., Kokalj A., Lazzeri M., Martin-Samos L., Marzari N., Mauri F., Mazzarello R., Paolini S., Pasquarello A., Paulatto L., Sbraccia C., Scandolo S., Sclauzero G., Seitsonen A. P., Smogunov A., Umari P., Wentzcovitch R. M. (2009), Quantum Espresso: a modular and open-source software project for quantum simulations of materials, J. Phys.: Condens. Matter, 21, 395502 (DOI: 10.1088/0953-8984/21/39/395502)

18. Perdew J. P., Burke K., Ernzerhof M. (1996), Generalized Gradient Approximation Made Simple, Phys. Rev. Lett., 77, 3865– 3868 (DOI: 10.1103/PhysRevLett.77.3865)
19. Vanderbilt D. (1990), Soft self-consistent pseudopotentials in a generalized eigenvalue formalism, Phys. Rev. B: Condens. Matter Mater. Phys. 41 (11), 7892– 7895 (DOI: 10.1103/PhysRevB.41.7892)
20. Heyd J., Scuseria G. E., Ernzerhof M. (2003), Hybrid functionals based on a screened Coulomb potential, J. Chem. Phys., 118, 8207– 8215 (DOI: 10.1063/1.1564060)
21. Du M.H. (2015), Density Functional Calculations of Native Defects in $CH_3NH_3PbI_3$: Effects of Spin-Orbit Coupling and Self-Interaction Error, J. Phys. Chem. Lett., 6, 1461– 1466 (DOI: 10.1021/acs.jpclett.5b00199)
22. Monkhorst H. J., Pack J. D. (1976), Special points for Brillouin-zone integrations, Phys. Rev. B, 13, 5188– 5192 (DOI: 10.1103/PhysRevB.13.5188)
23. Blochl P. E. (1994), Projector augmented-wave method, Phys. Rev. B, 50, 17953– 17979 (DOI: 10.1103/PhysRevB.50.17953)
24. Kresse G., Joubert D. (1999), From Ultrasoft Pseudopotentials to the Projector Augmented Wave Method, Phys. Rev. B: Condens. Matter Mater. Phys., 59, 1758– 1775 (DOI: 10.1103/PhysRevB.59.1758)
25. Kresse G., Hafner J. (1993), Ab initio molecular dynamics for liquid metals, Phys. Rev. B: Condens. Matter Mater. Phys., 47, 558 (DOI: 10.1103/PhysRevB.47.558.)

26. Kresse G., Hafner J. (1994), Ab Initio Molecular-Dynamics Simulation of the Liquid-Metal–Amorphous-Semiconductor Transition in Germanium, Phys. Rev. B: Condens. Matter Mater. Phys., 49, 14251– 14271 (DOI: 10.1103/PhysRevB.49.14251)
27. Kresse G., Furthmüller J. (1996), Efficiency of ab-initio total energy calculations for metals and semiconductors using a plane-wave basis set, Comput. Mater. Sci., 6, 15-50 (DOI: 10.1016/0927-0256(96)00008-0)
28. Kresse G., Furthmüller J. (1996), Efficient Iterative Schemes for ab initio Total-Energy Calculations Using a Plane-wave Basis Set, Phys. Rev. B: Condens. Matter Mater. Phys., 54, 11169– 11186 (DOI: 10.1103/PhysRevB.54.11169-11186)
29. Ashcroft, N. W., Mermin, N. D., (1976) Solid State Physics, Holt: New York
30. Fox, M., (2001) Optical Properties of Solids, 2nd ed. Oxford University Press, Oxford, UK
31. Billing D. G., Lemmerer A. (2007), Synthesis, Characterization and Phase Transitions in the Inorganic-Organic Layered Perovskite-Type Hybrids $[(C_nH_{2n+1}NH_3)_2PbI_4]$, n = 4, 5 and 6, Acta Crystallogr., Sect. B: Struct. Sci., 63, 735– 747 (DOI: 10.1107/S0108768107031758)
32. Mercier N., Louvain N., Bi W. (2009), Structural Diversity and Retro-Crystal Engineering Analysis of Iodometalate Hybrids CrystEngComm, 11, 720– 734 (DOI: 10.1039/b817891g)
33. Du K.Z., Tu Q., Zhang X., Han Q., Liu J., Zauscher S., Mitzi D. B. (2017), Two-Dimensional Lead(II) Halide-Based Hybrid Perovskites Templated by Acene Alkylamines: Crystal Structures, Optical Properties, and Piezoelectricity, Inorg. Chem., 56, 9291-9302 (DOI: 10.1021/acs.inorgchem.7b01094)
34. Meggiolaro D., De Angelis F. (2018), First-Principles Modeling of Defects in Lead Halide Perovskites: Best Practices and Open

Issues, ACS Energy Lett., 3, 2206-2222 (DOI: 10.1021/acsenergylett.8b01212)

35. Meggiolaro D., Mosconi E., Proppe A. H., Quintero-Bermudez R., Kelley S. O., Sargent E. H., De Angelis F. (2019), Energy Level Tuning at the MAPbI3 Perovskite/Contact Interface Using Chemical Treatment, ACS Energy Lett., 4 (9), 2181– 2184 (DOI: 10.1021/acsenergylett.)
36. Mahata A., Mosconi E., Meggiolaro D., De Angelis F. (2020), Modulating Band Alignment in Mixed Dimensionality 3d/2d Perovskites by Surface Termination Ligand Engineering, Chem. Mater., 32, 105– 113 (DOI: 10.1021/acs.chemmater.9b02560)
37. Ghosh D., Neukirch A. J., Tretiak S. (2020), Optoelectronic Properties of Two-Dimensional Bromide Perovskites: Influences of Spacer Cations, J. Phys. Chem. Lett., 11, 2955– 2964 (DOI: 10.1021/acs.jpclett.0c00594)
38. Ishihara T. (1994), Optical properties of PbI-based perovskite structures, J. Lumin., 60-61, 269– 274 (DOI: 10.1016/0022-2313(94)90145-7)
39. Umebayashi T., Asai K., Kondo T., Nakao A. (2003), Electronic Structures of Lead Iodide Based Low-Dimensional Crystals, Phys. Rev. B: Condens. Matter Mater. Phys., 67, 155405 (DOI: 10.1103/PhysRevB.67.155405)
40. Even J., Pedesseau L., Jancu J.M., Katan C. (2013), Importance of Spin–Orbit Coupling in Hybrid Organic/Inorganic Perovskites for Photovoltaic Applications, J. Phys. Chem. Lett., 4, 2999– 3005 (DOI: 10.1021/jz401532q)
41. Even J., Pedesseau L., Dupertuis M.A., Jancu J.M., Katan C. (2012), Electronic Model for Self-Assembled Hybrid Organic/perovskite Semiconductors: Reverse Band Edge Electronic States Ordering and Spin-Orbit Coupling, Phys. Rev. B: Condens. Matter Mater. Phys., 86, 205301 (DOI: 10.1103/PhysRevB.86.205301)

42. Dyksik M., Duim H., Zhu X., Yang Z., Gen M., Kohama Y., Adjokatse S., Maude D. K., Loi M. A., Egger D. A. (2020), Broad Tunability of Carrier Effective Masses in Two-Dimensional Halide Perovskites, ACS Energy Lett., 5, 3609-3616 (DOI: 10.1021/acsenergylett.0c01758)
43. Zhang L., Liang W. (2017), How the Structures and Properties of Two-Dimensional Layered Perovskites $MAPbI_3$ and $CsPbI_3$ Vary with the Number of Layers, J. Phys. Chem. Lett., 8, 1517– 1523 (DOI: 10.1021/acs.jpclett.6b03005)
44. Ma L., Dai J., Zeng X. C. (2017), Two-Dimensional Single-Layer Organic-Inorganic Hybrid Perovskite Semiconductors, Adv. Energy Mater., 7, 1601731 (DOI: 10.1002/aenm.201601731)
45. Mitzi D. B. (1996), Synthesis, Crystal Structure, and Optical and Thermal Properties of $(C_4H_9NH_3)_2MI_4$ (M = Ge, Sn, Pb), Chem. Mater., 8, 791– 800 (DOI: 10.1021/cm9505097)
46. Knutson J. L., Martin J. D., Mitzi D. B. (2005), Tuning the Band Gap in Hybrid Tin Iodide Perovskite Semiconductors Using Structural Templating, Inorg. Chem., 44, 4699– 4705 (DOI: 10.1021/ic050244q)
47. Pisanu A., Mahata A., Mosconi E., Patrini M., Quadrelli P., Milanese C., De Angelis F., Malavasi L. (2018), Exploring the Limits of Three-Dimensional Perovskites: The Case of $FAPb_{1-x}Sn_xBr_3$, ACS Energy Lett., 3, 1353– 1359 (DOI: 10.1021/acsenergylett.8b00615)
48. Zhao Y.Q. (2018), Layer-dependent transport and optoelectronic property in two-dimensional perovskite: $(PEA)_2PbI_4$, Nanoscale, 10 (18), 8677– 8688 (DOI: 10.1039/C8NR00997J)
49. Lei J. H., Zhao Y. Q., Tang Q., Lin J. G., Cai M. Q. (2018), High transport and excellent optical property of a two-dimensional single-layered hybrid perovskite $(C_4H_9NH_3)_2PbBr_4$: a theoretical study, Phys. Chem. Chem. Phys., 20, 13241– 13248 (DOI: 10.1039/C8CP01573B)

Chapter 4

Tuning Band Edge Composition of 2D Hybrid Perovskites with Spacer Cations

4.1. Introduction

Throughout the last decade, hybrid metal halide perovskites are in the frontline of high performing semiconductor research. In this context, three-dimensional (3D) materials with general formula AMX_3 (A = small organic cation $CH_3NH_3^+$; M = Pb, Sn, and Ge; X = I, Br, and Cl) are highly interesting due to their easy synthesis and exciting optoelectronic properties.*[1-7]* However, the 3D hybrid metal halide perovskite semiconductor materials have several environmental stability issues such as degradation in the presence of light and moisture.*[8-9]* To overcome these stability issues of 3D hybrid halide perovskites at operational condition, two dimensional (2D) perovskites are emerging as a potential candidate for their application in the photovoltaic devices.*[10-11]* In contrast to the 3D counterpart, the lower dimensional system ensures improved stability due to their strong intermolecular van der Waals interactions between the hydrophobic organic cations.*[12]* But this improved stability comes at the expense of compromised photovoltaic efficiency. Moreover, due to the large dielectric mismatch between the organic and inorganic layers of 2D perovskites, it behaves as multiple quantum wells (MQWs). The large organic cations in these materials act as barrier whereas inorganic slabs behave like wells.*[13-14]* However, there are four phases of 2D perovskites reported so far, such as Ruddlesden−Popper (RP), Dion−Jacobson (DJ), alternating cations in the interlayer space (ACI) and those based on alkyl diammonium cations (DC).*[15]* Among them RP and DJ phases of 2D materials are more common and highlighted in current days for photovoltaic application. The RP phases are the 2D perovskite materials with monovalent spacer cation having a general stoichiometry of $A'_2A_{n-1}M_nX_{3n+1}$ where A′ is the monovalent large organic spacer cation. In this case, the spacer cations are attached within the metal halide layer in such a way that the material acquires a staggered arrangement, and the consecutive inorganic layers are shifted by half unit cell from each other (Figure 4.1a). In RP phases, two organic spacer cation layers are present between two inorganic layers as a result there is a van der Walls gap between two organic layers and the primary ammonium tail of the cations are more flexible to move. Whereas, DJ phases of 2D perovskites are structured with divalent spacers with molecular formula $A''A_{n-1}M_nX_{3n+1}$ where A″ is the dipositive large organic spacer cations, having an eclipsed conformation. In case of DJ phase 2D perovskites, the metal octahedras stack exactly on top of each other (Figure 4.1b). Therefore, DJ phases feature single layer stacking of rigid dications between two metal halide layers. So, the van der Walls gaps present between two monocation layers in RP phases are absent here. Moreover, the short dications make the 2D perovskite geometry more compact and shortens the gap between inorganic slabs.

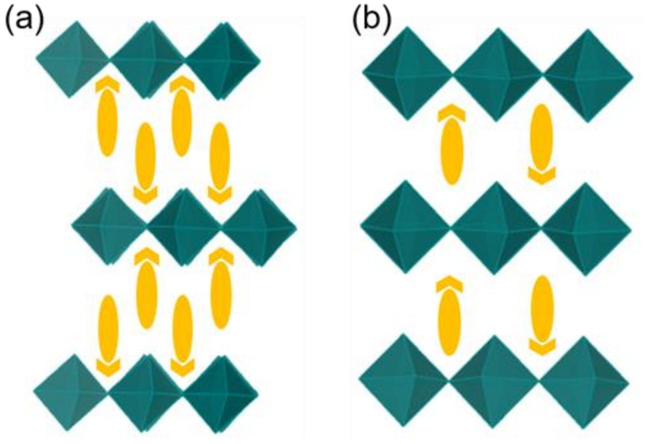

Figure 4.1: A schematic representation of (a) Ruddlesden Popper and (b) Dion Jacobson phase perovskites.

As a consequence of shorten gap between inorganic slabs, barrier height of the MQW reduces. Hence, band gap decreases along with facilitated carrier movement. In this context, Neukirch and co-workers have studied the suppressed carrier recombination in DJ phase perovskites due to the reduced structural dynamics.*[16]* This feature indicates the advantage of DJ phases over RP phases of 2D perovskites. Generally, the electronic structure at the band edges of these 2D perovskites are constitutes by the atomic orbitals of the metal and halides.*[17]* As a result, the band edge electronic properties of the 2D perovskites can be modulated by the engineering of the inorganic composition. The best replacement of Pb observed till date is Sn. But the performance of Sn based materials falls due to easy oxidation tendency of Sn^{2+} to Sn^{4+}. As a result of the oxidation of Sn, poor quality films are formed. In comparison, due to the large inert pair effect of Pb^{2+}, it is highly stable and generates high quality films.*[18]* Therefore, we have considered Pb as metal cation along with I as halide anion in the inorganic counterparts for our study. Further to this, the atomic orbitals of organic cations lie a few eV away from the band edges of the perovskite, as a result, the electronic structure of the material remains unaffected by the organic cation composition. So, the organic parts can only influence the electronic property indirectly by causing structural distortion in the inorganic octahedra via H-bond with the halides. However, it has been observed that organic cations having aromatic unit comes closure to the band edge states in comparison to the aliphatic one. Tretiak and co-workers have revealed that the organic cations with aromatic rings contribute prominently to the valence bands of 2D perovskites.*[19]* This is due to the high energy of π orbitals in aromatic spacer compared to σ orbitals in aliphatic one which produces destabilised HOMO and pushes organic components close to valence band edge of the material. Accordingly, any compositional modulation of the organic molecule that stabilises the LUMO of the organic cation may cause the prominent contribution of the cationic states to the perovskite conduction band edge. Henceforth, finding out an organic cation that has destabilised HOMO and stabilised LUMO can lead us to tune the electronic structure of 2D perovskites directly through organic spacer cation engineering. Hence, figuring out the perovskite electronic structure customizing potential of organic spacer cations is one of the major interests among the researchers. Besides, DJ phases 2D perovskites are gaining recent research interest as Kanatzidis and co-workers have reported piperidinium as well as pyridinium based organic spacers intercalated DJ phases show better photovoltaics performance.*[15,20]* Their work has ensured the scientific community about the great potential of DJ phases for the application in photovoltaics. Hence, rational design rule is highly appreciated for the understanding of high-performance photovoltaic devices based on DJ phase 2D perovskites. Therefore, search of the choices other than piperidinium and pyridinium ring is highly appreciated. Other than N, S atom is highly polarisable and has the ability to bound the electrons of the ring loosely which can stabilise the molecular orbitals. This property has been successfully used first by Chen and co-workers in their work where they have introduced the thiophene heterocyclic ring as the aromatic unit of the spacer cation and observed considerable charge carrier mobility, along with improvement in the carrier lifetime.*[21]* By fabricating these thiophene based RP phase perovskite solar cells they have achieved impressive photovoltaic efficiency. Similarly, Liu and co-workers have used 2,5-thiophenedimethylammonium and reported the thiophene derivative in DJ phase perovskite photovoltaics for the first time.*[22]* Therefore, an aromatic ring with N and S heteroatom can be a good choice for the stabilisation of LUMO of the cation. Although Kanatzidis and co-workers have utilized pyridinium ring as a spacer cation, another heterocyclic ring unit with S heteroatom (thiopyrylium) has not been introduced yet. Moreover, substitution in the aromatic ring can affect the electronic structure of the spacer cation. Hence, we have considered meta and para methyl ammonium substituted pyridinium and thiopyrylium cations such as 3-aminomethylpyridinium [3-AMP], 4-aminomethylpyridinium [4-AMP], 3-aminomethylthiopyrylium [3-AMThP] and 4-aminomethylthiopyrylium [4-AMThP] as organic spacer layer (Figure 4.2). Motivation behind choosing these units is to merge the advantages of DJ phases and sulphur-based spacer cations for the improvement of the photovoltaic efficiency. Furthermore, to figure out the effect of elemental substitution along the group we have added oxygen heteroatom containing pyrylium cations in our study. Notably, the pyrylium ring spacer cation based perovskites are yet to be explored for photovoltaic application. Hence, we have added 3-aminomethylpyrylium [3-AMPy] and 4-aminomethylpyrylium [3-AMPy] also as organic spacer layer (Figure 4.2). Keeping all those in mind, we present here a detailed theoretical study considering a set of spacer cations with different functionalities with PbI_4 inorganic unit to explore the scope of spacer cations to take control of the electronic structure of the 2D halide perovskites. At first, we have explored the properties of (3-AMP)PbI_4 and (4-AMP)PbI_4 DJ phase perovskites followed by nitrogen replacement with sulphur and oxygen. Hence, we have examined the photovoltaic properties of computationally modelled (3-AMThP)PbI_4, (3-AMPy)PbI_4, (4-AMThP)PbI_4 and (4-AMPy)PbI_4 systems. Moreover, we have demonstrated the dominating nature of organic components to the perovskite electronic structure. Our detailed study features the scope of spacer cation engineering to improve the properties of 2D perovskites for better application in photovoltaics.

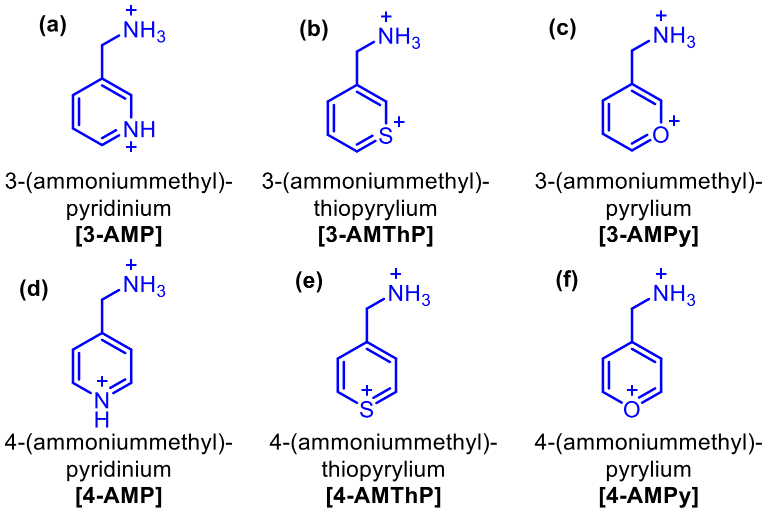

Figure 4.2: Dication organic spacers considered in this work.

4.2 Computational Methods

The plane wave program package Quantum Espresso (QE)*[23]* has been used for the density functional theory (DFT) calculations. The GGA-PBE*[24]* exchange correlation functional has been considered for the geometry relaxation. Scalar relativistic ultrasoft pseudopotentials*[25]* with electrons from 2s, 2p orbital for O, N, and C; 1s orbital for H; 5s, 5p orbital for I; and 6s, 6p, 5d orbital for Pb were included explicitly. For (3-AMP)PbI_4 and (4-AMP)PbI_4 structures, experimental cell parameters were kept fixed whereas ions were allowed to relax and plane wave basis set cutoffs have been considered 25 and 200 Ry for the smooth part of the wave functions and augmented density, respectively. For the other systems ions as well as cell parameters were allowed to relax and plane wave basis set cutoffs have been considered 50 and 400 Ry for the wave functions and augmented density, respectively. The DFT-D3 dispersion correction as formulated by Grimme*[26]* was applied for the relaxation of all the systems. We have used Monkhorst pack*[27]* k-point sampling of 4×4×1 for (3-AMP)PbI_4; (3-AMThP)PbI_4 ; (3-AMPy)PbI_4 and 4×4×4 for (4-AMP)PbI_4; (4-AMThP)PbI_4; (4-AMPy)PbI_4 2D perovskite-based systems. These methods have been previously used for similar 2D perovskite-based systems and reported to show excellent results compared to the experimental reports.*[28]* The formation energies of the materials have been calculated using the following equation (4.1):

$$\Delta E = E_{perov} - (4{*}E_{PbX_2} + 8{*}E_X + 4{*}E_{Cat}) \qquad 4.1$$

In the equation 1, E_{perov} is the total energy of the 2D perovskite material; E_{PbX_2} is the total energy of PbI_2 in their crystal phase; E_X is the energy of the isolated halide anion; E_{Cat} is the energy of isolated cation. Due to nonavailability of the halide salt (Mol-X_2) crystals of our considered organic ammonium cations we have calculated total energies of the isolated ions instead of calculating total energies of Mol-X_2 crystals. Similar method has been followed by De Angelis and coworkers for the calculation of formation energy in their work.*[28]* As the GGA-PBE functional miscalculate the band gap values, we have calculated the electronic structure using HSE06*[29]* hybrid functional considering 43%*[30]* Hatree-Fock exchange. Additionally, the relativistic spin orbit coupling (SOC) was included in all the electronic structure calculations. Norm-conserving pseudopotentials with electrons from I 5s, 5p; O, N, C 2s, 2p; H 1s; Pb 5s, 5p, 6s, 6p, 5d shells have been included explicitly. Plane wave basis set cutoff of 40 Ry has been considered for the smooth part of the wave functions and a Fock energy cutoff of 80 Ry has been chosen during HSE06+SOC calculations. Such methodologies have been successfully used by other groups for similar type of systems.*[31]* A Monkhorst pack k-point sampling of 2×2×1 and 2×2×2 was used for the meta and para methyl ammonium substituted pyridinium, pyrylium and thiopyrylium cation-based materials for HSE06+SOC calculations, respectively. To reduce the computational cost, we have calculated the band structures using GGA-PBE functional and considering SOC with full relativistic ultrasoft pseudopotentials. Furthermore, the charge carrier effective masses were calculated using the following equation (4.2)*[32]*:

$$m^{*} = \hbar^{2}\left(\frac{\partial^{2}E}{\partial k^{2}}\right)^{-1} \qquad 4.2$$

where, $\hbar$ is the reduced Planck constant, E is the band edge eigen value and k is the wave vector.

For ab initio molecular dynamics simulation calculations, we have used Vienna ab-initio Simulation Package (VASP).*[33-38]* In this case, geometry optimizations have been performed by projector-augmented wave (PAW) method within a plane-wave basis set of kinetic energy cutoff 500 eV and GGA-PBE functional.*[24]* A Γ-centered k-point grid of 4×4×1 and 4×4×4 was used for meta and para methyl ammonium substituted cation-based systems, respectively. The MD simulations were carried out using canonical ensemble at 300 K temperature controlled by a Nosé−Hoover thermostat*[39]* in a 10 ps trajectory with 1 fs timestep.

Further to these, Gaussian 09 D.01*[40]* suite of programme has been used for the calculation of the molecular energy levels of the considered isolated cations. The Pople basis set 6-311++G***[41-43]* and Becke 3-parameter Lee–Yang–Parr (B3LYP)*[44-48]* hybrid functional has been considered for the calculations. Also, we have done single point calculation using HSE06+SOC in Quantum Espresso to compare the trend using the Gaussian 09 programme.

4.3. Results and discussion

4.3.1. Structural properties and stability analysis

Table 4.1: Formation energies of all the considered 2D halide perovskite systems.

Perovskite	Formation energy per formula unit (eV)
(3-AMP)PbI_4	-3.64
(4-AMP)PbI_4	-3.77
(3-AMThP)PbI_4	-8.09
(4-AMThP)PbI_4	-8.23
(3-AMPy)PbI_4	-8.26
(4-AMPy)PbI_4	-8.53

At first, the stability of the considered 2D halide perovskites has been investigated using various stability analysis parameters. The other energetic stability related parameters such as formation energy values have been calculated as it is one of the fundamental parameters to ensure the feasibility of crystal formation. The detailed formula has been given in the methods section. As we have considered two known systems in our work, we have compared the formation energy of the designed systems with the known perovskites. All the calculated formation energies of the considered systems are tabulated in the Table 4.1. Table 4.1 shows that the designed 2D halide perovskites have more negative formation energies in comparison to the known ones assuring energetic stability of the designed systems. We can see that the modelled systems are ~4.5 eV more stable than the experimentally reported systems.

Table 4.2: Calculated lattice parameters (in Angstrom) of all the considered systems.

Perovskite	a	b	c
(3-AMP)PbI$_4$	9.122	8.779	19.830
(4-AMP)PbI$_4$	12.335	12.342	10.504
(3-AMThP)PbI$_4$	9.388	8.793	21.403
(4-AMThP)PbI$_4$	12.695	12.652	10.737
(3-AMPy)PbI$_4$	9.215	9.053	20.137
(4-AMPy)PbI$_4$	12.536	12.542	10.599

The calculated lattice parameters of the considered perovskite systems given in Table 4.2 shows that the length of the c-axis is larger in the modelled systems compared to that in the experimentally synthesized systems. This leads to the maximum interactions between the sulphur/oxygen atoms with the iodides, which in turn stabilizes the systems compared to the pyridinium spacer-based materials. So, we expect such materials can be synthesized.

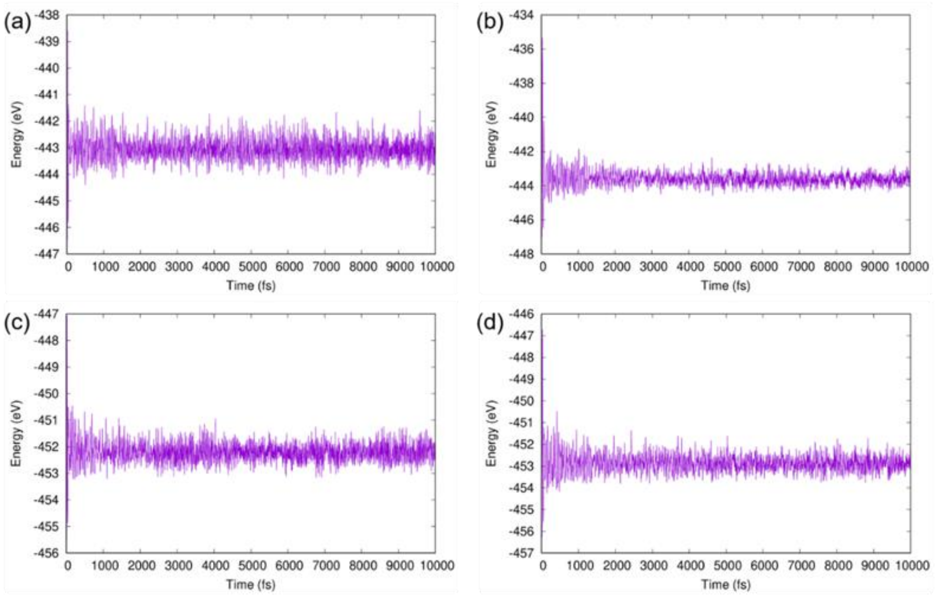

Figure 4.3: Ab initio molecular dynamics simulations of considered (a) (3-AMThP)PbI$_4$, (b) (4-AMThP)PbI$_4$, (c) (3-AMPy)PbI$_4$ and (d) (4-AMPy)PbI$_4$ 2D halide perovskites at 300 K.

For the photovoltaic application purpose, these materials will be exposed in the environment, hence we have examined the thermal stability of the systems in room temperature. Ab initio molecular dynamics (AIMD) simulations using a Nosé thermostat model have been performed with the NVT ensemble at 300 K temperature with a time step of 1 femtosecond (fs) for 10 picoseconds (ps). In Figure 4.3 we have presented the fluctuations of the total energy of the system with simulation time. Our simulation results show that there are no considerable changes in the total energy during the simulation (Figure 4.3) for the modelled systems. Therefore, the short simulation indicates that the structure may not easily convert into a new phase/structure immediately. As the structural pattern of the 2D halide perovskites including the orientation of the spacer cations between inorganic layers does not change much throughout the simulation, the geometries of these structures considered for our further study.

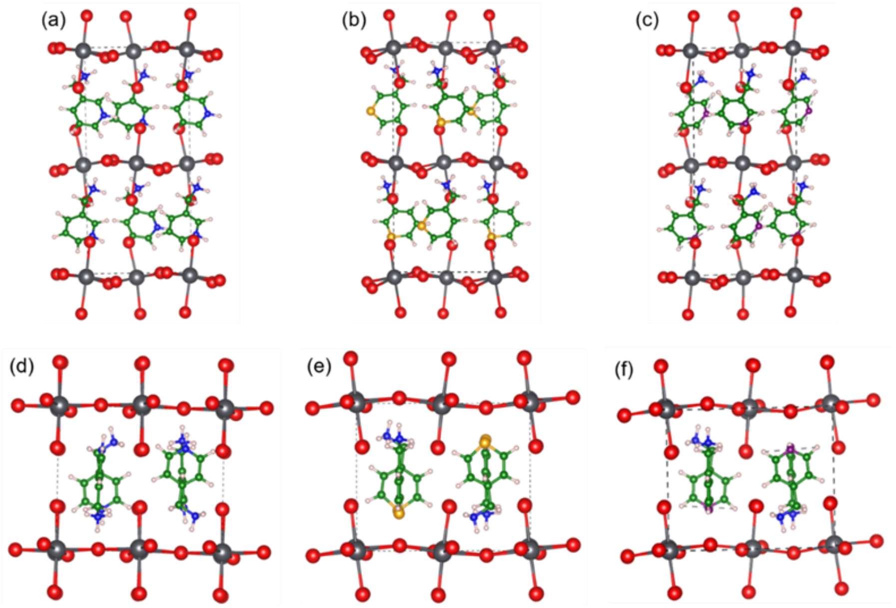

Figure 4.4: Optimized geometries of (a) (3-AMP)PbI$_4$, (b) (3-AMThP)PbI$_4$, (c) (3-AMPy)PbI$_4$, (d) (4-AMP)PbI$_4$, (e) (4-AMThP)PbI$_4$, and (f) (4-AMPy)PbI$_4$ 2D halide perovskites. Colors: hydrogen (white), carbon (green), nitrogen (blue), oxygen (purple), sulphur (yellow), iodine (red) and lead (grey).

Table 4.3: Experimental as well as theoretical Closest I···I contact distance

Perovskites	Closest I···I contact distance (Å)	
	Experimental	Theoretical
(3-AMP)PbI_4	4.20	4.20
(4-AMP)PbI_4	4.20	4.12

Table 4.4: Experimental as well as theoretical Pb-I bond distances of (3-AMP)PbI_4.

Experimental		Theoretical
Label	Distances (Å)	Distances (Å)
Pb(1)-I(2)#1	3.192(5)	3.229
Pb(1)-I(3)	3.042(10)	3.113
Pb(1)-I(4)	3.256(8)	3.290
Pb(1)-I(6)	3.095(8)	3.205
Pb(1)-I(7)	3.173(5)	3.213
Pb(1)-I(8)	3.254(6)	3.249
Pb(2)-I(1)#2	3.108(8)	3.163
Pb(2)-I(2)#3	3.200(5)	3.184
Pb(2)-I(3)#3	3.317(10)	3.267
Pb(2)-I(5)#3	3.237(9)	3.267
Pb(2)-I(7)#4	3.211(5)	3.217
Pb(2)-I(8)	3.117(6)	3.181

Table 4.5: Experimental as well as theoretical Pb-I-Pb bond angles of (3-AMP)PbI_4.

Experimental		Theoretical
Label	Angles (°)	Angles (°)
Pb(1)#4-I(2)-Pb(2)#8	163.05(19)	154.994
Pb(1)-I(3)-Pb(2)#8	167.8(4)	159.921
Pb(1)-I(7)-Pb(2)#1	165.9(2)	155.138
Pb(1)-I(8)-Pb(2)	168.4(2)	162.468

Table 4.6: Experimental as well as theoretical Pb-I bond distances of (4-AMP)PbI_4.

Experimental		Theoretical
Label	Distances (Å)	Distances (Å)
Pb(1)-I(1)	3.216(3)	3.360
Pb(1)-I(4)	3.171(4)	3.099
Pb(1)-I(5)	3.207(4)	3.224
Pb(1)-I(6)	3.192(4)	3.224
Pb(1)-I(7)	3.206(3)	3.247
Pb(1)-I(8)	3.199(3)	3.222
Pb(2)-I(2)	3.207(4)	3.226
Pb(2)-I(3)	3.174(3)	3.206
Pb(2)-I(5)#1	3.178(4)	3.223
Pb(2)-I(6)	3.159(4)	3.196
Pb(2)-I(7)#2	3.236(3)	3.241
Pb(2)-I(8)#3	3.226(3)	3.240

Table 4.7: Experimental as well as theoretical Pb-I-Pb bond angles of (4-AMP)PbI_4.

Experimental		Theoretical
Label	Angles (°)	Angles (°)
Pb(1)-I(5)-Pb(2)#7	148.68(11)	148.752
Pb(1)-I(6)-Pb(2)	152.11(12)	150.103
Pb(1)-I(7)-Pb(2)#8	147.71(11)	141.690
Pb(1)-I(8)-Pb(2)#9	148.15(12)	145.114

Perovskite systems with 4-aminomethyl substitution has proper DJ phase geometry where metal halide octahedra stack exactly on top of each other, that results from the symmetric nature of the spacer cation, whereas 3-aminomethyl substituted perovskites have offset geometries which is forced by the unsymmetrical spacer cations. As a result of the symmetric structure of the spacer cations, the methylammonium tail of (4-AMP)PbI_4 inserts much deeply to the octahedral cavity. Due to this, the Pb-I-Pb angle of (4-AMP)PbI_4 deviates much from ideal in comparison to that in (3-AMP)PbI_4. The structural parameters like bond angle, inorganic layer contact distance is known to influence the electronic structure. Here we have presented the geometrical parameters in Table 4.8 and analysed the results. The thiopyrylium ring is larger than pyridinium ring which is due to the larger radius of S atom compared to N as well as 2p-3p overlap in thiopyrylium enlarges the C-S bond length compared to C-N. Hence, the nearest I···I contact distance is large in (3-AMThP)PbI_4 and (4-AMThP)PbI_4 (Table 4.8) compared to that in (3-AMP)PbI_4 and (4-AMP)PbI_4. Whereas (3-AMPy)PbI_4 shows largest Pb-I-Pb bond angle among the six perovskites (Table 4.8). Therefore, the presence of the organic spacers has significant contribution in the structural arrangement of 2D halide perovskite systems.

Table 4.8: Structural properties of all the considered 2D halide perovskites.

Perovskite	Pb-I-Pb angle	Closest I···I contact distance (Å)
(3-AMP)PbI_4	160°	4.20
(4-AMP)PbI_4	149°	4.12
(3-AMThP)PbI_4	158°	4.46
(4-AMThP)PbI_4	158°	4.37
(3-AMPy)PbI_4	164°	4.40
(4-AMPy)PbI_4	152°	4.18

4.3.2. Electronic structure:

As our main purpose of this study is to tune the band edge state of the 2D halide perovskite materials through spacer cation modulation, we have performed HSE06+SOC calculations for the investigation of electronic structures of all these structures. In Table 4.9 we have presented the band gap values obtained using HSE06+SOC level of calculations and the calculated values are compared with the available experimental reports. Our calculated band gap value of 2.28 eV for (3-AMP)PbI_4 agrees well with the experimentally reported band gap value of 2.34 eV. Therefore, we can say that our considered level of theory is good enough for the calculation of band gap of other considered 2D halide perovskites. Between (3-AMP)PbI_4 and (4-AMP)PbI_4, the former possesses smaller band gap that can be attributed to its more ideal Pb-I-Pb bond angle of 160° compared to 149° in (4-AMP)PbI_4 (Table 4.8). Surprisingly, (3-AMThP)PbI_4 and (4-AMThP)PbI_4 exhibits significantly decreased band gaps (Table 4.9) in comparison to the (3-AMP)PbI_4 and (4-AMP)PbI_4 although two thiopyrylium based materials exhibit larger distance between the inorganic layers compared to that in the pyridinium based materials, and the thiopyrylium materials also show same deviation in the Pb-I-Pb angle. Notably, the pyrylium cation based perovskites also show decreased band gap but in a different pattern that is para methyl ammonium substituted spacer containing systems ((4-AMPy)PbI_4) have a lesser band gap (Table 4.9) than the ortho substituted one ((3-AMPy)PbI_4). Hence, in the case of thiopyrylium and pyrylium ring spacer intercalated materials, the band gap properties of the materials do not depend only on the inter-layer distance and structural distortions but also on the types of heteroatoms of the ring.

Table 4.9: The calculated band gap values (in eV) of the 2D perovskite along with available experimental reports.

Perovskite	HSE06+SOC band gap	Experimental band gap
(3-AMP)PbI_4	2.28	2.34[15]
(4-AMP)PbI_4	2.37	-
(3-AMThP)PbI_4	1.93	-
(4-AMThP)PbI_4	2.01	-
(3-AMPy)PbI_4	2.15	-
(4-AMPy)PbI_4	1.90	-

To obtain the explanations behind the unexpected trend of band gap values, we have investigated the partial density of states (Figure 4.5) of the perovskites and explored the elemental contribution to the valence band and conduction band. From Figure 4.5, we can see that in case of (3-AMP)PbI_4 and (4-AMP)PbI_4 there is a minor contribution of the cationic states in the conduction band edge where carbon components appear far away from the valence band edge. Carbon components of (3-AMP)PbI_4 and (4-AMP)PbI_4 appear 0.8 eV and 0.4 eV above the conduction band edges of the two materials. On the other hand, the valence band of (3-AMThP)PbI$_4$ and (4-AMThP)PbI$_4$ is dominated by I and Pb contributions and the conduction band is overshadowed by the cationic contribution which is different from the conventional hybrid metal halide perovskites. In these two compounds the Pb and I pDOS components in the conduction band comes few eV above the band edge. In (3-AMThP)PbI$_4$ Pb components appear 1.1 eV above the organic components whereas in (4-AMThP)PbI$_4$ contributions from inorganic moiety comes 0.5 eV above the cationic states. Similar dominating nature of cationic states to the conduction band minima also observed in two pyrylium based systems (3-AMPy)PbI$_4$ and (4-AMPy)PbI$_4$. In these two materials the conduction band minima are composed of carbon and oxygen components. Thus, incorporation of S and O as heteroatom in the ring of the spacer cation depicts a new picture of perovskite electronic structure.

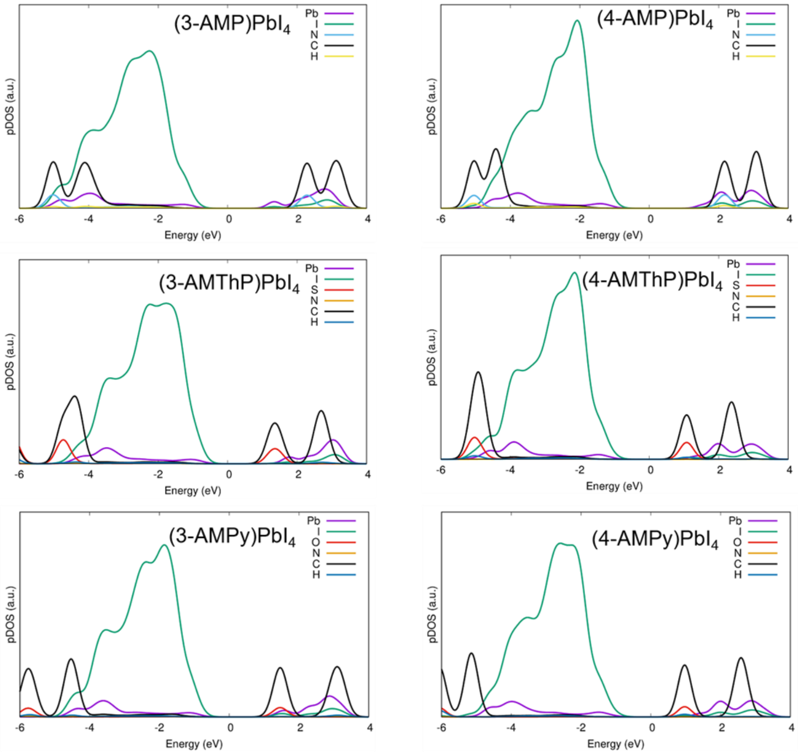

Figure 4.5: Partial density of states (pDOS) plots of considered 2D halide perovskites using HSE06+SOC level of calculations.

To further confirm the nature of electronic states at the band edges we have checked the contribution of the specific orbitals through charge density plots (Figure 4.6). By analyzing the charge density at the highest and lowest occupied orbitals, we have observed that the HOMO as well as LUMO of (3-AMP)PbI$_4$ are of Pb and I atoms where HOMO is constructed by the linear combination of Pb and I atoms and LUMO comes mainly from the Pb atoms of the perovskite. In case of (3-AMThP)PbI$_4$, the nature of HOMO is similar to that in (3-AMP)PbI$_4$ but LUMO is mainly constituted of thiopyrilium methyl ammonium cation. We have also crosschecked the HOMO-1 and LUMO+1 (Figure 4.6e-f) orbital contribution to the charge density in (3-AMThP)PbI$_4$ and observed similar trends. Similar types of change densities have also been observed in case of pyrylium ring spacer based perovskites (Figure 4.6g-h).

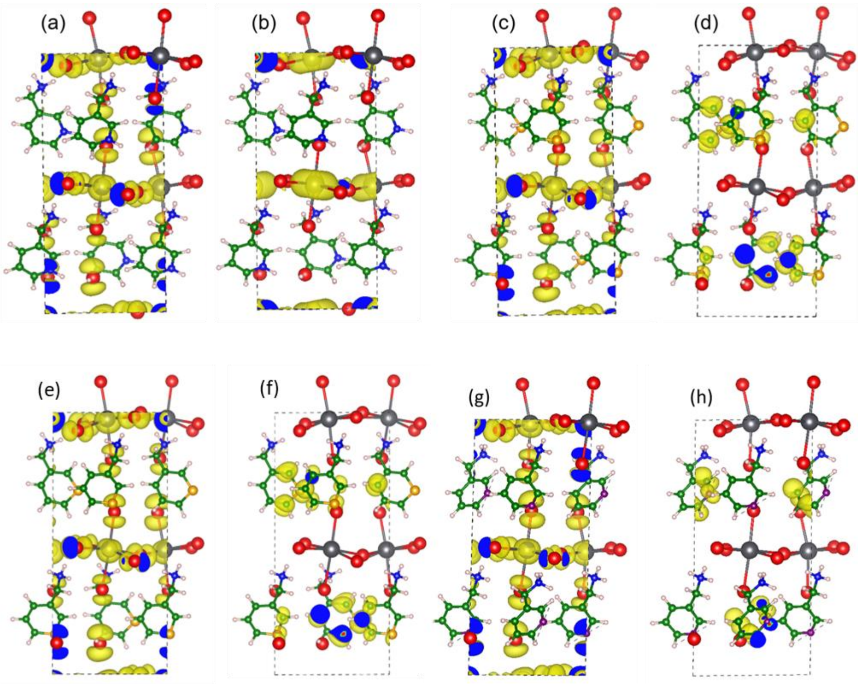

Figure 4.6: Charge Density Contribution from the specific orbital (a) HOMO, (b) LUMO of (3-AMP)PbI$_4$, (c) HOMO, (d) LUMO, (e) HOMO-1 (f) LUMO+1 of (3-AMThP)PbI$_4$ and (g) HOMO and (h) LUMO of (3-AMPy)PbI$_4$ 2D halide perovskite. Colours: hydrogen (white), carbon (green), nitrogen (blue), sulphur (yellow), iodine (red), lead (grey).

In general, such characteristics of HOMO/LUMO orbitals are very much unlikely in organic inorganic hybrid metal halide perovskites. So, we tried to know the reason behind this. Observing the density of states plots (Figure 4.5) we can notice that there is no significant overlap between the organic and inorganic components. However, overlap between C and S/O states is clearly visible and significant overlap is also present between Pb and I components. But we didn't notice any significant overlap between the states of inorganic (Pb, I) and organic (C, S/O, N, H) layers. In addition, if we closely look on the pDOS plots of pyridinium and thiopyrylium/pyrilium based materials then we notice that the nature and position of the Pb and I components almost remains same whereas the position and nature of the cationic components change. Hence, we did not find any dominant interaction that is responsible for this unusual behavior of the thiopyrylium/pyrilium based materials.

Table 4.10: Molecular orbital energies of all the considered isolated spacer cations. All energies are in eV.

Cation	QE			Gaussian		
	HOMO	LUMO	Gap	HOMO	LUMO	Gap
3-AMP	-12.94	-6.58	6.36	-16.81	-10.91	5.90
4-AMP	-12.86	-6.78	6.08	-16.73	-11.09	5.64
3-AMThP	-13.19	-7.40	5.79	-17.04	-11.67	5.37
4-AMThP	-13.13	-7.56	5.57	-16.97	-11.81	5.16
3-AMPy	-13.52	-7.57	5.95	-17.44	-11.92	5.52
4-AMPy	-13.41	-7.50	5.91	-17.31	-11.84	5.47

Since we could not find any dominant interactions between organic and inorganic part, the molecular properties of the free cations are investigated. Our calculated molecular orbital energy levels of the cations are listed in Table 4.10. Table 4.10 show that the molecular orbitals of thiopyrylium and pyrylium cations are significantly stable with respect to the pyridinium based systems. The result is quite expected as the S and O atoms in thiopyrylium and pyrylium are more polarized compared the pyridinium N atom. Hence, the former systems can be better electron donor. In addition, O is more electronegative than S and hence thiopyrylium can be more polarizable than the pyrylium. Thus, the energy stabilization order of the frontier molecular orbitals as pyrylium > thiopyrylium > pyridinium is understandable.

Next, we have calculated the band structures of all the considered 2D halide perovskites to understand the nature of the dispersion of the energy levels throughout the high symmetry points of the Brillouin zone also to predict the transport properties of the photo generated carriers. Band structure plots obtained using PBE+SOC are presented in Figure 4.7. The (4-AMP)PbI_4, (4-AMThP)PbI_4 and (4-AMPy)PbI_4 perovskites possess direct band gap at the Z point of the Brillouin zone. From the band plot of (4-AMP)PbI_4, one can see the nature of the bands near the edges are highly dispersive i.e., a high mobility of the photogenerated carriers. Moreover, according to our calculated results, the electron and hole masses in (4-AMP)PbI_4 material from Z to U direction are $1.33m_0$ and $1.87m_0$, respectively. While the hole mass in the Z- Γ direction is $2.07m_0$ predicting better out of plane transport probability of photogenerated hole compare to electron (Table 4.11). In case of (4-AMThP)PbI_4 and (4-AMPy)PbI_4, the energy levels in the valence bands are highly dispersive over the Brillouin zone. However in the case of (4-AMThP)PbI_4, the conduction band edge is less dispersive in nature, which can be attributed to the fact that in this material the conduction band edge is constituted of the organic spacer cation. One can notice that the conduction band edge energy levels of (4-AMP)PbI_4 differ with (4-AMThP)PbI_4 and (4-AMPy)PbI_4. More specifically, the flat organic bands shifted downwards in (4-AMThP)PbI_4 and (4-AMPy)PbI_4 with respect to the (4-AMPy)PbI4 which can be due to the stabilisation of the cationic molecular orbitals. The organic cations are of low dielectric nature in comparison to lead-iodide moiety (located in valence band edge), which may result in flat conduction band and higher effective masses for the photoexcited electrons.

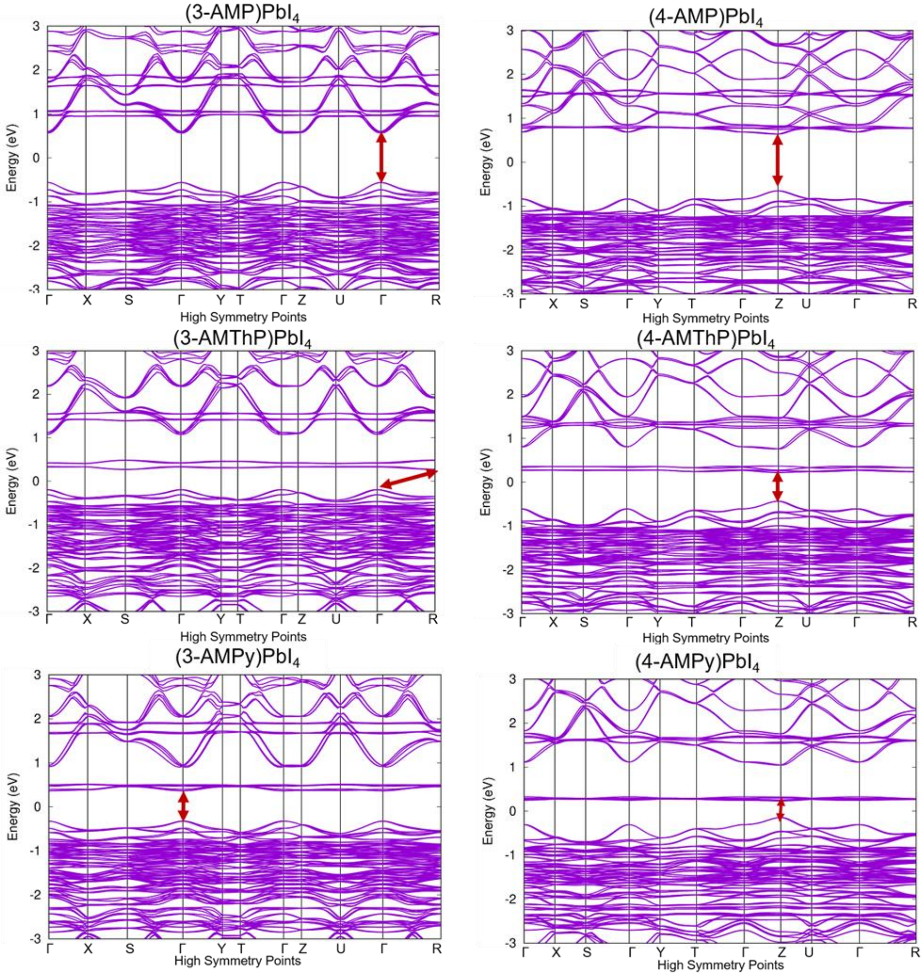

Figure 4.7: Band structure plots obtained using PBE+SOC method. Coordinates of the high symmetry points are: Γ = (0, 0, 0), X = (0.5, 0, 0), Y = (0, 0.5, 0), Z = (0, 0, 0.5), S = (0.5, 0.5, 0), T = (0, 0.5, 0.5), U = (0.5, 0, 0.5), and R = (0.5, 0.5, 0.5). The Fermi energy level is set to zero.

The calculated effective masses for holes are 1.33 m_0 and 1.26 m_0 in (4-AMThP)PbI$_4$ and (4-AMPy)PbI$_4$ perovskites, respectively (Table 4.11). Besides, the effective masses of electrons are very high. The (3-AMP)PbI$_4$ shows a direct band gap semiconductor nature with a fundamental band gap at the Γ-point. Our calculated effective masses of the charge carriers near band edges of (3-AMP)PbI$_4$ are 0.8 m_0, 1.03 m_0 for holes and 0.38 m_0, 0.38

m_0 for electrons along Γ to X, Y directions, respectively. Besides, along Γ to Z direction both electron and holes have large masses, the hole mass being 4.83 m_0 and the electron effective mass is too large.

Table 4.11: Effective masses of electrons and holes of the considered 2D halide perovskites.

Perovskites	Direction	m_h	m_e
(3-AMP)PbI$_4$	Γ-X	0.8	0.38
	Γ-Y	1.03	0.38
	Γ-Z	4.83	∞
(3-AMThP)PbI$_4$	Γ-X	1.17	-
	Γ-Y	1.44	-
	Γ-Z	1.88	-
	R-Γ	-	12.60
(3-AMPy)PbI$_4$	Γ-X	1.18	13.89
	Γ-Y	1.17	3.72
	Γ-Z	2.05	20.52
(4-AMP)PbI$_4$	Z-Γ	2.07	8.17
	Z-U	1.87	1.33
(4-AMThP)PbI$_4$	Z-Γ	2.04	15.09
	Z-U	1.33	24.30
(4-AMPy)PbI$_4$	Z-Γ	2.20	45.5
	Z-U	1.26	19.44

Similar downshifting of organic cationic states has been observed in the conduction band of (3-AMThP)PbI$_4$ and (3-AMPy)PbI$_4$. The (3-AMPy)PbI$_4$ is a direct band gap semiconductor with a band gap at the Γ point. The hole effective masses along Γ to X, Y and Z directions are 1.18 m_0, 1.17 m_0 and 2.05 m_0 respectively. Although the hole effective mass at Γ to Z direction is quite smaller in (3-AMPy)PbI$_4$ comparison to that in (3-AMP)PbI$_4$, the electron masses are too large due to the low dielectric nature of the conduction band edges. Surprisingly, (3-AMThP)PbI$_4$ has valence band at Γ point and conduction band at R i.e., shows indirect band gap. In this material, we have observed indirect band gap with the conduction band minima at R point situating 57.2 meV below the conduction band minima at Γ point i.e., the indirect gap lies a few meV below the direct gap. There are several studies on the Rashba splitting phenomenon in $MAPbI_3$ that generates indirect band gap by the splitting of conduction band extrema.*[49-50]* This phenomenon is responsible for the peculiar feature of the $MAPbI_3$ perovskite, possessing both strong absorption and long carrier lifetime. As the indirect band gap generated by Rashba spin splitting lies only few meV below the direct band gap, strong light absorption happens through direct transition whereas excited electrons can rest in the indirect conduction band without recombination. As in (3-AMThP)PbI_4 the indirect band gap at the R point situates only few meV below the direct gap at Γ, it can be expected that there will be a strong absorption at Γ point and then the photo excited electrons can relax at the R point as the recombination will be retarded due to the forbidden indirect transition. Interestingly, there is another lower point at S in conduction band just at 2 meV above the R point there also the electron can relax. This feature directs the possibility of reduced recombination rate of the photo generated electrons and holes and longer lifetime of the excitons. The origin of this behaviour is probably due to the low symmetry structure of (3-AMThP)PbI_4 that results from asymmetric geometry of the spacer cation. However, the conduction band of (3-AMThP)PbI_4 is also flat as it originates from the thiopyrilium cation which has smaller dielectric constant than inorganic lead iodide part of the perovskite. From the flat nature of the conduction band, we can expect generation of low mobility electrons. In comparison, the photogenerated holes will be highly mobile as they lie in inorganic moiety. Masses of the holes are 1.17 m0, 1.44 m0, 1.88 m0, along Γ to X, Y and Z directions respectively whereas the electron effective mass around conduction band edge is too large compared to the effective masses of holes. Therefore, the band characteristics of the sulphur based spacer cations of the perovskite systems can be tuned by the modification in the organic part.

4.4. Conclusions

In conclusion, we have designed new DJ phase perovskite materials with sulphur and oxygen atom containing hetero cyclic ring-based spacer cation. The advantages of the DJ phase perovskites and sulphur atom containing spacer cation intercalations were combined and investigated their thermodynamic, structural as well as electronic properties. We have compared the properties of the proposed materials with two well-known previously experimentally reported DJ phase materials. The calculated results reveal the scope of sulphur and oxygen containing hetero cyclic ring-based spacer cations in DJ phase perovskites. Substitution of nitrogen with sulphur and oxygen abruptly changes the nature of band edge states of these materials. Moreover, the compositions of the valence band and conduction band are completely different in thiopyrylium and pyrylium spacer-based materials compared to pyridinium based ones. In (3-AMThP)PbI_4, (3-AMPy)PbI_4, (4-AMThP)PbI_4 and (4-AMPy)PbI_4 the conduction band is totally composed of the carbon-sulphur and carbon-oxygen components which is still not reported as most of the cases band gap and nature of band edge states are controlled by the metal and halide units. Besides, we have found out that by changing the spacer cation from asymmetric 3-AMP to symmetric 4-AMP, position of the band gap changes from Γ to Z. Moreover, the band gap of (3-AMThP)PbI_4 is indirect in nature which concludes that the substitution of nonmetal atom on the spacer cation can also change the nature of the band structure significantly. The main findings of our work are: (i) the band edges of metal halide perovskites can be dominated by the organic contributions, (ii) in case of spacer cation dominated band edges, Pb-I-Pb bond angle distortion and inorganic layer contact distance may not have the control over the band gap of the material, (iii) optimizing the HOMO and LUMO energies of the organic cations we can regulate the electronic structure and band gap of 2D halide perovskite materials, (iv) among our considered material (3-AMThP)PbI_4 and (4-AMPy)PbI_4 have band gap value as low as 1.93 eV and 1.90 eV. Hence, our study opens up a new area of 2D halide perovskite research where the spacer cations directly contribute to the electronic structure of the material. Following our results, we can utilize the broad availability of organic cations and reach out to the material with optimum properties for the application in photovoltaic devices. In addition, our designed systems are found to be highly efficient for the application in optoelectronic devices.

4.5. References

1. Kojima A., Teshima K., Shirai Y., Miyasaka T. (2009), Organometal Halide Perovskites as Visible-Light Sensitizers for Photovoltaic Cells, J. Am. Chem. Soc., 131, 6050−6051 (DOI: 10.1021/ja809598r)
2. Lee M. M., Teuscher J., Miyasaka T., Murakami T. N., Snaith H. J. (2012), Efficient Hybrid Solar Cells Based on Meso-Superstructured Organometal Halide Perovskites, Science, 338, 643– 647 (DOI: 10.1126/science.1228604)
3. Burschka J., Pellet N., Moon S. J., Humphry-Baker R., Gao P., Nazeeruddin M. K., Grätzel M. (2013), Sequential Deposition as a Route to High-Performance Perovskite-Sensitized Solar Cells, Nature, 499, 316 (DOI: 10.1038/nature12340)
4. Saliba M., Orlandi S., Matsui T., Aghazada S., Cavazzini M., Correa-Baena J. P., Gao P., Scopelliti R., Mosconi E., Dahmen K.-H., De Angelis F., Abate A., Hagfeldt A., Pozzi G., Graetzel M., Nazeeruddin M. K. (2016), A Molecularly Engineered Hole-transporting Material for Efficient Perovskite Solar Cells, Nat. Energy, 1, 15017 (DOI: 10.1038/nenergy.2015.17)
5. Yang W. S., Noh J. H., Jeon N. J., Kim Y. C., Ryu S., Seo J., Seok S. I. (2015), High-Performance Photovoltaic Perovskite Layers Fabricated through intramolecular exchange, Science, 348, 1234– 1237 (DOI: 10.1126/science.aaa9272)
6. Yoshikawa K., Kawasaki H., Yoshida W., Irie T., Konishi K., Nakano K., Uto T., Adachi D., Kanematsu M., Uzu H. (2017), Silicon

Heterojunction Solar Cell with Interdigitated Back Contacts for A Photoconversion Efficiency over 26%, Nat. Energy, 2, 17032 (DOI: 10.1038/nenergy.2017.32)

7. Jena A. K., Kulkarni A., Miyasaka T. (2019), Halide Perovskite Photovoltaics: Background, Status, and Future Prospects, Chem. Rev., 119, 3036– 3103 (DOI: 10.1021/acs.chemrev.8b00539)
8. Frost J. M., Butler K. T., Brivio F., Hendon C. H., Van Schilfgaarde M., Walsh A. (2014), Atomistic Origins of High-Performance in Hybrid Halide Perovskite Solar Cells, Nano Lett., 14, 2584– 2590 (DOI: 10.1021/nl500390f)
9. Zhao Y., Zhu K. (2014), Optical Bleaching of Perovskite $(CH_3NH_3)PbI_3$ Through Room-Temperature Phase Transformation Induced by Ammonia, Chem. Commun., 50, 1605−1607 (DOI: 10.1039/C3CC48522F)
10. Smith I. C., Hoke E. T., Solis-Ibarra D., McGehee M. D., Karunadasa H. I. (2014), A Layered Hybrid Perovskite Solar-Cell Absorber with Enhanced Moisture Stability, Angew. Chem., Int. Ed., 53, 11232– 11235 (DOI: 10.1002/anie.201406466)
11. Stoumpos C. C., Cao D. H., Clark D. J., Young J., Rondinelli J. M., Jang J. I., Hupp J. T., Kanatzidis M. G. (2016), Ruddlesden–Popper Hybrid Lead Iodide Perovskite 2D Homologous Semiconductors, Chem. Mater., 28, 2852– 2867 (DOI: 10.1021/acs.chemmater.6b00847)
12. Quan L. N., Yuan M., Comin R., Voznyy O., Beauregard E. M., Hoogland S., Buin A., Kirmani A. R., Zhao K., Amassian A., Kim D. H., Sargent E. H. (2016), Ligand-Stabilized Reduced-Dimensionality Perovskites, J. Am. Chem. Soc., 138, 2649– 55 (DOI: 10.1021/jacs.5b11740)
13. Katan C., Mercier N., Even J. (2019), Quantum and Dielectric Confinement Effects in Lower-Dimensional Hybrid Perovskite

Semiconductors, Chem. Rev., 119, 3140– 3192 (DOI: 10.1021/acs.chemrev.8b00417)

14. Sapori D., Kepenekian M., Pedesseau L., Katan C., Even J. (2016), Quantum Confinement and Dielectric Profiles of Colloidal Nanoplatelets of Halide Inorganic and Hybrid Organic–Inorganic Perovskites, Nanoscale, 8, 6369– 6378 (DOI: 10.1039/C5NR07175E)
15. Li X., Ke W., Traoré B., Guo P., Hadar I., Kepenekian M., Even J., Katan C., Stoumpos C. C., Schaller R. D., Kanatzidis M. G. (2019), Two-Dimensional Dion-Jacobson Hybrid Lead Iodide Perovskites with Aromatic Diammonium Cations, J. Am. Chem. Soc., 141, 12880– 12890 (DOI: 10.1021/jacs.9b06398)
16. Ghosh D., Acharya D., Pedesseau L., Katan C., Even J., Tretiak S., Neukirch, A. J. (2020), Charge carrier dynamics in two-dimensional hybrid perovskites: Dion–Jacobson vs. Ruddlesden–Popper phases, J. Mater. Chem. A, 8, 22009– 22022 (DOI: 10.1039/D0TA07205B)
17. Umebayashi T., Asai K., Kondo T., Nakao A. (2003), Electronic Structures of Lead Iodide Based Low-Dimensional Crystals, Phys. Rev. B: Condens. Matter Mater. Phys., 67, 155405 (DOI: 10.1103/PhysRevB.67.155405)
18. Gangadharan D. T., Ma D. (2019), Searching for Stability at Lower Dimensions: Current Trends and Future Prospects of Layered Perovskite Solar Cells, Energy Environ. Sci., 12 (10), 2860– 2889 (DOI: 10.1039/C9EE01591D)
19. Ghosh D., Neukirch A. J., Tretiak S. (2020), Optoelectronic Properties of Two-Dimensional Bromide Perovskites: Influences of Spacer Cations, J. Phys. Chem. Lett., 11, 2955– 2964 (DOI: 10.1021/acs.jpclett.0c00594)
20. Mao L., Ke W., Pedesseau L., Wu Y., Katan C., Even J., Wasielewski M. R., Stoumpos C. C., Kanatzidis M. G. (2018), Hybrid Dion-Jacobson 2D Lead Iodide Perovskites, J. Am. Chem. Soc., 140, 3775– 3783 (DOI: 10.1021/jacs.8b00542)

21. Lai H., Kan B., Liu T., Zheng N., Xie Z., Zhou T., Wan X., Zhang X., Liu Y., Chen Y. (2018), Two-Dimensional Ruddlesden-Popper Perovskite with Nanorod-like Morphology for Solar Cells with Efficiency Exceeding 15%, J. Am. Chem. Soc., 140, 11639–11646 (DOI: 10.1021/jacs.8b04604)
22. Lu D., Lv G., Xu Z., Dong Y., Ji X., Liu Y. (2020), Thiophene-Based Two-Dimensional Dion-Jacobson Perovskite Solar Cells with over 15% Efficiency, J. Am. Chem. Soc., 142, 11114– 1112 (DOI: 10.1021/jacs.0c03363)
23. Giannozzi P., Baroni S., Bonini N., Calandra M., Car R., Cavazzoni C., Ceresoli, D., Chiarotti G. L., Cococcioni M., Dabo I., Dal Corso A., de Gironcoli S., Fabris S., Fratesi G., Gebauer R., Gerstmann U., Gougoussis C., Kokalj A., Lazzeri M., Martin-Samos L., Marzari N., Mauri F., Mazzarello R., Paolini S., Pasquarello A., Paulatto L., Sbraccia C., Scandolo S., Sclauzero G., Seitsonen A. P., Smogunov A., Umari P., Wentzcovitch R. M. (2009), Quantum Espresso: a modular and open-source software project for quantum simulations of materials, J. Phys.: Condens. Matter, 21, 395502 (DOI: 10.1088/0953-8984/21/39/395502)
24. Perdew J. P., Burke K., Ernzerhof M. (1996), Generalized Gradient Approximation Made Simple, Phys. Rev. Lett., 77, 3865– 3868 (DOI: 10.1103/PhysRevLett.77.3865)
25. Vanderbilt D. (1990), Soft self-consistent pseudopotentials in a generalized eigenvalue formalism, Phys. Rev. B: Condens. Matter Mater. Phys., 41 (11), 7892– 7895 (DOI: 10.1103/PhysRevB.41.7892)
26. Grimme S., Antony J., Ehrlich S., Krieg H. (2010), A Consistent And Accurate Ab Initio Parametrization Of Density Functional Dispersion Correction (DFT-D) For The 94 Elements H-Pu, J. Chem. Phys., 132, 154104 (DOI: 10.1063/1.3382344)

27. Monkhorst H. J., Pack J. D. (1976), Special points for Brillouin-zone integrations, Phys. Rev. B, 13 (12), 5188– 5192 (DOI: 10.1103/PhysRevB.13.5188)
28. Marchal N., Mosconi E., García-Espejo G., Almutairi T. M., Quarti C., Beljonne D., De Angelis F. (2021), Cation Engineering for Resonant Energy Level Alignment in Two-Dimensional Lead Halide Perovskites, J. Phys. Chem. Lett., 12, 2528– 2535 (DOI: 10.1021/acs.jpclett.0c03843)
29. Heyd J., Scuseria G. E., Ernzerhof M. (2003), Hybrid functionals based on a screened Coulomb potential, J. Chem. Phys., 118, 8207– 8215 (DOI: 10.1063/1.1564060)
30. Du M.H. (2015), Density Functional Calculations of Native Defects in $CH_3NH_3PbI_3$: Effects of Spin-Orbit Coupling and Self-Interaction Error, J. Phys. Chem. Lett., 1461– 1466 (DOI: 10.1021/acs.jpclett.5b00199)
31. Mahata A., Mosconi E., Meggiolaro D., De Angelis F. (2020), Modulating Band Alignment in Mixed Dimensionality 3d/2d Perovskites by Surface Termination Ligand Engineering, Chem. Mater., 32, 105– 113 (DOI: 10.1021/acs.chemmater.9b02560)
32. Ashcroft, N. W., Mermin, N. D., (1976) Solid State Physics, Holt: New York
33. Blochl P. E. (1994), Projector augmented-wave method, Phys. Rev. B, 50 (24), 17953– 17979 (DOI: 10.1103/PhysRevB.50.17953)
34. Kresse G., Joubert D. (1999), From Ultrasoft Pseudopotentials to the Projector Augmented Wave Method, Phys. Rev. B: Condens. Matter Mater. Phys., 59, 1758– 1775 (DOI: 10.1103/PhysRevB.59.1758)
35. Kresse G., Hafner J. (1993), Ab initio molecular dynamics for liquid metals, Phys. Rev. B: Condens. Matter Mater. Phys., 47, 558 (DOI: 10.1103/PhysRevB.47.558.)
36. Kresse G., Hafner J. (1994), Ab Initio Molecular-Dynamics Simulation of the Liquid-Metal–Amorphous-Semiconductor Transition in

Germanium, Phys. Rev. B: Condens. Matter Mater. Phys., 49, 14251– 14271 (DOI: 10.1103/PhysRevB.49.14251)

37. Kresse G., Furthmüller J. (1996), Efficiency of ab-initio total energy calculations for metals and semiconductors using a plane-wave basis set, Comput. Mater. Sci., 6, 15-50 (DOI: 10.1016/0927-0256(96)00008-0)
38. Kresse G., Furthmüller J. (1996), Efficient Iterative Schemes for ab initio Total-Energy Calculations Using a Plane-wave Basis Set, Phys. Rev. B: Condens. Matter Mater. Phys., 54, 11169– 11186 (DOI: 10.1103/PhysRevB.54.11169-11186)
39. Nosé S. (1984), A Unified Formulation of the Constant Temperature Molecular Dynamics Methods, J. Chem. Phys., 81, 511– 519 (DOI: 10.1063/1.447334)
40. Frisch M. J., Trucks G. W., Schlegel H. B., Scuseria G. E., Robb M. A., Cheeseman J. R., Scalmani G., Barone V., Mennucci B., Petersson G. A., Nakatsuji H., Caricato M., Li X., Hratchian H. P., Izmaylov A. F., Bloino J., Zheng G., Sonnenberg J. L., Hada M., Ehara M., Toyota K., Fukuda R., Hasegawa J., Ishida M., Nakajima T., Honda Y., Kitao O., Nakai H., Vreven T., Montgomery J. A., Peralta, Jr. J. E., Ogliaro F., Bearpark M., Heyd J. J., Brothers E., Kudin K. N., Staroverov V. N., Keith T., Kobayashi R., Normand J., Raghavachari K., Rendell A., Burant J. C., Iyengar S. S., Tomasi J., Cossi M., Rega N., Millam J. M., Klene M., Knox J. E., Cross J. B., Bakken V., Adamo C., Jaramillo J., Gomperts R., Stratmann R. E., Yazyev O., Austin A. J., Cammi R., Pomelli C., Ochterski J. W., Martin R. L., Morokuma K., Zakrzewski V. G., Voth G. A., Salvador P., Dannenberg J. J., Dapprich S., Daniels A. D., Farkas O., Foresman J. B., Ortiz J. V., Cioslowski J., Fox D. J. (2009), Gaussian 09, Revision B.01; Gaussian Inc.: Wallingford, CT.
41. Hehre W. J., Ditchfield R., Pople J. A. (1972), Self-consistent molecular orbital methods. XII. Further extensions of Gaussian-type basis sets for

use in molecular orbital studies of organic molecules, J. Chem. Phys., 56, 2257– 2261 (DOI: 10.1063/1.1677527)

42. Hariharan P. C., Pople, J. A. (1973), The influence of polarization functions on molecular orbital hydrogenation energies, Theor. Chim. Acta, 28, 213– 222 (DOI: 10.1007/BF00533485)
43. Krishnan R., Binkley J. S., Seeger, R., Pople J. A. (1980), Self-consistent molecular orbital methods. XX. A basis set for correlated wave functions, J. Chem. Phys., 72, 650– 654 (DOI: 10.1063/1.438955)
44. Becke A. D. (1988), Density-functional exchange-energy approximation with correct asymptotic behavior, Phys. Rev. A: At., Mol., Opt. Phys., 38, 3098– 3100 (DOI: 10.1103/PhysRevA.38.3098)
45. Becke A. D. (1993), Density-Functional Thermochemistry. Iii. The Role of Exact Exchange, J. Chem. Phys., 98, 5648– 5652 (DOI: 10.1063/1.464913)
46. Beck A. D. (1997), Density-functional thermochemistry. V. Systematic optimization of exchange-correlation functionals, J. Chem. Phys., 107, 8554– 8560 (DOI: 10.1063/1.475007)
47. Becke A. D. (1993), Density-Functional Thermochemistry. Iii. The Role of Exact Exchange, J. Chem. Phys., 98, 5648– 5646 (DOI: 10.1063/1.464913)
48. Lee C., Yang W., Parr R. G. (1988), Development of the Colle-Salvetti Correlation-Energy Formula into a Functional of the Electron Density, Phys. Rev. B: Condens. Matter Mater. Phys., 37, 785– 789 (DOI: 10.1103/PhysRevB.37.785)
49. Wang T., Daiber B., Frost J. M., Mann S. A., Garnett E. C., Walsh A., Ehrler B. (2017), Indirect to Direct Bandgap Transition in Methylammonium Lead Halide Perovskite, Energy Environ. Sci., 10, 509– 515 (DOI: 10.1039/C6EE03474H)
50. Azarhoosh P., McKechnie S., Frost J. M., Walsh A., Van Schilfgaarde M. (2016), Research Update: Relativistic Origin of Slow Electron-Hole

Recombination in Hybrid Halide Perovskite Solar Cells, APL Mater., 4, 091501 (DOI: 10.1063/1.4955028)

Chapter 5

Optimizing Alignment of Energy Levels between Organic and Inorganic Layers of 2D Hybrid Perovskites

5.1. Introduction

Recently, reduced dimensional perovskites have gained huge interest in the optoelectronic material research due to their impressive stability in operational condition.*[1-3]* These materials are the example of natural multiple quantum wells (MQW), where inorganic layers act as wells and organic cation layers act as barriers.*[4-5]* Among various reduced dimensional perovskites, the Ruddlesden Popper (RP) phase systems are in the front line of the study, that has a chemical formula of $A_2A'_{n-1}M_nX_{3n+1}$ where A and A′ are the spacer cation and cage cation respectively, M is metal, X is halide, and n is the thickness of the MQW that determines the extent of quantum and dielectric confinement along with the optical property of the material. The RP perovskite systems are versatile towards optoelectronic properties through their chemical and quantum mechanical degrees of freedom. Moreover, these materials are used to develop colourful LED, efficient solar cell, and spintronic devices.*[6-11]* But for perfect utilization of these 2D perovskite materials on a particular optoelectronic device, they demand specific electronic as well as optical property based on the requirements of that device.

Efficient optoelectronic material can be realized through organic spacer modulation by targeting specific properties from a molecular perspective.*[12]* With the ease of getting wide-ranging of organic cations and utilising their orbital energies to tune the energy levels of the perovskite material can lead us towards a selective property of our need. Hence, finding out the best material requires a high throughput understanding of the electronic structure and properties at the molecular level. One of the important requirements to make an efficient optoelectronic device is the alignment of the energy levels between organic and inorganic moieties of the hybrid perovskite material.*[13-15]* The results of the work of Stupp and co-workers*[16]* have suggested the great potential for functional improvement by using polynuclear rings containing ammonium cation and showcasing improved optoelectronic properties as an outcome of better match between organic and inorganic energy levels. Yang and co-workers*[17]* have also reported the presence of conjugated cationic states on the near edge states of the perovskite material.

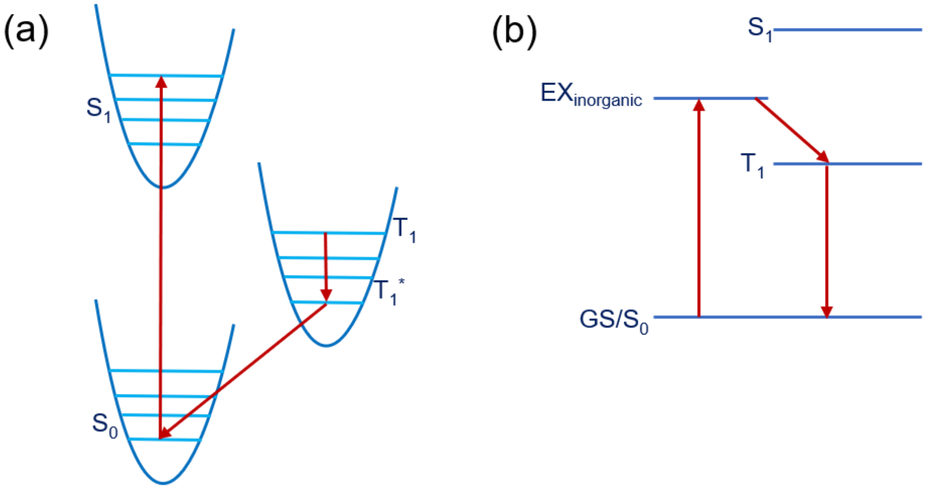

Figure 5.1: (a) A schematic illustration of the energy levels of an organic molecule. The S_0 and S_1 represents the singlet ground state and the first singlet excited state energy level, respectively. The T_1 and T_1^* represent the triplet state and relaxed triplet state energy level, respectively. (b) Possible inorganic to organic energy transfer mechanism, where $EX_{inorganic}$ represents the excitonic band of the inorganic unit.

Therefore, the electronic energy levels of the inorganic metal halide and organic moieties can be selectively aligned by applying several criteria on the organic cation such as extent of conjugation and effect of substitution. On the basis of the variation principle of the inorganic metal halide and organic cation electronic structures, 2D hybrid perovskite research community can find a proper direction. In this context, transfer of the excitonic energy from the inorganic metal halide unit to the lowest triplet states of the organic spacer is one of the main focuses over the past few years. In particular, the strong spin orbit coupling in inorganic perovskite results weakly bound Wannier-Mott excitons. Kandada and co-workers*[18]* have described the excitons in 2D perovskite quantum-well-like structures by a Wannier model. In contrast, the organic cations have strongly bound Frenkel excitons. Kunugita and co-workers*[19]* have observed the efficient energy transfer from Wannier excitons to the triplet state of naphthalene molecules in 2D perovskites. If the triplet state of the organic part of the optoelectronic material lies below the exciton level of inorganic perovskite (metal halide unit) i.e., it can induce an energy transfer from the inorganic to the organic triplet state (T_1) and a final phosphorescence emission from T_1^* to S_0.*[20]* The schematic diagram of the excited states of an organic molecule has been shown in Figure 5.1.

In a recent work, Wu and co-workers*[21]* demonstrated highly efficient solar cell based on their designed spacer cation 3-phenyl-2-propenammonium (PPA) which possess multifunctional properties. Along with the extra double bond induced extended conjugation, there are several more hydrogen atoms that cause notable H-contact with the inorganic layers. This feature resulted impressive performance of the solar cell devices composed of PPA spacer cation and PbI_4 as inorganic unit. However, the particular contribution of the PPA molecule on the electronic structure and properties of PPA based 2D hybrid perovskites are still remain unexplored. In addition, such conjugated spacer molecules have high potential to be utilised for preferred alignment of excited energy levels in inorganic and organic layers. Hence, the proper understanding about the alignment of the energy levels between inorganic and organic units of the material is highly desired for the typical application in optoelectronic devices. Neukirch and co-workers*[22]* have shown in their work that the energy level alignment between perovskite layer and spacer cations can be modulated through extended conjugation. However, they have not considered the conjugation extended to the close vicinity of the primary ammonium group. To distinguish the influence of the conjugated unit attached to the primary ammonium group we have taken PPA cation as our prime unit and played with the functional groups. And finally, we have analysed the functional group influence on the energy level alignment of PPA spacer cation-based perovskites.

Here, we have used density functional theory (DFT) to obtain the excitation energy levels of a set of organic cations. At first, we have studied the electronic properties of the two 2D hybrid perovskite materials containing PPA cation as spacer with molecular formula, $(PPA)_2PbI_4$ with n=1 and $(PPA)_2(MA)_{0.5}(FA)_{0.5}Pb_2I_7$ with n=2. Here, PPA is the spacer cation labelled as A while MA and FA are cage cations labelled as A′ in the general formula of $A_2A'_{n-1}M_nX_{3n+1}$. Where, MA and FA are the abbreviated forms of the methylammonium and formamidinium cations respectively. Then tried to explore the importance of conjugation in the spacer cation of 2D hybrid perovskite and how the conjugation can control the alignment of excited state energy levels between inorganic and organic layers. We have started with PPA and then checked the contribution of a set of functional groups ranging from electron withdrawing to electron donating. Also, we have taken into consideration the functional groups with extended conjugation. To identify the perfect match between inorganic metal halide unit and organic spacer we have calculated the lowest triplet excitation energies of the organic spacers. Moreover, the nature of the excitations at dynamic conditions have been investigated using the ab initio molecular dynamics (AIMD) simulation. Singlet and triplet excitation energies calculated in gas phase geometries give similar results to that obtained under the dynamic conditions. Finally, we have tried to match the considered organic cations with known perovskite exciton levels to predict the different type of energy level alignments.

5.2. Methods

For the geometry optimization and electronic structure calculation of the 2D hybrid perovskite materials we have used the Quantum Espresso (QE)*[23]* program package. Here we have adapted the GGA-PBE*[24]* exchange correlation functional for the geometry relaxation and considered scalar relativistic ultrasoft pseudopotentials*[25]* including electrons from 2s, 2p orbital for O, N, and C; 1s orbital for H; 5s, 5p orbital for I; and 6s, 6p, 5d orbital for Pb explicitly. A plane wave basis set cutoff of 50 and 400 Ry for the wave functions and augmented density have been used respectively. The perovskite systems ions as well as cell parameters were allowed to relax for all the calculations. Also, Monkhorst pack*[26]* k-point sampling of 4×4×1 was implemented with the DFT-D3 dispersion correction as formulated by Grimme*[27]* for the relaxation of all the systems. For more accurate prediction of the electronic structure of the material we used the HSE06*[28]* hybrid functional with 43%*[29]* Hatree-Fock exchange using the GGA-PBE optimized geometry. In addition, spin orbit coupling (SOC) was also considered for the electronic structure calculations using the HSE06 considering the sensitivity of higher elements towards relativistic effect. A plane wave basis set cutoff of 40 Ry for the smooth part of the wave functions and a Fock energy cutoff of 80 Ry was set during HSE06+SOC calculations along with a Monkhorst pack k-point sampling of 2×2×1. Also, we have taken norm-conserving pseudopotentials with electrons from I 5s, 5p; O, N, C 2s, 2p; H 1s; Pb 5s, 5p, 6s, 6p, 5d shells explicitly for the HSE06+SOC calculations. These methodologies are reported to give good results for such systems.*[30]*

Ab initio molecular dynamics simulations were done within the DFT framework as implemented in the Vienna ab initio simulation package (VASP).*[31-36]* The projector augmented-wave (PAW) method was used to describe the electron–core interaction within a plane-wave basis set of kinetic energy cutoff 500 eV and GGA-PBE functional.*[24]* A Γ-centered k-point grid of 4×4×1 was used to sample the Brillouin zone. The MD simulations were carried out using canonical ensemble at 300 K temperature controlled by a Nosé−Hoover thermostat in a 10 ps trajectory with 1 fs timestep.*[37]*

For the excitation energy levels calculations of the organic molecules, the Gaussian 09 D.01*[38]* suite of programme has been employed. The Pople basis set 6-311++G***[39-41]* and Becke 3-parameter Lee–Yang–Parr (B3LYP)*[42-46]* hybrid functional has been applied for the calculations. We have used the ΔSCF approach to calculate triplet excitations owing to its good predictive power for the S_0 geometry triplet and T_1^* geometry triplet energies.*[47]* Whereas, lowest energy singlet excitations are calculated using TDDFT*[48]* due to its reliability to predict singlet excitation energies in organic molecules for charge transfer and optical excitations.

5.3. Result and Discussion

5.3.1. 2D Hybrid Perovskites with PPA Spacer Cation

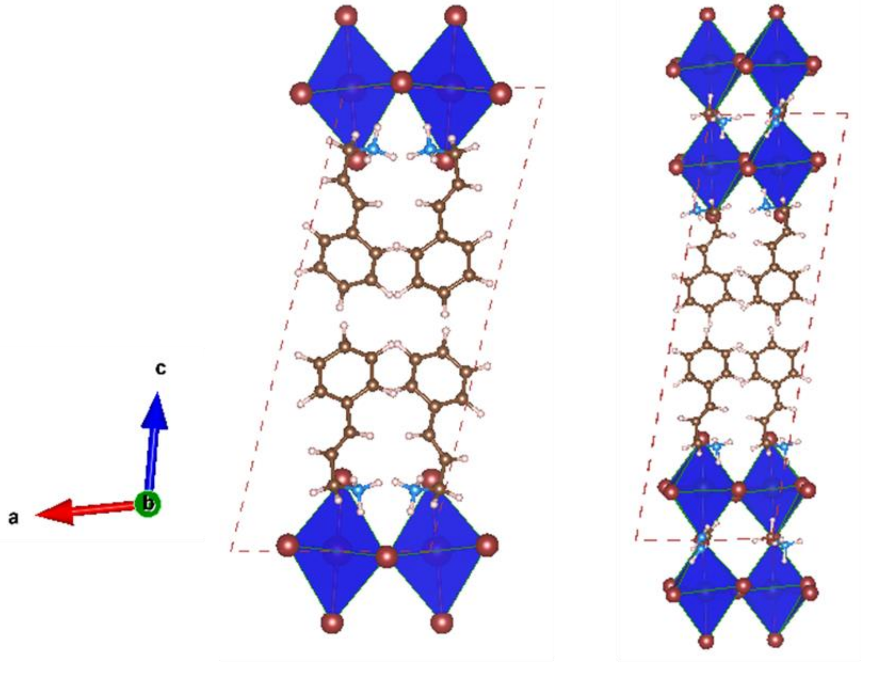

$(PPA)_2PbI_4$ $(PPA)_2(MA_{0.5}FA_{0.5})Pb_2I_7$

Figure 5.2: Optimised geometries of the considered 2D perovskites. Colours: hydrogen (white), carbon (brown), nitrogen (blue), iodine (wine) and lead (grey).

At first, we have discussed about the geometries and properties of PPA spacer cation based 2D lead halide perovskites (n=1-2). In the beginning we have studied $(PPA)_2(MA)_{0.5}(FA)_{0.5}Pb_2I_7$ which is a n=2 category 2D perovskite system. We have performed the geometry relaxation of this material starting from the experimentally reported crystal structure by Wu and co-workers.*[21]* Subsequently we have designed $(PPA)_2PbI_4$ computationally and performed the first principles calculations. Figure 5.2 displays the optimized structures of the considered two perovskites.

After performing the geometry optimization at the GGA-PBE level of theory we have performed single point calculations using the HSE06+SOC method to obtain more accurate band gap values. The HSE06+SOC calculated band gaps of $(PPA)_2PbI_4$ and $(PPA)_2(MA)_{0.5}(FA)_{0.5}Pb_2I_7$ are 2.26 and 1.99 eV, respectively. $(PPA)_2PbI_4$ is a pure 2D perovskite whereas $(PPA)_2(MA)_{0.5}(FA)_{0.5}Pb_2I_7$ is a quasi 2D perovskite possessing two metal halide layers in between the organic spacer layers. This imposes 3D contribution to the quasi 2D perovskite system. As a result of this 3D contribution, n=2 system possesses much lower band gap compared to the n=1 one. Despite of having larger spacer cation that forces to have larger inorganic layer distance, the band gap in $(PPA)_2PbI_4$ is smaller compared to other similar 2D hybrid perovskites such as $(PEA)_2PbI_4$, $(BA)_2PbI_4$ (~2.4 eV) calculated at same level of theory.*[49]* From this observation, we can infer the importance of conjugation in the spacer cation on the band gap of a 2D hybrid perovskite. Additionally, $(PPA)_2PbI_4$ have potential for application in optoelectronic devices. We have further continued our study extracting density of states of the materials to obtain the specific contributions from the elements to the electronic states of the material (Figure 5.3).

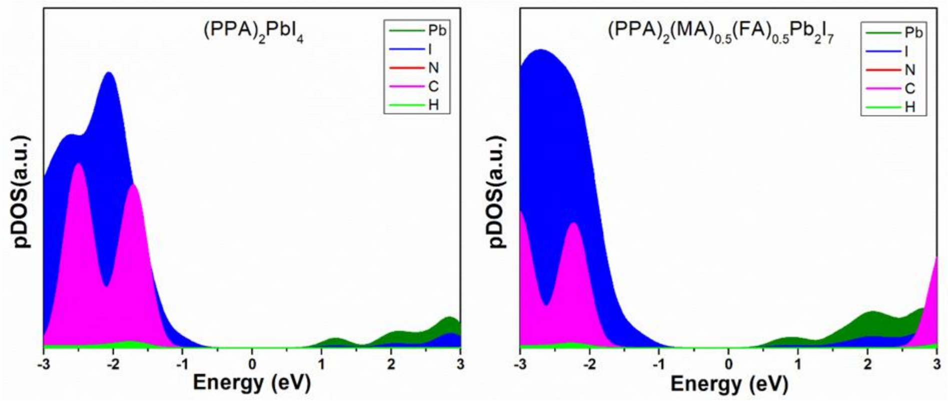

Figure 5.3: Projected density of states plots of the 2D perovskites

There is a noticeable contribution of the carbon components close to the edge of the valence band in $(PPA)_2PbI_4$ compared to that in the $(PPA)_2(MA)_{0.5}(FA)_{0.5}Pb_2I_7$. In the case of $(PPA)_2(MA)_{0.5}(FA)_{0.5}Pb_2I_7$, the small cage cations MA and FA are also present. Along with PPA, MA and FA have contributions to the organic components in the pDOS plot of $(PPA)_2(MA)_{0.5}(FA)_{0.5}Pb_2I_7$ perovskite. However, it is worth mentioning that in the $(PPA)_2PbI_4$ perovskite, there are no cage cations present, unlike in the $(PPA)_2(MA)_{0.5}(FA)_{0.5}Pb_2I_7$ perovskite. As a result, the contribution from the PPA spacer cation alone in the valence band edge of the $(PPA)_2(MA)_{0.5}(FA)_{0.5}Pb_2I_7$ is little less than that in the $(PPA)_2PbI_4$. For this reason, the carbon components in $(PPA)_2PbI_4$ are closer to the band edges in comparison to that in $(PPA)_2(MA)_{0.5}(FA)_{0.5}Pb_2I_7$. Apart from this, the carbon components in $(PPA)_2PbI_4$ contributes more significantly to the valence band edge with respect to $(PEA)_2PbI_4$.*[49]* Although the PPA spacer cation is slightly larger in size than PEA, it has one extra conjugated π-bond that is placing it more close to the valence band edge of the material. Hence, the position of the cationic states on the perovskite material electronic structure gives a clear idea about the influence of conjugation on the electronic structure that can be utilised for different application purpose. Although finding out the best choice of material for an optoelectronic device is difficult by studying different large perovskite system, we can get an idea of their electronic property only through exploring the excited state energy levels of organic spacer molecules.

5.3.2. Functionalization of PPA

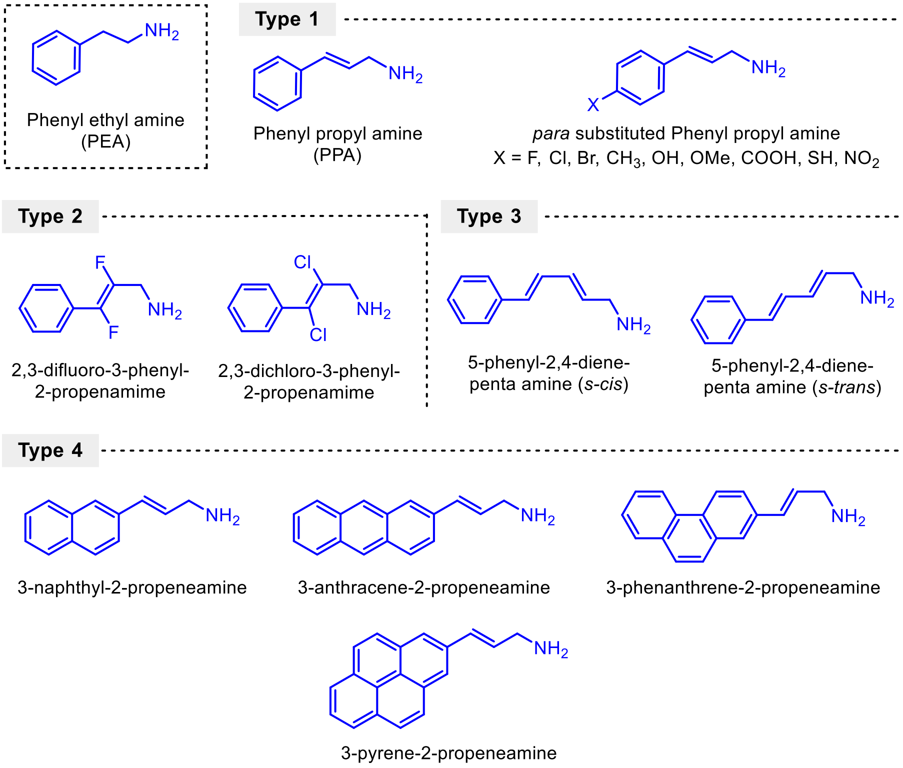

Figure 5.4: Molecular geometries of the organic spacers considered in this work

Analysing the density of states plots of the PPA based perovskites we enthused to study further about the properties of the organic cation. We have first studied excitation energy levels of the PPA molecule and checked the alignment of these excited states with the perovskite exciton levels. Following this, we have studied excited states of various molecules with functionalising PPA molecule in different aspects. Motivating from various experimental reports where people have used differently functionalised organic molecules as spacer cations in 2D perovskites, we have considered a set of amines for our work. Substituent groups have been added in para position of the phenyl ring in the PPA molecule ranging from electron donating to electron withdrawing nature along with the increase in extended conjugation. In Figure 5.4 we have illustrated the structures of the considered spacer molecules to obtain the excitation energy levels of a set of organic cations.

There are several reports of 2D perovskites with para substituted spacer cations.*[50-51]* We have classified our considered cations into four types. In the first type (type I), we have varied substituent group on the para position of the phenyl ring in PPA cation from electron withdrawing to electron donating in nature. Several electron donating/withdrawing based groups like halogen (-I, +R), CH_3 (+I), SH (+R), OH, OMe (-I, +R), COOH and NO_2 (-R) have been substituted at para position. There are easy synthetic methodologies to synthesise such para-substituted phenyl propyl amines.*[52]* In the case of type-II, we have checked the effects of electron withdrawing functionality through F/Cl substitutions on the C-C π bond of the propyl amine tail. In the next class (type-III), we have considered extended conjugation though one extra C-C π bond to propyl amine tail in the cis and trans configuration. Particularly, we have considered s-cis and s-trans isomer of 5-phenyl-2,4-diene-pentaamine. These amines can be synthesized using methodologies reported by Taylor and co-workers.*[53]* There were some reports of polynuclear ring ammonium-based 2D hybrid perovskites (n=1) where they have identified significant contribution from the organic spacers to the band edges of the perovskite material.*[16]* So, in the fourth type the phenyl ring was replaced by polynuclear rings.

For theoretical support of our calculated findings, we have compared the results reported by Neukirch and co-workers*[22]* for phenyl ethyl amine (PEA) and observed good agreement with their report. For phenyl ethyl amine (PEA), we have found the T_1 value as 4.38 eV (Table 5.1) whereas they have reported it as 4.43 eV. Similarly, T_1^* for phenyl ethyl amine were 3.73 eV and 3.77 eV as our calculated and their reported one respectively.

Table 5.1: Triplet and Singlet energy levels calculated on vacuum relaxed geometries. All energies are in eV. Previous theoretical reports are given in the parenthesis.

Amines	**T_1**	**T_1^***	**$S_0 \rightarrow S_1$**
Phenyl ethyl amine (PEA)	4.38 (4.43[21])	3.73 (3.77[21])	5.27 (5.43[21])
3-phenyl-2-propenamime (PPA)	3.28	2.68	4.68
4F-PPA	3.28	2.68	4.57
4Cl-PPA	3.20	2.63	4.51
4Br-PPA	3.19	2.62	4.47
4OH-PPA	3.20	2.64	4.41
4SH-PPA	3.06	2.54	4.23
$4CH_3$-PPA	3.24	2.32	4.60
$4OCH_3$-PPA	3.10	2.33	4.29
4COOH-PPA	3.02	2.52	4.30
$4NO_2$-PPA	2.88	2.42	3.73
2,4,6-NO_2-PPA	3.03	0.99	2.96
2,3-difluoro-3-phenyl-2-propenamime	3.23	2.12	4.67
2,3-dichloro-3-phenyl-2-propenamime	3.74	1.82	4.63
5-phenyl-2,4-diene-pentaamine(s-cis)	2.55	1.83	3.93
5-phenyl-2,4-pentadieneamine(s-trans)	2.58	2.02	4.08
3-naphthyl-2-propeneamine	2.93	2.52	4.00
3-anthracene-2-propeneamine	2.10	1.80	3.13
3-phenanthrene-2-propeneamine	3.05	2.53	3.70
3-pyrene-2-propeneamine	2.26	1.89	3.38

The triplet and singlet energy levels of PPA is quite interesting. Both the triplet and singlet energies decrease significantly in comparison to the PEA. The T_1 energy decreases from 4.38 eV in PEA to 3.28 eV in PPA (Table 5.1). Also, the T_1^* and S_1 energies decrease in PPA in comparison to PEA. Whereas varying substituent groups at para position of PPA didn't deliver any considerable change to the excitation energies. Rather, we have observed that irrespective of electron donating or withdrawing effect the main controlling factor is conjugation in the first type of cations as the increase in conjugation decreases triplet and singlet energies (Table 5.1). Among substituted cases the para nitro substitution gives the lowest T_1 energy (2.88 eV). Being curious we have added nitro group substitution on three positions (two ortho and one para). However, that increases the triplet energy to 3.03 eV (Table 5.1) with respect to one nitro substituted case (2.88 eV). This can be due to the hampering of the extended conjugation in presence of three nitro groups. However, the relaxed triplet energy (T_1^*) decreases noticeably. In the next type (type II) the addition of F atom on trans configuration of propyl double bond didn't change the excited energy levels significantly but addition of Cl in a similar manner increases the T_1 and decreases the T_1^* (Table 5.1). This could be due to the cancellation of -I effect from the two F atom at trans position in 2,3-difluoro-3-phenyl-2-propenamime. Whereas, in case of Cl substituent the large size of Cl and +R effect might be responsible for the increase in the energy of the triplet state. We observed that these substitutions couldn't help to improve the conjugation and lower the triplet energies. Hence, in the third type rather than further substitution we have tried to increase conjugation through increasing number of π bonds. And interestingly both the s-cis and s-trans conformation of 5-phenyl-2,4-diene-pentaamine significantly decrease triplet energies (Table 5.1). This happened due to the extension in the conjugation that stabilises the molecular orbitals. In our last class of cations (fourth) we have considered polynuclear rings (Table 5.1). We observed that in case of 3-naphthyl-2-propeneamine, the excited energy levels decrease in comparison to PPA whereas the triplet and singlet energies decrease noticeably for anthracene and phenanthrene based cations in 3-anthracene-2-propeneamine and 3-phenanthrene-2-propeneamine, respectively. But in 3-phenanthrene-2-propeneamine T_1 energy is larger even in comparison to 3-naphthyl-2-propeneamine. This is due to the antiaromaticity (NICS value 40.18) in the triplet state of 3-phenanthrene-2-propeneamine compared to the 3-naphthyl-2-propeneamine (NICS value 8.37). Much smaller triplet and singlet energies also observed in 3-pyrene-2-propeneamine. The lowest triplet energy value observed in 3-anthracene-2-propeneamine.

To verify the excitation energies at dynamic conditions we have performed AIMD simulations. We have taken two phases i.e., n=1 and n=2 of PPA based perovskites for the molecular dynamics simulation. After performing the simulation, we have calculated the T_1 energies of the cations. Our calculated T_1 energies demonstrated broadening of the excitation energies of the cations in presence of the perovskite environment.

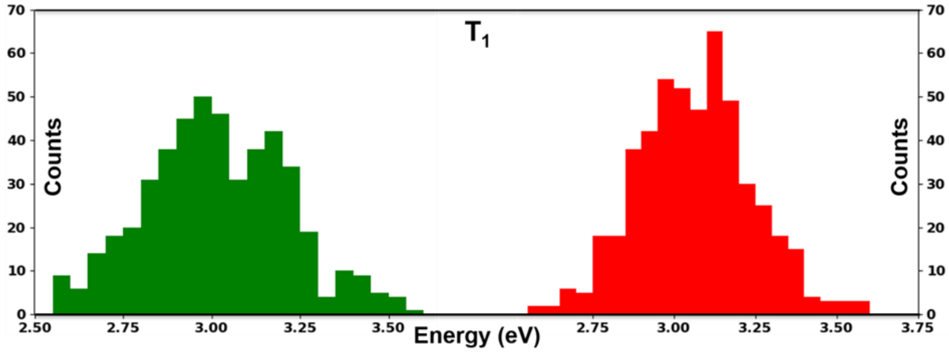

Figure 5.5: Histograms of T_1 energies obtained from post MD molecular geometries (n=1 green and n=2 red).

The broadening of the excitation energies of the organic molecules is due to the occurrence of thermal fluctuations in the perovskite environment. The bond angles as well as C-C, C-N and C-H bond lengths of the PPA molecule fluctuates randomly in the post equilibrium geometries due to the continuous heating and cooling processes during the simulation. In Figure 5.5 we have presented histograms of the T_1 excitation energies of organic molecular geometries obtained throughout the molecular dynamics simulations. We have extracted the geometries of the cations from the perovskite structures of the simulation cell and calculated the T_1 excitation energies. Notably, the PPA cation experience nearly similar broadening for both n=1 and n=2 phase of perovskites. The average values (3.0 - 3.2 eV) of the excitation energies of the molecular geometries obtained across the simulation cell are smaller than that of the isolated molecule (3.28 eV). This is a clear consequence of the fluctuations in the bond angle and bond lengths experienced in the post equilibrium geometries. Although the broadening of excitation energies is the evidence of the importance of finite temperature dynamics, the average value of the T_1 energy (3.1 eV) is close to the T_1 energy (3.28 eV) obtained from the relaxed geometries. So, we have used the excitation energies obtained from the relaxed geometries of the molecules to align the energy levels of organic cations with the perovskites.

5.3.3. Energy Level Alignment

In the inorganic layer of the perovskite the excitons are weakly bound Wannier−Mott excitons. Due to strong spin orbit coupling and highly dielectric nature of the metal halide layer the singlet and triplet excitonic levels are difficult to differentiate. Here we have considered the lowest excitonic energy from reference*[54-55]* as the perovskite exciton level. Whereas the low dielectric organic cations result strongly bound Frenkel excitons. Proper alignment of the perovskite exciton level with the triplet energy level of the organic cation can induce an energy transfer from the perovskite to the organic triplet and this energy can further radiatively transfer relaxing the molecule to the singlet state. This radiative energy transfer from triplet to singlet state of the organic cation can be utilised in different devices. By aligning the perovskite exciton level and calculated T1 energy we have predicted some preferred combinations of perovskite and organic spacer cation. In Table 5.2 we have listed the spacer cations connecting to the particular perovskite by which they are expected to form a material with the property of resonance energy transfer.

Table 5.2: Preferred combination of perovskite with the organic spacers predicted from our work. All energies are in eV. The reference numbers are given in the parenthesis.

Perovskite system	**Lowest exciton energy level (E_x) (From reference)**	**Expected preferred combination**
Pb_2I_7	2.15 [54]	3-anthracene-2-propeneamine (2.10)
PbI_4	2.50 [54]	3-pyrene-2-propenamime (2.26)
$PbBr_4$	3.20 [55]	4Cl-PPA (3.20) 4OH-PPA (3.20) 4Br-PPA (3.19) $4OCH_3$-PPA (3.10) 4SH-PPA (3.06) 3-phenanthrene-2-propeneamine (3.05) 2,4,6-NO_2-PPA (3.03) 4COOH-PPA (3.02) 3-naphthyl-2-propeneamine (2.93) $4NO_2$-PPA (2.88)
$PbCl_4$	3.70 [55]	-

We have started with n=2 Pb_2I_7 perovskite layer which has a lowest exciton energy level at 2.15 eV.*[54]* Among our considered ammonium cations only one spacer molecule is found to be appropriate for the preferred combination with this inorganic layer. For the energy transfer from this inorganic layer the best choice from our set of cations is the 3-anthracene-2-propeneamine that has a T_1 excitation level at 2.10 eV. This molecule has a low energy triplet state at 1.80 eV where the molecule can relax after the energy transfer from perovskite inorganic layer to T_1 and then further radiate emitting red light. The next inorganic layer we have listed in table is the n=1, I based PbI_4. In this case also we have got one spacer among our considered set of cations. The 3-pyrene-2-propenamime has a T_1 energy level at 2.26 eV can be a good combination with PbI_4 inorganic layer with an exciton energy level at 2.50 eV.*[54]* The excitonic energy can be transferred to the T_1(2.26 eV) state and then before radiative process the molecule can relax at T_1^* level of 1.89 eV. From the perovskite material of this combination, we can get red light.

Next inorganic perovskite candidate is Br based $PbBr_4$ with perovskite excitonic level at 3.20 eV.55 A total of ten spacer molecules screened out to offer the possibility of energy transfer from the perovskite exciton level to the high energy triplet level of the organic molecule. Among the ten spacers the Cl, Br, OH substitution at para position can emit at blue region. SH, COOH substitution at para position and NO_2 substitution at 2,4,6 position of the PPA molecule and 3-naphthyl-2-propeneamine are eligible for blue/cyan light emission. Whereas, OCH_3 and NO_2 substitution at para position of the PPA molecule are potential candidates for green light emission. Another candidate to have a choice with $PbBr_4$ is 3-phenanthrene-2-propeneamine that have a T_1 at 3.05 and T_1^* at 0.99 eV, a promising candidate for the emission in the IR region. But we didn’t find any preferred match from our selected spacer candidates for another halide Cl based $PbCl_4$ inorganic layer.

Although some of our selected spacers didn’t fit for proper energy level alignment with the four considered inorganic perovskite layer, they have potential for emission in various region. The PPA cation and its p-F and p-CH_3 substitutions comes with a high energy triplet state slightly above the exciton level of the $PbBr_4$ perovskite and much lower than $PbCl_4$. So, they are not capable to induce the excitonic energy transfer from the perovskite. In addition, s-cis and s-trans isomers of 5-phenyl-2,4-diene-pentaamine have T_1 energy (2.55 and 2.58 eV) slightly larger than PbI_4 inorganic layer. But they have T_1^* at 1.83 and 2.02 eV having potential for emission of red and orange lights respectively.

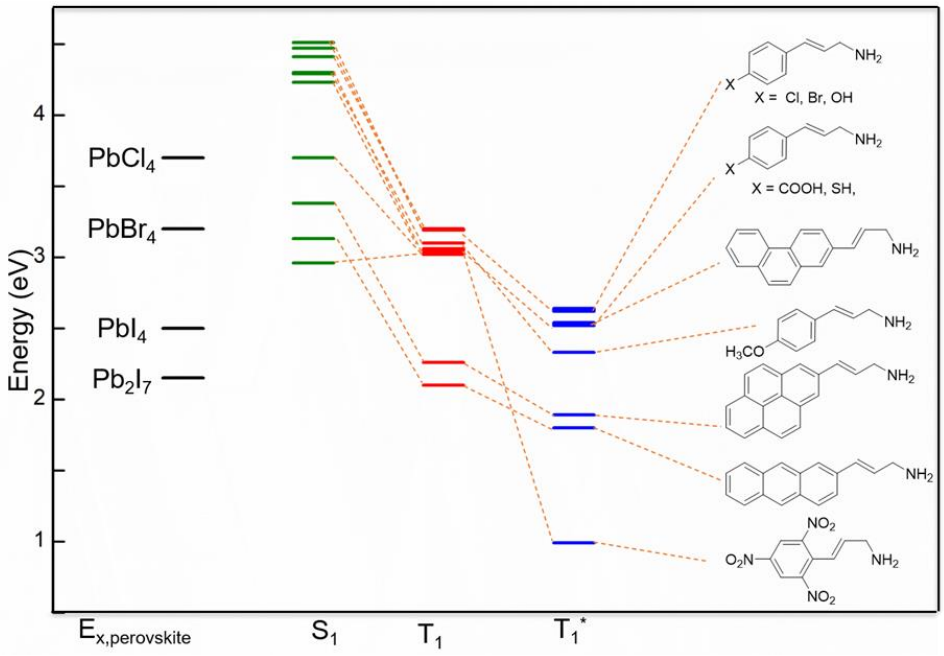

Figure 5.6: Alignment among the perovskite exciton levels and the excited states of the organic molecule.

In some of the spacers we have observed noticeably reduced S_1 energy level and even they sit below the exciton level of the metal halide layer. For these cases we can expect an excitonic energy transfer to the S_1 level. 3-anthracene-2-propeneamine and 2,4,6-NO_2-PPA have S_1 energy of 3.13 and 2.96 eV respectively. The S_1 level of these two cations situates below the excitonic energy level of $PbBr_4$ inorganic layer. Thus, we can have an excitonic energy transfer to the S_1 of these two cations when these will be combined with the $PbBr_4$ unit. Also, the 3-pyrene-2-propeneamine has an S_1 energy level at 3.38 eV which is below the excitonic energy of the $PbCl_4$ layer. So, this cation can induce an excitonic transition from $PbCl_4$ inorganic layer to its excited singlet state.

5.4. Conclusion

In conclusion, we have presented a detailed study about the predictability of the energy level alignment between inorganic and organic units of the 2D hybrid perovskites by analysing the excitation levels of the organic spacers. Our result unveils that the extension in conjugation rather than substituent group variation has significant contribution in the organic inorganic energy level alignments. We have calculated and investigated the excitation energy levels of a series of organic cations to find out the best combinations where induction of excitonic energy transfer from inorganic to organic would be possible and after this energy transfer of inorganic exciton to organic triplet excited state, the radiative emission could happen. This study is turn out to be successful to find out some preferred combinations those are able to emit different colours and can be used for different light emitting devices. By performing molecular dynamics simulations we have also verified the feasibility of our results at finite temperature conditions. Noticeably, our predicted combinations have high potentials for light emitting devices. Our study gives a clear direction for optimizing the hybrid perovskite properties through conjugated organic spacers and designing materials for optoelectronic devices.

5.5. References

1. Smith I. C., E. Hoke T., Solis-Ibarra D., McGehee M. D., Karunadasa H. I. (2014), A layered hybrid perovskite solar-cell absorber with enhanced moisture stability, Angew. Chem., Int. Ed., 53, 11232−11235 (DOI: 10.1002/anie.201406466)
2. Stoumpos C. C., Cao D. H., Clark D. J., Young J., Rondinelli J. M., Jang J. I., Hupp J. T., Kanatzidis M. G. (2016), Ruddlesden–Popper Hybrid Lead Iodide Perovskite 2D Homologous Semiconductors, Chem. Mater., 28, 2852−2867 (DOI: 10.1021/acs.chemmater.6b00847)
3. Quan L. N., Yuan M., Comin R., Voznyy O., Beauregard E. M., Hoogland S., Buin A., Kirmani A. R., Zhao K., Amassian A., Kim D.

H., Sargent E. H. (2016), Ligand-Stabilized Reduced-Dimensionality Perovskites, J. Am. Chem. Soc., 138, 2649−2655 (DOI: 10.1021/jacs.5b11740)

4. Katan C., Mercier N., Even J. (2019), Quantum and Dielectric Confinement Effects in Lower-Dimensional Hybrid Perovskite Semiconductors, Chem. Rev., 119, 3140−3192 (DOI: 10.1021/acs.chemrev.8b00417)
5. Sapori D., Kepenekian M., Pedesseau L., Katan C., Even J. (2016), Quantum confinement and dielectric profiles of colloidal nanoplatelets of halide inorganic and hybrid organic–inorganic perovskites, Nanoscale, 8, 6369−6378 (DOI: 10.1039/C5NR07175E)
6. Cho K. T., Grancini G., Lee Y., Oveisi E., Ryu J., Almora O., Tschumi M., Schouwink P. A., Seo G., Heo S. (2018), Selective growth of layered perovskites for stable and efficient photovoltaics, Energy Environ. Sci., 11, 952–959 (DOI: 10.1039/C7EE03513F)
7. Dohner E. R., Jaffe A., Bradshaw L. R., Karunadasa H. I. (2014), White-Light Emission from Layered Halide Perovskites, J. Am. Chem. Soc., 136, 13154−13157 (DOI: 10.1021/acs.accounts.7b00433)
8. Smith M. D., Karunadasa H. I. (2018), White-Light Emission from Layered Halide Perovskites, Acc. Chem. Res., 51, 619−627 (DOI: 10.1021/acs.accounts.7b00433)
9. Mao L., Ke W., Pedesseau L., Wu Y., Katan C., Even J., Wasielewski M. R., Stoumpos C. C., Kanatzidis M. G. (2018), Hybrid Dion–Jacobson 2D Lead Iodide Perovskites, J. Am. Chem. Soc., 140, 3775−3783 (DOI: 10.1021/jacs.8b00542)
10. Tsai H., Nie W., Blancon J. C., Stoumpos C. C., Soe C. M. M., Yoo J., Crochet J., Tretiak S., Even J., Sadhanala A., Azzellino G., Brenes R., Ajayan P. M., Bulović V., Stranks S. D., Friend R. H., Kanatzidis M. G. (2018), Stable Light-Emitting Diodes Using Phase-Pure Ruddlesden–Popper Layered Perovskites, Adv. Mater., 30, 1704217 (DOI: 10.1002/adma.201704217)

11. Wang J., Zhang C., Liu H., McLaughlin R., Zhai Y., Vardeny S. R., Liu X., McGill S., Semenov D., Guo H., Tsuchikawa R., Deshpande V. V., Sun D., Vardeny Z. V. (2019), Spin-optoelectronic devices based on hybrid organic-inorganic trihalide perovskites, Nat. Commun., 10, 129 (DOI: 10.1038/s41467-018-07952-x)
12. Mahal E., Mandal S. C., Pathak B. (2022), Band Edge Engineering of 2D Perovskite Structures through Spacer Cation Engineering for Solar Cell Applications, J. Phys. Chem. C, 126, 9937–9947 (DOI: 10.1021/acs.jpcc.2c01840)
13. Smith M. D., Connor B. A., Karunadasa H. I. (2019), Tuning the Luminescence of Layered Halide Perovskites, Chem. Rev., 119, 3104−3139 (DOI: 10.1021/acs.chemrev.8b00477)
14. Mitzi D. B., Chondroudis K., Kagan C. R. (1999), Vibronic Structure in Room Temperature Photoluminescence of the Halide Perovskite $Cs_3Bi_2Br_9$, Inorg. Chem., 38, 6246−6256 (DOI: 10.1021/acs.inorgchem.6b01571)
15. Traore B., Pedesseau L., Assam L., Che X., Blancon J.-C., Tsai H., Nie W., Stoumpos C. C., Kanatzidis M. G., Tretiak S., Mohite A. D., Even J., Kepenekian M., Katan C. (2018), Composite Nature of Layered Hybrid Perovskites: Assessment on Quantum and Dielectric Confinements and Band Alignment, ACS Nano, 3321−3332 (DOI: 10.1021/acsnano.7b08202)
16. Passarelli J. V., Fairfield D. J., Sather N. A., Hendricks M. P., Sai H., Stern C. L., Stupp S. I. (2018), Enhanced Out-of-Plane Conductivity and Photovoltaic Performance in n = 1 Layered Perovskites through Organic Cation Design, J. Am. Chem. Soc., 140, 7313−7323 (DOI: 10.1021/jacs.8b03659)
17. Xue J., Wang R., Chen X., Yao C., Jin X., Wang K.-L., Huang W., Huang T., Zhao Y., Zhai Y., Meng D., Tan S., Liu R., Wang Z.-K., Zhu C., Zhu K., Beard M. C., Yan Y., Yang Y. (2021), Reconfiguring the

band-edge states of photovoltaic perovskites by conjugated organic cations, Science, 371, 636−640. (DOI: 10.1126/science.abd4860)

18. Neutzner S., Thouin F., Cortecchia D., Petrozza A., Silva C., Kandada A. R. S. (2018), Exciton-polaron spectral structures in two-dimensional hybrid lead-halide perovskites, Phys. Rev. Mater., 2, 064605 (DOI: 10.1103/PhysRevMaterials.2.064605)
19. Ema K., Inomata M., Kato Y., Kunugita H., Era M. (2008), Nearly Perfect Triplet-Triplet Energy Transfer from Wannier Excitons to Naphthalene in Organic-Inorganic Hybrid Quantum-Well Materials, Phys. Rev. Lett., 100, 257401 (DOI: 10.1103/PhysRevLett.100.257401)
20. Elshanawany M. M., Ricciardulli A. G., Saliba M., Wachtveitl J., Braun M. (2021), Mechanism of ultrafast energy transfer between the organic–inorganic layers in multiple-ring aromatic spacers for 2D perovskites, Nanoscale, 13, 15668−15676 (DOI: 10.1039/D1NR04290D)
21. Xi J., Spanopoulos I., Bang K., Xu J., Dong H., Yang Y., Malliakas C. D, Hoffman J. M, Kanatzidis M. G., Wu Z. (2020), Alternative Organic Spacers for More Efficient Perovskite Solar Cells Containing Ruddlesden-Popper Phases, J. Am. Chem. Soc., 142, 19705− 19714. (DOI: 10.1021/jacs.0c09647)
22. Leveillee J., Katan C., Even J., Ghosh D., Nie W., Mohite A. D., Tretiak S., Schleife A., Neukirch A. J., (2019), Tuning Electronic Structure in Layered Hybrid Perovskites with Organic Spacer Substitution, Nano Lett., 19, 8732−8740 (DOI: 10.1021/acs.nanolett.9b03427)
23. Giannozzi P., Baroni S., Bonini N., Calandra M., Car R., Cavazzoni C., Ceresoli D., Chiarotti G. L., Cococcioni M., Dabo I., Corso A. Dal, Gironcoli S. de, Fabris S., Fratesi G., Gebauer R., Gerstmann U., Gougoussis C., Kokalj A., Lazzeri M., Martin-Samos L., Marzari N., Mauri F., Mazzarello R., Paolini S., Pasquarello A., Paulatto L., Sbraccia C., Scandolo S., Sclauzero G., Seitsonen A. P., Smogunov A., Umari P., Wentzcovitch R. M. (2009), QUANTUM ESPRESSO: a modular and open-source software project for quantum simulations of

materials, J. Phys.: Condens. Matter, 21, 395502 (DOI: 10.1088/0953-8984/21/39/395502)

24. Perdew J. P., Burke K., Ernzerhof M. (1996), Generalized Gradient Approximation Made Simple, Phys. Rev. Lett., 77, 3865−3868 (DOI: 10.1103/PhysRevLett.77.3865)
25. Vanderbilt D. (1990), Soft self-consistent pseudopotentials in a generalized eigenvalue formalism, Phys. Rev. B: Condens. Matter Mater. Phys., 41, 7892−7895 (DOI: 10.1103/PhysRevB.41.7892)
26. Monkhorst H. J., Pack J. D. (1976), Special points for Brillouin-zone integrations, Phys. Rev. B: Solid State, 13, 5188−5192 (DOI: 10.1103/PhysRevB.13.5188)
27. Grimme S., Antony J., Ehrlich S., Krieg H. (2010), A consistent and accurate ab initio parametrization of density functional dispersion correction (DFT-D) for the 94 elements H-Pu, J. Chem. Phys., 132, 154104 (DOI: 10.1063/1.3382344)
28. Heyd J., Scuseria G. E., Ernzerhof M. (2003), Hybrid functionals based on a screened Coulomb potential, J. Chem. Phys., 118, 8207−8215 (DOI: 10.1063/1.2204597)
29. Du M.-H. (2015), Density Functional Calculations of Native Defects in $CH_3NH_3PbI_3$: Effects of Spin-Orbit Coupling and Self-Interaction Error J. Phys. Chem. Lett., 6, 1461−1466 (DOI: 10.1021/acs.jpclett.5b00199)
30. Mahata A., Mosconi E., Meggiolaro D., Angelis F. De. (2020), Influence of Surface Termination on the Energy Level Alignment at the $CH_3NH_3PbI_3$ Perovskite/C60 Interface, Chem. Mater., 32, 105−113 (DOI: 10.1021/acs.chemmater.6b03259)
31. Blöchl P. E. (1994), Projector augmented-wave method, Phys. Rev. B, 50, 17953−17979 (DOI: 10.1103/PhysRevB.50.17953)
32. Kresse G., Joubert D. (1999), From ultrasoft pseudopotentials to the projector augmented-wave method, Phys. Rev. B: Condens. Matter Mater. Phys., 59, 1758 (DOI: 10.1103/PhysRevB.59.1758)

33. Kresse G., Hafner J. (1993), Ab initio molecular dynamics for liquid metals, Phys. Rev. B: Condens. Matter Mater. Phys., 47, 558 (DOI: 10.1103/PhysRevB.47.558)
34. Kresse G., Hafner J. (1994), Ab initio molecular-dynamics simulation of the liquid-metal–amorphous-semiconductor transition in germanium, Phys. Rev. B: Condens. Matter Mater. Phys., 49, 14251 (DOI: 10.1103/PhysRevB.49.14251)
35. Kresse G., Furthmüller J. (1996), Efficiency of ab-initio total energy calculations for metals and semiconductors using a plane-wave basis set, Comput. Mater. Sci., 6, 15−50 (DOI: 10.1016/0927-0256(96)00008-0)
36. Kresse G., Furthmüller J. (1996), Efficient iterative schemes for ab initio total-energy calculations using a plane-wave basis set, Phys. Rev. B, 54, 11169−11186 (DOI: 10.1103/PhysRevB.54.11169)
37. Nosé S. (1984), A unified formulation of the constant temperature molecular dynamics methods, J. Chem. Phys., 81, 511–519 (DOI: 10.1063/1.447334)
38. Frisch M. J., Trucks G. W., Schlegel H. B., Scuseria G. E., Robb M. A., Cheeseman J. R., Scalmani G., Barone V., Mennucci B., Petersson G. A., Nakatsuji H., Caricato M., Li X., Hratchian H. P., Izmaylov A. F., Bloino J., Zheng G., Sonnenberg J. L., Hada M., Ehara M., Toyota K., Fukuda R., Hasegawa J., Ishida M., Nakajima T., Honda Y., Kitao O., Nakai H., Vreven T., Montgomery J. A., Peralta, Jr. J. E., Ogliaro F., Bearpark M., Heyd J. J., Brothers E., Kudin K. N., Staroverov V. N., Keith T., Kobayashi R., Normand J., Raghavachari K., Rendell A., Burant J. C., Iyengar S. S., Tomasi J., Cossi M., Rega N., Millam J. M., Klene M., Knox J. E., Cross J. B., Bakken V., Adamo C., Jaramillo J., Gomperts R., Stratmann R. E., Yazyev O., Austin A. J., Cammi R., Pomelli C., Ochterski J. W., Martin R. L., Morokuma K., Zakrzewski V. G., Voth G. A., Salvador P., Dannenberg J. J., Dapprich S., Daniels

A. D., Farkas O., Foresman J. B., Ortiz J. V., Cioslowski J., Fox D. J. (2009), Gaussian 09, Revision B.01; Gaussian Inc.: Wallingford, CT.

39. Hehre W. J., Ditchfield K., Pople J. A. (1972), Self—Consistent Molecular Orbital Methods. XII. Further Extensions of Gaussian—Type Basis Sets for Use in Molecular Orbital Studies of Organic Molecules, J. Chem. Phys., 56, 2257–2261 (DOI: 10.1063/1.1677527)
40. Hariharan P. C., Pople J. A. (1973), The influence of polarization functions on molecular orbital hydrogenation energies, Theor. Chim. Acta, 28, 213–222 (DOI: 10.1007/BF00533485)
41. Krishnan R., Binkley J. S., Seeger R., Pople J. A. (1980), Self-consistent molecular orbital methods. XX. A basis set for correlated wave functions, J. Chem. Phys., 72, 650–654 (DOI: 10.1063/1.438955)
42. Becke A. D. (1988), Density-functional exchange-energy approximation with correct asymptotic behavior, Phys. Rev. A, 38, 3098–3100 (DOI: 10.1103/PhysRevA.38.3098)
43. Becke A. D. (1993), Density-functional thermochemistry. III. The role of exact exchange, J. Chem. Phys., 98, 5648–5652 (DOI: 10.1063/1.464913)
44. Becke A. D. (1997), Density-functional thermochemistry. V. Systematic optimization of exchange-correlation functionals, J. Chem. Phys., 107, 8554–8560 (DOI: 10.1063/1.475007)
45. Becke A. D. (1993), A new mixing of Hartree–Fock and local density-functional theories, J. Chem. Phys., 98, 1372–1377 (DOI: 10.1063/1.464304)
46. Lee C., Yang W., Parr R. G. (1988), Development of the Colle-Salvetti correlation-energy formula into a functional of the electron density, Phys. Rev. B: Condens. Matter Mater. Phys., 37, 785–789 (DOI: 10.1103/PhysRevB.37.785)
47. Gavnholt, J., Olsen, T., Engelund M., Schiøtz, J. (2008), Δ self-consistent field method to obtain potential energy surfaces of excited

molecules on surfaces Phys. Rev. B: Condens. Matter Mater. Phys., 78, 075441 (DOI: 10.1103/PhysRevB.78.075441)

48. Guido C. A., Knecht S., Kongsted J., Mennucci B. (2013), Benchmarking Time-Dependent Density Functional Theory for Excited State Geometries of Organic Molecules in Gas-Phase and in Solution, J. Chem. Theory Comput., 9, 2209 −2220 (DOI: 10.1021/ct400021c)
49. Mahal E., Mandal S. C., Pathak B. (2022), Understanding the role of spacer cation in 2D layered halide perovskites to achieve stable perovskite solar cells, Mater. Adv., 3, 2464−2474 (DOI: 10.1039/D1MA01135A)
50. Hu J., Oswald I. W. H., Stuard S. J., Nahid M. M., Zhou N., Williams O. F., Guo Z., Yan L., Hu H., Chen Z., Xiao X., Lin Y., Yang Z., Huang J., Moran A. M., Ade H., Neilson J. R., You W. (2019), Synthetic control over orientational degeneracy of spacer cations enhances solar cell efficiency in two-dimensional perovskites, Nat. Commun., 10, 1276 (DOI: 10.1038/s41467-019-08980-x)
51. Tremblay M.-H., Bacsa J., Zhao B., Pulvirenti F., Barlow S., Marder S. R. (2019), Structures of $(4\text{-Y-}C_6H_4CH_2NH_3)_2PbI_4$ {Y = H, F, Cl, Br, I}: Tuning of Hybrid Organic Inorganic Perovskite Structures from Ruddlesden–Popper to Dion–Jacobson Limits, Chem. Mater., 31, 6145−6153 (DOI: 10.1021/acs.chemmater.9b01564)
52. Wang K., Jiang P., Yang M., Ma P., Qin J., Huang X., Ma L., Li R. (2019), Metal-free nitrogen -doped carbon nanosheets: a catalyst for the direct synthesis of imines under mild conditions, Green Chem., 21, 2448−2461 (DOI: 10.1039/C9GC00908F)
53. Bastin R., Liron M., Taylor R. J. K. (2008), The Conversion of Carbonyl Compounds into Pentadienylamines by a Julia-Kocienski Olefination Procedure, Synlett., 14, 2183-2187 (DOI: 10.1055/s-2008-1078011)
54. Blancon J.-C., Tsai H., Nie W., Stoumpos C. C., Pedesseau L., Katan C., Kepenekian M., Soe C. M. M., Appavoo K., Sfeir M. Y., Tretiak S., Ajayan P. M., Kanatzidis M. G., Even J., Crochet J. J., Mohite A. D.

(2017), Extremely efficient internal exciton dissociation through edge states in layered 2D perovskites, Science, 355, 1288–1292 (DOI: 10.1126/science.aal4211)

55. Du K.-z., Tu Q., Zhang X., Han Q., Liu J., Zauscher S., Mitzi D. B. (2017), Two-Dimensional Lead(II) Halide-Based Hybrid Perovskites Templated by Acene Alkylamines: Crystal Structures, Optical Properties, and Piezoelectricity, Inorg. Chem., 56, 9291−9302 (DOI: 10.1021/acs.inorgchem.7b01094)

Chapter 6

Machine Learning Driven Prediction of Intramolecular Band Alignment Types in 2D Hybrid Perovskites

6.1. Introduction

Organic inorganic hybrid halide perovskites are semiconducting materials that have molecular formula of ABX_3 where A is a small cation like $CH_3NH_3^+$, B is a divalent metal (commonly Pb, Sn, Ge) and X is a halogen.*[1-4]* The decomposition tendency of small organic cation in presence of light and moisture destroys the 3D perovskite crystal structure. *[5-6]* Rather, large organic cations namely spacer cations stabilise the 2D perovskite structure with strong van der Waals (vdW) interaction.*[7-9]* Along with the environmental stability, the 2D hybrid perovskites possess high chemical flexibility exploring the wide variety of organic ammonium cations.

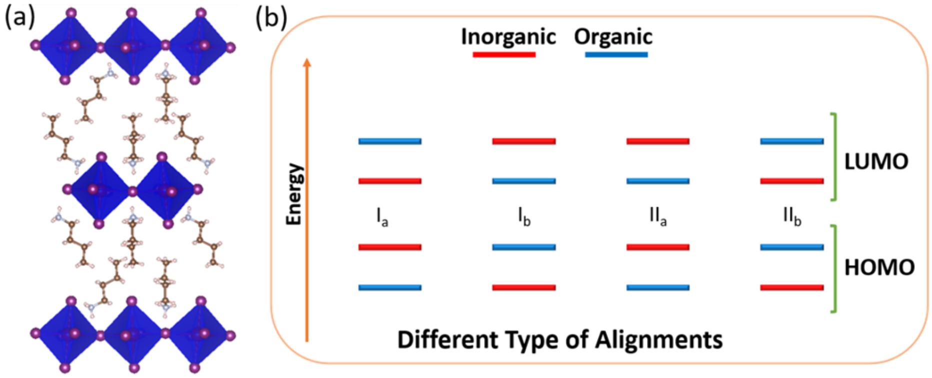

Scheme 6.1: Schematic diagram of (a) a typical 2D hybrid perovskite structure and (b) different types of intramolecular band alignments in 2D perovskite.

Notably, the large organic cations possess much smaller dielectric constant than the inorganic metal halide layers. Because of this dielectric mismatch, 2D hybrid perovskites are the examples of naturally occurring multiple quantum wells.*[10-11]* The broad availability of the organic spacers can represent different quantum well structure with varieties in carrier and excitation property which bring various aspects for their applications. Depending upon the nature of quantum well, these materials can be classified into four types (Scheme 6.1) with different intramolecular band alignments such as I_a, I_b, II_a, II_b. Here type I represents the materials where both the valence band and conduction band edges have contribution from same unit i.e., either both from inorganic (I_a) or both from organic (I_b). Whereas type II possesses the band edges from different counterparts. In type II_a, valence band and conduction band edges have contribution from organic HOMO and inorganic LUMO, respectively and vice versa is true for type II_b. In type I_a charge carriers are localised in inorganic component having possibility of inter-band excitonic transition whereas in type I_b, carriers are localised in organic component possessing a probability of π-π* transition. As a result, these types of materials are appropriate for the lasers and light emitting devices. On the other side, in case of type II materials the carriers are separated in two different units allowing longer carrier lifetime and thus suitable for photovoltaic applications.[*12-16]*

In this regard, Blum and co-workers have shown a direction to fine tune the range of 2D perovskite materials targeting a particular electronic property through quantum well aspect.*[17]* Lu et al. have also shown how spin orbit coupling in metal halide and HOMO LUMO energies of the organic cation control the intramolecular band alignments in these materials.*[18]* Du and co-workers have demonstrated the role of polycyclic amines in tuning the band alignments of 2D hybrid perovskites.*[19]* In our recent first principle-based study, we have shown that heterocyclic ring pyrilium and thiopyrilium based spacer cations can directly contribute to band edges of the 2D hybrid perovskite materials.*[20]* Finding out the best material for a selective application from this wide availability is a difficult job by studying every individual material experimentally or computationally. Therefore, it is highly important that we develop a model that can predict the electronic property of the system from its chemical composition so that we can identify the material of our desired property easily.

In recent years machine learning (ML) has played important role in the scientific research areas. Wang and co-workers have applied ML algorithms to discover stable lead-free hybrid perovskite.*[21]* Casttelli and co-workers have used it to predict the band gap of hybrid metal halide perovskites.*[22]* Liang et al. have predicted the band gap of 2D hybrid perovskites using ML whereas Wu and co-workers have developed a ML model to predict the formability of the low dimensional hybrid perovskites and classified them to 2D forming and Non 2D forming cases.*[23-24]* However, prediction of the electronic structure of the 2D hybrid perovskite materials is still unexplored. In this aspect, classification of these materials based on their electronic structures would be much appreciated and beneficial for the perovskite research community.

In the present work, we have first time classified the 2D halide perovskites to type I and type II band alignment quantum wells. Using the same dataset, we have further attempted to classify them into I_a, I_b, II_a, and II_b using multiclass classification approach. We have also tried to classify type I and type II materials to their corresponding class I_a-I_b and II_a-II_b separately considering individual dataset of type I and type II, respectively. For this purpose, we have utilised physical as well as chemical properties of organic and inorganic units as features. Further, from feature coefficient analysis we are able to find out the feature-output relations and to give insights on the contribution of the features towards the output. In Scheme 6.2 we have picturised the flowchart of our work. Classification of 2D halide perovskites to its different band alignment types can help us in selecting the suitable material with desired features for their applications.

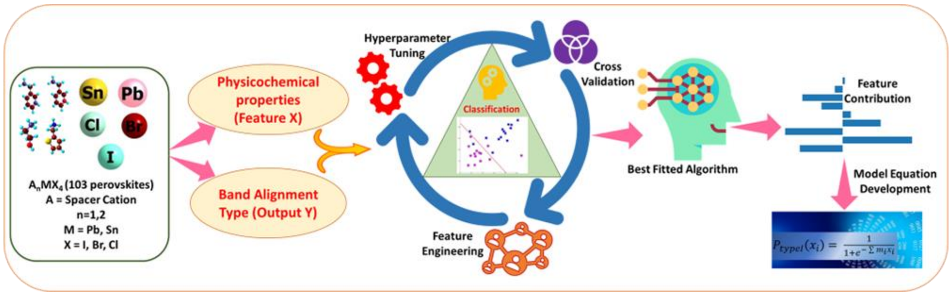

Scheme 6.2: Scheme of machine learning workflow for current study.

6.2. Methods

To obtain the intramolecular band alignments of the layered hybrid perovskite materials we have performed electronic structure calculations using the Quantum Espresso (QE) program package.*[25]* Single point calculations at the HSE06+SOC level was performed. HSE06 hybrid functional with 43% Hatree-Fock exchange along with plane wave basis set cutoff of 40 Ry for the smooth part of the wave functions and a Fock energy cutoff of 80 Ry was set during HSE06+SOC calculations along with a Monkhorst pack k-point sampling.*[26-28]* Also, we have taken norm-conserving pseudopotentials with electrons from I 5s, 5p; Br 4s, 4p; Cl 3s, 3p; O, N, C 2s, 2p; H 1s; Pb 5s, 5p, 6s, 6p, 5d; Sn 4s, 4p, 5s, 5p, 4d; shells explicitly for the HSE06+SOC calculations. These methodologies are reported to give good results for such systems.[29] After the single point calculations we have extracted the pDOS plots to identify the band alignment types. HOMO LUMO energies of the inorganic metal halide units were calculated using the same HSE06+SOC method. For this we have taken a single MX_6 unit neutralizing with four methyl ammonium cations. HOMO and LUMO energies of the six metal halide octahedral units were aligned with respect to the C 1S orbital energy.

For the calculation of HOMO LUMO energies of the isolated organic molecules the Gaussian 09 D.01 suite of programme has been employed.*[30]* The Becke 3-parameter Lee–Yang–Parr (B3LYP)*[31-35]* hybrid functional has been implemented for the calculations. 6-311++G***[36-38]* basis set as formulated by John Pople was used.

6.3. Result and Discussion

6.3.1. Data Collection

The primary requirement of ML based work is the model training. A total of 103 2D perovskite materials has been considered and their band alignment types were detected by performing density functional theory

(DFT) calculation as well as from available theoretical reports. In the considered perovskite set, Pb and Sn are present as metal atom whereas Cl, Br and I are present as halogen with 80 different ammonium spacer cations (Figure 6.1).

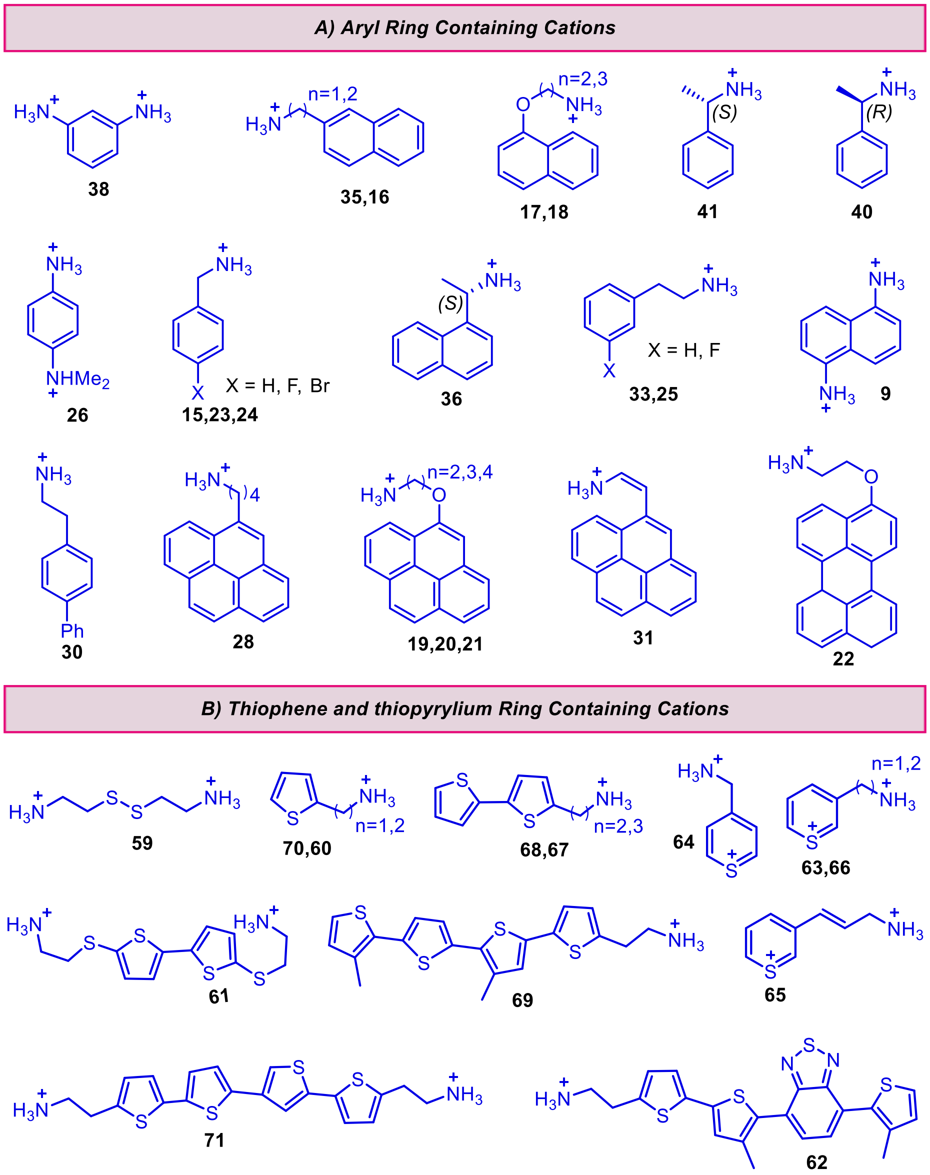

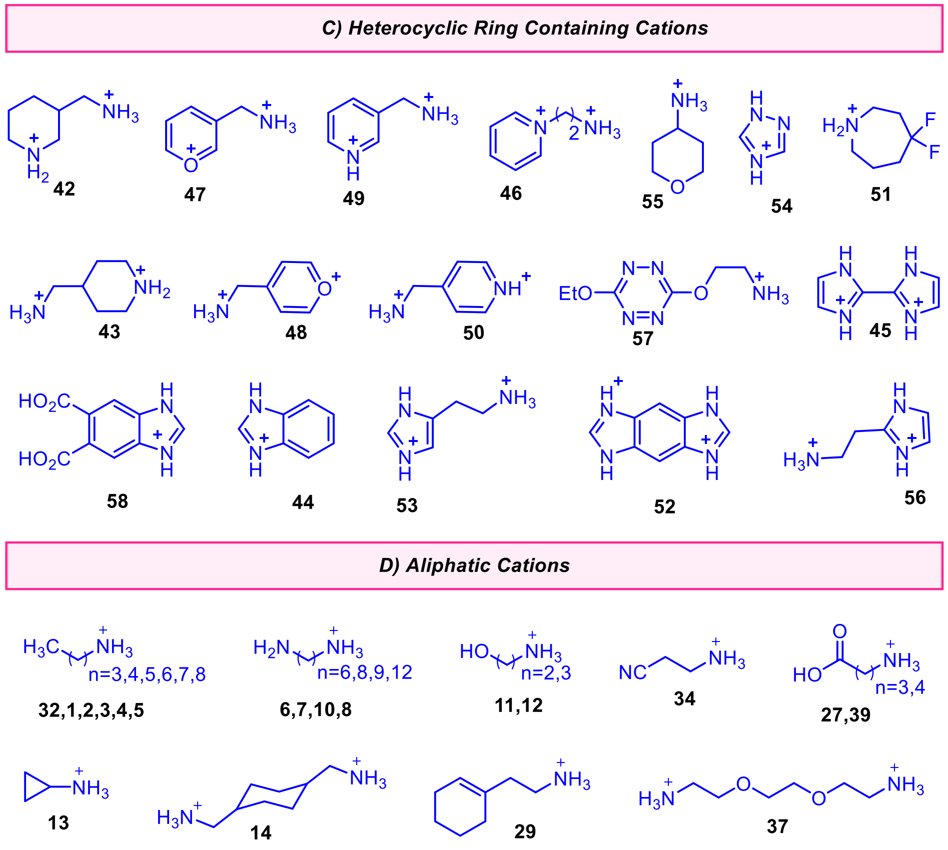

Figure 6.1: List of ammonium cations contained in the 2D hybrid perovskite materials selected in this study.

Here, we have attempted to classify the considered perovskite materials based on their intramolecular band alignment types. In order to perform that, we have employed different molecular features of the perovskite material components as input. First, various ML algorithms were trained with these input features and their corresponding class as output. Afterwards, optimization of the hyperparameters of each of the considered models was performed followed by the selection of the best predictive model based on their classification accuracy. Finally, we have validated the predictability of the model by applying it on few newly designed materials, unknown to the trained model.

In this study, we have denoted the classification of the perovskite materials as output Y. 84 materials are collected from the 2D perovskite database developed by Tarasov and co-workers.*[39]* After performing single point calculations on those crystal structures at the hybrid functional (HSE06) along with spin orbit coupling (SOC) level, we have plotted the projected density of states (pDOS). Other 19 materials and their corresponding pDOS plots were obtained by literature review.*[19,20,40,41]* Analysing the pDOS plots, we have figured out their band alignment types and employed those as target for the classification. In Figure 6.2 we have demonstrated the band alignment types of 30 selected perovskites containing all four types of alignments.

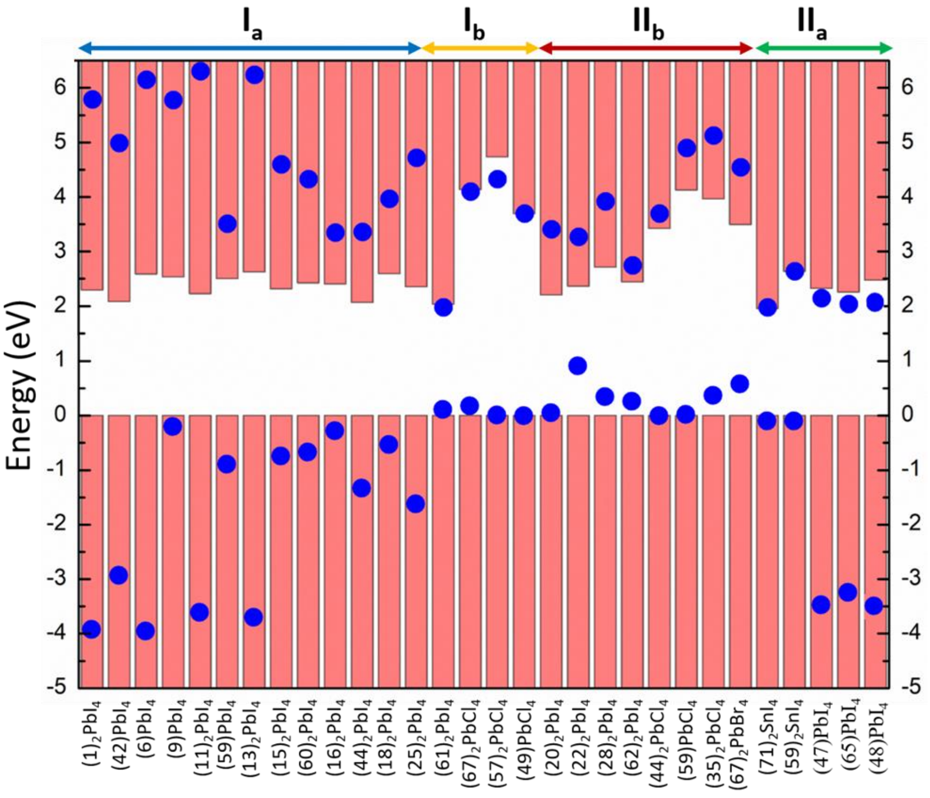

Figure 6.2: Band Alignment Types of 30 selected perovskites containing all four types of alignments. The structure of the numbered cation listed in the Figure 6.1.

6.3.2. Feature Selection

Feature selection is one of the most important parts in ML-based studies as simple and vital features may lead to a superior predictive model to predict the output accurately. For the inorganic units we have considered the electronegativities of metal and halogen atoms along with the HOMO and LUMO energies of the MX_6 octahedral unit as features. To obtain this we have taken a single MX_6 unit from the optimized methylammonium metal halide unit cell with four methyl ammonium cations (Figure 6.3) to make them neutral and performed single point calculation with HSE06+SOC method. For the organic cations, we have calculated the HOMO and LUMO energies and utilized them as features. These calculations have been done in Gaussian 09 software.

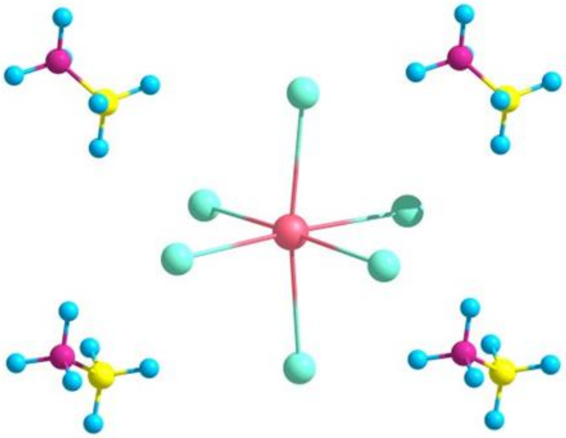

Figure 6.3: Single MX_6 unit with four methyl ammonium cations.

To obtain some physicochemical properties of the ammonium cations, we have also considered some of the molecular descriptors. In general, target properties often depend on the molecular descriptors as physical and chemical properties are directly correlated with those parameters in many of the cases. Here, target property i.e., types of band alignments can be represented as the function of several molecular descriptors. These input descriptors can be transformed into useful chemical information through a mathematical procedure using the described function with respect to the target.

Table 6.1: Selected features

Feature Name	Description
1. Organic HOMO	HOMO energy of the organic cation
2. Organic LUMO	LUMO energy of the organic cation
3. Inorganic HOMO	HOMO energy of the inorganic metal halide unit
4. Inorganic LUMO	LUMO energy of the inorganic metal halide unit
5. Metal Electronegativity	Electronegativity of the metal atom
6. Halogen Electronegativity	Electronegativity of the halogen atom
7. Eccentricity	Eccentricity of the organic cation
8. Molar Mass	Molar Mass of the organic cation
9. Ring Count	Number of rings present in the organic cation
10. Aromatic Ring Count	Number of aromatic rings present in the organic cation
11. Heterocyclic Ring Count	Number of heterocyclic rings present in the organic cation
12. Hydrogen Bond Donor Count	Number of functional groups having H-bond donors present in the organic cation
13. Hydrogen Bond Acceptor Count	Number of H-bond acceptor atoms present in the organic cation
14. Formal Charge	Formal Charge of the organic cation
15. Topological Polar Surface Area	Contribution of the polar atoms to the van der Waals surface area of the organic cation
16. Polarizability	Polarizability of the organic cation
17. Molar Refractivity	Molar Refractivity of the organic cation
18. van der Waals Volume	van der Waals volume of the organic cation
19. van der Waals Surface Area	van der Waals surface area of the organic cation
20. Minimum Projection Radius	Minimum radius of the organic cation when projected on a 2D plane

These molecular descriptors not only contain experimental properties such as molar refractivity, dipole moment, polarizability, and, in general, physicochemical properties but also include theoretical molecular descriptors derived from symbolic representations such as hydrogen bond donor and acceptor count, topological polar surface area, vdW volume, vdW surface area etc. We have taken the help of ChemAxon's Chemicalize platform to calculate the chemical descriptors for our work. To create the descriptors, we have drawn the structure of the ammonium cations there and calculated the descriptors. Among generated descriptors we have selected those features having direct influence on our output. In addition, another feature eccentricity which is the longest topological distance starting from the N atom inside the amine, we have calculated following the method described by Wu and co-workers in their recent paper. *[24]* The list of the selected features and their description is given in Table 6.1.

6.3.3. Model Selection

Data training is the key process of any ML project. Using the considered data set we have performed model selection through hyperparameter tuning on different classifiers available in open source scikit-learn package.*[42]* Six such different classifiers (Section 1.4.4.7, Chapter 1) starting from simplest Logistic Regression, Ridge Classifier to complex models like Support Vector Machine, K-Nearest Neighbour, Bagging Classifier and Random Forest Classifier were selected for model training process. After tuning of all the considered models with respect to their various hyperparameters we obtained the best fitted model with its optimized hyperparameters. Next, to be assured about the stability of the models, we have used RepeatedStratified 5-fold cross-validation (Section 1.4.4.6, Chapter 1) and calculated the cross-validation accuracy of each of the considered models.*[42]* Moreover, we have again divided the total data into training set (~70%) and test set (~30%) keeping their ratio fixed for type I and type II data in both training and test set and predicted for test set using the model trained by training set. In Table 6.2 we have tabulated best fitted model hyperparameters for all the considered ML models along with their test and cross-validation accuracy scores. The parameters other than hyperparameters related to the considered models are automatically estimated during the training process.

Table 6.2: Optimized hyperparameters and accuracy scores of considered ML algorithms.

Classification Algorithms	**Optimized Hyperparameters**	**Cross Validation (Average accuracy)**	**Test Accuracy**
Logistic Regression	C: 0.01, penalty: l2, solver: lbfgs, tol:1e^{-4}	0.83	0.86
Ridge Classifier	alpha: 0.8, solver:'auto', tol:1e^{-4}	0.83	0.79
Support Vector Machine	C=50, kernel=rbf, degree=3, gamma = 'scale', coef0 = 0.0, max_iter = -1	0.83	0.90
K Nearest Neighbor	metric: manhattan, n_neighbors: 7, weights: uniform, algorithm:'auto', leaf_size:30, p:2	0.82	0.86
Random Forest Classifier	Criterion:"gini",max_features: log2, n_estimators:10,min_samples_leaf:1,min_samples_leaf:2	0.84	0.86
Bagging Classifier (Random Forest as the base classifier)	n_estimators: 100, min_samples:1, max_features:1	0.84	0.93

The best cross validation as well as test accuracy score 0.84 and 0.93 respectively, were achieved with Bagging classifier. Other algorithms also come up with nearly similar cross validation accuracy score in the range of 0.82 to 0.84 and similar test accuracy score ranging from 0.79 to 0.93.

Interestingly, the simplest algorithm logistic regression also results in good cross validation accuracy score (0.83) as well as test accuracy score (0.86).

Table 6.3: Predicted probability of test dataset (the numbers in the compound names are the numbers of the organic cations mentioned in Figure 6.1)

Compound	**Type**	**Predicted probability**	
		Type I	**Type II**
$(22)_2PbI_4$	II	0.23	0.77
$(71)PbCl_4$	II	0.24	0.76
$(71)PbBr_4$	II	0.24	0.76
$(48)PbI_4$	II	0.43	0.57
$(63)PbI_4$	II	0.19	0.81
$(63)PbBr_4$	II	0.19	0.81
$(70)_2PbCl_4$	II	0.74	0.26
$(4)_2PbI_4$	I	0.98	0.02
$(5)_2PbI_4$	I	0.99	0.01
$(6)PbI_4$	I	0.96	0.04
$(59)_2PbI_4$	I	0.79	0.21
$(13)_2PbI_4$	I	0.88	0.12
$(42)PbI_4$	I	0.88	0.12
$(24)_2PbI_4$	I	0.66	0.34
$(25)_2PbI_4$	I	0.85	0.15
$(45)_2PbI_4$	I	0.76	0.24
$(36)_2PbBr_4$	I	0.66	0.34
$(55)_2PbBr_4$	I	0.94	0.06
$(33)_2PbI_4$	I	0.83	0.17
$(34)_2PbI_4$	I	0.93	0.07
$(71)_2SnI_4$	II	0.33	0.67
$(15)_2SnCl_4$	II	0.78	0.22
$(26)PbCl_4$	II	0.69	0.31
$(53)SnI_4$	I	0.99	0.01
$(41)_2SnI_4$	I	0.82	0.18
$(15)_2SnBr_4$	I	0.78	0.22
$(44)_2PbBr_4$	I	0.89	0.11
$(77)PbCl_4$	I	0.88	0.12
$(52)PbI_4$	I	0.47	0.53

We found out that the logistic regression model fails for four systems which is mainly due to the strong overlap of inorganic and organic units at the band edges (Table 6.3). This implies that those wrong predictions are not solely due to wrong training of the model rather there is a hindrance in distinguishability due to the overlap of two different units at band edges. Hence, we can go ahead with logistic regression for our further analysis due to its simplicity, interpretability, as well as good predictability to retain generalizability and transferability of the proposed model. Although we have achieved better accuracy with the Bagging Classifier, due to the complexity of these model we did not move forward with this. Rather we focused mainly on the transparency of the algorithm.

6.3.4. Feature Analysis

Apart from this, realization of the feature output relationship is important for the advancement of the ML analysis. For example, many of the selected features are highly correlated to each other. Among our generated features, polarizability and molar refractivity are highly correlated. Whereas, molar mass is correlated with vdW volume, vdW surface area, polarizability and more. Formal charge of the cation is correlated with HOMO and LUMO energies of the cation. There is strong correlation between the HOMO and LUMO energies of the inorganic unit (metal halide octahedra) and the electronegativities of metal and halide. Reduction of these features (i.e., dimensionality) would not harm the accuracy of the model rather will make the model simpler. In this regard, we have calculated the Pearson correlation coefficients (PCCs) and presented the plot in Figure 6.4.*[43]* Again, correlated features can also be helpful in many cases. In this regard, considering the logistic regression algorithm, we have analysed the model accuracy by deleting the correlated features one by one and observed similar results with only nine features (Table 6.4).

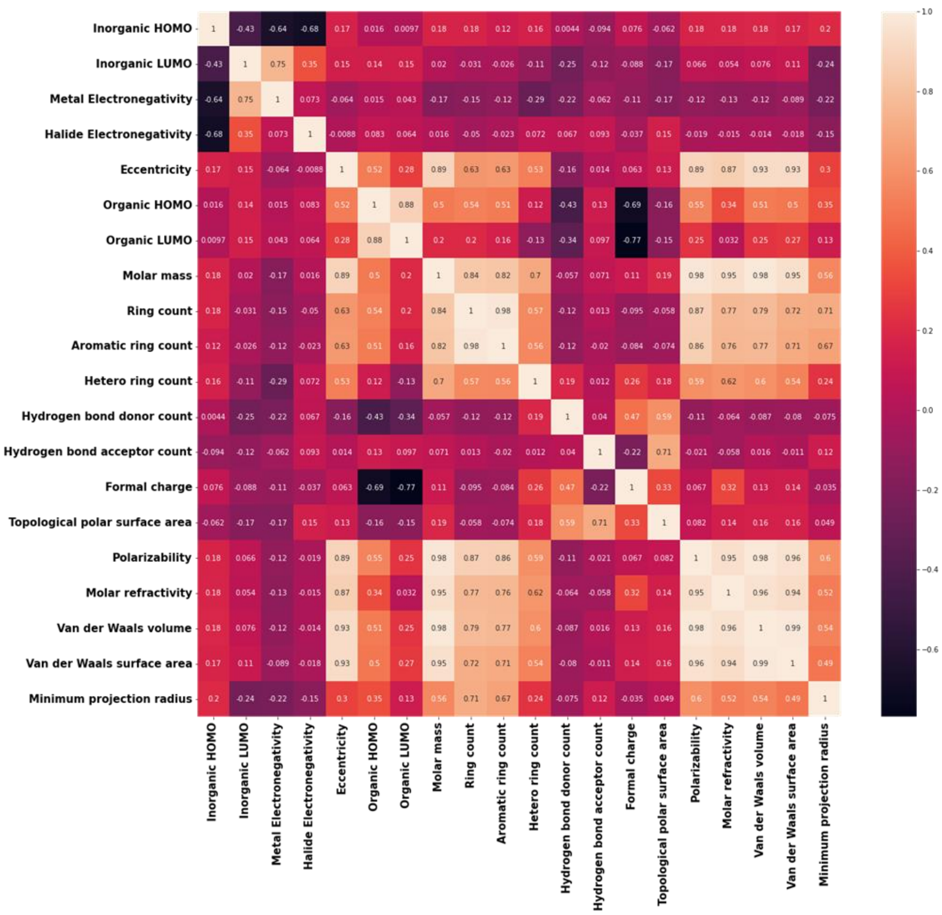

Figure 6.4: Correlation matrix of the selected features with Pearson correlation coefficients.

Table 6.4: Finally selected 9 features upon feature engineering.

Serial No.	Selected features
1	Organic HOMO (OH)
2	Organic LUMO (OL)
3	Inorganic HOMO (IH)
4	Inorganic LUMO (IL)
5	Metal Electronegativity (ME)
6	Halogen Electronegativity (HE)
7	Hydrogen Bond Donor Count (HBDC)
8	Hydrogen Bond Acceptor Count (HBAC)
9	Polarizability (α)

Also, we have used the recursive feature elimination method for selection of the proper combination of features to improve the accuracy and obtained the plot for accuracy score vs. number of features (Figure 6.5). Interestingly, the accuracy score increased slightly (0.89) with twelve features compared to the previous accuracy score (0.86) with nine features. Therefore, based on the recursive feature elimination method, important features such as LUMO energy of the inorganic unit and electronegativity of the metal need to be excluded. On the other hand, highly correlated features such as polarizability-molar refractivity (PCC:0.95), and polarizability-van der Waals surface area (PCC:0.96) need to be included. This happens because this method ranked the features according to their weightage or coefficient evaluated by a certain algorithm. However, we know that HOMO and LUMO energies of the organic and inorganic components play important role to tune the band alignments. So, instead of relying only on the feature selection method, we focused on our scientific understanding about the feature output relation and continued with nine features.

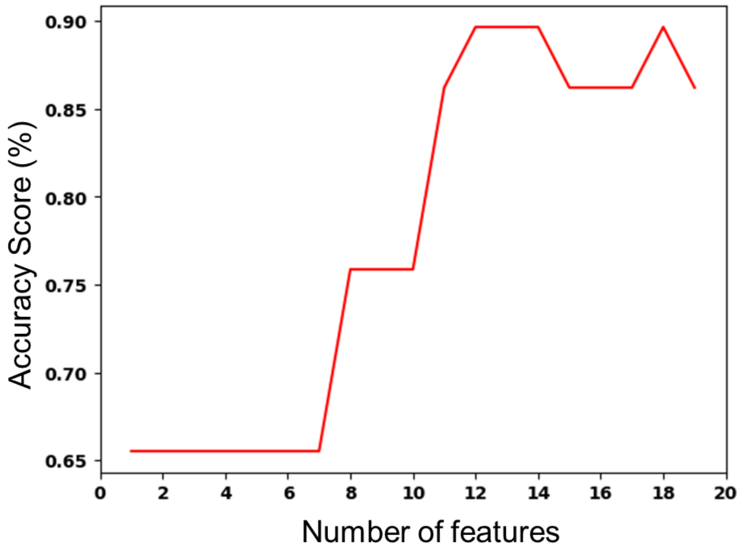

Figure 6.5: Accuracy score vs. number of features plot

Notably, these nine features are sufficient to classify the materials with good accuracy (90%). We could reach good accuracy in the classification prediction as there is a strong inherent relation between the band alignment of 2D perovskites and their molecular and elemental features. We have noticed that the valence band edge of the material is mainly constituted of the organic cation if the HOMO of the organic cation is less stabilised. On the other hand, the conduction band edge of the material is constituted of organic spacer cation when we have a stabilised LUMO orbital of organic cation. This is very much consistent with the previous reports too. *[18-19,41,44]* For example, Shu and coworkers have demonstrated that the frontier molecular orbitals of organic spacer cations as well as inorganic layers can be the key factors for to determine their band alignment types. *[44]* Similarly, Lu and co-workers and Du and co-workers have showed the possibility of four types of intramolecular band alignment quantum wells with changing the different types of organic spacer cations.*[18-19]* Scanlon and co-workers have also shown that metal halide variations keeping the spacer cation fixed can also lead to different band compositions.*[41]* Also, other molecular features such as hydrogen bond donor/acceptor count can be an important factor for the prediction of band alignment types. Molecular feature such as polarizability of the organic spacer cation significantly influences the geometry as well as orbital energies of the cation which have been also shown by Yang and co-workers and we have also studied this in detail theoretically in our previous work.*[45,20]* Hence, there is a good relation between the molecular features and band alignment types. We have also observed there can be a good relation between the band alignment types and elemental features of the organic/inorganic unit. For example, as we go down the halogen group, the HOMO orbital energy increases and therefore dominates the valence band edge of the material. Therefore, for our future analysis we will use these features only.

6.3.5. Classification Metrices

Next, the evaluation of the considered models has been performed. Performance metrices are very useful for evaluating the operation capability of the considered model and gain insights into the dataset containing diverse data points. There are some metrices that evaluate quality of the classification algorithm performance. Here, we have used classification accuracy, F1 score, precision and recall justifying the model. All these we can calculate from the confusion matrix (Section 1.4.4.9, Chapter 1). From the obtained confusion matrix (Figure 6.6, left) with the considered test dataset, we have observed that type I and type II materials have been correctly predicted for 18 and 8 instances, respectively. Interestingly, only once type I material is predicted as type II, whereas type II as type I for twice. So, from this observation, we can conclude that our proposed model can be applicable for the other unexplored materials with a satisfactory accuracy.

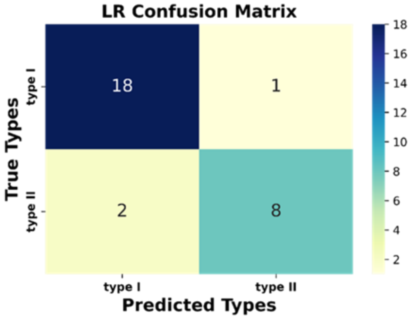

Class	Precision	Recall	f1-score
type I	0.90	0.95	0.92
type II	0.89	0.80	0.84

Figure 6.6: Confusion matrix (left) and classification parameters (right) for type I and type II classification of considered 2D perovskite.

Again, in Figure 6.6 (right) we have tabulated the calculated values of the classification metrices. For the positive class (type I) we got precision, recall and f1-score as 0.90, 0.95 and 0.92, respectively. Whereas, for the negative class these metrices are 0.89, 0.80 and 0.84, respectively. So, the model is ready to implement on the unknown datasets.

In continuation we performed binary classification on the type I and type II materials separately and observed an improved accuracy score. For the binary classification of type I materials into I_a-I_b, with 71 pieces of data and type II materials into II_a-II_b with 32 pieces of data, we have found up to 93%

and 98% average cross-validation accuracy, respectively (Table 6.5). For I_a-I_b binary case we have separated the total 71 data to 50 in the train set and 21 in the test set. And in case of II_a-II_b binary classification where we have total 32 data instances and divided them to 21 and 11 in the train and test sets respectively.

Table 6.5: Optimized hyperparameters and accuracy scores of binary classification between type I_a-I_b and type II_a-II_b and multi class classification between four types (I_a, I_b, II_a, II_b) using logistic regression.

Classification	**Optimized Hyperparameters**	**Cross Validation (Average accuracy)**	**Test Accuracy**
I_a-I_b	C: 0.01, penalty: l2, solver: liblinear	0.93	0.90
II_a-II_b	C: 100, penalty: l2, solver: liblinear	0.98	1.00
Multi class (I_a, I_b, II_a, II_b)	C: 1.0, penalty: l2, solver: liblinear	0.76	0.72

We have further tried to classify the materials to their four distinct classes: I_a, I_b, II_a, II_b. For that we have performed multiclass classification with logistic regression using one vs. rest method and achieved 76% average cross-validation accuracy (Table 6.5). For the multiclass classification we used the same train and test sets that has been used in the I-II binary classification case. That is 74 instances in the train set and 29 instances in the test set. In this case due to imbalanced dataset that means unequal ratio of four classes we have observed low accuracy. Further, we have separated all these three datasets to train-test sets and performed classification to obtain classification metrices and confusion matrix. Although, the overall result is good for I_a-I_b classification, it can be easily understood from confusion matrix (Figure 6.7a) that training of I_b is not proper due to its less number in the dataset. In the case of II_a-II_b binary classification we have a nearly equal ratio of two classes. From the tabulated classification metrices (Table 6.6) and confusion matrix (Figure 6.7b) we can notice very good classification results for the II_a-II_b binary classification. This observation is entirely due to good ratio of two classes in the dataset. So, although we can get a reasonably good confusion matrix in case of type I-II classification, we believe that the confusion matrix results for the prediction of all the individual classes (I_a, I_b, II_a, II_b) with the same model can be improved if we can make a balance in training data for all the individual classes to be predicted. Unfortunately, till date, reported type I_b materials are much less compared to the type I_a materials.

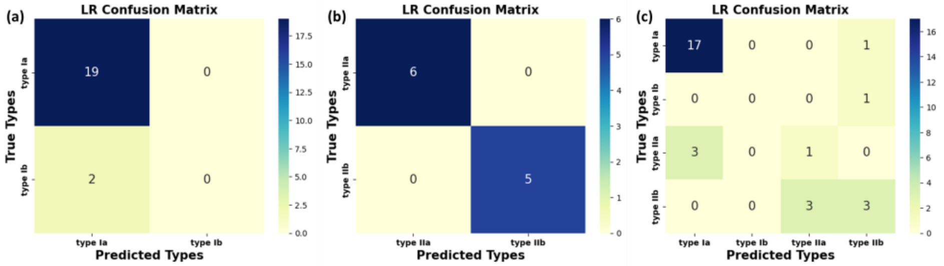

Figure 6.7: Confusion matrix for (a) type II_a and type II_b (b) type II_a and type II_b and (c) multi class classification of considered 2D perovskite.

Table 6.6: Classification metrices

Classification	Class	Precision	Recall	f1-score
Ia-Ib	type I_a	0.90	1.00	0.95
	type I_b	0.00	0.00	0.00
IIa-IIb	type II_a	1.00	1.00	1.00
	type II_b	1.00	1.00	1.00
Multi class (I_a, I_b, II_a, II_b)	type I_a	0.85	0.94	0.89
	type I_b	0.00	0.00	0.00
	type II_a	0.25	0.25	0.25
	type II_b	0.60	0.50	0.55

6.3.6. Model Justification

Table 6.7: Predicted probability of test dataset (the numbers in the compound names are the numbers of the organic cations mentioned in Figure 6.1)

Compound	**Type**	**Predicted probability**	
		Type I	**Type II**
$(22)_2PbI_4$	II	0.23	0.77
$(71)PbCl_4$	II	0.24	0.76
$(71)PbBr_4$	II	0.24	0.76
$(48)PbI_4$	II	0.43	0.57
$(63)PbI_4$	II	0.19	0.81
$(63)PbBr_4$	II	0.19	0.81
$(70)_2PbCl_4$	II	0.74	0.26
$(4)_2PbI_4$	I	0.98	0.02
$(5)_2PbI_4$	I	0.99	0.01
$(6)PbI_4$	I	0.96	0.04
$(59)_2PbI_4$	I	0.79	0.21
$(13)_2PbI_4$	I	0.88	0.12
$(42)PbI_4$	I	0.88	0.12
$(24)_2PbI_4$	I	0.66	0.34
$(25)_2PbI_4$	I	0.85	0.15
$(45)_2PbI_4$	I	0.76	0.24
$(36)_2PbBr_4$	I	0.66	0.34
$(55)_2PbBr_4$	I	0.94	0.06
$(33)_2PbI_4$	I	0.83	0.17
$(34)_2PbI_4$	I	0.93	0.07
$(71)_2SnI_4$	II	0.33	0.67
$(15)_2SnCl_4$	II	0.78	0.22
$(26)PbCl_4$	II	0.69	0.31
$(53)SnI_4$	I	0.99	0.01
$(41)_2SnI_4$	I	0.82	0.18
$(15)_2SnBr_4$	I	0.78	0.22
$(44)_2PbBr_4$	I	0.89	0.11
$(77)PbCl_4$	I	0.88	0.12
$(52)PbI_4$	I	0.47	0.53

We have proposed 17 new perovskite materials to validate our model. These 17 new materials we have designed and calculated their properties using DFT. Accounting the good predictability of the logistic regression algorithm we have applied this algorithm with the optimized hyperparameters to the new modelled dataset and observed an accuracy score of 0.88. Our model fails to predict the cases when there is a strong overlap of organic and inorganic components in the band edges. Hence, our model is capable enough to identify type I and type II materials properly. The materials with their predicted and actual class have been shown in supporting information (Table 6.7). Among the materials we have designed, four are type II band alignment quantum well. Although finding type II material is a challenging task, we became successful to find out four such materials which can be useful for future applications.

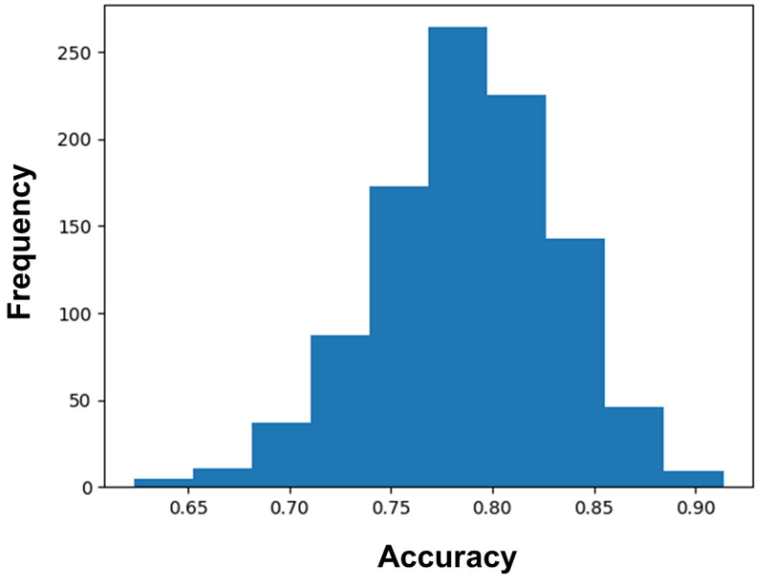

Figure 6.8. Frequency vs. accuracy plot.

Again, we have confirmed the performances of the model by calculating confidence interval using 1000 bootstrap iterations. From these bootstrap iterations, we have found 95% likelihood of classification accuracy between 69% and 87%. However, it can be noticed from the Figure 6.8 that the major portions of the iterations are shifted towards the accuracy score greater than

0.75. It certainly indicates the good predictive capability and as well as stability of the model.

6.3.7. Model Formulation

For the generalizability and transferability of a model, proper formulation from chemical understanding and model analysis is necessary. We have calculated the feature contribution coefficients of the finally selected nine features (Figure 6.9). Implementing these values in logistic regression, we can formulate a probability equation to predict the band alignment type of a 2D perovskite easily.

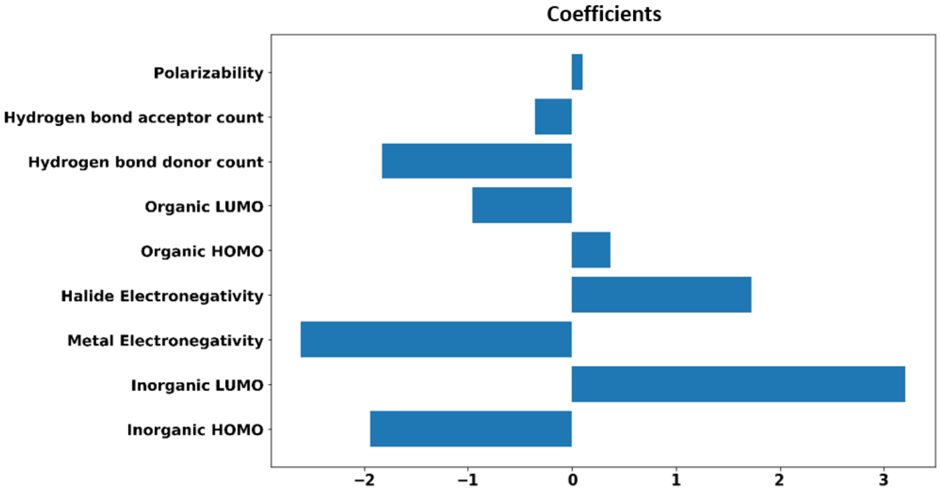

Figure 6.9: Features contribution of the finally selected nine features towards output Y.

According to the logistic regression algorithm the probability of a positive label ($P_{typeI}(x_i)$) can be represented as,

$$P_{typeI}(x_i) = \frac{1}{1+e^{-\sum m_i x_i}} \qquad \ldots (1)$$

$$\log \frac{P_{typeI}}{1-P_{typeI}} = c + \; m_i x_i \qquad \ldots (2)$$

Where, m is the feature contribution coefficient and x is the value of feature.

From the implemented algorithm used for our considered dataset, the derived equation can be expressed as

$$log\frac{P_{typeI}}{1-P_{typeI}} = -1.58 - 1.93 \times IH/eV + 3.20 \times IL/eV - 2.60 \times ME +$$

$$1.72 \times HE + \ 0.37 \times OH/eV - \ 0.96 \times OL/eV - \ 1.82 \times HBDC - \ 0.35 \times$$

$$HBAC + 0.10 \times \alpha/\text{Å}^3 \qquad \text{... (3)}$$

From the feature contribution coefficients, we can obtain the mathematical form of trained ML model and provide chemical insights. Here, from the Figure 6.9 we can see that some features have positive contribution whereas some has negative contribution. Since our calculated orbital energies (HOMO and LUMO of organic and inorganic units) are with negative sign they will give an overall reverse contribution for the classification. That means the positively contributing features are contributing for the negative classes and vice versa.

Inorganic-Organic HOMO/LUMO coefficients are contributing in the following order: inorganic LUMO > inorganic HOMO > organic LUMO > organic HOMO. Inorganic HOMO and organic LUMO have negative contribution coefficients. However, type of band alignment depends on the relative position of these energy levels, and they are highly interdependent with respect to other features as well. Moreover, the inorganic HOMO-LUMO values we have considered as a fixed value for a particular inorganic unit, but this can be changed in presence of different organic spacer cations. Hence, it is difficult to explain in the light of physicochemical perspective.

Electronegativity of metal and halide are contributing for the negative and positive class, respectively. More electronegative halide will make lower energetic molecular orbitals. For a material having highly stable organic LUMO can make the conduction band with organic dominance and stability of the inorganic HOMO might help to form a type I band alignment with organic-organic combination.

Polarizability is also contributing positively as per the feature analysis. This indicates that the more polarisable organic cation will tend to form perovskite with type I band alignment. As we know, highly conjugated organic cations are electron rich in nature and thus more polarisable in nature, and the previous reports demonstrate that such polarisable molecules have small HOMO-LUMO gap.*[46-47]* Hence, we can tune the valance/conduction band edges of the material with polarisable organic cation.

Hydrogen bond donor and acceptor count has negative contribution towards the output that increases the possibility of type II band alignment perovskite material. Hydrogen bond donor count means hydrogens available for formation of H-bonds with inorganic layer halides. Strong H-bonding with the halides will decrease the overlap between halogen and metal, which in turn will increase HOMO and LUMO gap between the inorganic unit. Hydrogen bond acceptor count is responsible for intramolecular H-bonding, which makes the spacer cation rigid and reduce their interaction with the metal halide layer. Smaller interaction with the organic unit will keep the inorganic layer undistorted and the overlap between the metal and halide orbitals will be larger, which will decrease the HOMO LUMO gap of inorganic unit.*[45]* Thus, probability of type II band alignment perovskite increases with high hydrogen bond donor and acceptor nature of the organic unit.

We have analysed the effects of the important features those are mainly contributing to the classification. All these features have some distinct contribution for making the material type I or type II band alignment quantum well. But these features are interdependent to each other. That means no single feature can itself make a material to be in positive class or negative class. Such that one feature is providing a significant contribution to put a perovskite in the positive class, but the material will be in the positive class depending on the performance of the other features.

6.4. Conclusion

In conclusion, we have successfully classified 2D hybrid perovskites to type I and type II band alignment quantum well and extracted the strategy to obtain a specific electronic property as well. Excellent classification accuracy score of 0.90 has been found with the simplest logistic regression algorithm using nine important features. Moreover, utilising feature contribution coefficients, HOMO and LUMO of the inorganic as well as organic units and metal-halogen electronegativities are found to be the most contributing features. Additionally, we have validated our model with unknown 7 hybrid perovskite materials and found reasonably good accuracy score (0.86). Our model has misidentified only one type II material as type I which has merged contribution at the band edge from the both organic and inorganic parts. Apart from this, we have tried to classify among all the four band alignment types (type I_a, I_b, II_a, II_b) using multiclass classification and also classified type I and II towards I_a-I_b and II_a-II_b band alignment types. Finally, we have established an equation for predicting the probability of finding band alignment types based on our calculated feature contribution coefficients. Overall, our proposed strategy opens a new direction to the utilization of ML for the screening of 2D perovskites for various applications.

6.5. References

1. Kojima A., Teshima K., Shirai Y., Miyasaka T. (2009), Organometal Halide Perovskites as Visible-Light Sensitizers for Photovoltaic Cells, J. Am. Chem. Soc., 131, 6050−6051 (DOI: 10.1021/ja809598r)
2. Lee M. M., Teuscher J., Miyasaka T., Murakami T. N., Snaith H. J. (2012), Efficient hybrid solar cells based on meso-superstructured organometal halide perovskites, Science, 338, 643−647 (DOI: 10.1126/science.1228604)
3. Burschka J., Pellet N., Moon S.-J., Humphry-Baker R., Gao P., Nazeeruddin M. K., Grätzel M. (2013), Sequential deposition as a route

to high-performance perovskite-sensitized solar cells, Nature, 499, 316 (DOI: 10.1038/nature12340)

4. Jena A. K., Kulkarni A., Miyasaka T. (2019), Halide Perovskite Photovoltaics: Background, Status, and Future Prospects, Chem. Rev., 119, 3036−3103 (DOI: 10.1021/acs.chemrev.8b00539)
5. Frost J. M., Butler K. T., Brivio F., Hendon C. H., Schilfgaarde M. van, Walsh A. (2014), Atomistic Origins of High-Performance in Hybrid Halide Perovskite Solar Cells, Nano Lett., 14, 2584− 2590 (DOI: 10.1021/nl500390f)
6. Zhao Y., Zhu K. (2014), Optical bleaching of perovskite $(CH_3NH_3)PbI_3$ through room-temperature phase transformation induced by ammonia, Chem. Commun., 50, 1605−1607 (DOI: 10.1039/C3CC48522F)
7. Smith I. C., Hoke E. T., Solis-Ibarra D., McGehee M. D., Karunadasa H. I. (2014), A layered hybrid perovskite solar-cell absorber with enhanced moisture stability, Angew. Chem., Int. Ed., 53, 11232−11235 (DOI: 10.1002/anie.201406466)
8. Stoumpos C. C., Cao D. H., Clark D. J., Young J., Rondinelli J. M., Jang J. I., Hupp J. T., Kanatzidis M. G. (2016), Ruddlesden–Popper Hybrid Lead Iodide Perovskite 2D Homologous Semiconductors, Chem. Mater., 28, 2852−2867 (DOI: 10.1021/acs.chemmater.6b00847)
9. Quan L. N., Yuan M., Comin R., Voznyy O., Beauregard E. M., Hoogland S., Buin A., Kirmani A. R., Zhao K., Amassian A., Kim D. H., Sargent E. H. (2016), Ligand-Stabilized Reduced-Dimensionality Perovskites, J. Am. Chem. Soc., 138, 2649−2655 (DOI: 10.1021/jacs.5b11740)
10. Katan C., Mercier N., Even J. (2019), Quantum and Dielectric Confinement Effects in Lower-Dimensional Hybrid Perovskite Semiconductors, Chem. Rev., 119, 3140−3192 (DOI: 10.1021/acs.chemrev.8b00417)
11. Sapori D., Kepenekian M., Pedesseau L., Katan C., Even J. (2016), Quantum confinement and dielectric profiles of colloidal nanoplatelets

of halide inorganic and hybrid organic–inorganic perovskites, Nanoscale, 8, 6369−6378 (DOI: 10.1039/C5NR07175E)

12. Wei K., Jiang T., Xu Z., Zhou J., You J., Tang Y., Li H., Chen R., Zheng X., Wang S., Yin K., Wang Z., Wang J., Cheng X. (2018), Ultrafast Carrier Transfer Promoted by Interlayer Coulomb Coupling in 2D/3D Perovskite Heterostructures Laser Photonics Rev., 12, 1800128. (DOI: 10.1002/lpor.201800128)
13. Chondroudis K., Mitzi D. B. (1999), Electroluminescence from an Organic−Inorganic Perovskite Incorporating a Quaterthiophene Dye within Lead Halide Perovskite Layers, Chem. Mater., 11, 3028− 3030 (DOI: 10.1021/cm990561t)
14. Liang D., Peng Y., Fu Y., Shearer M. J., Zhang J., Zhai J., Zhang Y., Hamers R. J., Andrew T. L., Jin S. (2016), Color-Pure Violet-Light-Emitting Diodes Based on Layered Lead Halide Perovskite Nanoplates, ACS Nano, 10, 6897−6904 (DOI: 10.1021/acsnano.6b02683)
15. Yin J., Li H., Cortecchia D., Soci C., Bredas J.-L. (2017), Excitonic and Polaronic Properties of 2D Hybrid Organic–Inorganic Perovskites, ACS Energy Lett., 2, 417−423 (DOI: 10.1021/acsenergylett.6b00659)
16. Blancon J. C., Stier A. V., Tsai H., Nie W., Stoumpos C. C., Traore B., Pedesseau L., Kepenekian M., Katsutani F., Noe G. T., Kono J., Tretiak S., Crooker S. A., Katan C., Kanatzidis M. G., Crochet J. J., Even J., Mohite A. D. (2018), Scaling law for excitons in 2D perovskite quantum wells, Nat. Commun., 9, 2254 (DOI: 10.1038/s41467-018-04659-x)
17. Liu C., Huhn W., Du K.-Z., Vazquez-Mayagoitia A., Dirkes D., You W., Kanai Y., Mitzi D. B., Blum V. (2018), Tunable Semiconductors: Control over Carrier States and Excitations in Layered Hybrid Organic-Inorganic Perovskites, Phys. Rev. Lett., 121, 146401 (DOI: 10.1103/PhysRevLett.121.146401)
18. Zhang L., Zhang X., Lu G. (2020), Intramolecular Band Alignment and Spin-Orbit Coupling in Two-Dimensional Halide Perovskites, J. Phys. Chem. Lett., 11, 6982−6989 (DOI: 10.1021/acs.jpclett.0c02135)

19. Han D., Chen S., Du M.-H. (2021), Role of Polycyclic Aromatic Alkylammonium Cations in Tuning the Electronic Properties and Band Alignment of Two-Dimensional Hybrid Perovskite Semiconductors, J. Phys. Chem. Lett., 12, 9754−9760 (DOI: 10.1021/acs.jpclett.1c02603)
20. Mahal E., Mandal S. C., Pathak B. (2022), Band Edge Engineering of 2D Perovskite Structures through Spacer Cation Engineering for Solar Cell Applications, J. Phys. Chem. C, 126, 9937–9947 (DOI: 10.1021/acs.jpcc.2c01840)
21. Lu S., Zhou Q., Ouyang Y., Guo Y., Li Q., Wang J. (2018), Accelerated discovery of stable lead-free hybrid organic-inorganic perovskites via machine learning, Nat Commun, 9, 3405 (DOI: 10.1038/s41467-018-05761-w)
22. Saidi W.A., Shadid W., Castelli I.E. (2020), Machine-learning structural and electronic properties of metal halide perovskites using a hierarchical convolutional neural network, npj Comput. Mater., 6, 36 (DOI: 10.1038/s41524-020-0307-8)
23. Wan Z., Wang Q.D., Liu D., Liang J. (2021), Prediction of band gap for 2D hybrid organic–inorganic perovskites by using machine learning through molecular graphics descriptors, New J. Chem., 45, 9427-9433 (DOI: 10.1039/D1NJ01518D)
24. Lyu R., Moore C. E., Liu T., Yu Y., Wu Y. (2021), Predictive Design Model for Low-Dimensional Organic-Inorganic Halide Perovskites Assisted by Machine Learning, J. Am. Chem. Soc., 143, 12766− 12776 (DOI: 10.1021/jacs.1c05441)
25. Giannozzi P., Baroni S., Bonini N., Calandra M., Car R., Cavazzoni C., Ceresoli D., Chiarotti G. L., Cococcioni M., Dabo I., Corso A. Dal, Gironcoli S. de, Fabris S., Fratesi G., Gebauer R., Gerstmann U., Gougoussis C., Kokalj A., Lazzeri M., Martin-Samos L., Marzari N., Mauri F., Mazzarello R., Paolini S., Pasquarello A., Paulatto L., Sbraccia C., Scandolo S., Sclauzero G., Seitsonen A. P., Smogunov A., Umari P., Wentzcovitch R. M. (2009), QUANTUM ESPRESSO: a

modular and open-source software project for quantum simulations of materials, J. Phys.: Condens. Matter, 21, 395502 (DOI: 10.1088/0953-8984/21/39/395502)

26. Heyd J., Scuseria G. E., Ernzerhof M. (2003), Hybrid functionals based on a screened Coulomb potential, J. Chem. Phys., 118, 8207−8215 (DOI: 10.1063/1.1564060)
27. Du M.-H. (2015), Density Functional Calculations of Native Defects in $CH_3NH_3PbI_3$: Effects of Spin–Orbit Coupling and Self-Interaction Error, J. Phys. Chem. Lett., 6, 1461-1466 (DOI: 10.1021/acs.jpclett.5b00199)
28. Monkhorst H. J., Pack J. D. (1976), Special points for Brillouin-zone integrations, Phys. Rev. B: Solid State, 13, 5188−5192 (DOI: 10.1103/PhysRevB.13.5188)
29. Mahata A., Mosconi E., Meggiolaro D., De Angelis F. (2020), Modulating Band Alignment in Mixed Dimensionality 3D/2D Perovskites by Surface Termination Ligand Engineering, Chem. Mater., 32, 105−113 (DOI: 10.1021/acs.chemmater.9b02560)
30. Frisch M. J., Trucks G. W., Schlegel H. B., Scuseria G. E., Robb M. A., Cheeseman J. R., Scalmani G., Barone V., Mennucci B., Petersson G. A., Nakatsuji H., Caricato M., Li X., Hratchian H. P., Izmaylov A. F., Bloino J., Zheng G., Sonnenberg J. L., Hada M., Ehara M., Toyota K., Fukuda R., Hasegawa J., Ishida M., Nakajima T., Honda Y., Kitao O., Nakai H., Vreven T., Montgomery J. A., Peralta, Jr. J. E., Ogliaro F., Bearpark M., Heyd J. J., Brothers E., Kudin K. N., Staroverov V. N., Keith T., Kobayashi R., Normand J., Raghavachari K., Rendell A., Burant J. C., Iyengar S. S., Tomasi J., Cossi M., Rega N., Millam J. M., Klene M., Knox J. E., Cross J. B., Bakken V., Adamo C., Jaramillo J., Gomperts R., Stratmann R. E., Yazyev O., Austin A. J., Cammi R., Pomelli C., Ochterski J. W., Martin R. L., Morokuma K., Zakrzewski V. G., Voth G. A., Salvador P., Dannenberg J. J., Dapprich S., Daniels

A. D., Farkas O., Foresman J. B., Ortiz J. V., Cioslowski J., Fox D. J. (2009), Gaussian 09, Revision B.01; Gaussian Inc.: Wallingford, CT.

31. Hehre W. J., Ditchfield K., Pople J. (1972), A. Self—Consistent Molecular Orbital Methods. XII. Further Extensions of Gaussian—Type Basis Sets for Use in Molecular Orbital Studies of Organic Molecules, J. Chem. Phys., 56, 2257–2261 (DOI: 10.1063/1.1677527)
32. Hariharan P. C., Pople J. A. (1973), The influence of polarization functions on molecular orbital hydrogenation energies, Theor. Chim. Act., 28, 213–222 (DOI: 10.1007/bf00533485)
33. Krishnan R., Binkley J. S., Seeger R., Pople J. A. (1980), Self-consistent molecular orbital methods. XX. A basis set for correlated wave functions, J. Chem. Phys., 72, 650–654 (DOI: 10.1063/1.438955)
34. Becke A. D. (1988), Density-functional exchange-energy approximation with correct asymptotic behavior, Phys. Rev. A, 38, 3098–3100 (DOI: 10.1103/PhysRevA.38.3098)
35. Becke A. D. (1993), Density-functional thermochemistry. III. The role of exact exchange, J. Chem. Phys., 98, 5648–5652 (DOI: 10.1063/1.464913)
36. Becke A. D. (1997), Density-functional thermochemistry. V. Systematic optimization of exchange-correlation functionals, J. Chem. Phys., 107, 8554–8560 (DOI: 10.1063/1.475007)
37. Becke A. D. (1993), A new mixing of Hartree–Fock and local density-functional theories, J. Chem. Phys., 98, 1372–1377 (DOI: 10.1063/1.464304)
38. Lee C., Yang W., Parr R. G. (1988), Development of the Colle-Salvetti correlation-energy formula into a functional of the electron density, Phys. Rev. B: Condens. Matter Mater. Phys., 37, 785–789 (DOI: 10.1103/PhysRevB.37.785)
39. Marchenko E. I., Fateev S. A., Petrov A. A., Korolev V. V., Mitrofanov A., Petrov A. V., Goodilin E. A., Tarasov A. B. (2020), Database of Two-Dimensional Hybrid Perovskite Materials: Open-Access

Collection of Crystal Structures, Band Gaps, and Atomic Partial Charges Predicted by Machine Learning, Chem. Mater., 32, 7383−7388 (DOI: 10.1021/acs.chemmater.0c02290)

40. Xue J., Wang R., Chen X., Yao C., Jin X., Wang K.-L., Huang W., Huang T., Zhao Y., Zhai Y., Meng D., Tan S., Liu R., Wang Z.-K., Zhu C., Zhu K., Beard M. C., Yan Y., Yang Y. (2021), Reconfiguring the band-edge states of photovoltaic perovskites by conjugated organic cations, Science, 371, 636−640. (DOI: 10.1126/science.abd4860)
41. Wang Z., Ganose A. M., Niu C., Scanlon D. O. (2019), Two-dimensional eclipsed arrangement hybrid perovskites for tunable energy level alignments and photovoltaics, J. Mater. Chem. C, 7, 5139−5147 (DOI: 10.1039/C9TC01325C)
42. Pedregosa F., Varoquaux Gramfort G., A., Michel V., Thirion B., Grisel O., Blondel M., Prettenhofer P., Weiss R., Dubourg V., Vanderplas J., Passos A., Cournapeau D. (2011), Scikit-learn: Machine learning in Python, J. Mach. Learn. Res., 12, 2825–2830
43. Tibshirani R. (1996), Regression shrinkage and selection via the lasso, J. R. Stat. Soc. Ser. B. 58, 267−288 (DOI: 10.4236/ojs.2020.101009)
44. Yao Y., Cao D., Yan J., Zhang M., Chen X., Shu H. (2022), Spacer Cation Engineering of Two-Dimensional Hybrid Perovskites with Tunable Band Alignment and Optoelectronic Properties, J. Phys. Chem. C, 126, 8408–8416 (DOI: 10.1021/acs.jpcc.2c01969)
45. Ni C., Huang Y., Zeng T., Chen D., Chen H., Wei M., Johnston A., Proppe A. H., Ning Z., Sargent E. H., Hu P., Yang Z. (2020), Angew. Chem., Int. Ed., 59, 13977−13983 (DOI: 10.1002/anie.202006112)
46. Kamada K., Ueda M., Nagao H., Tawa K., Sugino T., Shmizu Y., Ohta K. (2000), Molecular Design for Organic Nonlinear Optics: Polarizability and Hyperpolarizabilities of Furan Homologues Investigated by Ab Initio Molecular Orbital Method, J. Phys. Chem. A, 104, 4723−4734 (DOI: 10.1021/jp993806y)

47. Jezowski S. R., Baer R., Monaco S., Mora-Perez C. A., Schatschneider B. (2017), Unlocking the electronic genome of halogenobenzenes, Phys. Chem. Chem. Phys., 19, 4093−4103 (DOI: 10.1039/C6CP07403K)

Chapter 7

Scope for Future Works

7.1. Scope for Future Works

This thesis work involves understanding of the stability, structural as well as electronic properties of 2D hybrid perovskites with variation in spacer cation using density functional theory, molecular dynamics simulations and machine learning methods. In the first chapter, we have analysed the moisture stability of 2D perovskites, revealed their possible degradation route and identified the most stable surface in contact with water. Following this study, finding out the proper cation dependence of perovskite stability in humid environments and identifying the features of spacer cations that would provide the material better stability needs to be explored. Also, how the stability and degradation behaviour changes with the variation of metal and halide atoms would be an important area to focus on in perovskite research. Electronic structure of the 2D perovskites in presence of moisture could be another direction to investigate. How the band gap, charge carrier mobility, and optical absorption of the material are affected after interaction with water molecules need to be explored. In our next chapter analysing the structure property relationship of 2D perovskites we found strong correlation between M-X-M bond angle and band gap. In recent years scientists have shown great potential of machine learning (ML) algorithms in development and understanding of chemical problems. In this regard a ML based approach majorly focussed on the structure property relationship of 2D perovskites could be explored. By applying an unsupervised learning approach, we can gain valuable insights into this topic. Also, we have shown the importance of spacer cation engineering to take control over band edge composition of perovskite material. Following this, the defect properties of 2D perovskites could be an interesting topic that needs to be investigated. Formation energies of cation generated defect states for the perovskites having cation dominated band edges could reveal some unusual behaviour that has impact on the optoelectronic property of the material. In addition, influence of external pressure on the electronic structure of the 2D perovskites is another area to be focused. Investigation on the Sn and Ge based perovskites should be done to find better alternatives of Pb based perovskites. Since the Sn and Ge metals have a high tendency to oxidation thereby machine learning prediction could accelerate the process of finding stable and efficient Sn and Ge based 2D perovskites. In the fifth chapter by aligning the energy levels of organic and inorganic parts of 2D perovskites we have find out some preferred organic-inorganic combinations having potential for their applications in LEDs. Employment of machine learning methods in finding such combination is another way to enrich the perovskite field to enhance their application in LEDs. In the last chapter of this thesis, we have performed machine learning based classification of 2D perovskites to their intramolecular band alignment types. In this regard machine learning based prediction of electronic structure of 2D perovskites is a necessary work to do. More specifically, formulation of machine learning models for the prediction of density of states, band structure, optical properties, and charge carrier mobilities efficiently using easily obtainable molecular or elemental features would be highly beneficial in the perovskite research.